UNIVERSITÀ DEGLI STUDI
DI MODENA E REGGIO EMILIA

Dottorato di ricerca in Models and Methods for Materials and Environmental Sciences (M3ES)

Ciclo XXXV

Computer simulation of nucleation and crystallization of silicate glasses

Federica Lodesani

Relatore (Tutor): Prof. Alfonso Pedone

Coordinatore del Corso di Dottorato: Prof. Stefano Lugli

TABLE OF CONTENTS

ABSTRACT

Glass materials can crystallize in particular conditions. When the crystallization process happens in an uncontrolled way a loss of performance and transparency is obtained, and we talk about devitrification. Instead, controlled crystallization is desired because it improves mechanical, optical and chemical properties, obtaining glass-ceramic materials. Glass-ceramics are polycrystalline materials obtained by the partial crystallization of crystalline phases in a glass matrix, through a thermal process. The first glass-ceramic discovered was based on Lithium Disilicate ($Li_2Si_2O_5$, LS_2) composition and its nucleation has been extensively studied to improve the manufacturing process and enhance the properties. Although LS_2 is mainly known to nucleate homogeneously, researchers have also observed the participation of metastable phases (such as Lithium Metasilicate, LS) in nucleation. Experimentally it is difficult to obtain clear information about the formation of the very first embryo of crystallization because it is a phenomenon that takes place at the nanometer level. On the other hand, computational techniques that study phenomena at an atomistic level can provide information at the interested length scale. Molecular Dynamics is widely used in the study of the structure and mechanical properties of glasses, but only recently its potentialities have been tested in the field of nucleation. The main problem of MD is the accessible timescale: glasses have a high viscosity leading to nucleation time longer than accessible MD simulation time. Metadynamics (MetaD) has been successfully applied to study the nucleation of several molecular or metallic systems. However, its application in the glass-forming system is limited to SiO_2, giving excellent results.

My PhD project was focused on the application of MD and MetaD to study LS_2 crystallization using several methods and protocols. The following are summaries of the chapters that make up the thesis itself.

The first chapter is a presentation of glasses and glass ceramics, pointing out the most important features of these materials. A brief literature review of experimental and computational studies about the crystallization of LS_2 is also reported.

The second chapter describes some of the most popular nucleation theories. The Classical Nucleation Theory, CNT, is based on the formation of a spherical nucleus that can grow when it reaches a critical dimension. Although CNT is widely accepted and used, it has some shortcomings derived from the necessary approximations that are made in the formulation. The Generalized Gibbs approach, GGA, is an evolution of the CNT that considers the formation of intermediate states between the liquid and the crystal, while the two-step method separates the nucleation process in density and structural fluctuations.

The third chapter is dedicated to the presentation of computational methods employed in this thesis, starting from Molecular Dynamics and the force-field used to simulate the system, moving to Metadynamics, including the reweighting technique to recover the free energy surface (FES) from the biased simulation, and the temperature rescaling method used to recover the FES at a temperature starting from the simulation

at a different temperature. Finally, a presentation of Collective Variables (CVs), which are used either to drive a simulation or to analyze it.

The calculation of the melting temperature is a requirement to study the crystallization by computational technique because it depends on the employed force-field and is thus different from the experimental one. In chapter four the mechanical and thermodynamic melting temperatures of LS_2 and LS are determined. The mechanical melting temperature, obtained following the phase transition during the heating of the system, overestimates the computational melting temperature because it depends on the heating rate used and on the hysteresis of the system. The phase-coexistence method is used to calculate the thermodynamic melting temperature, which is more reliable because it seeks the temperature at which a system composed of both crystal and liquid phases interfaced, can coexist without dissolving nor crystallizing.

In chapter five, we developed two approaches to studying nucleation with MD. The first is an exploring method, which looks for structural similarities between the crystal and the glass and identifies a propensity for the crystallization of that crystal. The presence of crystalline embryos of LS_2, LS and LP (Li_3PO_4) was investigated in bulk and surface models of glasses with the stoichiometric composition of LS_2 and with the inclusion of a small amount of P_2O_5, LS_2P1 ($33Li_2O\ 66SiO_2\ 1P_2O_5$). LS_2 embryos are found preferentially in the bulk assisted by the presence of the P_2O_5, while LS embryos form on the surfaces, due to a higher concentration of Li ions.

The Free Energy Seeding method, FESM, is presented in the same chapter, and used to extract thermodynamic information of crystallization in a glass matrix. The critical radii and the activation energies extracted for LS_2 and LS are in fair agreement with experimental data, even though with a large error on the nucleation free energies. Interfacial energy is considered intrinsically using this method. Studying the change of the Steinhardt order parameter from the center of the nucleus to the glass matrix, the width of the interface is investigated, and increases as the temperature increases.

In the sixth chapter, the crystallization of β-cristobalite from SiO_2 melt is used as a prime example for testing MetaD simulation. We have investigated the effect of MetaD parameters, temperature and size dimensions on the convergence of the simulations and the estimation of the Free Energy Surfaces. Advice on how to set up a MetaD simulation with glass-forming liquids is provided, and the efficiency of the temperature-rescaling method is proved.

Finally, MetaD has been applied to the LS_2 system to study its nucleation mechanism in chapter 7. The CV chosen for driving the MetaD simulation is the intensity of a particular X-ray diffraction peak. One CV is used initially, and one crystallization path is observed, with the exploration of a small region of the phase space. The FES associated with this transformation is extracted and a step mechanism is recognized. When two CVs are used a much broader phase space is explored, giving access to three distinct nucleation pathways. The most favorable one passes through the formation of a disordered layered structure (obtained

also with 1 CV). The second pathway involves the formation of phase-separated structures composed of nuclei of β-cristobalite crystals surrounded by lithium-rich phases in which metasilicate chains are formed. The conversion of these structures to the stable lithium disilicate crystal involves an intermediate structure whose silicate layers are connected by silicate rings with a low energy barrier. The third pathway is highly unlikely because of the huge energy barrier involved. This path also involves the passage through a phase-separated structure of an indefinite silica region surrounded mainly by amorphous lithium oxide.

Chapter 1. Introduction

Crystallization is a ubiquitous phenomenon and highly relevant to many industrial and technological applications (e.g., bone formation, pharmaceuticals, meteorology, and metallurgy) (1–4). Understanding this process is a basic requirement in glass science for either developing glass-ceramic materials with tailored properties or avoiding uncontrolled devitrification.

Devitrification, mostly observed on the glass surface, is an undesired phenomenon in glass manufacturing because the formation of crystals in the products often deteriorates their transparency, strength, and in general, their performances. In the case of nuclear waste vitrification, radiogenic heat induces the formation of soluble crystalline phases (5,6), resulting in radioactive pollution due to the leakage of radioactive waste from the glassy matrix. On the other hand, technologies for controlling crystallization have contributed to society since they enable us to develop glass-ceramic products with exceptional optical, mechanical and chemical properties (7). Thus, knowledge of the mechanism, kinetics and thermodynamics of crystal nucleation and crystallization in oxide glass is fundamental to designing a glass-ceramic system that exactly fulfills the requirements for any application.

Crystallization is a two-step process involving nucleation and crystal growth. Nucleation starts with the appearance of subcritical crystalline nuclei, which must reach a critical dimension to initiate the growth of the crystal. The formation of nuclei can occur through two mechanisms: heterogeneous and homogeneous. Heterogeneous, or surface, nucleation is triggered by the presence of foreign solid particles, impurities, catalysts, or the surface. On the other hand, homogeneous nucleation starts from the bulk, from random fluctuations of the structure that lead to the formation of the crystalline embryo. Among silicate glasses, there are compositions that are more reluctant to homogeneously crystallize, due to the stability of the liquid, the crystalline phase, or the viscosity. Most glass-forming substances, in fact, undergo surface nucleation and there are instead only a few cases where the predominant and favorable nucleation occurs in the bulk (8).

Crystallization and glass formation are competitive processes, and nucleation is the “bottleneck” of crystallization; therefore, it is fundamental to understand the thermodynamics and kinetics of this transformation. Unraveling the origin of the nucleation mechanism in glass forming liquids is still a challenging issue in the glass science community. Several theories have been developed to describe the thermodynamics and kinetics of nucleation, such as the classical nucleation theory (CNT) or the two-step

model presented in chapter 2. However, the identification of the sub-nanometer nuclei hampers the clear observation of nucleation dynamics at the atomic scale, limiting the descriptions proposed by the theories, which are usually based on experimental observations. For these reasons, in recent years, computational techniques, such as molecular dynamics, have been applied to study nucleation.

Among computational techniques, molecular dynamics (MD) is established to be the most efficient in glass science, especially to obtain a description of the microscopic structure and mechanical properties (9–11). MD allows the simulation of systems containing up to tens of thousands of atoms, giving a reliable description of the glass studied. Moreover, it is useful to describe the dynamics of the system up to microseconds. However, the main issue in studying nucleation in glassy systems by molecular dynamics is their slow crystallization rate and high viscosity, which make this phenomenon a rare event and not accessible in the simulation time.

In this PhD project, supported by AGC Inc. (Japan), we have applied and developed suitable computational protocols and techniques to approach this process in vitreous materials already investigated experimentally, such as silica (SiO_2) and lithium disilicate ($Li_2O{\cdot}2\ SiO_2$: LS_2). Prediction of the nucleation features in more complex systems is the ultimate purpose of our investigation.

1.1. Definition of glass

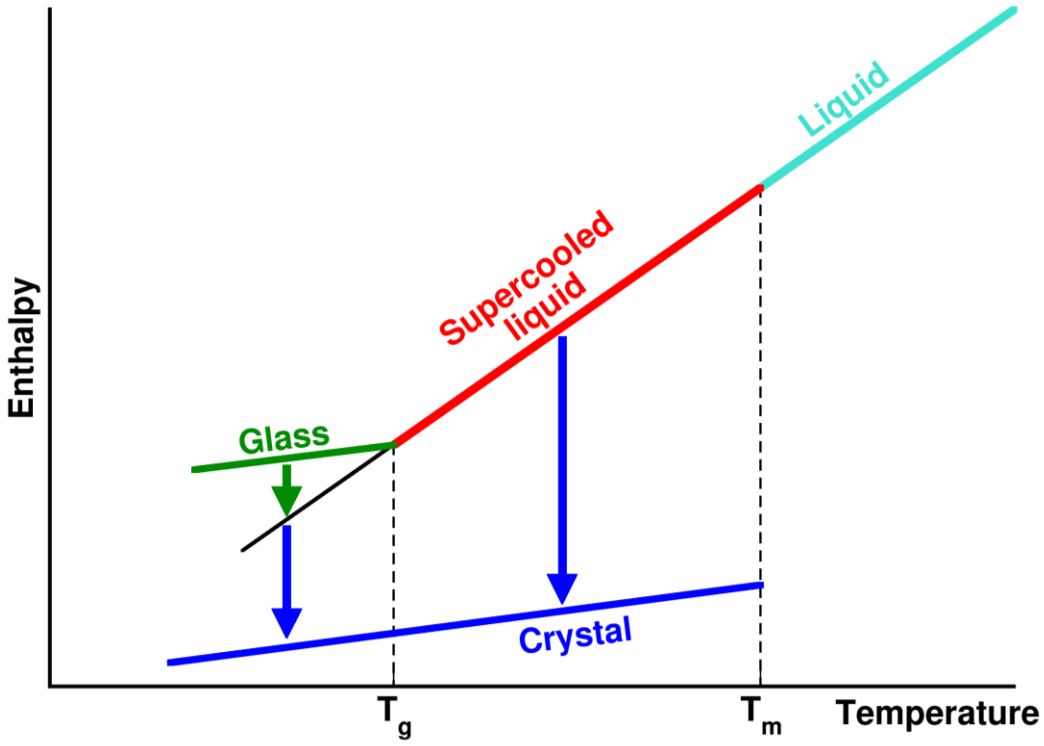

FIG. 1.1. Enthalpy versus temperature plot for a generic glass-forming material.

"Glass is a nonequilibrium, non-crystalline condensed state of matter that exhibits a glass transition. The structure of glasses is similar to that of their parent supercooled liquids (SCL), and they spontaneously relax toward the SCL state. Their ultimate fate, in the limit of infinite time, is to crystallize."

There exist several definitions to describe the glass state, but the one proposed by Zanotto and Mauro in a recent paper (12) is probably one of the most accurate and complete, and it is commonly understood using the enthalpy versus temperature diagram, in figure 1.1.

Liquids that are stable thermodynamically exist only at temperatures higher than the melting point, T_m, while below this temperature, the crystalline phase is the most thermodynamically stable structure, which is characterized by a short, medium and long-range order. The crystalline phases are obtained when a liquid is cooled down with a sufficiently slow quenching rate below T_m. Some materials have a very slow crystallization rate; thus, they can be undercooled below T_m without crystallizing, obtaining the so-called "supercooled liquid", SCL. The SCL is a metastable phase that exists between the T_m and glass transition temperature, T_g, and eventually, after a certain time, it undergoes crystallization, if it overcomes a thermodynamic barrier. The time necessary for SCL to crystallize depends mainly on the temperature and the chemical composition of the material, and some materials may reach the vitreous state without crystallizing, when the crystallization rate is very slow. The glassy state exits below the glass transition temperature, T_g, and it is thermodynamically unstable, therefore, spontaneously relaxes to the SCL state, at any temperature different from 0 K. Glasses are characterized, unlike crystal state, by a short, sometimes medium-range order, but they lack in long-range order. The T_g is defined as the temperature at which the glass transition takes place, and the average relaxation time of the SCL, τ_R, is about of the same order of magnitude of the observation time, t_{obs}, experimental time during which an event is observed. Below T_g the relaxation time, τ_R, is larger than the observation time, thus apparently the liquid "freezes" without crystallizing and the atoms are undetectably moving. Either way, at any temperature different from 0 K, for observation time sufficiently long, $t_{obs} \gg \tau_R$, any glass or SCL relaxes and finally crystallizes.

In the definition proposed at the beginning there is no limitation to the chemical nature of the glass material. In the past century numerous glass compositions have been discovered: from oxide glasses, most traditionally known, but still subject of countless studies because of their versatility and almost infinite possibilities in application they offer; relatively novel non-oxide glasses, such as chalcogenide, fluoride, bromide, oxyfluoride, oxynitride and others (13,14). Moreover, the number of known organic, polymer and metallic alloys glass materials is increasing (15,16). Glasses are an outstanding class of materials with a wide variety of possible applications and opportunities for improvement.

1.2. Silicate glasses and the atomic-scale structure

Oxide glasses are a class of materials that contain one oxide or a combination of several oxides to impart certain properties to the material (17). The backbone of oxide glasses is made up of network formers that

form covalent bonds with oxygen. The most common glass-forming non-metal oxides are silica (SiO_2), borate (B_2O_3) and phosphate (P_2O_5). The network former cations are connected to one another by bridging oxygen (BO), creating a three-dimensional network. The high T_m and high T_g of oxide glasses are determined by the presence of covalent bonds between oxygen and non-metal cations, making their industrial production highly expensive.

Network modifier oxides like Li_2O, Na_2O and K_2O are added to lower the working temperatures (18). These metal ions, mainly alkaline or alkaline earth, form ionic bonds with oxygen and generate non-bridging oxygen (NBO) in the glass forming network. The presence of metallic ions reduces the connectivity and the number of covalent bonds in the glass, with the consequent decrease in the working temperatures. Some other oxides can be added to the glass composition for substituting the former cations in the network. These oxides can behave either as network formers or as modifiers, which is why they are called intermediates. TiO_2, PbO and Al_2O_3 are a couple of examples (19–21).

The silicate glasses, on which this work is focused, are largely utilized as bulk glass in windows, containers, and other applications (22,23). They are made of SiO_2 mixed with network modifiers oxides and/or other additives. The network-forming cations are silicon atoms, which combine with oxygen atoms to form tetrahedral structural units with four Si-O bonds (24,25).

Glass structure is investigated at the short and medium-range order. The short-range order refers to the local order around cations (bond distances, intra-tetrahedral angles and coordination numbers). The medium-range order is usually described by reporting the Q^n distributions, where Q stands for quaternary and indicates the tetrahedral coordination and n is the number of BOs bonded to the Si atom. In pure SiO_2, all Si atoms are connected to 4 BOs, and the network consists of only Q^4 units. When network modifiers are added to the composition, NBOs are formed, and a distribution of different Q^n species is generated. The possible Q^n species are represented in figure 1.2. The distribution of Q^n species provides an indication of the degree of polymerization of the structure.

The connectivity of the network formers, the distance correlations between network formers and network modifiers, the spatial distribution of the network modifier species, as well as the ring size distributions, all contribute to the description of the intermediate-range order.

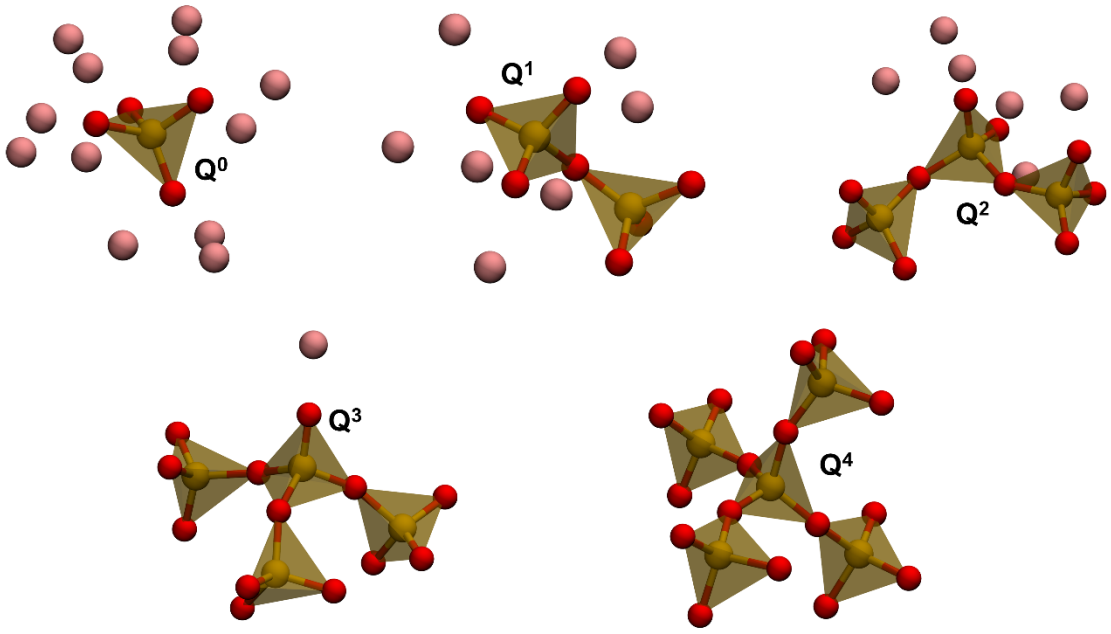

FIG. 1.2. Q^n structural units. Silicon atoms are represented with yellow tetrahedra, red spheres are oxygen and pink spheres are a generic modifier cation.

1.3. Glass ceramics

Glass-ceramics (GC) are polycrystalline materials formed through the controlled nucleation and partial crystallization of inorganic glasses (26) with one or more crystalline phases dispersed in the glass matrix. The degree of crystallinity varies between 0.5 % and 99.5 %, but it is generally between 30 – 70 %.

The manufacture of glass-ceramics materials is based on a simple thermal process properly devised to control nucleation and crystal growth. An optimal GC product should be composed of nanosized and randomly oriented grains generally without the formation of voids, microcracks or other porosity. The productive process is divided into two steps. During the first step, the glass is produced with the fast quench of a melt, with the desired shape. In the second step the glass is heated up to a temperature near the glass transition temperature, T_g, to allow structural rearrangement and achieve nucleation, then the system is heated up to a higher temperature to allow the growth of crystals (27). This second thermal process can be repeated several times. In most cases, some nucleating agents are added to the glass composition to improve the nucleating process, such as TiO_2, ZrO_2, CeO_2, Fe_2O_3 (28), non-metal oxides, P_2O_5 (29,30), or colloidal metal nanoparticles (31).

The material produced has indeed many advantages: relatively fast productive process, the possibility to tailor the nano and micro-structure, very low or absence of porosity, the possibility of spanning a large variety of compositions. The properties of GC materials depend on both the composition and the micro-structure. The chemical composition controls the workability and the glass-forming ability, while the micro-structure affects most of the mechanical and optical properties (32).

The peculiarities of these materials have led to the development of products that find applications both in common use and in specialized fields. Non-porous materials and materials with a low thermal expansion coefficient can be employed in the production of pots, plates or mirror for telescopes, GC insulator are used in the hard-disk technology, while the high toughness, strength and opalescence of GC such lithium disilicate, are exploited in dentistry for teeth restoration (33).

It is thus clearly important to understand the kinetic and thermodynamic characteristics of the nucleation process, to develop and make the most of these extraordinary materials and meet the requirements to any application (34).

1.4. An interesting case of study: lithium disilicate

The first glass-ceramic material was discovered in 1950 by Stookey (35) and was based on the lithium disilicate system. The enhanced mechanical and thermal properties of lithium disilicate glass-ceramics make them ideal substrates to produce heat and corrosion-resistant coatings and to fabricate dental restoration prostheses (36–38).

Since the discovery of the first lithium disilicate glass-ceramic, many efforts have been devoted to disclose the nucleation and crystallization mechanisms relating to glass compositions, thermal treatment, and the addition of nucleating agents in order to understand and control the microstructures that in turn affect properties (39–41). Albeit LS_2 glass is expected to be one of the few compositions that exhibits homogeneous nucleation, the precipitation of metastable phases in the early stage of crystallization of LS_2 glass or in neighboring compositions was observed in several studies (39,40,42–52). Studies on nearly stoichiometric compositions have reported the formation of lithium metasilicate ($Li_2O{\cdot}SiO_2$; LS) at low temperatures and short periods of thermal treatment (43,46,47,53,54). But it is also claimed that this phase disappears for longer treatments and does not interfere with the overall crystallization kinetics of lithium disilicate, which is the main phase that forms homogeneously.

Instead, in non-stoichiometric compositions and/or in the presence of nucleating agents, the LS phase was proposed as a precursor of the LS_2 phase through heterogeneous crystallization (39,40,42,48–50,55,56). In these cases, the most accepted mechanism is that, at low temperature, LS is the primary phase in initial crystallization, which increases the concentration of SiO_2 in the residual glass matrix and, thus, triggers cristobalite formation. At elevated temperatures, the two phases combine, giving rise to lithium disilicate crystals.

Metastable phases different from LS have also been detected (42,45,46,57,58). Both Deubener and Iqbal (42,45) discussed the involvement of intermediate phases in the nucleation process of the lithium disilicate. Metastable phases with stoichiometry close to the LS_2 composition have been observed by XRD during the crystallization stages (45,57,58). The first to appear, referred to as α'-LS_2, has several peaks not in common with the stable LS_2. The conversion to another intermediate phase, β'-LS_2, is proposed, which has a better

match in the XRD pattern with the stable LS_2. The crystallization concludes with the conversion into the equilibrium LS_2 phase.

In contrast to the aforementioned works, Burgner (59,60) and Zanotto (61,62) did not identify any metastable phase formation in the nucleation process of the LS_2. Burgner (60) investigated possible causes for this discrepancy, namely, the glass preparation procedure, the glass composition, the water content or a deficiency of the XRD technique to detect the possible appearance of metastable phases.

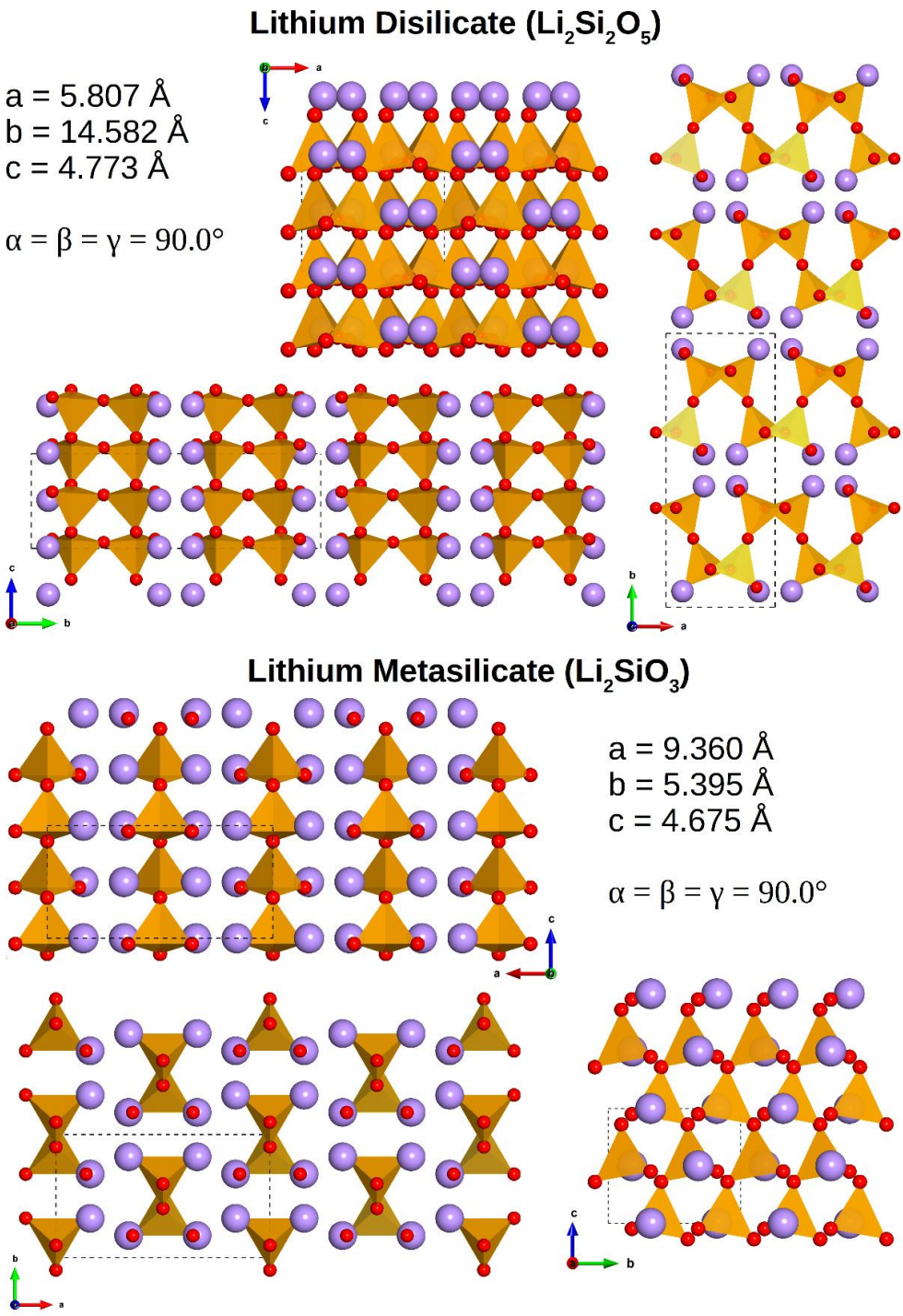

FIG. 1.3. Structure of the LS and LS_2 crystals along different orientations and unit cell parameters. Yellow tetrahedral represents silicon, red and pink spheres represent oxygen and lithium ions, respectively.

The prior formation of intermediate phases was also suggested because it would justify the underestimation of several orders of magnitude of the nucleation rate of LS_2, since the formation of metastable phases in the early stage of crystallization would decrease the activation energy of the process.

An argument in favor of homogeneous nucleation is the structure of the stable LS_2 (63) and LS (64) crystalline systems, which are presented in figure 1.5. LS_2 crystal has a double layer of silica structure with Li ions in the interlayers, whereas LS crystal has chain-like silica structures surrounded by Li ions. The two phases have quite different stoichiometry and symmetry, so the conversion from one phase to another looks like a high-energy process.

Very recently, the problem of the crystallization of LS_2 was approached using computational techniques (65–68). The first work was proposed by McKenzie et al. (65,66) who combine molecular dynamics and Monte Carlo methods to calculate the nucleation free energy of both LS_2 and LS. The Monte Carlo technique was used for cluster formation, building clusters with different sizes and shapes, and an implicit solvent model was used to describe the environment in which nucleation takes place. They find that the LS is more likely to precipitate out of solution, but for larger nuclei, the two crystals become equally stable, and they also find the critical crystal dimension, which agrees well with experiments. One of the main advantages of this technique is that it considers the shape of the crystal to be different from the spherical one, which is an assumption of CNT (see chapter 2). The main issue is assuming a uniform density and charge in the background of the crystalline nucleus. In particular, the formation of LS crystal from an LS_2 glass would inevitably result in a local phase separation, which would increase the strain at the nucleus interface.

Sun et al. (67) investigated the growth of lithium disilicate, beginning with a slab-model composed of a crystalline and a glass layer, resulting in a glass/crystal interface. They considered several orientations of the LS_2 crystal, and they studied the evolution of the slab during an MD simulation. They observed the ordering of the atoms in the glass in an LS_2-fashion near the crystal surface, and according to the investigated surface, there was a higher or lower level of ordering. However, they could observe only the very first stages of growth because the viscosity of the glass phase hampers the simulation of this event.

The last work combines experiment and simulation observations to investigate structural rearrangements below T_g (68). Studying the crystallization of LS_2 using solid-state NMR and RAMAN techniques, they observed relaxation and nucleation without detectable changes in the network former unit distribution of the glassy silicon-oxide network. Instead, relaxation of the frozen supercooled melt and nucleation of LS_2 crystals occurs principally in terms of a changing lithium local environment. They used MD simulations to confirm the distribution of Li cations in the glass, which in their model are not randomly distributed in the LS_2 glass but show a certain degree of clustering. In this work, they confirmed the good reliability of the modeled structure; however, the mechanism of nucleation was not investigated.

Despite the many efforts made in the past, the major controversy concerns the participation and influence of metastable phases in the LS_2 crystallization kinetics and is still being debated, remaining an extremely important open question.

Chapter 2. Nucleation Theories

The theoretical knowledge of nucleation, growth, crystallization processes in glass-forming melts is a key issue not only to avoid undesirable crystallization (devitrification) in glass formation, but also for the control of desired crystallization (glass-ceramics) (69,70).

Nucleation (1,69,71–75) is usually described by resorting to Classical Nucleation Theory (CNT). Therefore, we will present it first. However, since several approximations are made, the CNT usually does not provide nucleation rates matching the experimental ones and alternative theories have been proposed. One of the most successful, the two-step theory, will be briefly presented at the end of the chapter.

2.1. Classical nucleation theory (CNT)

The nucleation process can take place through two mechanisms:

- Homogeneous nucleation, which is a stochastic process, where the probability of the formation of crystalline nuclei is the same throughout the entire sample volume.
- Superficial nucleation or heterogeneous nucleation, which takes place in preferential sites, such as solid particles, surfaces, and interfaces.

This theory provides kinetics and thermodynamics description to both mechanisms, which are detailed in the following paragraphs.

2.1.1. Homogeneous nucleation

The CNT is based on some hypothesis: (i) whatever its size, the crystalline nucleus has the same macroscopic (such as density, structure, composition) and thermodynamic properties of the stable crystalline phase that will form; (ii) the initial germ of nucleation have spherical shape with radius r, to minimize the surface between crystal and supercooled liquid; (iii) the surface energy is constant, it does not depend on the nucleus dimension (*capillarity approximation*) and on the temperature.

When the glass is heated up near or above the glass transition temperature, T_g, the viscosity of the system decreases, and the particles have a higher mobility. At this condition there is a non-zero probability of

forming structural units similar to the crystalline phase. The stability of these structural units, called embryos, depends on their dimensions, radius r, and it is described with the nucleation free energy, ΔG or W, equation 2.1.

$$W(r) = -\frac{4}{3}\pi r^3(\Delta G_v - \varepsilon) + 4\pi r^2 \gamma_{sl} \tag{2.1}$$

The nucleation free energy is composed of two positive contributions and one negative. The interfacial energy per unit area, γ_{sl}, corresponds to the formation of a melt/crystal surface, therefore, is a positive contribution to W. The second positive term is the strain, ε, that is created due to the difference in the density between the two phases. While the negative term is due to the volume formation of a crystalline phase, ΔG_v, which corresponds to the free energy difference between liquid (G_l) and crystal (G_c) per unit volume $\Delta G_v = \frac{G_l - G_c}{V_m}$, where V_m is the molar volume of the crystal phase. Since the crystalline phase below the melting temperature is the most stable phase, the volume contribution is negative $(\Delta G_v > 0)$ and it stabilizes the embryo formed. The nucleation free energies and the three contributions are shown as a function of the nucleus dimension in figure 2.1.

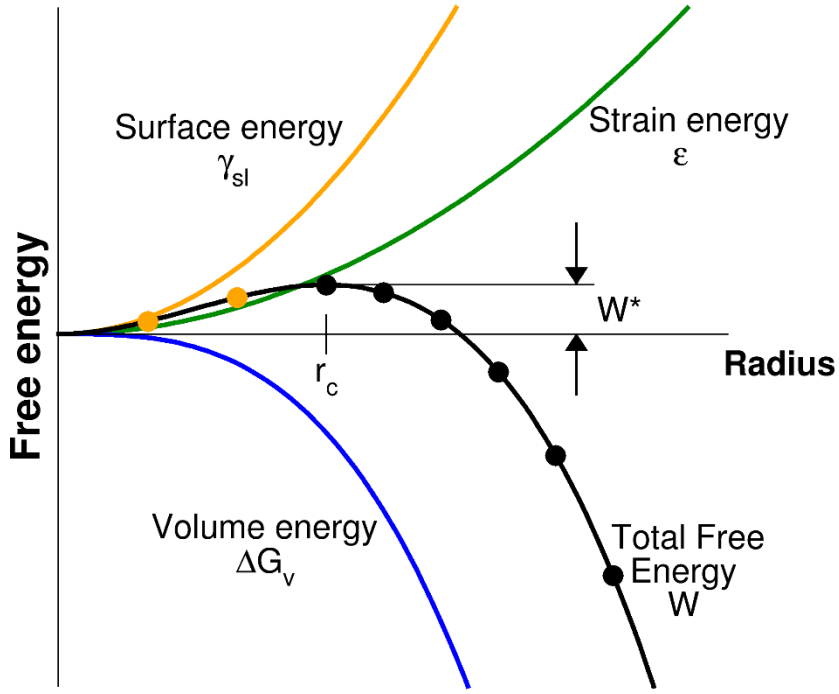

FIG. 2.1. Variation of the work of formation, W, and its surface, strain, and volume components as a function of the nuclei size, r.

The nucleation free energy has a maximum in the position of the critical radius, r_c. Therefore, if the embryo formed has dimension lower than the critical size, it dissolves back to liquid, because the surface and strain terms are predominant over the volume term, while if the dimensions are bigger than r_c, the nucleus becomes energetically stable and may grow to minimize the system energy.

The strain, ε, is usually neglected because nucleation takes place in a liquid that can easily relax to reduce the stresses while the nucleus is forming. The formula can be rewritten as:

$$W(r) = -\frac{4}{3}\pi r^3 \Delta G_v + 4\pi r^2 \gamma_{sl} \,. \tag{2.2}$$

The maximum of the nucleation free energy, ΔG^* or W^*, is the critical work of formation of a critical cluster with radius r_c and corresponds to the thermodynamic barrier for the nucleation process. It can be determined imposing $\partial W/\partial r = 0$, obtaining:

$$r^* = \frac{2\gamma_{sl}}{\Delta G_v} \tag{2.3}$$

$$W^* = \frac{16}{3}\pi \frac{\gamma_{sl}^3}{\Delta G_v^2} \tag{2.4}$$

The ΔG_v can be determined from equation 2.5:

$$\Delta G_v V_m = \Delta H_m \left(\frac{T_m - T}{T_m}\right) - \int_T^{T_m} \Delta C_p(T')dT' + T\int_T^{T_m} \frac{\Delta C_p(T')}{T'}dT' \tag{2.5}$$

Where ΔH_m and T_m are respectively the molar enthalpy of fusion and the melting temperature, and $\Delta C_p = C_p^l - C_p^c$ is the difference between the thermal capacity of the liquid and the crystal at constant pressure. However, the ΔG_v is usually calculated using the Turnbull approximation (76), assuming $\Delta C_p = 0$, described by equation 2.6:

$$\Delta G_v = \frac{\Delta H_m}{V_m}\left(\frac{T_m - T}{T_m}\right) \tag{2.6}$$

The nucleation free energy is the thermodynamic contribution to the steady-state nucleation rate, I_{st}, as predicted by CNT. I_{st} corresponds to the number of formed nuclei per time unit at a given temperature:

$$I_{st} = I_0 \, exp\left(-\frac{W^* + \Delta G_D}{k_B T}\right), \qquad I_0 = 2N_1 \frac{k_B T}{h}\left(\frac{a^2 \gamma_{sl}}{k_B T}\right)^{\frac{1}{2}} \tag{2.7}$$

Where k_B is the Boltzmann constant, I_0 is a pre-exponential factor, with N_1 the number of atoms in the unit volume of a dimension, and h is the Planck constant. ΔG_D is the activation free energy of the diffusive process, that describes the transfer of a species through the melt/liquid surface and represents the kinetic barrier of nucleation, thus it is usually difficult to estimate.

The ΔG_D is related to the diffusion coefficient, D, which can, for reasons of simplicity, be approximated to a transport property easily measurable, the viscosity, η, by using the Stokes-Einstein relation (77):

$$exp\left(-\frac{\Delta G_D}{k_B T}\right) \propto D = \frac{k_B T}{3\pi\lambda\eta} \tag{2.8}$$

With λ the jump distance, ~ twice the ionic radius. With this approximation equation 2.7 can be rewritten as:

$$I_{st} = I_0 \frac{k_B T}{3\pi\lambda\eta} exp\left(-\frac{W^*}{k_B T}\right) \quad (2.9)$$

In this formulation only a few parameters must be known to calculate the nucleation rate of a certain system: the viscosity, which is easy to obtain since it is a macroscopic property, and W^*, where ΔG_v is easily extracted from experimental values of melting enthalpy, while γ_{sl} is the most complex term. The latter can be determined by a fitting procedure of the experimental I_{st} at different temperatures, combining equation 2.9 with equation 2.4 obtaining:

$$log\frac{\eta}{T} = -\frac{16\pi\gamma_{sl}^3}{3k_B}\frac{1}{\Delta G_v^2 T} + log\frac{I_0}{I}\frac{k_B}{3\pi\lambda} \quad (2.10)$$

If the CNT equation is correct, it is possible to obtain a linear trend from the $\log\frac{\eta}{T}$ against $\frac{1}{\Delta G_v^2 T}$ and extract γ_{sl} from the slope (78).

The nucleation rate is affected by the temperature, for the CNT we must analyze how both the thermodynamic and kinetic terms are affected. With a decrease of temperature, the thermodynamic barrier decreases, on the opposite side the kinetic inhibition increases, because the system becomes more viscous. Therefore, the nucleation rate has a maximum, I_{max}, at a temperature T_{max} where the two contributions are balanced. CNT reproduces well the temperature dependence of the nucleation rate, even though it fails in the prediction of the magnitude of I_{st}, with calculated values several orders of magnitude lower than the experimental result (79–81).

2.1.2. Problematics of the CNT in homogeneous nucleation

A first explanation of the discrepancy between experiments and CNT results is the formation of metastable phases that act as precursors of the energetically stable phase. If the metastable phase forms it can change the mechanism of nucleation, therefore the CNT is not able to explain this behavior. On the other hand, if the metastable phases have a “short life”, as in the case of lithium disilicate as reported in several studies (see paragraph 1.4), and dissolve back to liquid they do not interfere with the kinetic of nucleation of the main crystalline phase (61).

We have seen that the contribution of the strain, ε, has been neglected in the calculation of the nucleation free energy, however, this term can be considered and the critical work of formation of a critical cluster becomes:

$$W^* = \frac{16}{3}\pi\frac{\gamma_{sl}^3}{(\Delta G_v - \varepsilon)^2} \quad (2.11)$$

The inclusion of this term in CNT has been tested and observed that this is not the cause of the failure of the theory (82).

The capillarity approximation is also a limitation to the derivation of CNT, in fact it is assumed that the interfacial energy γ_{sl} is independent from the nuclei dimensions and the temperature. The temperature dependence of the surface energy has been investigated by fitting the surface energy as a function of the temperature using experimental nucleation rates. The interfacial energy presents a linear trend above the temperature at which the nucleation rate is maximum T_{max}, $\gamma_{sl}(T) = a + b\,T$, while below T_{max}, $\gamma_{sl}(T)$ is no longer linear and the reason is still unclear (72). However, the fitted $\gamma_{sl}(T)$ is calculated using experimental nucleation rates that depend on the critical nuclei, which indeed depends on the temperature. Therefore, the temperature and size of crystal dependency of γ_{sl} must be separated in two factors: dependency on a planar surface at the temperature T, and on the dimension of the crystal. These two contributions are decoupled in the formulation of Tolman (83):

$$\gamma_{sl}(r) = \frac{\gamma_0}{1 + \frac{2\delta}{r}} \tag{2.12}$$

Where γ_0 is surface energy for the planar surface and δ is the Tolman parameter, which is the width of the interfacial region between the coexistence phases. When the fitting of the nucleation rate is done using the relation in equation 2.10, it is possible to recover the agreement between the experimental and calculated magnitude of the nucleation rate, however, the temperature dependency below T_{max} is not reproduced (84).

Recently, Zanotto et al. (85,86) have reconsidered the alleged failure of the CNT below T_{max}, proposing another possible issue, which is the experimental time to investigate the nucleation process. In fact, if the steady-state regime has not been reached it will inevitably introduce error in the measurement of the nucleation rate. Therefore, they measured the nucleation rate applying a steady-state criterion and they found a good agreement between experimental results and CNT, in most of investigated cases, proving that the break at T_{max} is not a common feature of all glass-formers.

2.1.3. Heterogeneous nucleation

The theory to describe heterogeneous nucleation is more complex than the homogeneous case, for this reason other approximations are assumed. Firstly, it is assumed that the surface of the heterogeneity is large compared to the size of the nucleating particle, moreover the total interfacial energy is isotropic and thus minimized if the transformation product has the shape of a spherical cap on the heterogeneity surface. The minimization of the surface energy contribution reduces the thermodynamic barrier of the heterogeneous mechanism, which is usually lower than the barrier for the bulk formation of a crystalline nucleus.

The thermodynamic barrier of nucleation over a planar surface, W^*_{het}, is described by equation 2.13.

$$W^*_{het} = W^* \phi(\theta), \qquad \phi(\theta) = \frac{1}{2} - \frac{3}{4}cos\,\theta + \frac{1}{4}cos^3\,\theta \tag{2.13}$$

Where $\phi(\theta)$ is a function ranging between 0 and 1 that depends on the contact angle θ.

The nucleation rate for the heterogeneous nucleation becomes:

$$I_{st}^{het} = N^s \frac{k_B T}{h} exp\left(-\frac{W^* \phi(\theta) + \Delta G_D}{k_B T}\right) \quad (2.14)$$

Where N^s substitutes N_1 in the pre-exponential factor as the number of structural units in contact with the surface per volume unit. The surfaces can be represented by dispersed solid particles acting as nucleating sites. The availability of these sites influences the nucleation rate, which becomes constant when the saturation of the sites is approached.

The measurement of the heterogeneous nucleation rate is experimentally tricky because the small number of sites is usually saturated before the crystalline nuclei become visible thanks to the high activity of nucleation, therefore I_{st}^{het} must be calculated at saturation level (87).

2.1.4. Homogeneous vs heterogeneous

We have discussed that heterogeneous nucleation is in general energetically favored over homogeneous nucleation, however, the latter is easier to control, forming a more uniform distribution of crystals in the liquid matrix, thus preferred from an applicative point of view. Since there are several cases of glasses that present homogeneous nucleation, it is interesting and fundamental to understand in which cases and the reasons why this mechanism can be preferred.

In literature (88–90), it was proposed the correlation between the mechanism of crystallization and the *reduced glass transition temperature* $T_{gr} = T_g/T_m$. When T_{gr} increases, the maximum nucleation rate I_{max} decreases until the system does not exhibit homogeneous nucleation on laboratory time scales, the threshold value is about $T_{gr} \cong 0.58 - 0.60$. If a glass has $T_{gr} < 0.6$ it presents homogeneous nucleation and T_{max} can be both measured and calculated by the CNT at a temperature higher than the T_g, whereas if $T_{gr} > 0.6$ the experimental T_{max} cannot be measured and the expected value from CNT is lower than the T_g, resulting in a preference for the heterogenous mechanism. A low T_{gr} suggests a larger range of temperature where the liquid is undercooled before crystallizing, therefore a high undercooling represents a high thermodynamic driving force for internal nucleation.

In the last decades, researchers have reported the emergence of a connection between structural features of the glass and the mechanism of crystallization, in particular highlighting that structural similarities between glass and crystal, especially at short and medium range, indicate a tendency to homogeneous nucleation (8). Let's consider two extreme cases: if the structure of the liquid is similar to the crystalline, the necessary structural reorganization will be limited, with a low kinetic barrier and low interfacial energy γ_{sl}, with instead a reduce in the volume contribution ΔG_v. However, the nucleation rate depends on the thermodynamic barrier W^*, which in turn depend on the ratio $\gamma_{sl}^3/\Delta G_v^2$ as seen in equation 2.4, hence the

contribute of γ_{sl} is predominant and I_{st} increases. In the opposite case, if the two structures are dissimilar, there will be a higher volume contribution, but the structural reorganization needed will be consistent, as well as the surface energy, resulting in low homogeneous nucleation rates.

2.2. Other theories

As presented in the previous paragraphs, in CNT the energy barrier for nucleation results from a change in size rather than composition and structure. This simplification limits the applicability to only simple crystallization, and it might be a reason why CNT severely underestimates the nucleation rates in silicate systems (69,91).

2.2.1. Generalized Gibbs approach (GGA)

The Generalized Gibbs approach (GGA) (92,93) is based on experimental observations showing that the properties and structure of the nuclei can deviate from those of the macroscopic phases (52,59,94,95). This theory predicts the possibility of reaching the final stable state through a discrete series of metastable phases for which the energetic barrier to be overcome is small, as proposed with Ostwald's rule of stages (70,96). GGA is based on the CNT but properly considering a change in composition during the nucleation process, as shown in figure 2.2.

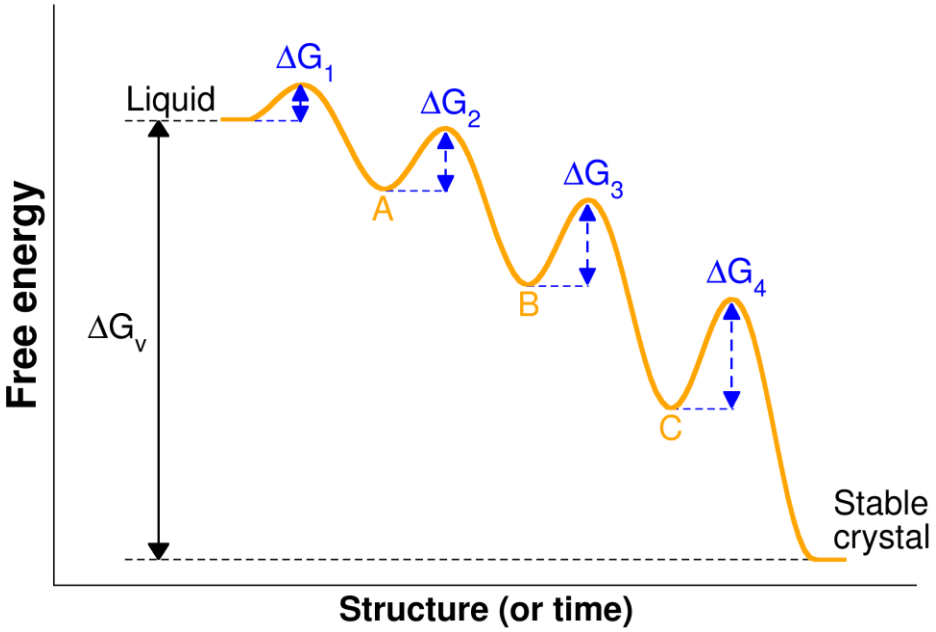

FIG. 2.2. Schematic representation of nucleation considering different metastable intermediate phases (A, B, C) before reaching the stable crystal phase (97).

Critical parameters (r_c and W^*) are similar to those obtained from CNT, but considering the composition α of the nucleus:

$$r_c = -\frac{2\gamma_{sl}}{c_\alpha \Delta G_v}, \qquad W^* = \frac{16\pi\gamma_{sl}^3}{3(c_\alpha \Delta G_v)^2} \tag{2.15}$$

c_α, is the volume concentration of the new phase, therefore, r_c is defined not only in the maximum of W, but also as the minimum value of W^* among all allowed compositions. In GGA the nucleus size changes during the nucleation process, meanwhile the composition changes from the initial state until, once the critical dimensions are reached, structure and composition evolve to those of the macroscopic crystal, and eventually grow. The energetic barrier W^* in GGA is lower than in CNT because the composition changes reduce the interfacial energy (69).

2.2.2. Two-step model

During the crystallization of a solid from a liquid phase, two order parameters must be considered to distinguish the two phases: density and structure. As explained, CNT considers that the two parameters evolve simultaneously, thus the germ of crystallization has the density and atomic organization of the stable crystal. If the two parameters do not evolve, contemporary CNT does not provide a correct description of the nucleation process.

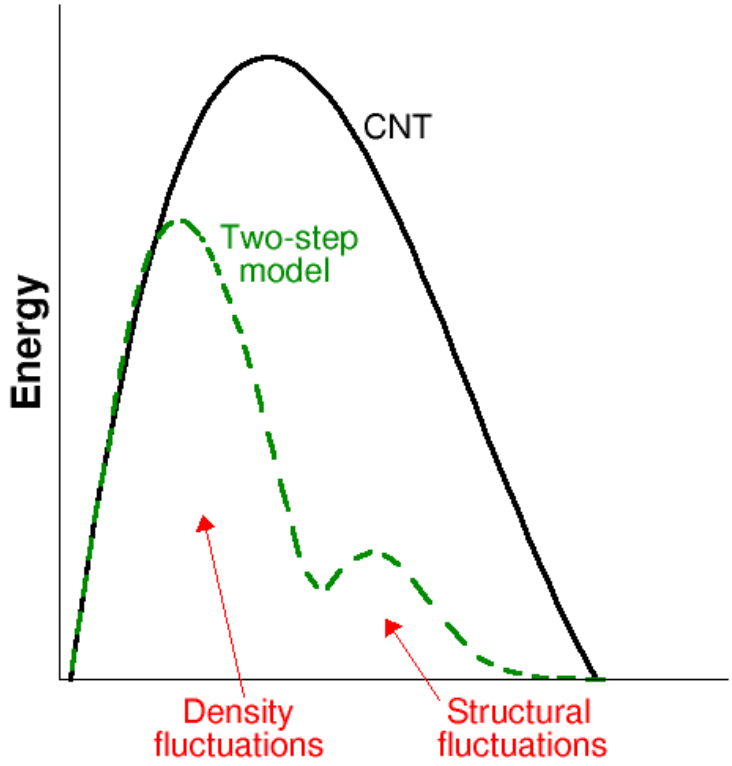

FIG. 2.3. Energetic barriers in the two step models compared to CNT model (98).

Based on experimental observation, the two-steps model (74,98,99), assumes a temporal separation between the density and structural fluctuations. First, local disordered regions with composition and density different, usually higher, from those of the initial liquid phase are formed, and then a structural reorganization inside this region leads to the appearance of the crystals, as shown in figure 2.3. As in the case of GGA, the two energetic barriers to overcome in the step model are lower than the single energy barrier from CNT.

Chapter 3. Computational techniques: MD and MetaD

This chapter offers a general overview of the methodologies and the simulation techniques applied in the present thesis. Each property of a system can be analyzed and investigated by employing the correct methodology.

Molecular dynamics is a technique based on classical mechanics that operates at atomistic level, thus often applied to condensed phase systems (solid or liquid state), with the aim of extracting bulk properties of a system starting from an atomistic basis. It is the most efficient technique for studying the properties of non-crystalline materials, such as glasses thanks to the accessible length scale that can be used. The theory of molecular dynamics is briefly introduced with a description of the force field employed in the study of the lithium disilicate system.

The second part of this chapter describes metadynamics which is an enhanced sampling technique that is a well-known technique used to study rare events, such as crystallization. Metadynamics is based on altering the stability of the phases visited during the molecular dynamics simulation, thus it is not a stand-alone technique, but it is extremely powerful to understand events that are not accessible to the molecular dynamics solely. The theory of metadynamics is presented, with descriptions of algorithms and collective variables used to investigate the crystallization of lithium disilicate.

3.1. Molecular Dynamics simulations

Molecular Dynamics (100,101), MD, is a technique based on classical mechanics used to study structural, dynamic and thermodynamic features of a system. The system is generally represented by point particles with a mass and a charge interacting through bonding and non-bonding terms.

MD generates points correlated in the time and in the phase space, propagating an initial set of coordinates and velocities using Newton's second law of motion. The initial coordinates of the particles in an MD simulation can be selected from x-ray diffraction studies, especially when dealing with crystals, while the velocities are assigned in accordance with the target temperature through a Maxwell-Boltzmann distribution (102). An interatomic potential (U) must be defined to describe the interaction between the particles, and

the gradient allows the calculation of the forces acting on each particle of the system (F_i). The system is then allowed to evolve in time by solving the equation of motion (eq. 3.1).

$$F_i(t) = \frac{-dU(t)}{dr_i} = \frac{d^2 r_i(t)}{dt^2} m_i \tag{3.1}$$

The force F_i acting on the i-th atom with mass m_i generates an acceleration on the atom causing the change of the velocity (v_i) and position (r_i) of the particle:

$$\frac{dv_i(t)}{dt} = \frac{1}{m_i} F_i \tag{3.2}$$

$$\frac{dr_i(t)}{dt} = v_i \tag{3.3}$$

Equations 3.2 and 3.3 are the analytical expressions for Newton's equation, while we need discrete equations for MD applications (103). There are several algorithms that can approximate the solution and they are implemented in MD software. The algorithm allows the simulation of the evolution of a system within small temporal steps of finite size called time-step (Δt). The most common algorithm, the Verlet leapfrog (104,105), requires values of the position, $r_i(t)$, and forces, $F_i(t)$, at a time t while velocities are half a step behind, v_i. Velocities and positions are alternatively evaluated each time-step with the following formula:

$$v_i\left(t + \tfrac{1}{2}\Delta t\right) \leftarrow v_i\left(t - \tfrac{1}{2}\Delta t\right) + \Delta t \, \frac{F_i(t)}{m_i} \tag{3.4}$$

$$r_i(t + \Delta t) \leftarrow r_i(t) + \Delta t \, v_i\left(t + \tfrac{1}{2}\Delta t\right) \tag{3.5}$$

The velocity at the time t is evaluated from the average of the velocities calculated half a time-step either side of time t. From the evaluation of the instantaneous position and velocities, several properties can be calculated, kinetic energy, potential energy, temperature, etc. If these properties have large fluctuations or drifts, the time-step is probably too large. Therefore, the choice of the time-step is indeed a key factor in an MD simulation.

In the simulation of realistic systems in condensed phase, the dimension of the simulation box should be extremely large to reproduce the bulk properties excluding the influences of the surface. However, the number of atoms in macroscopic structures is out of the range of possibility of MD. To reduce the computational effort, the simulation box can be represented as a three-dimensional cell with virtual walls that define a unit of repetition in the three-dimensional space, called periodic cell. This is the basis of the periodic boundary conditions (PBC) (106). The periodic cell is assumed to be surrounded by replicated images of the main periodic cell and each image is an exact replica of the others, meaning that the contents and the dynamics of all images are the same. Only the dynamics of the main periodic cell is computed. The total number of atoms is conserved, since if a particle leaves the box from one side of the simulation box, its image-particle will enter from the opposite side of the box, and the motion of the atoms is described in an almost infinite system, removing the surface effects.

The main factor to consider with PBC is to prevent particles from interacting with their images, which would introduce long-range symmetry and artifacts in the simulation. A cut-off radius must be defined as a maximum distance for the evaluation of the interatomic potential, which is not longer than half the length of the shortest side of the simulation box.

3.1.1. The potential energy

The total internal energy of a model is calculated as the summation of the kinetic and the potential energies. The kinetic energy depends on the velocities of each particle of the system while the potential energy is described by a function that depends on the coordinates of the *N* particles in the model, $U(r_1, \dots r_N)$. The potential function, or force field, uses implicitly the Born-Oppenheimer approximation (107), thus, there is no explicit inclusion of the electronic structure of the system: such effects are subsumed into the potential function. The potential function is commonly expanded as follows:

$$U(r_1, \dots r_N) = \sum_{i=1}^{N} \varphi_i(r_i) + \sum_{i=1}^{N-1} \sum_{j=i+1}^{N} \varphi_{ij}(r_i, r_j) + \sum_{i=1}^{N-2} \sum_{j=i+1}^{N-1} \sum_{k=j+1}^{N} \varphi_{ijk}(r_i, r_j, r_k) + \dots \quad (3.6)$$

Where φ_i is the potential energy acting on atom i due to an external field, if present, φ_{ij} is the two-body energy which depends only on the positions of pairs of atoms i and j, φ_{ijk} are the three-body terms depending on the positions of atoms i, j and k. The expansion extends to four-body terms which are used in inorganic materials, especially for modeling planar-trigonal anions, such as carbonates or borates, not subject of this thesis.

In many cases, especially for oxides and silicates, it is common to approximate U by including only the two-body components (108–113). Energy is assumed to depend on the inter-ion distance $r_{ij} = |r_i - r_j|$ and may be usefully decomposed into a long-range coulombic term and a short-range term:

$$\varphi_{ij}(r_{ij}) = \frac{z_i z_j e^2}{r_{ij}} + V_{ij}(r_{ij}) \quad (3.7)$$

where z_i and z_j are the ionic charges and $V_{ij}(r_{ij})$ is the short-range interaction which can be attributed to the repulsion between electron charge clouds, van der Waals attraction, electron polarizability.

3.1.2. Description of employed force field

In most cases, the force fields available in literature for the study of oxide glasses are composed only by dispersive-repulsion and van der Waals attraction (113). In this thesis we have used a modification of the potential developed in 2006 by Pedone et al. (114), called PMMCS, which is based on a rigid ionic model, with partial charges to handle the partial covalency. It is composed of a short-range Morse function with a repulsive contribution (B_{ij}/r^{12}) necessary to model the interactions at high temperature and pressure; a repulsive part of the Buckingham potential for the Li-Li interactions The analytical form of the potential function is

$$U_{ij}(r_{ij}) = \frac{z_i z_j e^2}{r_{ij}} + D_{ij}\left(\left\{1 - exp\left[-a_{ij}\left(r_{ij} - r_{ij}^0\right)\right]\right\}^2 - 1\right) + \frac{B_{ij}}{r_{ij}^{12}} + A_{ij} exp\left(-\frac{r_{ij}}{\rho_{ij}}\right) \quad (3.8)$$

where D_{ij}, a_{ij} and r_{ij}^0 are pair parameters of atoms i and j of the Morse function, B_{ij} is the repulsive contribution constant for the couple $i-j$, A_{ij} and ρ_{ij} are pair parameters for the repulsive part of the Buckingham potential. The original version of the PMMCS was parameterized using structural parameters and elastic constants of several crystalline oxide, silicates and aluminosilicates and it was composed only of pairwise interactions with the Morse and the repulsive part (r^{-12}) of equation 3.8. However, since it is known that the inclusion of only pairwise interactions leads to structure with large overestimation of the inter-tetrahedral angles T-O-T (115–117), we have included a three-body term to better reproduce the Si-O-Si, Si-O-P and P-O-P inter-tetrahedral angles. The screened harmonic exponential decaying three-body function has been used:

$$U(r_{ij}, r_{ik}, \theta_{ijk}) = \frac{k_{\mathrm{ijk}}}{2}\left(\theta_{ijk} - \theta_{ijk}^0\right)^2 \exp\left(-\left(\frac{\mathrm{r_{ij}}}{\rho_1} + \frac{\mathrm{r_{ik}}}{\rho_2}\right)\right) \quad (3.9)$$

Where k_{ijk}, θ_{ijk}^0, ρ_1 and ρ_2 are parameters connected to the force constant, reference angle of the $i-j-k$ triplet and the decay function along the $i-j$ and $i-k$ bonds, respectively.

The three-body term parameters have been fitted using as training set the PES of the $(HO)_3Si\text{-}O\text{-}Si\text{-}(OH)_3$, $(HO)_3Si\text{-}O\text{-}PO\text{-}(OH)_2$ and $(HO)_2\text{-}OP\text{-}O\text{-}PO\text{-}(OH)_2$ dimers computed as a function of the inter-tetrahedral angles at the PBE0/6-311+G(d,p) level using the Gaussian09 code (118).

The A_{ij} and ρ_{ij} parameters for the Li-Li interactions have been fitted using the structure of the $Li_2Si_2O_5$ and Li_2SiO_3 crystal. All parameters are reported in table 3.1.

TABLE 3.1. Charges and parameters for modified PMMCS potential.

MORSE				
Pairs	D_{ij} **(eV)**	a_{ij} **(Å^{-2})**	r_{ij}^0 **(Å)**	B_{ij} **(eV Å^{12})**
$Si^{2.4}$-$O^{-1.2}$	0.340554	2.006700	2.100000	1.0
$Li^{0.6}$-$O^{-1.2}$	0.001114	3.429500	2.681360	2.0
$P^{3.0}$-$O^{-1.2}$	0.831326	2.585830	1.770790	1.0
$O^{-1.2}$-$O^{-1.2}$	0.042395	1.379316	3.618701	100.0
BUCKINGHAM				
Pairs	A_{ij} **(eV)**	ρ_{ij} **(Å^{-2})**		

$Li^{0.6}$-$Li^{0.6}$	176990.1	0.1736		
SCREENED HARMONIC THREE-BODY				
Angle	k_{ijk} (eV rad^{-2})	θ^{0}_{ijk} (deg)	ρ_1 (Å)	ρ_2 (Å)
Si-O-Si	16.9	109.47	1.0	1.0
Si-O-P	32.4	75.00	1.0	1.0
P-O-P	34.4	81.00	1.0	1.0

In principle the interaction potentials have infinite range, because the contribution of the interatomic potential has a non-zero value no matter the separation between atoms. However, the value of the potential becomes negligible once the separation gets beyond a certain distance, thus a cut-off condition for any pair is usually applied. By calculating the interaction within the cut-off distance only, it is assumed that the interaction is zero with farther distances. The entity and the chosen scheme of the cut-off is important because it can create discontinuities in the calculated forces, which can give rise to artifacts. This parameter is usually optimized during the parametrization of the force-field. In PMMCS force-field the cut-off is different in the calculation of long-range coulombic interactions and short-range function, whose magnitude decreases faster, and values of 12 Å and 5.5 Å are the respective cut-off distances. Especially for the long-range cut-off should be considered the limitation imposed by the PBC, so the cut-off must agree with the box dimension, as discussed above.

3.1.3. Coulombic interactions

The classical approach to evaluate Coulomb energies and related forces in a simulation with periodic boundary conditions (PBC) is the Ewald summation method (119,120), where the sum over all Coulomb pair interactions is decomposed into a real space and a reciprocal space part:

$$U_{elec,Ewald} = \frac{1}{2}\sum_{i=1}^{N}\sum_{j=1}^{N}\left[q_i q_j\left(\sum_{n}\frac{\mathrm{erfc}\left(\alpha|r_{ij}+n|\right)}{|r_{ij}+n|}+\frac{1}{\pi L^3}\sum_{k\neq 0}\frac{4\pi^2}{|k|^2}\exp\left(-\frac{\pi^2|k|^2}{\alpha^2}\right)\cos\left(k\cdot r_{ij}\right)\right)\right] - \frac{\alpha}{\pi^{1/2}}\sum_{i=1}^{N}q_i^2 \quad (3.10)$$

N is the number of electrostatic particles, the sum over n is a sum over all periodic box replicas with integer coordinates $n=(l,m,n)$, and the prime indicates $i=j$ are neglected for $n=0$. L is the cell length, α is the damping or convergence parameter with units of Å^{-1}, k are the reciprocal vectors and are equal to $2\pi\, n/L^2$ and $erfc$ is the complementary error function.

The first two terms are convergent summations, the first one is in the real space (shorter range), the second in the reciprocal space (longer range). The last term is a particle self-term that is constant. The convergence parameter α plays an important role in balancing the computational cost between the two terms of the summation. Usually, this method involves utilization of the fast Fourier transform (for the evaluation of the second term) obtaining a not negligible computational effort.

An approximation of Ewald is usually applied, the Smoothed Particle Mesh Ewald (SPME) (121), which has the main difference in the treatment of reciprocal terms. By means of an interpolation procedure involving (complex) B-splines, the sum in reciprocal space is represented on a three-dimensional rectangular grid. In this form the Fast Fourier Transform (FFT) may be used to perform the primary mathematical operation, which is a 3D convolution. The efficiency of these procedures greatly reduces the cost of the reciprocal space sum when the range of k vectors are large.

However, if the assumption that long range Coulomb interactions (the reciprocal term in eq 3.10) in ionic or condensed systems gives a small contribution to the total potential, due to screening effect, it should be possible to neglect that term (122). A cutoff radius (R_c) must be defined which allows one to include all the interactions needed to have a good description of the system. Usually, a cutoff radius of about 10 Å is necessary to obtain a good agreement with the Ewald method (123) then it is possible to eliminate the reciprocal part and assume zero interactions at higher distance than R_c. This is the Wolf summation method, which, for a good description of the system, needs a correction that considers the neutralization of the charge contained within the cutoff radius and the continuity of energy and force at R_c. The first problem can be solved by placing the opposite charge on the cutoff radius surface, that, it is important to underline, in a glass should be close to neutrality. For the continuity, from potential formula and its derivative which can be found in the reference (123), the Wolf potential, or damped shifted force model, is

$$U_{elec,Wolf}(r) = q_i q_j \left[\frac{\mathrm{erfc}(\alpha r)}{r} - \frac{\mathrm{erfc}(\alpha R_c)}{R_c} + \left(\frac{\mathrm{erfc}(\alpha R_c)}{R_c^2} + \frac{2\alpha}{\pi^{1/2}}\frac{e^{-\alpha^2 R_c^2}}{R_c}\right)(r - R_c)\right], r \leq R_c \quad (3.11)$$

All terms described are in the real space with a correction which depends on R_c. This approximation is a computationally efficient alternative to the Ewald summation for typical modern molecular simulations.

3.1.4. Statistical ensembles

In MD simulations, the Newtonian dynamics that describes the evolution of a system maintaining constant energy, volume and particle numbers is used, sampling the microcanonical ensemble (NVE). However, this situation is unrealistic since the conditions do not correspond to the experimental one, where the temperature is constant, and the energy and the volume can usually fluctuate. The two most common alternative ensembles are the NVT and NPT ensembles.

In simulations performed in the canonical NVT ensemble (124), the system is combined with a thermostat that gradually adds and subtracts energy to the system to maintain the temperature at the desired reference value. The kinetic energy is in fact modified by scaling the atomic velocities with an adequate frequency.

When the isobaric-isothermal NPT ensemble is invoked (125), both temperature and pressure are maintained constant. In addition to the thermostat, a barostat is coupled to the system to control the pressure. The barostat adjusts the volume of the system, scaling all atomic coordinates.

Another statistical-mechanics ensemble employed is the isoenthalpic-isobaric NPH one which maintains constant enthalpy and pressure. It is the analogue of the microcanonical ensemble constant-volume, constant energy, in which the size of the unit cell is allowed to vary. Enthalpy remains constant when the pressure is maintained fixed without any temperature control.

3.1.5. Ergodic hypothesis and calculation of average properties

The resolution obtained with classical MD cannot find counterevidence with experimental data, because no experiment can provide information about position and velocities in a certain moment for each atom of a system. An experimental measure is a temporal average of the property for macroscopic samples, made of an Avogadro number of atoms. Therefore, we need to extract average information from the simulation to compare them with experiments.

If in an MD simulation the phase space is properly sampled, the ergodic hypothesis is valid. An ensemble average (over many copies of the system) can be replaced by a time average for a single copy of the system. This is valid for sufficiently long averaging time t, where the time average does not depend on the initial conditions (126).

The experimental property A_{obs}, measured as the average over a large number of atoms, close to Avogadro number, can be represented as the temporal average of the property $A\big(\Gamma(t)\big)$ starting from a point of the phase space accumulated during the trajectory.

$$A_{obs} = \langle A\big(\Gamma(t)\big)\rangle_{time} = \lim_{t_{obs}\to\infty} \frac{1}{t_{obs}} \int_0^{t_{obs}} A\big(\Gamma(t)\big)dt \tag{3.12}$$

Obviously, it is not possible to extend the integration in an infinite time, therefore the average is calculated during a sufficiently long time t_{obs} to satisfy equation 3.12. In MD simulation the motion equations are solved over a finite number of time-steps τ_{obs}, and equation 3.12 can be written in terms of this variable.

$$A_{obs} = \langle A\big(\Gamma(t)\big)\rangle_{time} = \frac{1}{\tau_{obs}} \sum_{\tau=1}^{\tau_{obs}} A\big(\Gamma(t)\big) \tag{3.13}$$

3.2. Metadynamics

Molecular dynamics (MD) simulations are limited to the study of events occurring at a short timescale (of the order of few ms). Therefore, MD simulations can provide information related to the structure but are not effective to study the complete rare event, such as crystallization in glass-forming liquids, because crystals form and grow slowly over time. Brute-force MD simulations are applicable to study nucleation only for model Lennard-Jones liquids, compounds, and metallic alloys in which the phase transition occurs with very high nucleation rates ($>10^{35}$ nuclei$\cdot$cm^{-3}s^{-1}) (76,127–129). For systems exhibiting lower nucleation rates due to higher viscosity, other techniques accelerating the nucleation have been developed and applied. These rare events need an extended timescale to be observed because the relevant systems are characterized by several metastable states separated by high barriers that lead to kinetic bottlenecks. The low possibility to cross the barriers slows down the sampling of the phase space and thus the simulation of the event.

Advanced sampling methods aim to overcome the time-scale limitation of computer simulation (130). Most enhanced sampling techniques are based on the identification of a few important order parameters named collective variables (CVs). The fluctuations of these CVs are critical for the occurrence of the rare event thus, it is introduced a bias to sample these variables. In the last decade, enhanced sampling techniques have been used to explore the phase space reconstructing the free energy surface (FES) as a function of CVs appropriate to describe and follow crystallization. Metadynamics (MetaD) (131,132) is one of the most used enhanced sampling techniques. It has been applied to a wide range of systems from the nucleation of molecules (133,134) and compounds (135) to metals (136) and alloys (137–139). Recently, the method has been applied to study the crystallization of glass-forming liquids such as silica (140).

In this section these enhanced sampling techniques will be briefly presented. Starting from Metadynamics to Well-Tempered Metadynamics, presenting the importance of the choice of the collective variables (CVs) and the techniques to evaluate the free energy surface. Finally, the temperature rescaling procedure will be introduced.

3.2.1. The collective variable space

Considering a phenomenon, it can be hard to describe it in the phase space associated with the atomic coordinates ($\boldsymbol{R}$). It is often possible to describe a physical/chemical process in terms of a small number of coarse descriptors of the system ($\boldsymbol{s}$):

$$\boldsymbol{s}(\boldsymbol{R}) = (\boldsymbol{s}_1(\boldsymbol{R}), \boldsymbol{s}_2(\boldsymbol{R}) \dots, \boldsymbol{s}_d(\boldsymbol{R})) \tag{3.14}$$

This coarse-grained descriptor is defined as collective variable (CV) which is a non-linear function of the atomic coordinates. The CV should be able to: a) describe all key features of the transformation we are

interested in, b) distinguish between the metastable states involved, c) include all slow degrees of freedom. Once CVs are defined, the equilibrium distribution of the CVs ($P(\boldsymbol{s})$) can be defined as well:

$$P(\boldsymbol{s}) = \int \delta[\boldsymbol{s} - \boldsymbol{s}(\boldsymbol{R})]P(\boldsymbol{R})d\boldsymbol{R} = \langle \delta[\boldsymbol{s} - \boldsymbol{s}(\boldsymbol{R})]\rangle \tag{3.15}$$

where $P(\boldsymbol{R})$ is the equilibrium distribution with respect to the atomic coordinates. From the distribution defined in equation 3.15, the free energy surface (FES) ($F(\boldsymbol{s})$) can be extracted:

$$F(\boldsymbol{s}) = -\frac{1}{\beta}\log P(\boldsymbol{s}) \tag{3.16}$$

where $\beta = 1/k_B T$ is the inverse thermal energy. If the choice of the CV is appropriate, the FES contains all relevant information about the investigated system (141,142).

The FES is studied to understand the relative stability of the metastable phases involved. The relative free energy difference between two states *A* and *B* can be calculated from the integration of the probability of the regions associated to the states in the CV space:

$$\Delta F_{A,B} = -\frac{1}{\beta}\log\frac{\int_A d\boldsymbol{s} e^{-\beta F(\boldsymbol{s})}}{\int_B d\boldsymbol{s} e^{-\beta F(\boldsymbol{s})}} \tag{3.17}$$

In an ergodic system, it is in principle possible to sample the phase space in a conventional simulation and accumulate the $P(\boldsymbol{s})$ simply by counting. However, since the timescale of the simulation is usually not sufficiently long and because of the high barriers that can be encountered, the sampling of the phase space is non-ergodic. The simulation will observe only the fluctuation in the region of the local equilibrium state, remaining stuck in one state, producing a non-realistic $F(\boldsymbol{s})$.

3.2.2. Enhanced sampling techniques

The sampling of the phase space can be enhanced by considering a bias potential $V(\boldsymbol{s}(\boldsymbol{R}))$ that depends on the CV value. Considering this potential, introduced as umbrella sampling the first time in 1977 (143), the distribution of the CV can be reformulated:

$$P_V(\boldsymbol{s}) = \int \delta[\boldsymbol{s} - \boldsymbol{s}(\boldsymbol{R})]P_V(\boldsymbol{R})d\boldsymbol{R} = \frac{e^{-\beta[F(\boldsymbol{s})+V(\boldsymbol{s})]}}{\int d\boldsymbol{s}\, e^{-\beta[F(\boldsymbol{s})+V(\boldsymbol{s})]}} \tag{3.18}$$

where $P_V(\boldsymbol{s})$ is the distribution of the biased ensemble. This potential allows a proper sampling of the phase space, thus knowing $V(\boldsymbol{s})$ allows us to reconstruct the FES of the system. Collecting the biased distribution and the bias potential, the unbiased distribution can be recovered and the $F(\boldsymbol{s})$ can be computed from the distribution. From the CV space, it is possible to estimate R-dependent functions $O(\boldsymbol{R})$. Knowing the

relation $P(\boldsymbol{R}) \propto P_V(\boldsymbol{R}) e^{\beta V(\boldsymbol{s}(\boldsymbol{R}))}$, $O(\boldsymbol{R})$ of the unbiased ensemble is evaluated by reweighting each configuration obtained in the biased ensemble by the value of the acting bias:

$$\langle O(\boldsymbol{R}) \rangle = \frac{\langle O(\boldsymbol{R}) e^{\beta V(\boldsymbol{s}(\boldsymbol{R}))} \rangle_V}{\langle e^{\beta V(\boldsymbol{s}(\boldsymbol{R}))} \rangle_V} \tag{3.19}$$

where the right side of these equations is calculated in the biased ensemble. This equation is valid in a static bias regime.

In the umbrella sampling case, the bias potential is designed to fill completely the wells of the CV phase space, producing an equal probability of exploring any point of the phase space. Indeed, in this case the $F(\boldsymbol{s}) = -V(\boldsymbol{s})$. In an unknown system, we do not know a priori the FES, thus the bias cannot be defined at the beginning of the simulation. How the bias potential is built is one of the main differences between enhanced sampling techniques.

From the first designed, umbrella sampling (144), going through one of the most popular, metadynamics (MetaD) (145,146), and its evolutions (132,147–149), enhanced sampling methods are proving to be an essential tool to disclose the property of molecule or materials and otherwise inaccessible phenomena.

3.2.3. From Metadynamics to Well-tempered metadynamics

In standard MetaD simulations (145), the potential energy is built on-the-fly with a history-dependent bias potential $V(\boldsymbol{s}, t)$, which is composed of Gaussian functions accumulated along the simulation:

$$V(\boldsymbol{s}, t) = \sum_{t' < t} \omega \exp\left[-\sum_{\alpha=1}^{N_{CV}} \frac{\left(\boldsymbol{s}_\alpha - \boldsymbol{s}_\alpha(t')\right)^2}{2\sigma_\alpha^2} \right], t' = k\tau \tag{3.20}$$

Considering N_{CV} the number of CV used for the MetaD simulation, and α the identifier for each CV, ω is the height of the Gaussian centered in the visited point of the CV space, $\boldsymbol{s}_\alpha(t')$, at each MetaD step, t', with a width σ_α. Each MetaD step is k-times the Gaussian deposition time, τ. Therefore, at each deposition time a new Gaussian is added to the potential, and the final potential, at time t is the sum of all accumulated Gaussians in the CV phase space. The free energy landscape along the selected set of CVs is evaluated by considering that at infinite time the FES is the inverse of the bias potential except for a constant value C:

$$V(\boldsymbol{s}, t \to \infty) = -F(\boldsymbol{s}) + C \tag{3.21}$$

MetaD does not require a priori knowledge of the landscape, but on the other hand the convergence is in theory reached at infinite time and very long simulation time or several runs are required. Moreover, overfilling is a disadvantage and a waste of computational resources. Several techniques have been developed to improve MetaD and the Well-Tempered case is an effective example.

In Well-Tempered Metadynamics (WTMetaD) (147), the height of the Gaussian added at each timestep is scaled down by a factor, which depends on the bias already accumulated in the explored point and a bias factor, γ:

$$V(\boldsymbol{s},t)=\sum_{t'<t}\omega\exp\left[-\frac{1}{\gamma-1}\beta V(\boldsymbol{s}(t'),t')\right]\exp\left[-\sum_{\alpha=1}^{N_{CV}}\frac{\left(\boldsymbol{s}_\alpha-\boldsymbol{s}_\alpha(t')\right)^2}{2\sigma_\alpha^2}\right],t'=k\tau \tag{3.22}$$

where β is the inverse thermal energy, the factor $(\gamma-1)\beta^{-1}$ is sometime referred to as $k_B\Delta T$. The bias factor is an indicator of how fast the height of Gaussians will decrease during the simulation, and it determines a fictitious temperature along the biasing CV, which is $(T+\Delta T)=\gamma T$. In the WTMetaD, the bias potential tends to increase with the same intensity at each point in the CV space, which results in faster convergence than non-tempered MetaD by avoiding the exploration of very high-energy regions. From the accumulated bias potential, the free energy surface of the investigated transition in a converged regime can be estimated as:

$$F(\boldsymbol{s})=-\frac{\gamma}{\gamma-1}V(\boldsymbol{s}) \tag{3.23}$$

The procedure to determine the bias potential is crucial for accurately reconstructing the FES, and the selection of the parameters is sensitive to convergence time of the simulation. The collective variable is the first and most important choice when MetaD or WTMetaD are used. Height, ω, width, σ, and bias factor, γ, are the WTMetaD parameters, which define the shape of the Gaussians added during the simulation and the deposition time, τ, defines the frequency of construction of the bias potential. In the WTMetaD environment the convergence and overfilling issues are solved.

As discussed above, in the case of the unbiased MD simulations, the FES is computed by unbiased ensemble averages $\langle O(\boldsymbol{R})\rangle$, where $\boldsymbol{R}$ represents the atomic configurations of the system. Contrarily, in WT case the FES can be calculated using the reweighting procedure (150), which recovers the FES along CVs biased in the WTMetaD simulations. Each configuration of the trajectory is weighted according to the bias deposited. Then, the unbiased Boltzmann probability distribution $P(\boldsymbol{R})$ of the $\boldsymbol{R}$ coordinates is estimated by reweighting the biased distribution $P_V(\boldsymbol{R},t)$:

$$P(\boldsymbol{R})=P_V(\boldsymbol{R},t)w_V(\boldsymbol{R}),w_V(\boldsymbol{R})=e^{\beta\left(V(\boldsymbol{s}(\boldsymbol{R}),t)-c(t)\right)} \tag{3.24}$$

where the exponential part is the weight for each configuration $w_V(\boldsymbol{R})$, and $c(t)$ is a time-dependent function of the offset energy, which estimates the work done by the bias. An increase of the offset energy indicates that the FES approaches an asymptotic approximation. In fact, once the applied bias becomes quasi-stationary, the adiabatic limit is reached, and, thus, the FES is recovered. The offset energy, $c(t)$, can be evaluated using different formulas (150,151), in this work we used the one suggested in the review of Valsson et al. (130):

$$c(t) = \frac{1}{\beta}\log\frac{\int d\boldsymbol{s}\exp\left[\frac{\gamma}{\gamma-1}\beta V(\boldsymbol{s},t)\right]}{\int d\boldsymbol{s}\exp\left[\frac{1}{\gamma-1}\beta V(\boldsymbol{s},t)\right]} \tag{3.25}$$

The average of a general observable can be estimated from the trajectory as the unbiased ensemble $\langle O(\boldsymbol{R})\rangle$:

$$\langle O(\boldsymbol{R})\rangle = \langle O(\boldsymbol{R})e^{\beta\left(V(\boldsymbol{s}(\boldsymbol{R}),t)-c(t)\right)}\rangle_V \tag{3.26}$$

It is thus possible to extract the probability distribution for each CV, $\boldsymbol{s}'$, using eq. 3.24 and 3.26. Then, according to equation 3.18, we obtain:

$$P(\boldsymbol{s}') = \int \delta[\boldsymbol{s}' - \boldsymbol{s}'(\boldsymbol{R})]P(\boldsymbol{R})d\boldsymbol{R} = \int \delta[\boldsymbol{s}' - \boldsymbol{s}'(\boldsymbol{R})]P(\boldsymbol{R},t)e^{\beta(V(\boldsymbol{s}(\boldsymbol{R}),t)-c(t))}d\boldsymbol{R} \tag{3.27}$$

from which the FES along any CV, biased or not biased, can be easily calculated using equation 3.16.

3.2.4. The block analysis

The error of the FES is evaluated using the so-called block analysis (152).

A set of block dimensions is defined $\boldsymbol{n}$. For each size of the set n_i

- the total trajectory of the simulation is divided into blocks containing n_i configurations;
- the FES is computed in each block of configurations generated;
- the error is computed from the comparison between the FESs obtained.

The simulation is judged to be converged when the error remains constant with an increase of the block sizes.

3.2.5. The temperature rescaling procedure

Usually, it is necessary to recover the probability distribution at a temperature different from the one used in the original simulation. The data contained in the trajectory can be reweighted to obtain ensemble averages at different temperatures. We call this procedure temperature rescaling. In this method, the probability distribution, $P_T(\boldsymbol{R})$, calculated by a WTMetaD simulation at temperature T is reweighted to estimate the probability distribution at a different temperature T', $P_{T'}(\boldsymbol{R})$. The idea is similar to the reweighting calculation using eq. 3.24. The reweighting factors, w, for a canonical ensemble (NVT) and an isothermal-isobaric ensemble (NPT) are respectively defined as:

$$\begin{gathered} P_{T'}(\boldsymbol{R}) = P_T(\boldsymbol{R})w_{ensemble}(\boldsymbol{R}), \\ w_{NVT}(\boldsymbol{R}) = e^{(\beta-\beta')U(\boldsymbol{R})} \\ w_{NPT}(\boldsymbol{R}) = e^{(\beta-\beta')(U(\boldsymbol{R})+pV)} \end{gathered} \tag{3.28}$$

where $U(\boldsymbol{R})$ is the internal energy of each configuration, $U(\boldsymbol{R}) + pV$ is the enthalpy, and β and β' are the inverse thermal energies using the original and target temperatures.

The above equation is impractical in an unbiased simulation since the overlap between the distributions of energy at different temperatures is only significant for neighboring temperatures. But when the distributions are altered because of the presence of a bias potential, the overlap increases. Thus, the rescaling temperature procedure must be combined with a reweighting procedure to start from a biased distribution.

3.2.6. Collective variable for crystallization

The central aspect of collective variable-based techniques is to define one or more CVs to describe the slow degrees of freedom of the system. As described above, the CV's fluctuations are enhanced to sample metastable states in the phase space. In the context of crystallization, the CVs are designed to distinguish between the particles in the crystal and liquid or dispersed in solution phases (141,153,154). Unfortunately, it can be hard to define a CV that describes all the slow degrees of freedom of a system, because of the complexity of the system. A collective variable is in this case "suboptimal", therefore reaching convergence becomes more difficult and requires longer simulations, but it is still possible to converge them (140,142).

In literature, several different CVs have been applied in the study of crystallization. In the next paragraphs, the three CVs used in this research for biasing or analyzing the investigated system are summarized: intensity of X-ray diffraction peak, Steinhardt order parameter and the local entropy fingerprint.

3.2.6.1. Intensity of X-ray diffraction peaks

The intensity of a particular X-ray diffraction (XRD) peak was chosen as the CV in a recent paper of Niu et al. (140), which studied the crystallization of liquid silica.

The choice of using this property is a fair choice since the XRD peak's intensity depends on the long-range order of a structure, which is present in a crystalline structure but absent in non-crystalline systems. Also, XRD can be obtained experimentally and compared with computed results, as shown in other two works where the crystallization of perovskites was investigated (137,139). Therefore, the intensity of the XRD peak can be a good choice.

It is usually calculated using Debye formula (155):

$$I(\boldsymbol{Q}) = \frac{1}{N}\sum_{j=1}^{N}\sum_{i=1}^{N} f_i(\boldsymbol{Q}) f_j(\boldsymbol{Q}) \frac{\sin\left(\boldsymbol{Q}\cdot r_{ij}\right)}{\boldsymbol{Q}\cdot r_{ij}} W\left(r_{ij}\right) \tag{3.29}$$

where $f_i(\boldsymbol{Q})$ and $f_j(\boldsymbol{Q})$ are the atomic scattering form factors, $\boldsymbol{Q}$ is the scattering vector modulus and r_{ij} is the distance between atoms i and j. $W\left(r_{ij}\right)$ is the Lorch function used to overcome the artifacts due to the finite simulation box, and it is calculated as:

$$W(r_{ij}) = \frac{\sin(\pi\ r_{ij}/R_c)}{\pi\ r_{ij}/R_c} \tag{3.30}$$

where R_c is the upper limit of r_{ij}.

Contrarily to the previous work by Niu et al., where $I(\boldsymbol{Q})$ was evaluated using all atoms, it can be convenient to evaluate this property only on a certain type of atoms to reduce the computational cost (139,156,157). This topic will be discussed when the CV is chosen according to the studied system.

By comparing the XRD patterns of crystalline and glass/liquid structures, the $\boldsymbol{Q}$ value exhibiting the biggest difference in the intensity peak is selected as an effective CV. Note that $\boldsymbol{Q}$ value is converted to a scattering angle 2θ as:

$$Q = \frac{4\pi}{\lambda}\sin\theta \tag{3.31}$$

where λ is the wavelength of the radiation.

3.2.6.2. Steinhardt local order parameters

An order parameter that is sensitive to an ordered or disordered environment of the atoms contained in the model can be used when a mixed crystal/amorphous system must be studied, since it allows us to distinguish between the crystalline nucleus and its interface with the glassy/liquid matrix.

The Steinhardt order parameters has been widely used to distinguish between the liquid or glassy state to one or more crystal phases (158) and has proven to be one of the most efficient. The l-order Steinhardt parameter $Q_l(i)$ for atom i is defined by:

$$Q_l(i) = \sqrt{\frac{4\pi}{2l+1}\sum_{m=-l}^{l}|q_{lm}(i)|^2} \tag{3.32}$$

where

$$q_{lm}(i) = \frac{1}{N(i)}\sum_{j=1}^{N(i)} Y_{lm}(r_{ij}) \tag{3.33}$$

Where the index j runs on the $N(i)$ neighbors of atom i within a certain cutoff (R_1). $Y_{lm}(r_{ij})$ is a spherical harmonic with a vector displacement r_{ij} from atoms i and j. The subscript l is a free integer parameter that confines m between $-l$ and $+l$. To calculate the local degree of order around a central ion we have also computed the local $Q_l^{loc}(i)$ parameter by taking the average dot product between the complex $q_l^*(i)$ vector on the central atom and the $q_l(j)$ vector on the atoms in the first coordination sphere:

$$Q_l^{loc}(i) = \frac{1}{N(i)} \sum_{j=1}^{N(i)} \sum_{m=-l}^{+l} q_{lm}^*(i)\, q_{lm}(j) \tag{3.34}$$

This parameter measures the extent to which the orientation of the atoms in the first coordination sphere of atom *j*, defined by (R_2), matches the orientation of the central atom.

The average $\bar{Q}_l(i)$ and local average $\bar{Q}_l^{loc}(i)$ parameter for atom *i* can be computed as the average of the $Q_l(i)$ and $Q_l^{loc}(i)$ parameters of its neighboring atoms with a certain radius (R_2).

$$\bar{Q}_l(i) = \frac{Q_l(i) + \sum_j \sigma(r_{ij}) Q_l(j)}{1 + \sum_j \sigma(r_{ij})} \tag{3.35}$$

$$\bar{Q}_l^{loc}(i) = \frac{Q_l^{loc}(i) + \sum_j \sigma(r_{ij}) Q_l^{loc}(j)}{1 + \sum_j \sigma(r_{ij})} \tag{3.36}$$

Where $\sigma(r_{ij})$ is a switching function that acts on the distance between atoms i and j. This function should define the first coordination sphere, assuming a value of 1 when the atom j belongs to the first coordination, and it is 0 otherwise.

This order parameter can be used as CV, computing the average of all interested atoms, or individually to describe the structure.

3.2.6.3. Local entropy fingerprint

The local entropy fingerprint is useful to identify atoms with a crystal-like environment in a structure. The entropy of the atom i is calculated with the following formula (136):

$$s_S^i = -2\pi\rho k_B \int_0^{R_{max}} \left[g_m^i(r) \log g_m^i(r) - g_m^i(r) + 1 \right] r^2 dr \tag{3.37}$$

where R_{max} is an upper integration limit that in principle should be tend to infinity, ρ is system's density and $g_m^i(r)$ is the radial distribution function centered at the i-th atom and defined as:

$$g_m^i(r) = \frac{1}{4\pi\rho r^2} \sum_j \frac{1}{\sqrt{2\pi\sigma_S^2}} e^{-(r-r_{ij})^2/(2\sigma_S^2)} \tag{3.38}$$

where j are the neighbors of atom i and σ_S is a broadening parameter.

The average local entropy $\bar{s}_S^i$ for atom i is computed as the average of the local entropies of its neighboring atoms within a certain radius R_a:

$$\bar{s}_S^i = \frac{s_S^i + \sum_j \sigma(r_{ij}) s_S^j}{1 + \sum_j \sigma(r_{ij})} \tag{3.39}$$

where $\sigma(r_{ij})$ is a switching function that acts on the distance between atoms *i* and *j*. This function should define the first coordination sphere, assuming a value of 1 when the atom j belongs to the first coordination, and it is 0 otherwise.

The average local entropy can be calculated only on a selected type of atom to improve the ability to discriminate between crystalline and non-crystalline environments.

Chapter 4. Melting temperature

The computational determination of the melting point (T_m) is a prerequisite for studying crystallization phenomena. The computational melting temperature depends strongly on the interatomic potential, the system size and the method used to compute it. Despite this, once this temperature is individuated, all the other events are considered relative to this temperature.

There are different methods to evaluate the melting point of a crystal. The most used are described in ref (159). In general, depending on the way it is determined we can distinguish between the so-called mechanical and thermodynamic melting temperature. The first one, which is obtained by a heating/quenching procedure, depends mostly on the hysteresis of the system in response to a chosen heating/quenching rate. The thermodynamic melting temperature is obtained from the thermal equilibration of a crystal-liquid interface. This is obtained when the difference in free energy between the phases is zero, thus has more significant physical meaning.

The mechanical and thermodynamic melting temperature of lithium disilicate (LS_2) and lithium metasilicate (LS) have been evaluated.

4.1. Mechanical melting point

To determine the mechanical melting temperature, we first equilibrated the crystalline phases (both LS_2 and LS), starting from the experimental obtained crystalline structure (63,64), at a temperature of 300 K and a pressure of 0 bar. The supercells used were obtained by multiplying the LS_2 and LS unit cell, respectively, for 6x2x5 and 3x5x6, obtaining simulation boxes containing 2160 atoms each. Then we heated up to 3000 K the system with a heating rate of 5 K/ps in the NPT ensemble. We followed the changing volume and potential energy per formula unit (f.u.) during the heating procedure, and we plot it in figure 3.1.

The estimation of the melting point is measured in the jump of both the volume and the potential energy, obtaining $T_m \cong$ 1800 K and $\cong$ 1750 K for LS_2 and LS respectively. Both values overestimate the experimental data (LS_2: 1307 K and LS: 1474 K) (8).

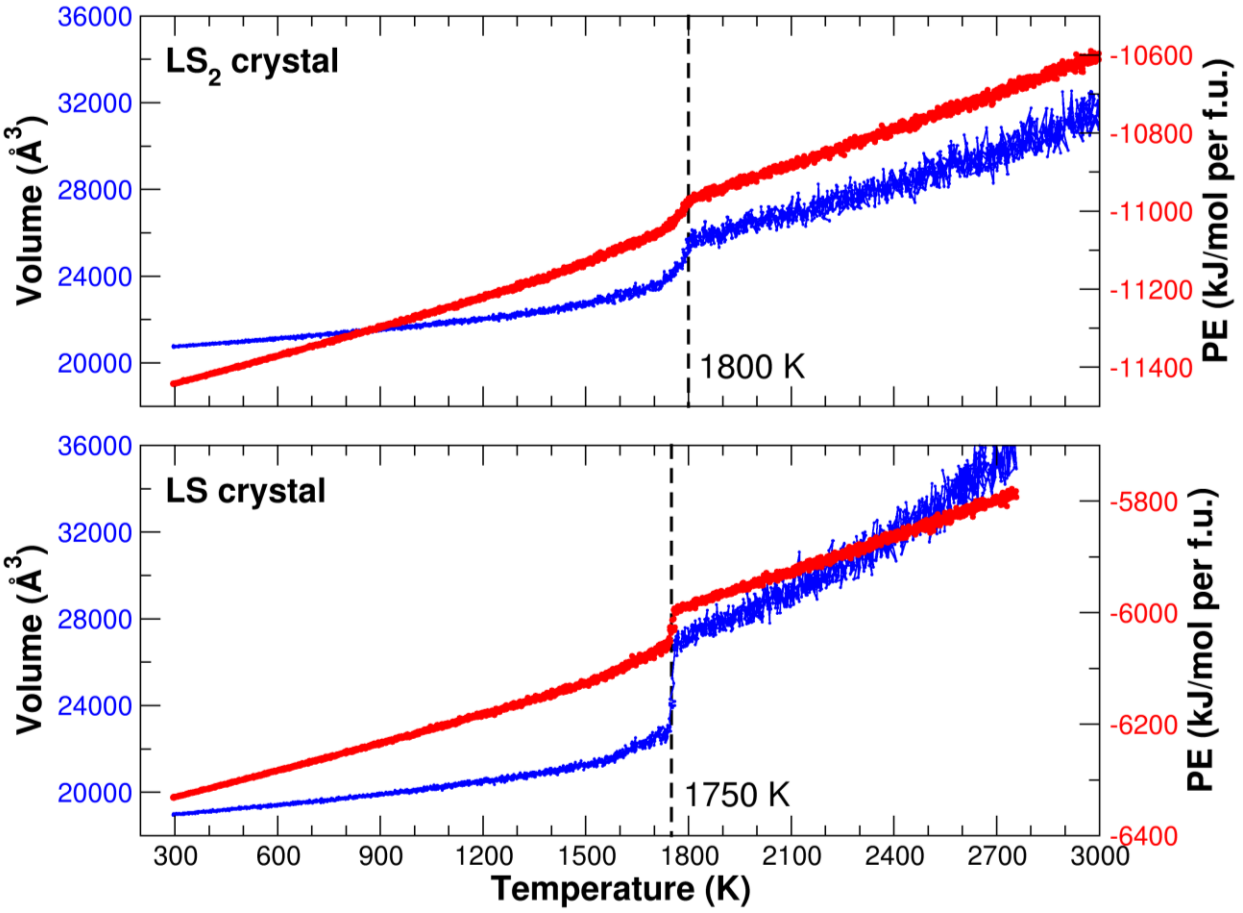

FIG. 4.1. Volume and potential energy per formula unit (f.u.) as a function of temperature during the heating of LS_2 and LS crystal with a heating rate of 5 K/ps. The dashed line represents the extracted melting point.

The original procedure, described in (159,160), foresees the heating and cooling of the system and the extraction of the superheating and supercooling temperatures from the evolution of the potential energy. The melting point is computed as the average between the two temperatures However, because it is not possible to observe the crystallization of LS_2 and LS crystal during the quench of the melt phase, it was not possible to extract the supercooling temperature in our study. The temperature that we have extracted is thus the superheating temperature and it overestimates the melting point. The overestimation of this value is due to the application of PBC, which eliminates surfaces where melting is initiated in real samples. Thus a huge cooling rate is used in computer simulations with respect to the one used in experiments, as discussed in ref (161,162). The resulting value of this method depends strongly on the hysteresis of the system; hence it is important to choose a more precise method.

4.2. Thermodynamic melting point

To obtain the thermodynamic melting temperature, we used the phase-coexistence technique. In literature, different versions of this technique have been developed, two of them will be presented in this section.

4.2.1. The Dozhdikov method

The following technique has been proposed by Dozhdikov et al. (157,160,163). In this method, the starting configurations are built as rectangular parallelepipeds with one of the three dimensions around 3 times larger than the other two dimensions by replicating the crystalline unit cell to obtain a super-cell, we choose here for example that the z-direction is three times x and y. During the first stage, the cell is equilibrated in the NVE ensemble. It is then brought to an expected melting temperature, T_{es}, at atmospheric pressure in the NPT ensemble. In the third stage, position and velocities of half atoms along z-axis of the system are fixed, while the other half is heated to higher temperature, T_h, in the $NP_{zz}T$ ensemble to reach complete melting of this region. In this way half of the system is liquid whereas the other is crystalline. Subsequently, the melted region is cooled to T_{es} in the $NP_{zz}T$ thermostat-barostat obtaining a box where the two regions are in different phases but same pressure and temperature. During the fifth stage, the whole system is allowed to relax in the NPH ensemble at atmospheric pressure. After 10 ns of MD simulation, the system reaches equilibrium where different situations may occur. If the crystalline side melts or the melted region crystallizes, the procedure must be repeated starting from stage 2 changing T_{es} or T_h. If the two phases coexist then melting temperature can be extracted from the statistical temperature, stage 6.

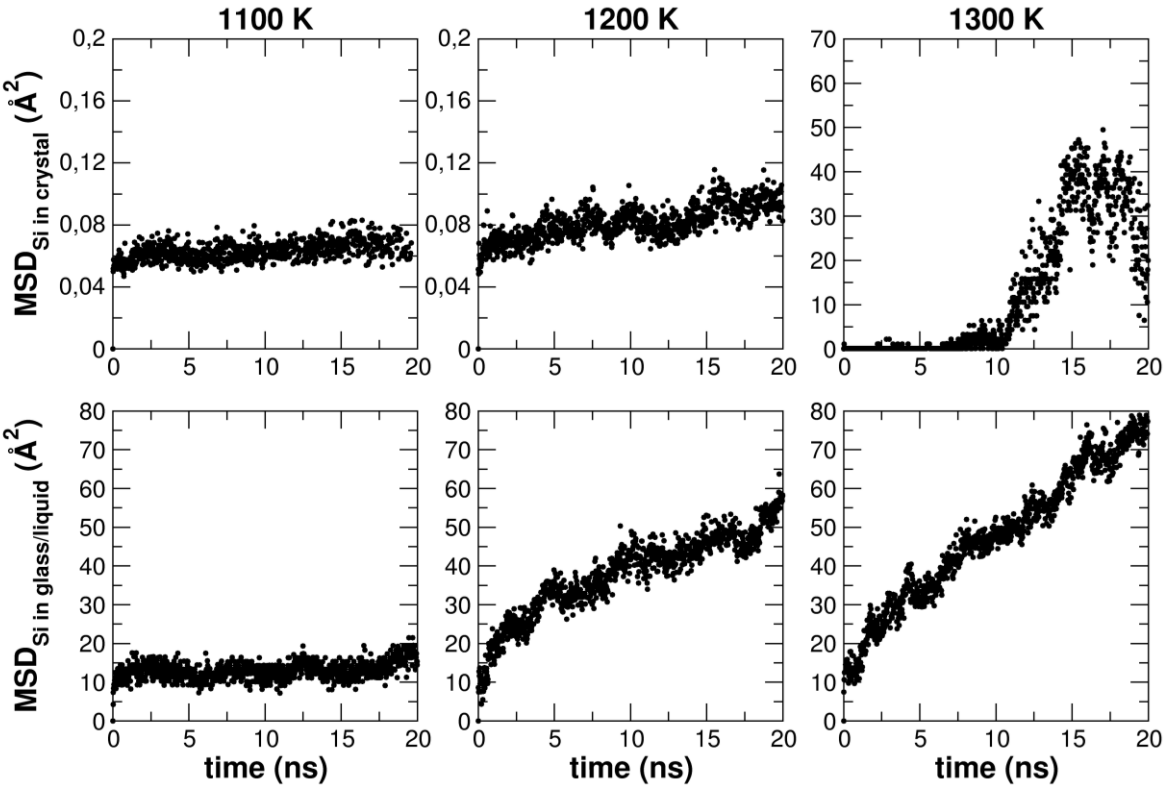

FIG. 4.2. Example of mean square displacement of Si atoms in the crystal side (upper) and glassy or liquid side (bottom) in the two-phases super-cell at three different temperatures.

To check the phase coexistence we first used a visual inspection of the interface, using VMD (164) to visualize the structure. The stability and persistence of the crystalline phase confirm that the temperature is equal or lower than the T_m. However, we do not observe the crystallization of the liquid side, thus

understanding the phase coexistence visually may be tricky and eventually inaccurate. A more reliable method is to compute the mean square displacement (MSD) of the group of Si atoms both for the crystal and liquid/glass phases. The two groups are defined at the beginning of the procedure, when the two-phase model is built. It is known, that in liquid the displacement depends linearly on time and the slope of this line is proportional to the self-diffusion coefficient. In the solid phase the Si mean-square displacement fluctuates near a certain constant value and the coefficient of self-diffusion equals to zero. Figure 4.2 reports how the MSD of Si atoms in the crystal and glass/liquid side changes according to the temperature. The melting temperature in the example is 1200 K, in fact in the liquid side the MSD has a linear trend, while in the crystalline side the MSD is almost constant. At $T > T_m$, Si atoms in the crystalline side start to diffuse, while at $T < T_m$ Si atoms in the liquid/glassy side are less mobile.

4.2.1.1. Effect of the box dimension on the melting temperature

The Dozhdikov method has been applied to investigate how the melting temperature changes with the system dimension. The supercells used for LS_2 and LS were obtained by replicating the respective unit cells for the factors reported in table 4.1, containing the reported number of atoms.

TABLE 4.1. Replicating factors and number of atoms in each created supercell for LS2 and LS systems.

LS_2	**2x2x2**	**3x3x3**	**4x5x5**	**5x6x6**	**6x7x7**
n° atoms	288	972	3600	6480	10584
LS	**3x2x2**	**5x3x3**	**7x4x4**	**8x5x6**	**9x6x7**
n° atoms	288	1080	2688	5760	9072

The direction along which the crystal/melt surface was generated is, respectively, x and y for LS_2 and LS, according to the super-cells that were created. The biphasic systems are depicted in figures 4.4 and 4.5, where the interface is clearly visible. The temperature range, T_{es}, under investigation is 800 K to 1400 K, with intervals of 50 K, while T_h values tested are 2000 K, 2500 K and 3000 K. The calculated melting temperatures are reported in figure 4.3 and decrease, increasing the number of atoms.

When the number of atoms is 3600 or higher, the LS_2 melting temperature converges at 1200 K, while LS reaches convergence from 5760 atoms at 1150 K. Therefore, we obtain a T_m of 1200 ± 50 K for LS_2 and 1150 ± 50 K for LS, both values are in fair agreement with the experimental values (LS_2 1307 K, LS 1474 K) (8) even though the relative trend is not reproduced.

These observations confirm that the calculated melting temperature depends on the size of the system investigated, therefore for obtaining reliable results it is fundamental to use large boxes.

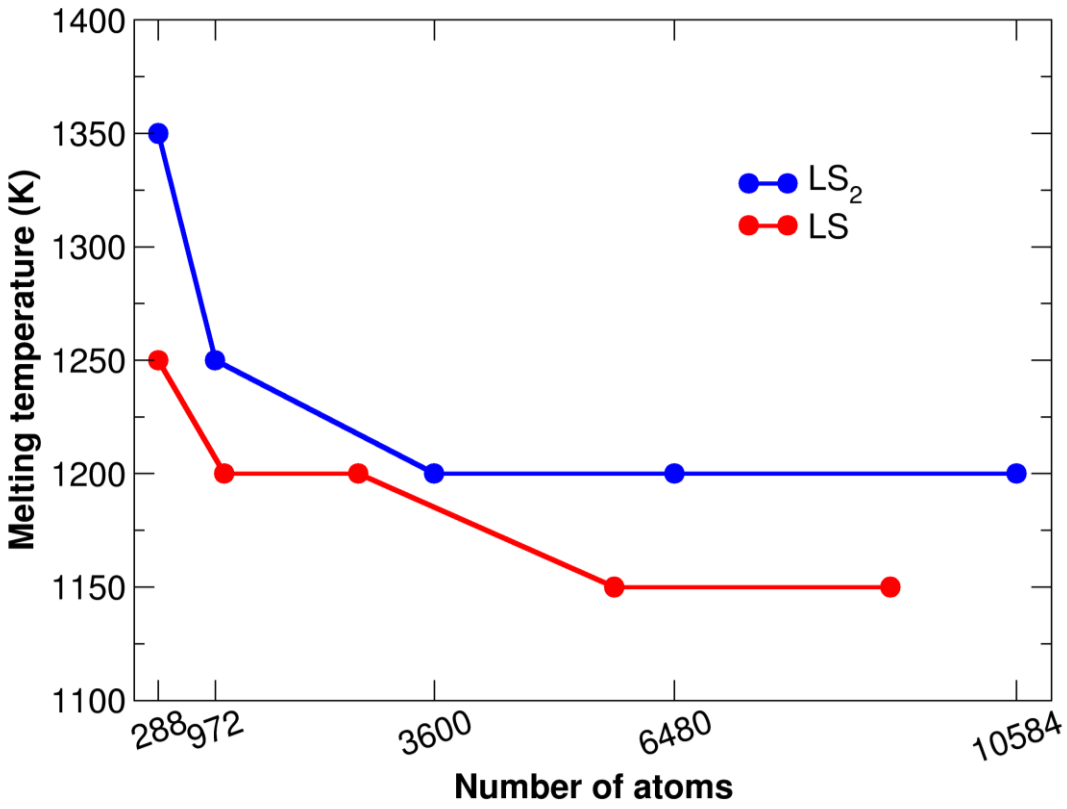

FIG. 4.3. Calculated melting temperature versus the number of atoms contained in the simulation box.

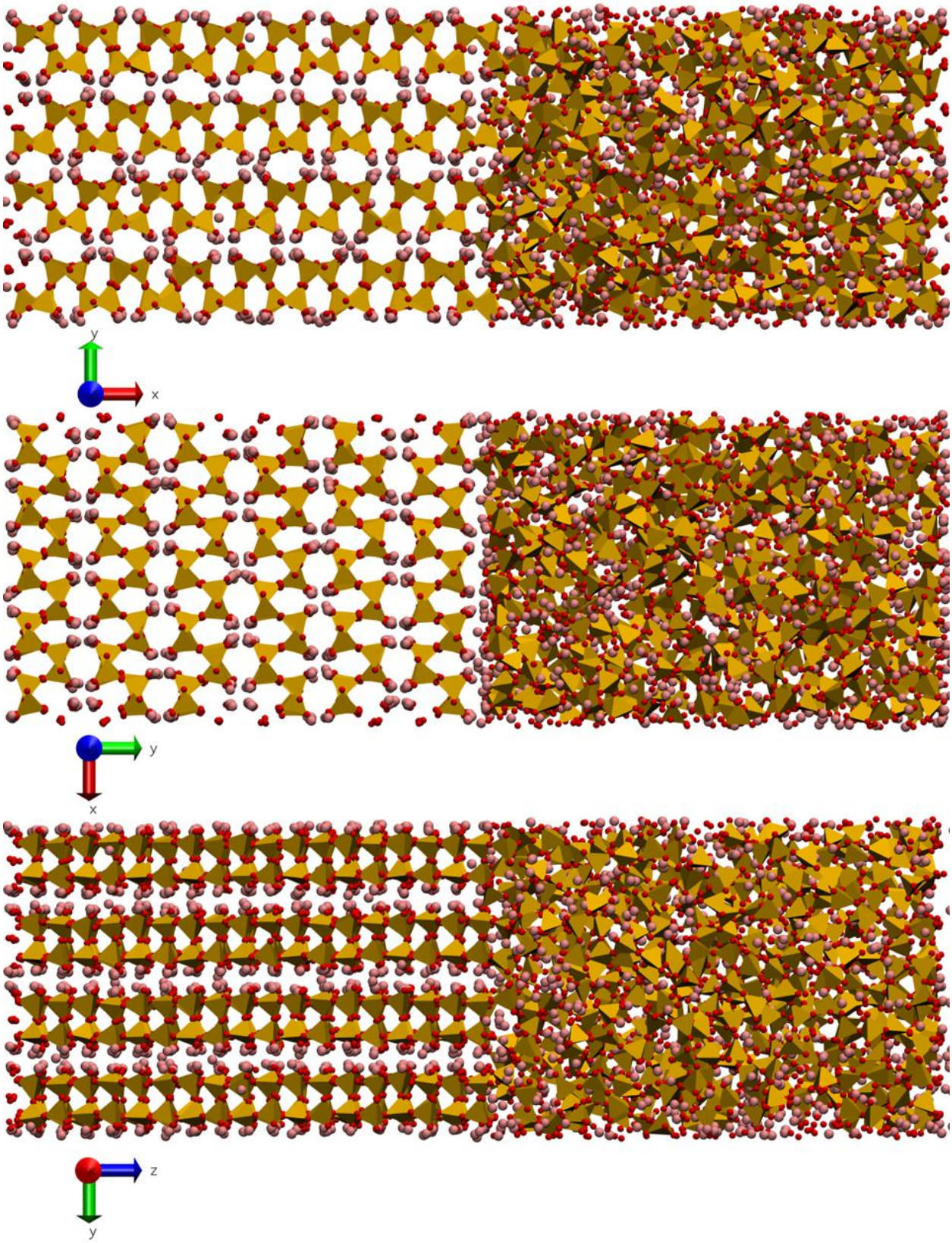

FIG. 4.4. Examples of biphasic systems generated for the calculation of the melting temperature of LS_2 crystals. Yellow tetrahedra represent silicon coordination, red and pink spheres represent oxygen and lithium ions, respectively. From up to bottom the supercells are obtained by replicating the unit cell 15x2x6, 5x6x6, 5x2x18 times and contain 6480, 6480, 6480 atoms, respectively.

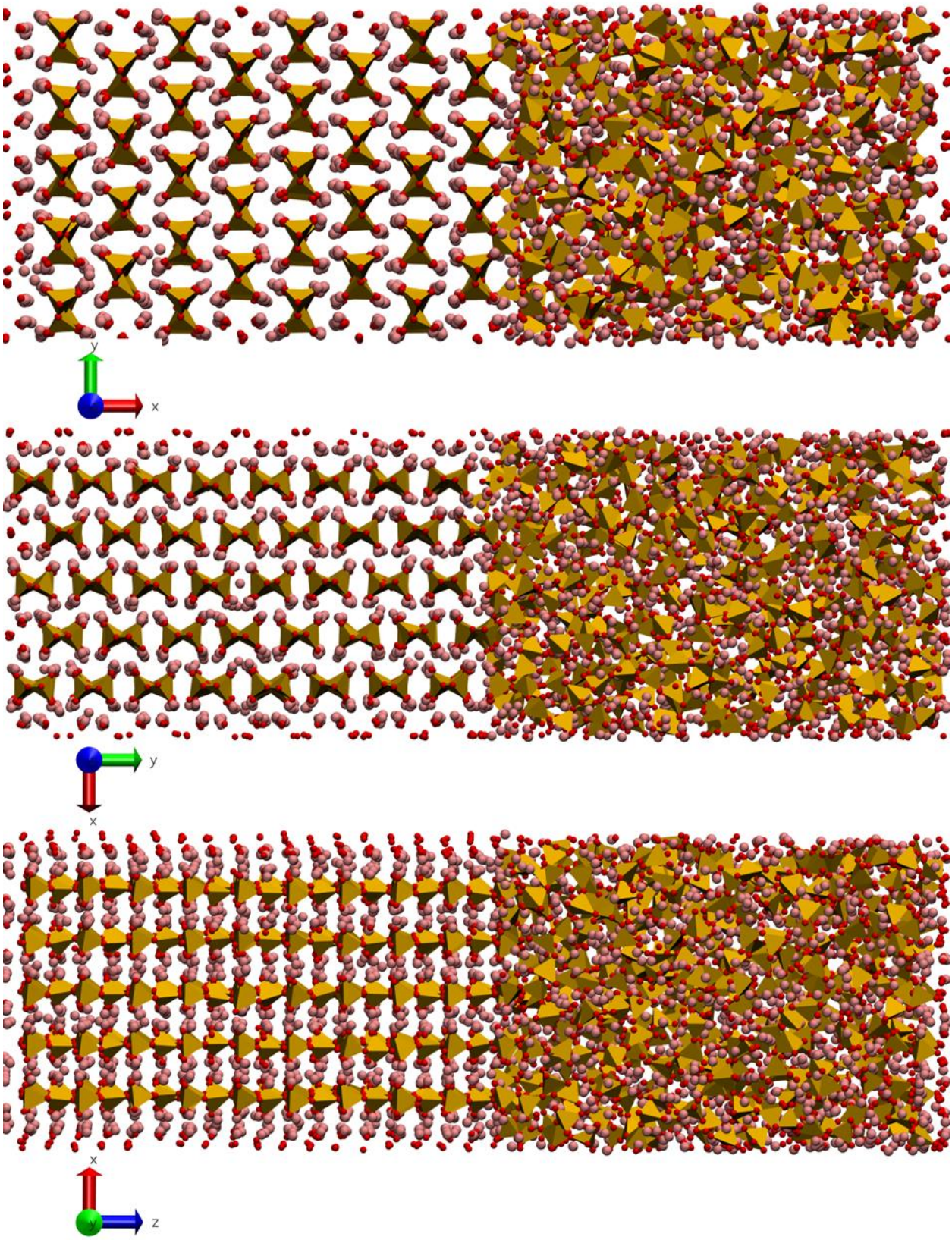

FIG. 4.5. Examples of biphasic systems generated for the calculation of the melting temperature of LS crystals. Yellow tetrahedra represent silicon coordination, red and pink spheres represent oxygen and lithium ions, respectively. From up to bottom the supercells are obtained by replicating the unit cell 8x5x6, 3x16x6, 5x2x18 times containing 5760, 6912 7776 atoms, respectively.

4.2.1.2. Effect of the crystal orientation on the melting temperature

It is also interesting to investigate if the direction along which the melt/crystalline interface created influences or not the resulting melting temperature. The super-cells reported in table 4.2 have been created for this purpose and shown in figures 4.4 and 4.5.

TABLE 4.2. Replicating factors, number of atoms and melting temperature of created supercell for LS_2 and LS systems with liquid/solid surface in x – y – z directions.

		x-direction	**y-direction**	**z-direction**
LS_2	Replication	15x2x6	5x6x6	5x2x18
	n° atoms	6480	6480	6480
	T_m (K)	1100	1200	950
LS	Replication	8x5x6	3x16x6	3x6x18
	n° atoms	5760	6912	7776
	T_m (K)	1150	1100	900

The direction of creation of the interface affects the face of the crystal exposed, that, as we can see from table 4.2, influences the T_m. In LS_2, y-direction has the highest melting temperature since the crystal is cut in the interlayer (figure 4.4), while it has a lower T_m when the layer is interrupted by the interface, x, and z directions. LS has a similar T_m in x and y-direction where the chains are parallel to the interface, and a lower T_m when the chains are perpendicular to the interface (figure 4.5). Therefore, depending on which face a crystalline nucleus exposes in the glass matrix it will have a different stability.

4.2.2. The Chen method

The second phase-coexistence technique presented, has been developed by Chen et al. (165) and employed in several studies (159,166,167). For the LS_2 crystal, a super-cell containing 6480 atoms has been used and the solid/liquid interface has been created replicating the crystalline box 5x6x6. For the LS crystal a super-cell containing 5760 atoms has been employed and the starting configuration to obtain the solid/liquid interface has been created by replicating the crystalline cell 8x5x6, considering the minimum reliable dimension obtained in paragraph 4.2.1.1. The following procedure has been applied on both samples. The starting system is heated up to 1000 K, temperature assumed lower than the T_m, and then the box is divided along one direction into two equal parts (y-direction for LS_2, and x-direction for LS). The position of the atoms in one of the two sides are kept fixed, while the other side is melted at 3000 K for 500 ps in NVT ensemble to generate the melt and then cooled down at 1000 K to create a glassy side. The box is finally

relaxed at 1000 K in the NPT ensemble without fixing any atomic position for 500 ps. The biphasic systems produced using the described procedure are reported in figures 4.4 and 4.5, which is the same used with the first method, paragraph 4.2.1. An interface is generated between the two phases which is submitted to a free energy difference between the two sides, larger difference if the temperature is far from the T_m, lower if the working temperature is near the T_m. This difference is the driving force for the dissolution or, eventually, growth of the crystalline side.

To find the temperature at which the two phases coexist, it is necessary to heat up the system at different temperatures, increasing from 1100 K to 1400 K in 50 K intervals. At each temperature the potential energy is monitored for 20 ns of simulation. In figure 4.6 it is reported the evolution of the potential energy, normalized for the number of formula units, and calculated as a difference from the beginning of 20 ns of simulation. The enthalpy of the system can also be used for this purpose; however, the fluctuations are significantly larger than the potential energy and because it provides the same results, the potential energy has been chosen as monitored observable.

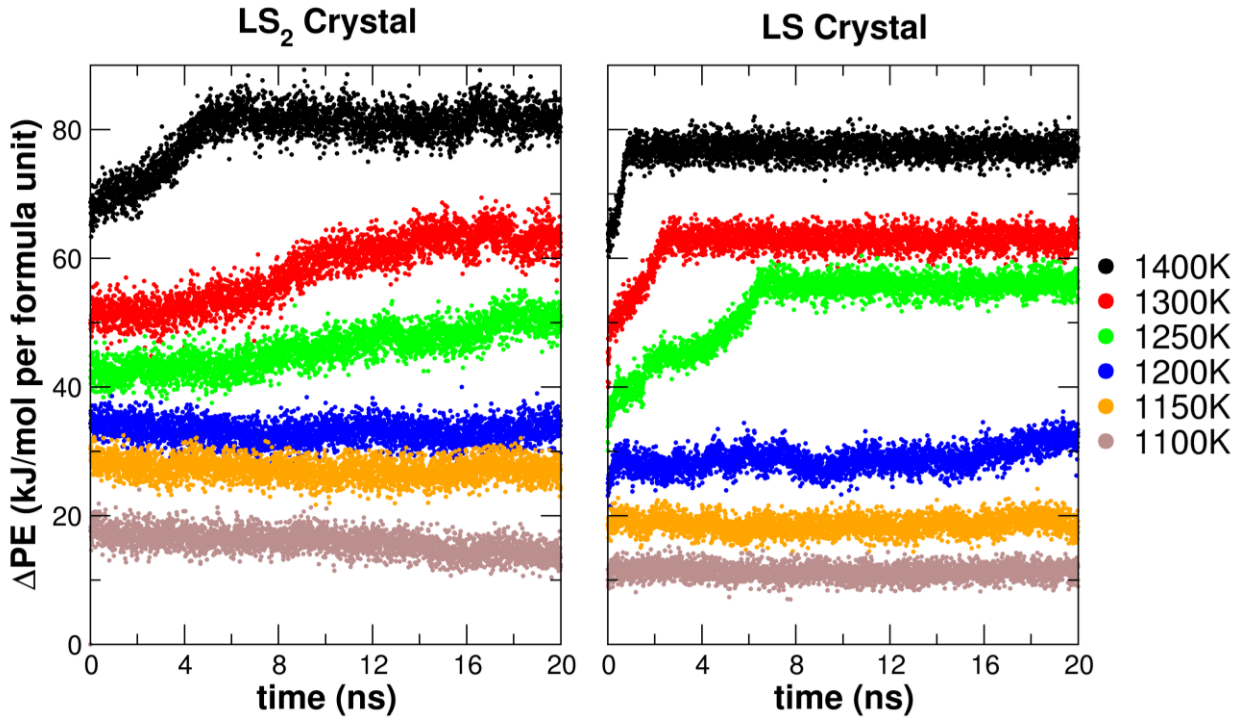

FIG. 4.6. Potential energy of LS_2 (on the left) and LS (on the right) versus time at selected temperatures above and below melting temperature. It is calculated as a difference from the potential energy of the starting configuration. For temperatures above melting point, the potential energy increases, whereas at and below it, the potential energy is practically constant.

Above 1200 K in the LS_2 system, the potential energy increases as the liquid phase progresses, whereas at 1200 K and 1150 K, the energy remains constant. The dissolution of the crystalline phase is affected by the simulation time; to observe the growth of the crystalline side, simulation times out of the accessible timescale of MD should be simulated. Therefore, we obtain a melting temperature of 1200 ± 50 K. The LS shows a similar behavior, however at the end of the 20 ns the crystalline side starts to melt at 1200 K,

resulting in a melting temperature of 1150 ± 50 K. Both values are in perfect agreement with the Dozhdikov method. Therefore, both methods seem to be reliable for the determination of the thermodynamic melting temperature.

Chapter 5. Simulating crystallization by Molecular Dynamics

Several experimental techniques are used to study nucleation, i.e., optic and electronic microscopies, differential scanning calorimetry, atomic force microscopy and X-ray experiments. It is indeed hard to obtain spatial and temporal information with high resolution since nucleation takes place at the length scale of the nanometer. Therefore, the comprehension of this phenomenon is far from exhausted.

Computer simulations are a fundamental tool to overcome the length scale problem and Molecular Dynamics, MD, is the most suitable technique to address this topic (chapter 3).

In this chapter different approaches to study the nucleation using the MD will be presented. It is first investigated how the similarity between the glassy structure and the crystalline phases gives indication about the possible crystallization of a phase. Thus, we investigate the structure of bulk and surface of two glass models, and we look for the presence of crystalline embryos in the models. The first glass structure is composed of Li_2O $2SiO_2$ (LS_2), and the second one differs by the addition of a small amount of P_2O_5, $33Li_2O$ $66SiO_2$ $1P_2O_5$ (LS_2P1). P_2O_5 is usually used as a nucleating agent in the industry. The crystalline phases searched are $Li_2Si_2O_5$ (LS_2), Li_2SiO_3 (LS) and Li_3PO_4 (LP).

The second approach is based on the seeding method, where a crystalline nucleus is inserted into a glass matrix and its evolution, dissolution or growth, is followed. However, the high viscosity of oxide glasses does not allow us to observe the growth of a crystalline nucleus in the time frame of the simulation. Therefore, it is evaluated the free energy of systems containing nuclei with different sizes, to follow the stability of these nuclei and find the critical one. Crystalline nuclei of LS_2 and LS are inserted into a glass matrix with the overall composition of LS_2. The nuclei have spherical shapes with different radii ranging from 6 Å to 14 Å and their evolution is studied and compared with expected results from the Classical Nucleation Theory (CNT).

5.1. Research of embryos: CLUSTER program

5.1.1. Cluster analysis: the algorithm

The aim of this analysis is to explore atomic aggregates whose stoichiometry and structure are similar to a particular crystalline phase that is thought to nucleate and crystallize from the glass forming liquid. The cluster analysis has been performed using a new FORTRAN90 code based on the one developed in the past by Pedone (168) (Cluster code). The program analyses the glass structure generated through MD simulations and systematically samples the stoichiometry and local structure around each atomic species (for example lithium, oxygen, or silicon in lithium silicate glasses). Then, it compares the extracted clusters with a reference crystal phase ($Li_2Si_2O_5$ for example), which is expected to form in the glass.

A similar approach, known as the Adaptive Template Method, has been applied to identify crystal lattice types (FCC, BCC and HPC) in hard sphere systems (169). In our algorithm, a similar idea with the Adaptive Template Method was combined with our original Cluster code (168), which enables us to investigate more complicated crystals with multiple species in multicomponent glasses. Here, we introduce the detailed procedure of the extended algorithm.

The program performs the following steps:

1. Read a trajectory file of MD simulations (in this work, DL_POLY REVCON file) and a crystal structure with a unit cell (P1 symmetry) to be explored. Then, specify a reference atom of the crystal structure.

2. Count the number of each atomic species within a spherical region with radius r_k around the reference atom of the crystal structure. The numbers of species are stored in a reference vector R_A, which is noted as (N_{Li}, N_{Si}, N_O) for the LS_2 glass, for example. In the case of the LS_2P1 glass, the reference vector R_A has one more dimension as (N_{Li}, N_{Si}, N_O, N_P).

3. Subsequently, put a center of a spherical probe on an atom whose atomic type is the same with the reference atom in the MD trajectory. Then, count the number of each species in the spherical probe with a radius r_k, which defines a vector $\chi_{A,j}$ for atom j.

4. Evaluate the Hamming distance $\delta_j(r_K) = \left|R_A(i) - \chi_{A,j}(i)\right|$ to measure the similarity of the local structure in the MD trajectory to the reference crystal.

5. Repeat the steps from #2 to #4 with varying the proof radius r_k from a minimum (r_{min}) to a maximum (r_{max}) value every small increment (dr). Then, evaluate the cumulative distance for atom j at the radius r_k is computed, as $\Delta_j(r_k) = \sum_{r_{min}}^{r_k} \delta_j(r_k)$. The atom with smaller cumulative displacement is judged to possess more similar microstructure to that of the crystal explored.

At the end, the code outputs: i) PDB files with atomic structure of the best cluster found for each radius; ii) a statistic on the best clusters found at each radius and a distribution of the cumulative distances of all the target species in the glass.

It is worth to note that when the increment dr is small (i.e. 0.1 Å), the cumulative distance of atom j $\Delta_j(r_k)$ gives an idea of the degree of matching between the total distribution function of the reference atom in the crystal and the total distribution function of each atom in the glass. In this work, the analysis has been carried out using r_{min} = 2.0 Å, r_{max} = 6.0 Å, dr = 0.2 Å without considering oxygen atoms.

5.1.2. Computational details

The LS_2 and LS_2P1 glasses were generated using MD simulations by employing the modified PMMCS force-field described in chapter 3.1.2. The LS_2P1 composition was investigated to understand the effect of P_2O_5 on the structure and nucleation of $Li_2Si_2O_5$ and Li_2SiO_3 crystals in the glass since it is well known that addition of P_2O_5 promotes the precipitation of the LS_2 crystal and the formation of glass-ceramics (29,40).

Glass structural models containing 13500 and 12160 atoms were generated for LS_2 and LS_2P1 glasses, respectively, through the melt and quench approach by MD simulations (10) described below. Four replicas of each glass model have been examined to confirm the reproducibility of the results and to estimate the variability in the glass properties. The DL_POLY2.14 package (170) was used to integrate the equation of motions with a time step of 2 fs. The initial configurations were generated by randomly placing the atoms in a cubic box, whose size corresponds to the experimental density. Table 5.1 lists the number of the atomic species and the experimental density used to determine the unit cell size (5.4 nm for LS_2 and 5.2 nm for LS_2P1).

TABLE 5.1. Number of atomic species in the simulation boxes, cubic box side (L_{box}) and experimental density used to determine it.

	Li	**Si**	**P**	**O**	**L_{box} (Å)**	**Density (g/cm^3)**
LS_2 Glass	3000	3000	-	7500	54.26	2.34
LS_2P1 Glass	2640	2640	80	6800	52.41	2.35

The systems were heated and held at 3500 K for 100 ps, which is sufficient to melt the samples and remove the memory of the initial configurations. The liquids were then monotonically cooled to 300 K with a cooling rate of approximately 5 K/ps. The cooled glass structures were subjected to a final equilibration run of 200 ps. In these cases, the canonical ensemble (NVT) was employed, and Nosé-Hoover thermostat was used to control the temperature (frictional constants set to 0.2 ps). The coulomb interactions were calculated by the Ewald summation method with a cut-off distance of 12 Å. The short-range interactions

were evaluated using cut-off values of 5.5 Å. Snapshots of the final glass structures are reported in figure 5.1.

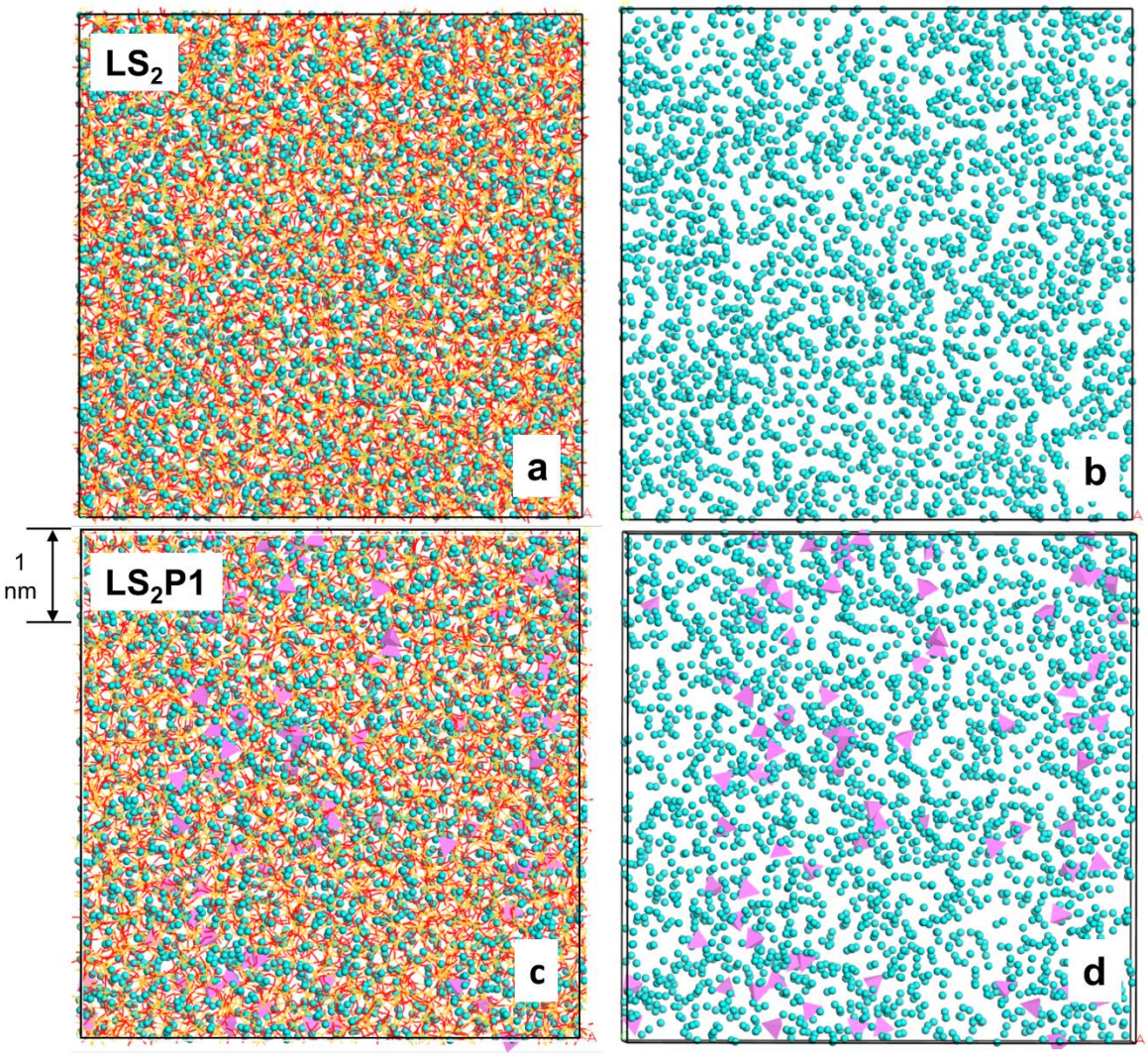

FIG. 5.1. Snapshot of the MD-derived bulk structural model of the LS_2 glass showing all the ions in the box (a) and Li ions only (b). Snapshot of the LS_2P1 glass showing all the ions in the box (c) and Li ions (cyan spheres) and PO_4 tetrahedra (pink) only (d).

In addition to the bulk glass models with periodic conditions, slab models with two surfaces were created by eliminating periodic boundary conditions in the z-axis. The slab models were replicated in x-axis one time to have larger surface areas and thus more statistics, then the systems were heated from 300 K to 1800 K with a heating rate of 5 K/ps and cooled down at 300 K with the same cooling rate to relax the surface structure. In figure 5.2 the top and lateral views of the slabs created are reported, and two rough surfaces are generated along the z-axis.

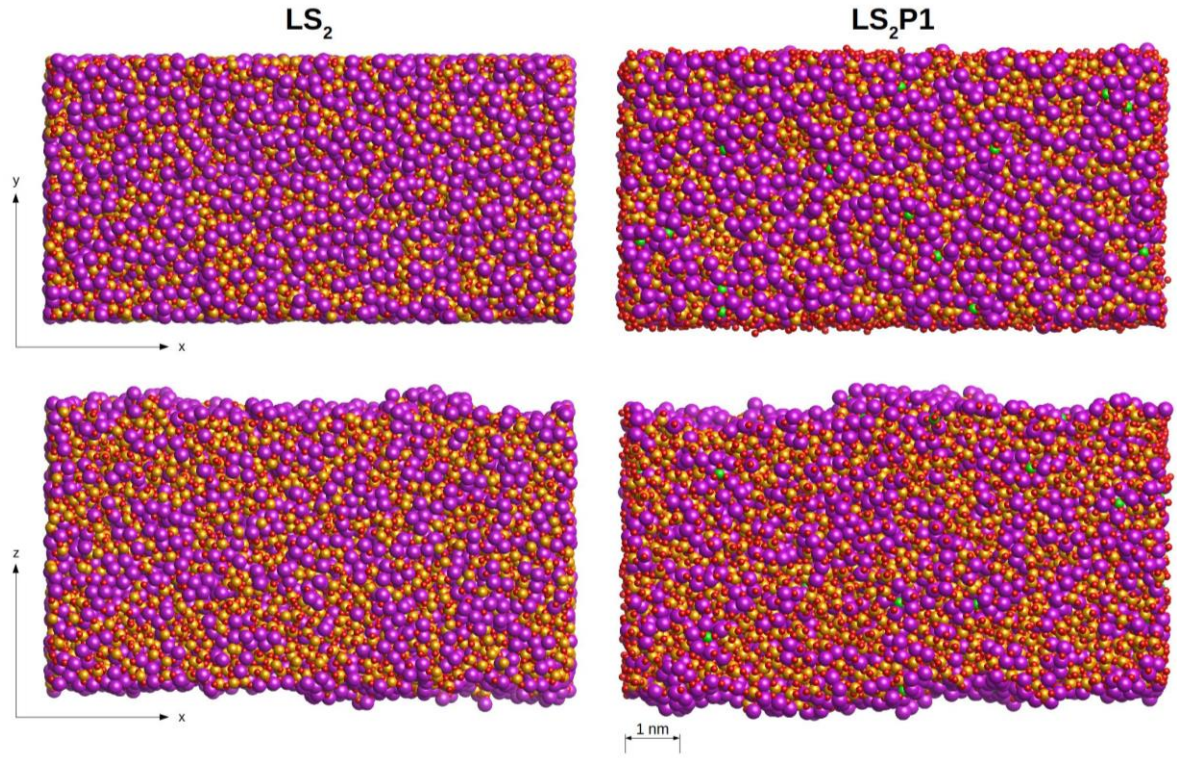

FIG. 5.2. Top and lateral view of the surface of the LS_2 and LS_2P1 glasses. Li, Si and O ions are, respectively, represented by violet, yellow and red spheres. Orthophosphate units are represented as green tetrahedral.

5.1.3. Bulk and surface structures

Homogeneous nucleation is usually associated with the similarity of short and intermediate-range structures between the glass forming liquid and the crystal that crystallizes from it (8,73,171,172). Since the short-range structures measured by the cation-oxygen distances, coordination numbers and the O-Si-O, O-Li-O bond angle distributions are not distinguishable between LS_2 and LS crystals as well as between the crystals and the frozen melts, we only give our attention to the structural differences in intermediate-range order. The intermediate-range structures are described by Li-Li distributions and the Q^n distributions, representing the degree of polymerization of the network.

Figure 3.4 shows the bulk structures of the LS_2 and LS_2P1 glasses at 300 K. A visual inspection of the atomistic configurations reveals that phosphorous atoms form orthophosphate units and tend to segregate each other. The units attract Li ions, forming Li-richer regions around PO_4 units. Indeed, the Q^n distribution of the P species (not reported) reveals that 98.8% of PO_4 units are Q^0 species, in excellent agreement with NMR experiments on similar glasses (52).

TABLE 5.2. Q^n distribution and network connectivity (NC) of the silica network for the LS_2 and LS_2P1 glasses.

	Q^1	Q^2	Q^3	Q^4	NC

LS_2 Glass	2.2	21.0	51.3	25.4	3.0
LS_2P1 Glass	1.4	18.7	49.4	30.5	3.1

Table 5.2 compares the Q^n distribution of silicon and the network connectivity (NC) representing the average number of BO per silicon for the two glasses. More Q^4 silicon and larger NC of the LS_2P1 glass reveal that the silica network is slightly more polymerized than the LS_2 glass. This is a consequence of the existence of the orthophosphate units, which attract Li ions to balance their negative charge, depleting Li ions around the silica network and thus Q^4 silicon increases. In both glasses, silicon is predominantly present as Q^3 species as in the case of LS_2 crystal, which is formed by two tetrahedral layers of silicon (100% Q^3 species) (figure 1.3). The amount of the Q^2 silicon species, which are the majority in the LS crystal, are around 20% in both glasses. The Li-rich regions can be seen in figure 5.3 as a formation of percolation channels of Li ions; these are highlighted by the worm-like Li distribution sandwiched between chains and sheets of silica. An extended ordering over four alkali coordination shells is also revealed by the Li-Li pair distribution function (PDF) drawn in figure 5.3. In this figure, the Li-Li PDFs of LS and LS_2 crystals and LS_2 and LS_2P1 glasses at 300 K are also compared. The Li-Li PDF of LS_2 crystal is composed of pairs of peaks thanks to the symmetry of the crystalline structure, figure 1.3. The Li-Li coordination peak at 2.7 Å is observed for all investigated systems, however the remaining peaks do not match between the different structures.

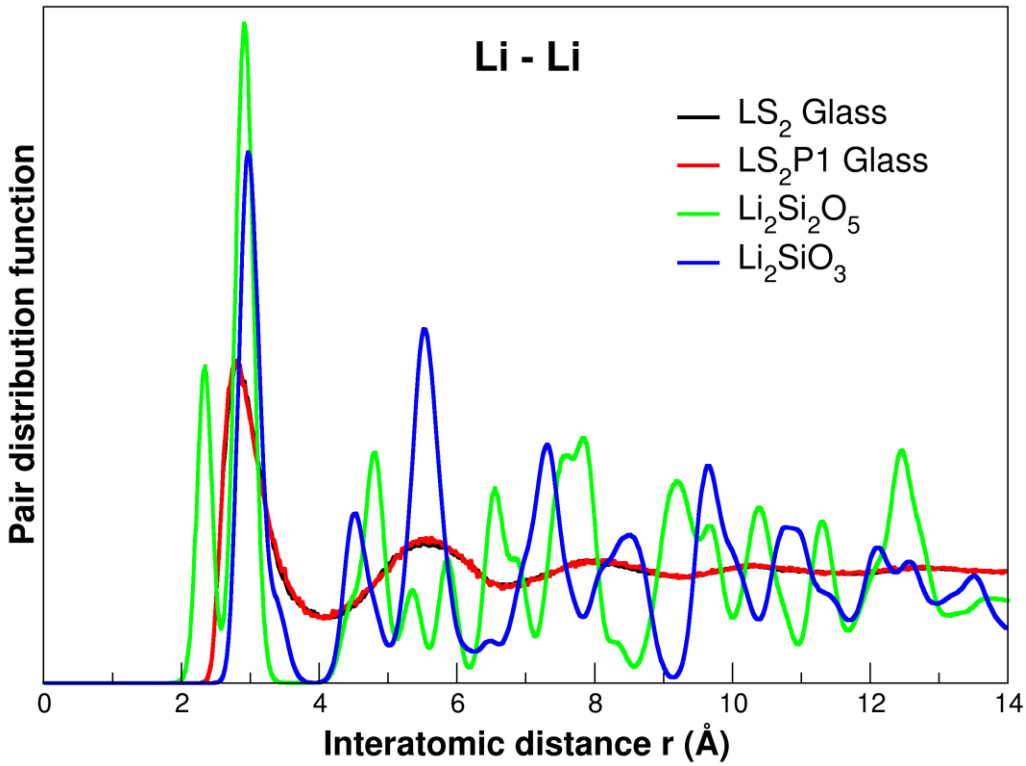

FIG. 5.3. Li-Li Pair Distribution Function of the LS_2 and LS_2P1 glasses compared to LS_2 and LS crystals.

The other useful parameter, for probing structural resemblance or dissimilarity between crystalline and glassy phases, is the Li-Li homonuclear M_2 second moment (171). The M_2 second moment is related to the

Li-Li distance correlation and can be an ability index of a glass to be transferred to a crystal with the same stoichiometry. It is computed using the van Vleck equation (173):

$$M_{2,Li-Li} = 0.9562 \frac{1}{N_{Li}} \left(\frac{\mu_0}{4\pi}\right)^2 \gamma_{Li}^4 \hbar^2 \sum_{i=1}^{N_{Li}-1} \sum_{j=i+1}^{N_{Li}} r_{ij}^{-6} \quad (5.1)$$

where N_{Li} is the number of the Li atoms in the simulation box, μ_0 is the vacuum permittivity, γ_{Li} is the gyromagnetic ratio and r_{ij} is the distance between atoms i and j. The calculated $M_{2,Li-Li}$ for the LS_2 and LS_2P1 glasses are of 49.7 and $49.6 \cdot 10^6$ rad^2s^{-2} and closer to that of the LS_2 crystal ($M_{2,Li-Li}$=$57.8 \cdot 10^6$ rad^2s^{-2}) than the LS crystal ($M_{2,Li-Li}$=$75.7 \cdot 10^6$ rad^2s^{-2}).

Another criterion to judge the structural similarity between glass and crystal is the comparison of densities. If glass and crystal structures are similar, densities must be similar as well. Experimental data, concerning the correlation between the density and the nucleation mechanism (174), demonstrate that when the density difference between the two phases $\left(\Delta\rho/\rho_{glass}\ \%\right)$ is higher than 10% the homogeneous nucleation does not occur in observable time. In these cases, heterogeneous nucleation is usually favored. However, the condition of the small difference of density is a necessary but not sufficient condition to guarantee the structural similarity and the nucleation mechanism. In fact, two structures can be extremely different but have similar densities (174). In table 5.3 experimental and calculated values of the densities of LS_2 and LS crystal and LS_2 glass are reported.

TABLE 5.3. Experimental and calculated values of density for LS_2 glass and crystal and LS crystal, with relative density difference $\left(\Delta\rho/\rho_{glass}\ \%\right)$.

	Experimental ρ (g/cm^3)	**Calculated ρ (g/cm^3)**	**Relative error %**		**$\Delta\rho/\rho_{glass}$ %**	
LS_2 Glass	2.35	2.38	1.28			
LS_2 Crystal	2.45	2.40	-2.04		**Exp**	4.26
					Calc	0.84
LS Crystal	2.52	2.45	-3.16		**Exp**	7.23
					Calc	2.94

The LS crystal presents a larger difference in density with the LS_2 glass than the stoichiometric crystal both from experimental data and calculated results. The calculated values are lower than the experimental, but the trend is kept. Both have a relative difference lower than 10% meaning that the homogeneous nucleation is possible for both crystalline structures.

Combining the two analysis, it seems unlikely, but not impossible, that the LS crystal can nucleate homogeneously from the bulk of the melt, as suggested in some of the previous experimental (43) and computational works (65), while LS_2 has a higher probability to nucleate homogeneously.

5.1.4. Nucleus of crystals in bulk and on surface

Another hypothesis to explain and predict the crystallization of a specific phase from a glass forming liquid involves the clustering of specific atoms forming embryos of the crystal with subcritical dimensions. These embryos, formed during the fast quenching of the melt, can trigger the nucleation during heat treatment and be considered as structural markers for the prediction of the crystallization of a particular phase. MD simulation is an exceptional method to detect such extremely small embryos, which is indeed difficult to be found experimentally. To test this hypothesis, we performed a cluster analysis on the bulk structure of the two simulated glasses using the modified Cluster code described in chapter 5.1.1.

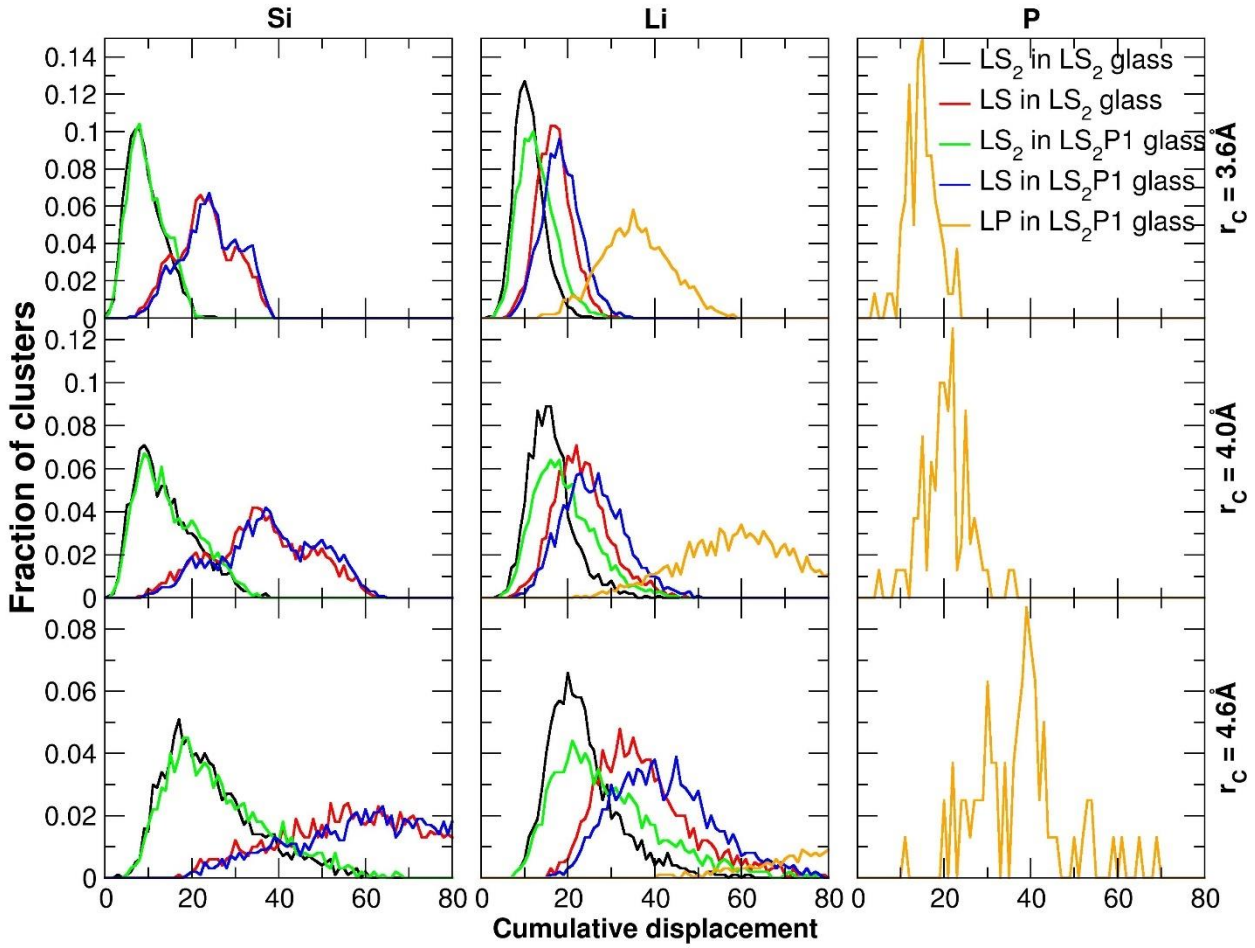

FIG. 5.4. Distribution of cumulative distances (with respect to Li_2SiO_3, $Li_2Si_2O_5$ and Li_3PO_4 crystals) of clusters of radii 3.6, 4.0 and 4.6 Å centered on Silicon (left), Lithium (middle) and Phosphorous (right) for the LS_2 and LS_2P1 glasses.

Figure 5.4 reports the distribution of the cumulative displacements of atomic clusters similar to the Li_2SiO_3, $Li_2Si_2O_5$ and Li_3PO_4 crystals in the LS_2 and the LS_2P1 glass within a sphere of radius of 3.6, 4.0 and 4.6 Å centered on Li, Si and P, respectively. The figure shows that silicon and lithium environments in the glass

structure are similar to the LS_2 crystal rather than the LS one at any radii. However, the discrepancy is more evident for silicon since the two distributions are more separated than the ones for the clusters centered on lithium. It is interesting to note that the distribution of the clusters centered on Li shifts to higher cumulative distances by P_2O_5 addition, revealing that the formation of embryos similar to the metasilicate phase is disfavored in the LS_2P1 glass. Figure 3.8 shows the most LS_2 crystal–like embryo obtained by means of a sphere of 4.6 Å radius centered on Li in the LS_2P1 glass. The embryo contains 7 Li and 6 Si atoms as in the reference cluster of the crystal and shows a layered structure like the one of the LS_2 crystal. Moreover, an embryo whose stoichiometry and structure resembles the LP crystals (see figure 5.5), is also found in the LS_2P1 glass when the radius of sphere is 4.0 Å, agrees with the experimental fact that the lithium orthophosphate crystal phase appears as a secondary phase (52).

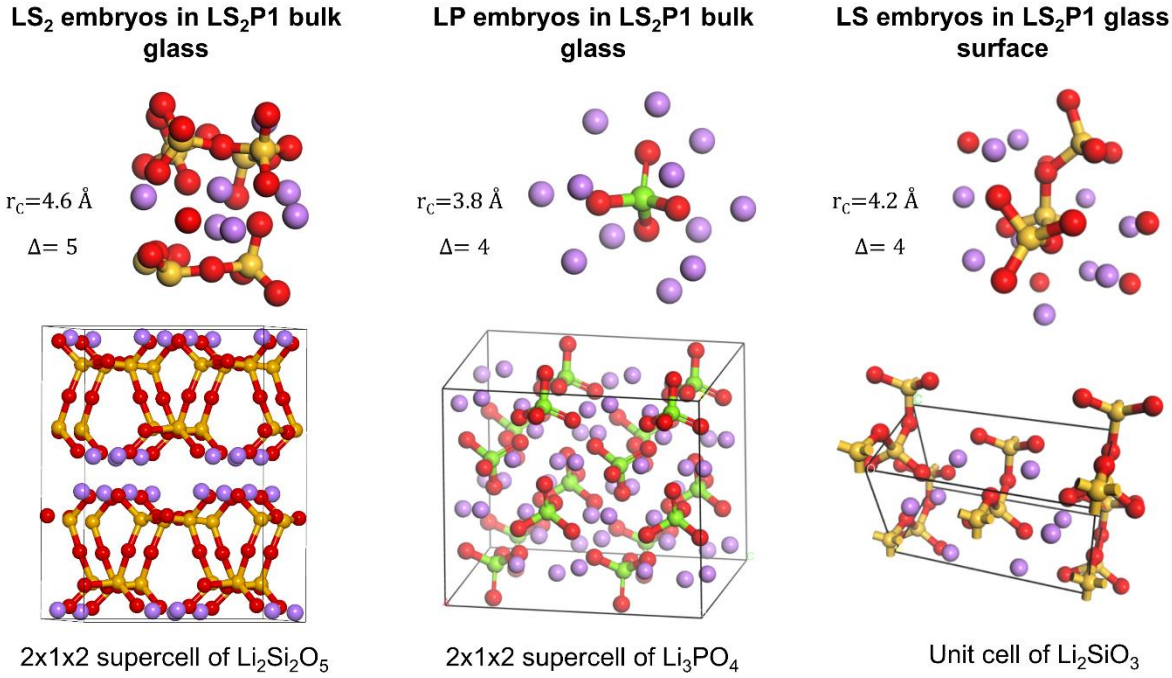

FIG. 5.5. Embryos of $Li_2Si_2O_5$ (LS_2), Li_2SiO_3 (LS) and Li_3PO_4 (LP) found in LS_2P1 glass and structures of the three crystals.

Interestingly, the situation drastically changes at the glass surfaces. Figure 5.2 shows the top and lateral views of the slab models for the LS_2 and LS_2P1 glasses. The figure demonstrates that the surface is much richer in Li ions than the bulk. During the formation of the glass surface the structure undergoes a drastic rearrangement with Li ions (violet spheres) aggregating in layers and forming percolation channels that flow to a surface to the other side. The abundance of Li ions at the glass surface is also confirmed by analysing the fraction of each element along the z-direction as shown in figure 5.6. Indeed, the first atomic layer at the surface is exclusively composed of lithium ions, the second by oxygen ions and the third by silicon ions. The concentration profiles also show that the P ions, albeit present in small quantities, tend to gather at the subsurface rather than in the bulk.

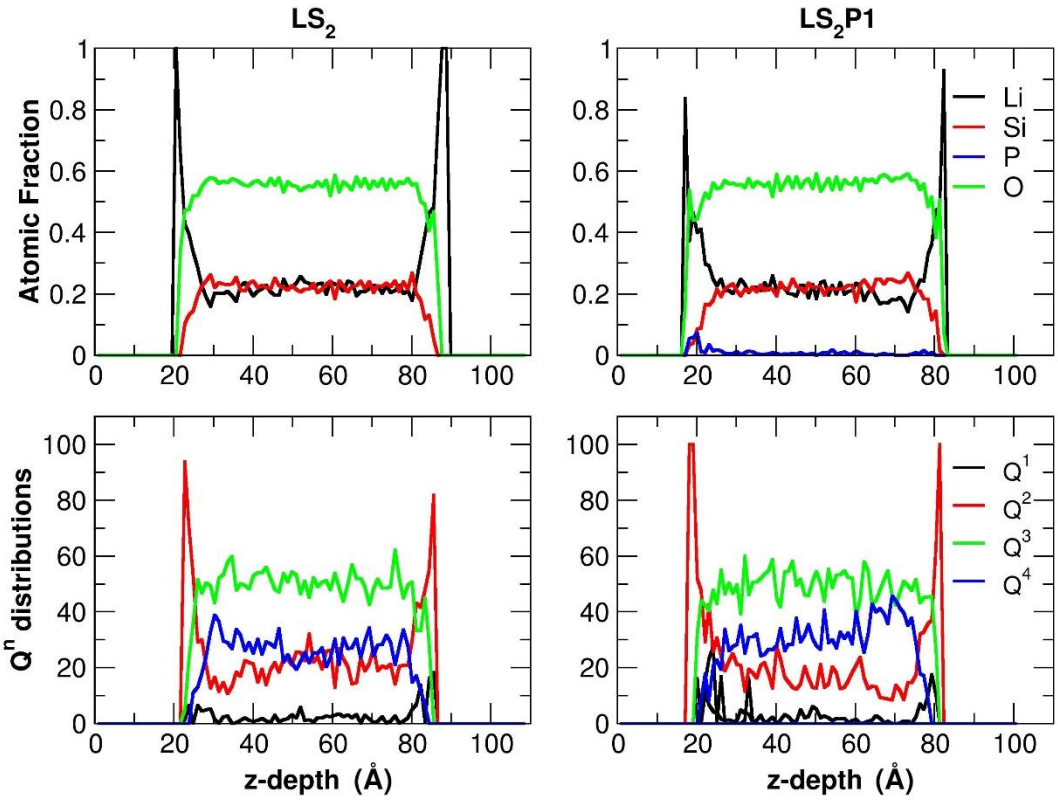

FIG. 5.6. Z-depth profiles of the atomic fraction of Li, Si, P and O ions and Q^n distributions of Si ions in the LS_2 and LS_2P1 glass surface models.

In addition, the Q^n distributions of silicon change considerably during the surface formation since the migration of Li ions to the surface leads to breaking of Si-O-Si bonds and reducing the connectivity of silicon. In fact, figure 5.6 reveals that silicon ions at the glass surface are almost exclusively Q^2 species (~80 – 90% in the LS_2 and 100% in the LS_2P1 glass) as in the case of the LS crystal. This finding is extremely interesting and demonstrates that the surface provides favorable stoichiometric conditions for the nucleation and crystallization of the LS crystal rather than LS_2 one. Indeed, figure 5.5 shows an atomic cluster possessing analogous structure and stoichiometry analogous to the LS crystal found on the LS_2 glass surface. The cluster is constituted by a chain of three SiO_4 units surrounded by 10 Li ions, similarly to the chain present in the LS crystal. On the contrary, LS-like embryos with the same cumulative displacements were not found in the bulk of the glass model. It seems thus unlikely that the LS crystal phase nucleates homogeneously from the bulk of the glass in these glasses.

5.2. Seeding method

In addition to the morphological analysis, we have also evaluated the thermodynamics on the nucleation of both LS_2 and LS crystals inside the LS_2 glass.

According to CNT, as shown in chapter 2.1.1, the growing of a spherical crystalline embryo into a glass matrix produces an increase in the W of the transformation. The maximum of the curve (W^*) is reached when the critical crystalline embryo is formed (with N_c number of atoms or radius r_c). If the nucleus

overcomes this size, the free energy of the transformation decreases monotonically. Once the critical radius is determined as well as free energy difference between the fluid and the crystal (ΔG_v) and the attachment rate of particles at the critical cluster, the nucleation rate (I_{st}) can be calculated, see formula 2.2. In theory it is possible to evaluate all thermodynamics and kinetic parameters that describe the transformation with the CNT formula.

Espinosa et al. (175) described a procedure to evaluate the required parameters, the "seeding method". It consists in inserting an embryo of a given shape (named "seed") in the supercooled fluid. The seed has a spherical shape with a crystalline structure and has a different stability according to the working temperature. Starting from such configuration, the number of particles is monitored at different temperatures. If the temperature is higher than the one at which the seed is stable, the seed will melt, while if the temperature is lower, the seed will grow, and particles will attach to the crystalline seed. This method has been applied to different systems (175–180), to identify at each T_c the critical embryo N_c, followed by the computation of the attachment rate of particles.

The big limitation that is encountered in the present study is that it is not possible to observe the growth of the crystalline embryo because of the high viscosity of the glassy matrix. In chapter 4.2.2, in 20 ns of simulation of the biphasic system, we could never observe the growth of the crystalline side, even though the dimensions were bigger than the critical cluster (crystalline side replicated in two dimensions) and the temperature was lower than the melting point. This analysis proves the non-applicability of the seeding method to our system.

Therefore, we developed a modification of the seeding method to evaluate the critical radius and the free energy barrier of the nucleation, the Free-Energy Seeding Method (FESM).

5.3. Free-Energy Seeding Method

The idea of this method is not to simulate dissolution and nucleation, explicitly, even though our approach also embeds a spherical nucleus of the LS or LS_2 crystal with different radii into a fully explicit lithium disilicate (LS_2) glass melt. Instead, we evaluated the energy profile as a function of the cluster radius. From this energy profile, it is possible to extract the nucleation activation energy, the critical size of the cluster, and the interfacial free energy, which can avoid the possible timescale problem to observe dissolution and growth in our highly viscous systems.

5.3.1. Generation of the starting configurations

The embedded systems have been built as follows. First, we built a crystal model. For the modeling of LS_2 nucleus in the LS_2 glass, we replicated the unit cell of the LS_2 crystal 10x4x10 times to generate a box containing 14400 atoms, and the side lengths of the simulation box varied accordingly to the experimental density of the LS_2 glass. On the other hand, to model the LS nucleus in the LS_2 glass matrix, after replicating

the lithium metasilicate unit cell by 5x10x8 times to create a supercell with 9600 atoms, subsequently, the simulation box was enlarged to have the same density of the LS_2 glass. Then, 1600 SiO_2 formula units were randomly added in the vacuum space in the simulation box to maintain the overall compositions and density, same as those of LS_2 glass. It is worth mentioning that system size effect is presumable in these calculations, and thus, we restricted the volume of the embedded crystal nucleus to less than 10 % of the total simulation box to avoid the artifact.

Finally, in both cases, an atom was randomly chosen and the positions of the atoms locating within a distance r_{sphere} from the central atom were fixed as an embedded crystal cluster (seed). Then, the cluster embedded systems were melted and quenched using the same procedure employed to generate the bulk structural models (described in chapter 5.1.2) with fixing the position of the seed, generating a model with a crystal embedded in a glassy matrix. The structure is then fully relaxed at room temperature for 500 ps in the NVT ensemble. In figures 5.7 and 5.8 the starting configurations and the glassy matrix containing the crystalline seed (8 Å as an example) are shown in a frontal and lateral views for the LS_2 and LS crystals, respectively.

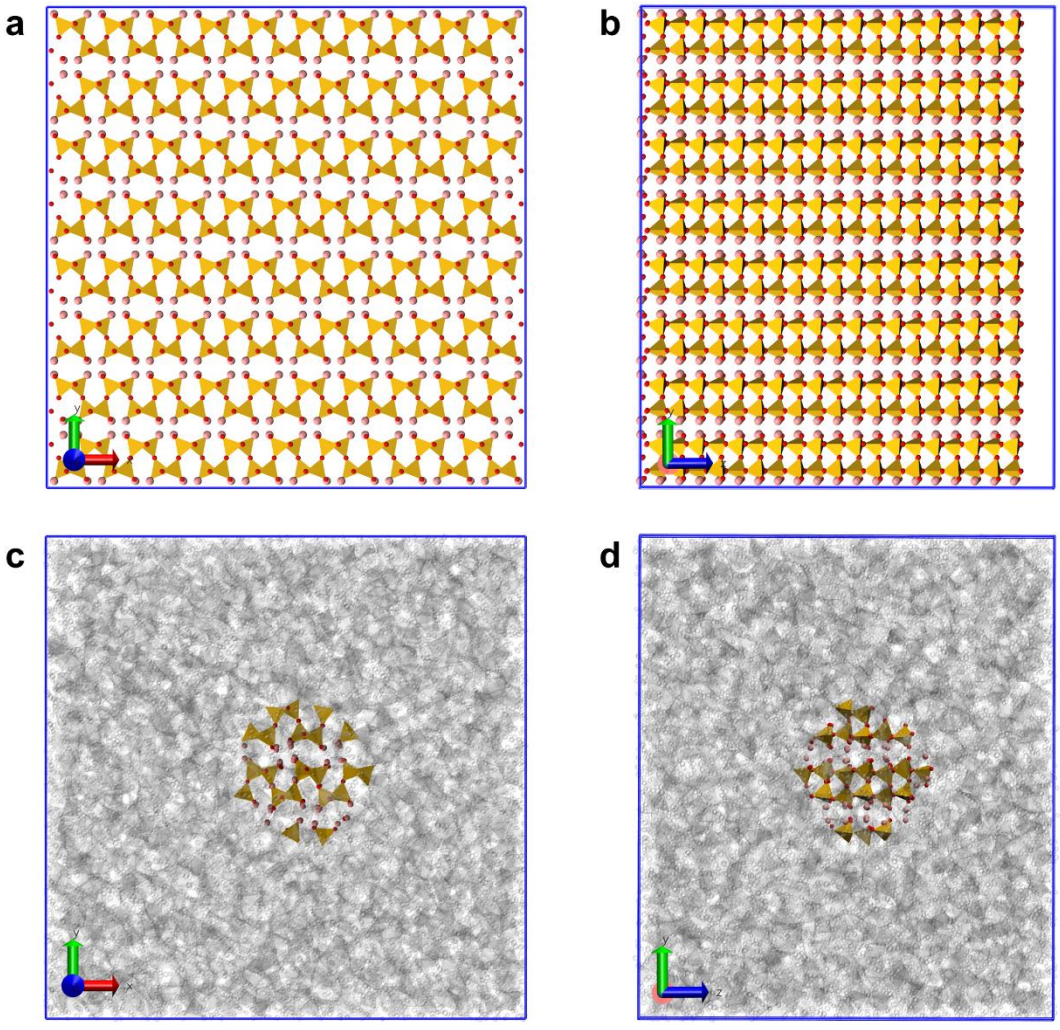

FIG. 5.7. (a, b) Two views of the starting box ($Li_2Si_2O_5$ crystal) and (c, d) the final box at 300 K with a LS_2 crystal nucleus with a radius of 8 Å, embedded into the LS_2 glass matrix. Orange tetrahedral represent silicon whereas red and pink spheres represent oxygen and lithium ions, respectively.

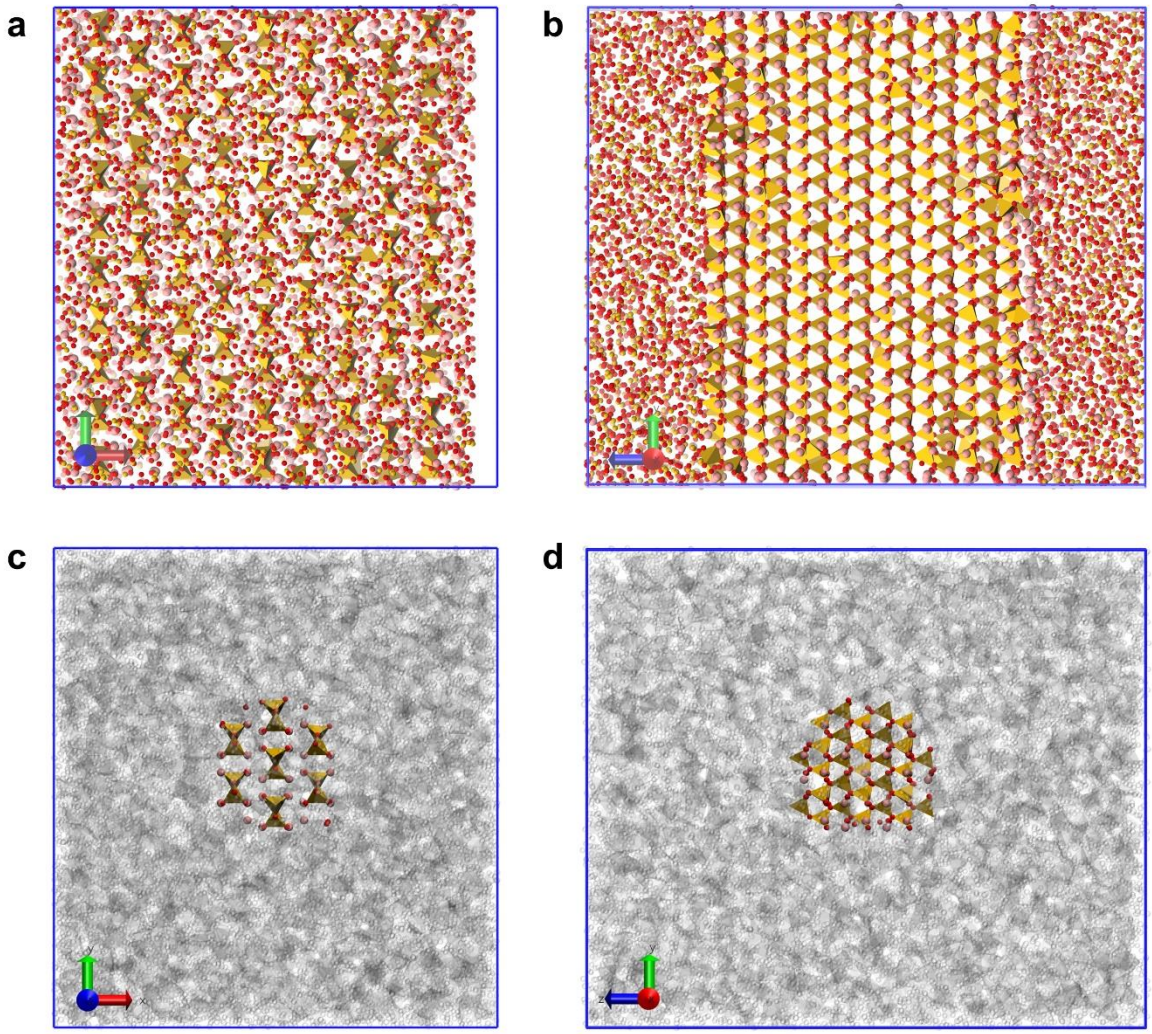

FIG. 5.8. (a, b) Two views of the starting box (Li_2SiO_3 crystal with SiO_2 random placed in the vacuum space) and (c, d) the final box at 300 K with a LS crystal nucleus with a radius of 8 Å, embedded into the remaining glass matrix. Orange tetrahedral represent silicon whereas red and pink spheres represent oxygen and lithium ions, respectively.

Finally, the model was equilibrated for 2.4 ns at 800 K and 1000 K to investigate the temperature effect. During this equilibration, the positions of the atoms of the embedded crystals were also relaxed without constraints. Nuclei with r_{sphere} from 6 to 14 Å were created and 7 replicas for each system were examined to have sufficient statistics.

5.3.2. Free energy calculation

To evaluate the energy differences between crystal, glass, and the cluster-embedded models, MD simulations on the LS_2 glass and LS_2 and LS crystals were also performed (four replicas each). For all the aforementioned systems, the internal energy (E_S) of the system was accumulated and the Helmholtz free energy (A_S) of the state S (S refer to the crystal, glass and embedded system states) computed using the thermodynamic formulas (181)

$$A_S = -k_B T \, log \langle e^{-\frac{E_S}{k_B T}} \rangle \tag{5.1}$$

The free energy of nucleation (W) with cluster radius r is then computed as

$$W(r) = A_{CryGlass}(r) - A_{Glass} \tag{5.2}$$

Where $A_{CryGlass}$ and A_{Glass} are Helmholtz free energy of the crystal embedded system and the glass, respectively. In our calculations, we used the Helmholtz free energy of the glass as a reference. In CNT, the free energy of nucleation of a spherical nucleus with negligible strain energy is assumed to be composed of surface free energy and volume free energy as described in chapter 2.1.1. We try to reproduce the trend describe by CNT plotting the W with different crystalline radii, which allows us to individuate the r_c.

The interfacial free energy, γ_{sl}, which governs largely the crystal nucleation rate, is assumed to be equal to that of a planar interface and thus to be independent on the nucleus size. This is known as the capillarity approximation and is one of the most serious shortcomings of CNT, paragraph 2.1.2 for details. A benefit of our approach is that the interfacial free energy is not an input parameter independent of the nucleus size and temperature but is a property that varies inherently with the nucleus dimension and the temperature. The interfacial free energy can be computed from the MD simulations using equation 5.3 obtained from equation 2.2:

$$\gamma_{sl}(r) = \frac{W(r) + \frac{4}{3}\pi r^3 \Delta A_v}{4\pi r^2} \tag{5.3}$$

It is thus necessary to calculate the ΔA_V at a defined temperature, which is the free energy difference between the melt and the crystal per unit volume of the crystal (V_m).

$$\Delta A_V = \frac{A_{Glass/melt} - A_{Cry}}{V_m} \tag{5.4}$$

We used T = 800 K in this work to make our results comparable to that reported by McKenzie et al. (65) (that used a hybrid MD/MC/implicit approach to compute the free energy of nucleation of the LS and LS_2 crystals inside the LS_2 glass) and to the experimental data (72).

It should be noted that since the temperature, 800 and 1000 K, are below the computational melting point, the effect of the temperature on the free energy profiles is investigated assuming that the topology of the crystal/glass interface is similar. In other words, we do not investigate the dynamic evolution of the crystal growth with temperature but generate equilibrated model systems containing a crystal nucleus in an amorphous LS_2 matrix, as previous Monte Carlo simulations (65).

5.3.3. Free energy of crystal nucleation

We apply the FESM method described above to obtain further insights on the possible mechanisms of nucleation from the LS_2 glass forming liquid, computing the Helmholtz free energies of the LS and LS_2 crystals formation. In this free energy calculation, we modeled a spherical crystal nucleus embedded into a

glass model as seen in figure 5.7 and 5.8 and examined the size dependency of the nucleation free energy for both LS_2 and LS crystals at 800 K. The Helmholtz free energy profiles are reported in figure 5.9. The error bar in this figure represents standard deviation of free energies evaluated by seven independent replicas. As expected from CNT, the free energy first increases and then decreases after reaching the maximum energy (barrier for nucleation) at the critical radius, figure 5.10. It is worth highlighting that LS_2 clusters with radius less than 5 Å were not considered to build the free energy profile in figure 5.9 (a). The free energy of such embryos formed during the glass formation is expected to be almost zero, because, as shown in chapter 5.1.4, crystalline clusters up to radii of 4.6 Å have a certain probability to form in the pure glass. Moreover, LS clusters of such small sizes lose the crystalline structure during relaxation at room temperature, which indicates their instability. According to the figure, at 800 K the critical radii for both LS and LS_2 crystals are around 7 Å in excellent agreement with previous experimental estimations (182).

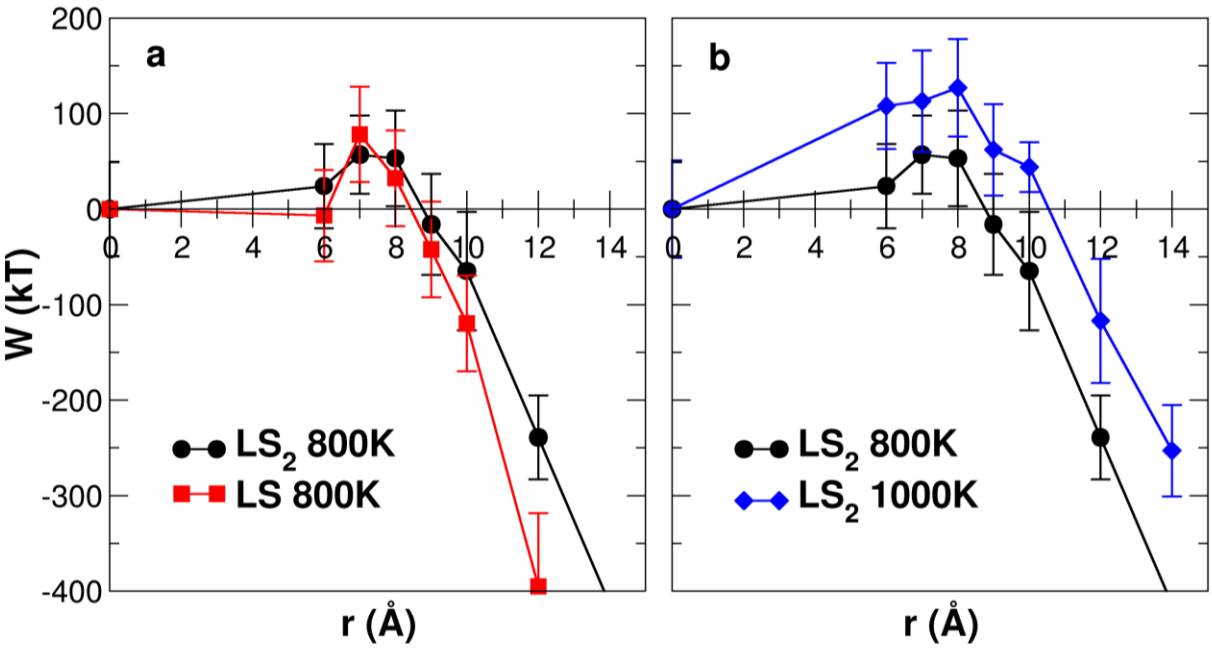

FIG. 5.9. Free energy of nucleation for (a) the LS and LS_2 crystals in the LS_2 glass at 800 K and (b) the LS_2 crystals in the LS_2 glass at 800 K and 1000 K with relative standard deviation.

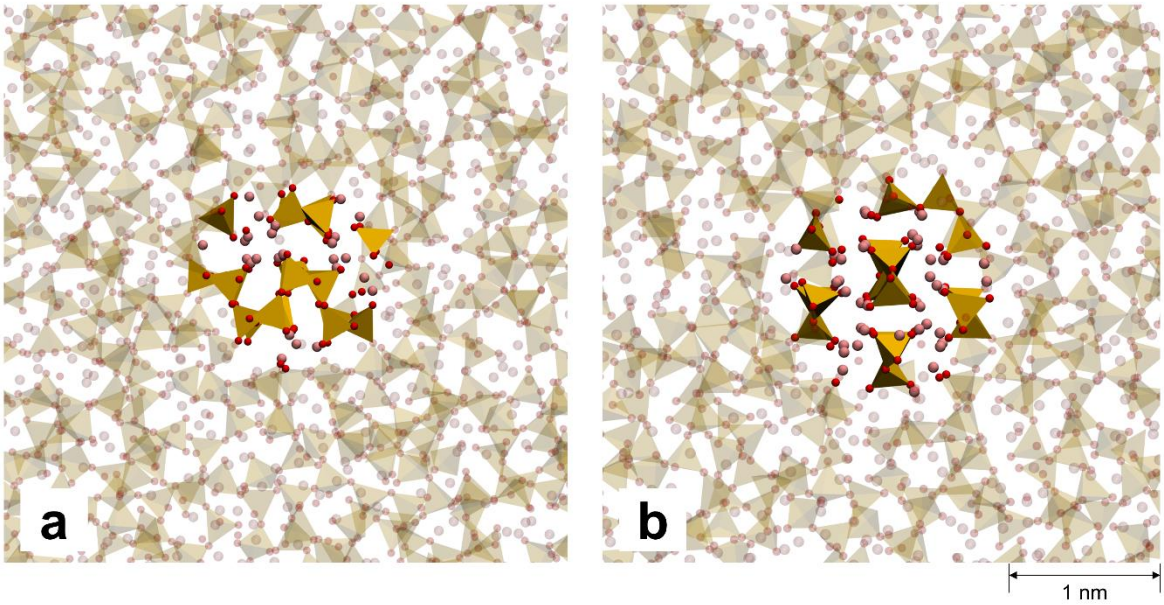

FIG. 5.10. Structure of boxes with critical size nuclei. On the left glass with LS_2 composition with the critical nucleus of $Li_2Si_2O_5$ crystal. On the right, glass with LS_2 composition with the critical nucleus of Li_2SiO_3 crystal.

The computed Helmholtz free energy barrier for nucleation (W) of the LS_2 crystal at 800 K is about 59 kT, which agrees fairly well with the experimentally estimated ones, which are ranging from 35 and 50 kT at the temperature from 700 to 800 K (72). The large variability associated with the free energy is due to the variability of the energy of frozen liquid structures generated through the standard MD quenching protocols. In fact, the fast quenching of the melts prevents the good sampling of the free energy surface and thus glass structures with different energies are easily generated (183). Nevertheless, considering the unfavorable conditions in stoichiometry and structural similarities for the LS crystal in the bulk glass as discussed above, it is expected that the LS crystal can crystallize preferentially on the glass surface through the heterogeneous nucleation mechanism. Indeed, the energy barrier of heterogeneous nucleation (W^*_{het}) is lower than that of the homogeneous one (W^*_{hom}) according to a geometric factor $\phi(\theta)$, which depends on the wetting angle between the solid and liquid at the interface (71) as shown in chapter 2.1.3. Further developments are required to extend the FESM method to investigate heterogeneous nucleation.

McKenzie et al. (65) used a hybrid MD/MC approach to compute the free energy of nucleation of the LS and LS_2 crystals inside the LS_2 glass considered as an implicit medium. In their method, the nucleation free energy (NFE, W) was evaluated by considering three contributions: the cluster formation, the cluster to crystal transition and the cluster solvation energy. The thermodynamic barrier was estimated to be 40 kT and 34.5 kT for the LS_2 and LS crystals, respectively.

They showed that the NFE is higher for the LS_2 than for the LS at smaller cluster dimension, but its value crossovers at around 4–5 formula units, and thus it was stated that the LS crystal first nucleates, and then it transforms to the LS_2 with a thermodynamic barrier of 28.3 kT. A smaller free energy of nucleation at small cluster radius for the LS phase is also observed in our simulations, but since none of the two methods

investigates the reactive pathway and the kinetics associated to an eventual crystalline phase transition from the LS to LS_2, explicitly, it is difficult to make speculation on the phase transformation. Both our results and those by McKenzie et al. (65) are in good agreement with the facts experimentally measured by Differential Thermal Analysis (DTA) and SEM observations by Soares et al. (184). In fact, the DTA data values have shown that two exothermic peaks appear at 615–680 °C and 750–800 °C, and these peaks are associated with the crystallization of the LS and LS_2 phases, respectively, by XRD measurement. Morphological observations by SEM have also confirmed the occurrence of these two crystallization mechanisms since needle-like and granular crystals were detected in the microstructure of samples including LS and LS_2, respectively. The authors have also found that, in the early stage of crystallization in the LS_2 glass, both the LS and LS_2 crystals nucleate simultaneously and independently (43), as explained in paragraph 1.4. Further, the analysis of the crystallization kinetics through the Johnson–Mehl–Avrami equation suggested that the surface crystallization (Avrami exponent $n = 1$) associated to the first peak rather than volume crystallization (Avrami exponent $n = 3$) associated to the second peak is dominant in the crystallization process. This is because the activation energy (225–275 kJ/mol) of the former is substantially lower than that of the latter (425–500 kJ/mol). Therefore, the LS crystal nucleates at the glass surface because favorable stoichiometric and thermodynamic conditions for its precipitation are present, whereas the LS_2 crystal appears in the bulk of the glass.

The effect of the temperature on the nucleation free energy profile was investigated only for the nucleation of the LS_2 crystal, as shown in figure 5.9 (b). Although error bars are relatively large, both the critical size and the activation energy barrier increases with temperature as expected.

In conclusion of this section, it is worth summarizing advantages of the FESM method, despite the not negligible error associated with the calculation of the free energy of the glass state. Firstly, it should be emphasized that our method inherently includes the surface energy penalty during the creation of the melt/crystal interface and the strain energy at the interface. To the best of our knowledge, the surface energy contribution was implicitly subsumed in the solvation term (parameterized for a particular system) of the hybrid MC method used by McKenzie et al. (65,66) The MC simulation highlighted that the strain energy term does not play an important role in nucleation above the glass transition temperature, thereby the contribution is usually neglected (82).

The interfacial free energy, γ_{sl}, associated to the formation of the melt/crystal interface for the LS_2 nucleus with critical size using equation 5.3 calculated at 800 K and 1000 K is respectively 0.3 ± 0.1 and 0.4 ± 0.1 J/m^2. These values are comparable to the value estimated by Fokin et al. (185) when accounting both the temperature and size dependence of the crystal/liquid surface energy.

Moreover, as shown above, our approach can be used to compute the thermodynamic barrier for homogeneous crystal nucleation at different temperatures. This would be useful because the thermodynamic barrier has been shown to exhibit an unusual increase with a decrease in temperature below

the maximum nucleation rate for a variety of oxide glass-forming liquids (82). Although the internal elastic stresses arising from the density misfits between the crystal and liquid phases might play a role, the phenomenon is still not completely understood and should be the object of future investigations (82).

The approach is applicable to any system of interest since the parameters needed are only the interatomic force field for MD simulations. An advantage with respect to the original seeding method (175) is that it allows extracting thermodynamic parameters of the nucleation process in high viscous liquids. Finally, all-atomistic MD simulations can provide information on the structure of the melt/crystal interface, which are hardly accessible from experiments. For instance, figure 5.11 (a) shows the computed local order Q_6^{loc} Steinhardt parameter (see chapter 3.2.6.2) of silicon atoms from the center of the LS and LS_2 crystal nuclei (of radius 10 Å shown in figure 5.11 (b)) to the glass matrix at 800 K. The ability of the Steinhardt parameters to distinguish between the crystalline and glass phases was assessed. The most satisfying parameter obtained was indeed Q_6^{loc}, calculated on Si ions, using R_1 = 5.3 Å and R_2 = 3.7 Å, with a home-made script.

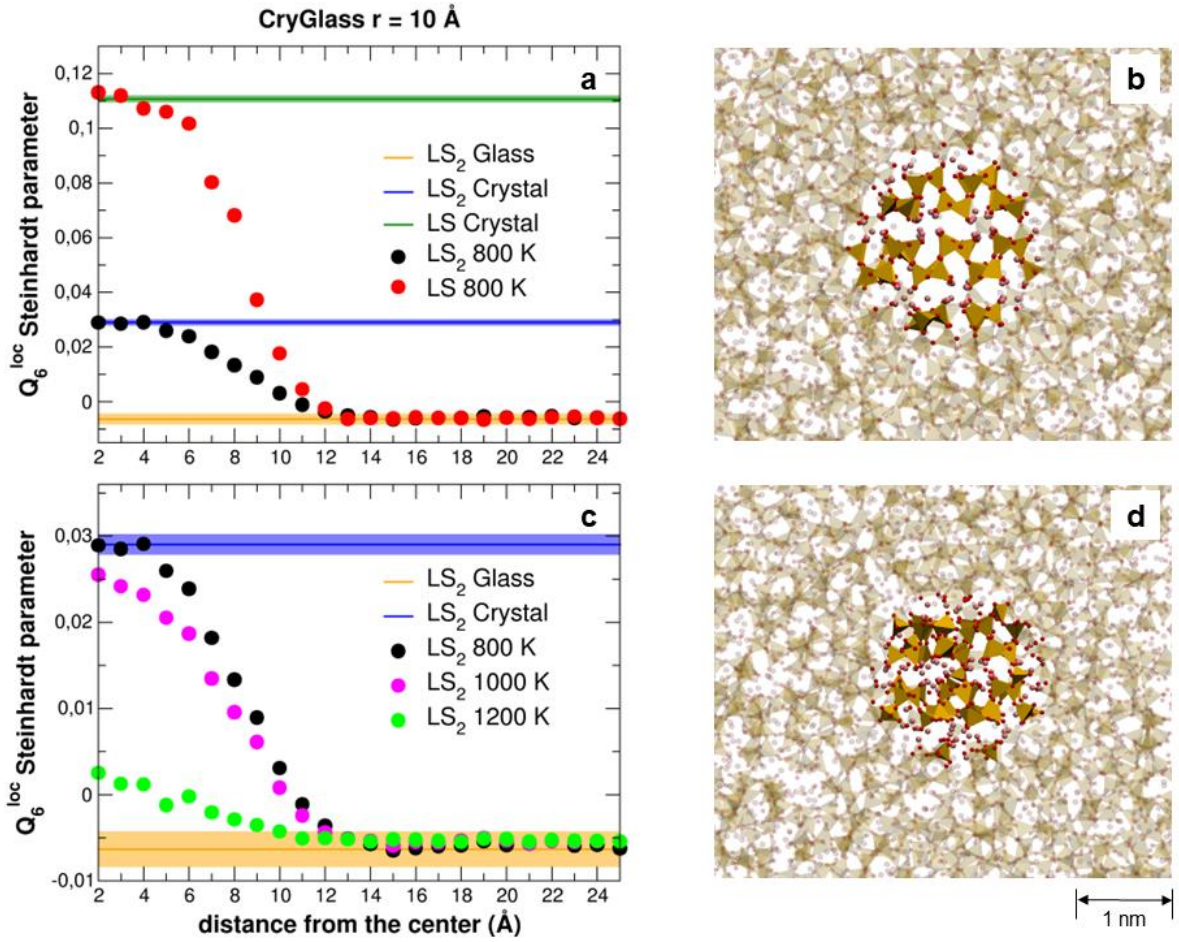

FIG. 5.11. (a) Q_6^{loc} Steinhardt parameter of silicon atoms from the center of the LS or LS_2 crystal nuclei to the glass matrix at 800 K. (c) Computed Q_6^{loc} parameter for silicon atoms from the center of the LS_2 crystal nuclei (with radius of 10 Å) to the glass matrix at 800 K, 1000 K and 1200 K. (b, d) Glass with LS_2 composition with an embedded nucleus of $Li_2Si_2O_5$ crystal with radius of 10 Å equilibrated at 800 K (b) and 1200 K (d).

The gradual change of Q_6^{loc} Steinhardt parameter demonstrates gradual structural transition from the crystal to the glass (melt) structure and the profile allows us to measure the interface thickness in both cases. The LS_2 crystal/LS_2 glass interface thickness is of about 4 Å and less than that of the LS crystal/LS_2 glass, which is about 6 Å. This may be due to the greater flexibility of the Q^2 chains in the LS crystal that easily lose the perfect order at the interface with the glass. In figure 5.11 (c), the Q_6^{loc} parameters were compared at 800 K, 1000 K and 1200 K to understand the effect of the temperature on the LS_2 crystal/glass interface. The figure shows that the interface slightly enlarges in about 1–2 Å at 1000 K, while the Q_6^{loc} value in the cluster approaches to that in the glass matrix and the crystalline order is almost lost at 1200 K. A visual inspection according to figure 5.11 (d) reveals that the layered structure of the crystal is still maintained even though some of the Si–O bonds in the silicate network break and form again. The seed has disordered layers structure at 1200 K.

5.4. Limits of molecular dynamics

Classical MD simulations were used to shed light on the crystal nucleation process in the bulk and at the surface of the stoichiometric lithium disilicate glasses. We employed a modified cluster-exploring algorithm to detect subnano-scale nuclei in the initial crystallization stage, and the free energy calculation using a modified seeding method for the first time in multicomponent oxide glasses. Our simulations suggest that lithium disilicate and lithium metasilicate crystals nucleate independently. The former would appear homogeneously from the bulk, whereas the latter can heterogeneously nucleate only on the glass surface where favorable exogenous conditions are present. Therefore, the failure of CNT in predicting the magnitude of the steady state nucleation rate is not due to the formation of metastable phases as suggested in some of earlier investigations (43,52,184).

As observed in previous works, homogeneous nucleation is associated with the similarity in intermediate range-order morphology of modifier cations between the crystal and the glass. In fact, the Li–Li second moments computed on the bulk glass model is remarkably close to that of the LS_2 crystal. The structural analysis using the improved cluster algorithm reveals that embryos with radii of 4 – 4.5 Å nucleate during glass formation both in the bulk and on the surface, with the stoichiometry and structure very similar to those of the LS_2 and LS crystals. Another interesting finding is that the addition of the nucleating agent P_2O_5 leads isolated orthophosphate units' formation that attracts Li ions and promotes Li_3PO_4 embryos in the glass. This phenomenon facilitates crystallization of lithium metasilicate crystals on the surface where chains of Q^2 silica species surrounded by Li ions are dominant, rather than inside the bulk.

The FESM allowed us to compute the free energy of nucleation for the LS_2 and LS crystals in the stoichiometric LS_2 glass and to investigate the effect of the temperature. The critical radii obtained are in excellent agreement with experimental estimations, and the activation energy barriers are comparable to the experimental data. This seems to confirm that both crystal phases form obeying the CNT if the capillarity approximation is overcome. That is inherently assumed in the FESM, the values of

thermodynamic properties such as the interfacial free energy are indeed size dependent. Therefore, we confirm that the FESM is a powerful approach to study nucleation in glass, for instance to predict which crystals would nucleate easier or extract key thermodynamic parameters as a function of nucleus size, temperature, and pressure.

Unfortunately, the limitations that we encountered in using these techniques are of prime importance. The formation of the crystalline embryo is a non-accessible phenomenon as well as the formation of different metastable phases. It is not possible to simulate the transformation from a phase to another or the dynamics of nucleation or growth. The viscosity, the low mobility of the atoms, is the constraints that we must overcome. Another approximation is the shape of the crystalline embryo: in the FESM we have assumed that the stable crystalline nucleus has a spherical structure, following the CNT. But according to the symmetry of a crystalline phase it is possible that the surface energy is optimized if the nucleating crystal has a different shape.

Chapter 6. Assessment of the Metadynamics parameters on the crystallization process

In chapter 3.2, metadynamics (MetaD) has been presented as a technique capable of driving crystallization in highly viscous materials. However, the literature on the application of such techniques on glass forming liquids is limited to the study of silica crystallization (140). To apply it on our target system, lithium disilicate, it is important to understand how to set-up the MetaD simulation parameters and recover converged free energy surfaces (FES) depending on the system we are working with.

To obtain converged FESs (141,186) simulations time of microseconds can be required (140) and to minimize the time needed to reach convergence, optimization of the MetaD simulation set-up is fundamental. Several review articles (186) provide guidelines to appropriately choose the CVs and other parameters in MetaD simulations for organic and biological systems where CVs usually depend on few constitutive atoms, and FESs converge in nanoseconds. Contrarily, for the study of nucleation/crystallization the CVs depend on a large number of atoms. For example, one of the most used CVs to represent the degree of crystallinity is the intensity of specific peaks in the XRD patterns, which is evaluated from the positions of hundreds of atoms in the simulation box (140). Therefore, in the study of crystallization of highly viscous systems the MetaD simulation set-up used for molecular systems cannot be applied, and further investigation is necessary for effective MetaD simulations.

A systematic study of the effect of MetaD parameters, temperature, and system dimension is carried out in this chapter to effectively obtain converged Free-Energy Surfaces in glass-forming liquids. We selected silica as a prototypical material of silicates because β-cristobalite can relatively easily crystalize through MetaD simulations owing to its simple microstructure.

6.1. Description of SiO_2

Silica, SiO_2, is one of the most abundant minerals in the Earth's crust and it is widely used in many fields, from engineering to pharmaceutical industries and microelectronics. Silica basic units are SiO_4 tetrahedra that are connected to each other sharing a corner, edges or faces. Therefore, there are many silica

polymorphs depending on how the tetrahedra are interconnected and organized (187). Clearly the stability of different polymorphs is different depending on temperature and pressure. β-cristobalite crystallizes from liquid silica at around 2000 K under equilibrium conditions (188,189) and the tetrahedra are arranged in a cubic diamond lattice, as shown in figure 6.1. In liquid silica, SiO_4 tetrahedra are organized in a disordered network.

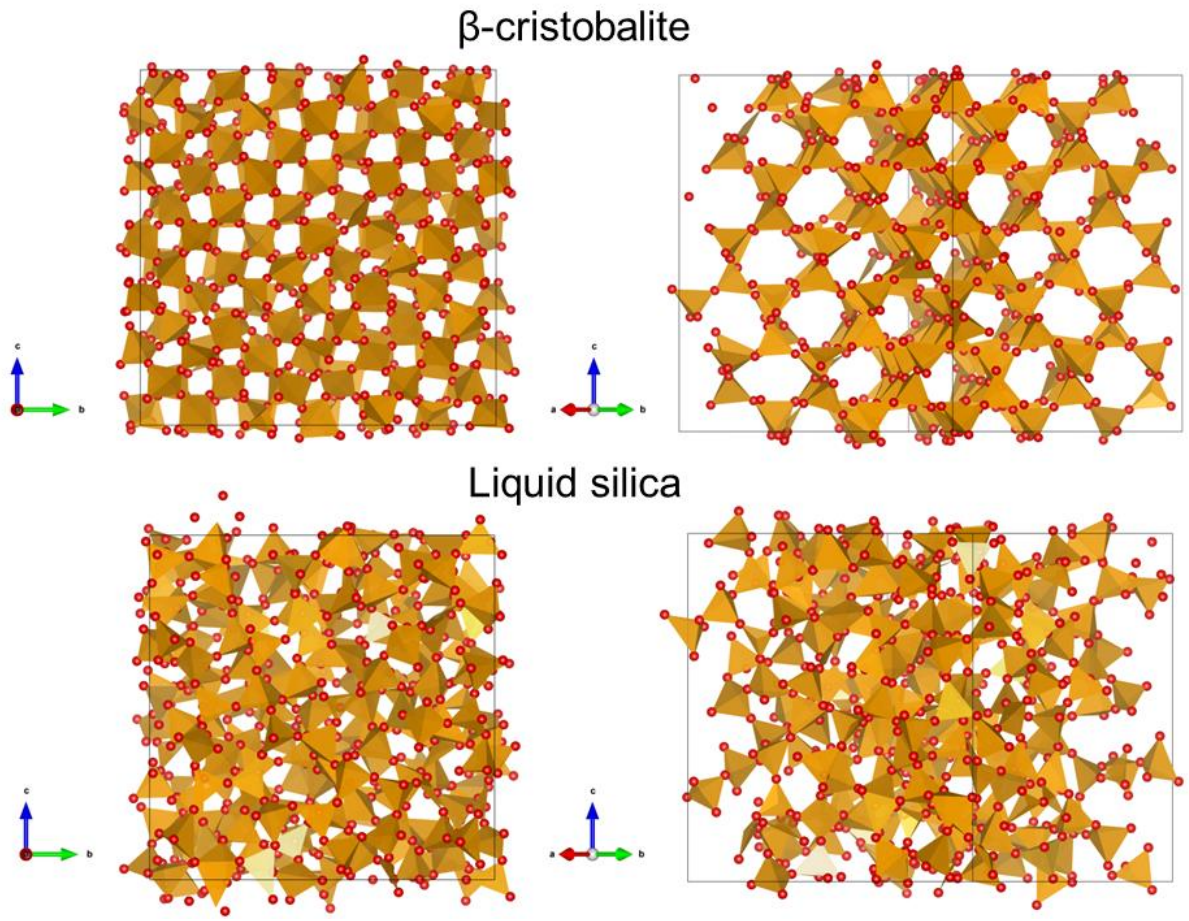

FIG. 6.1. Models' structures of β-cristobalite and liquid silica.

It is not easy to simulate the crystallization of β-cristobalite from liquid silica. The main reasons are the number of different polymorphs that can crystallize according to the conditions, and the time limitation of the computer simulation itself. Liquid silica is a glass forming liquid; therefore, its crystallization is a rare event and its simulation using molecular dynamics would require computer time that is non-accessible today. Enhanced sampling techniques make the crystallization process accessible, as shown by the study reported in ref. (140) carried out by means of metadynamics.

6.1.1. Collective variable

As discussed in chapter 3.2.6, the CV must be able to distinguish between the phases involved in the transformation we are interested in. For the study of the crystallization of silica, the intensity of an XRD peak has proven to be efficient to drive the transformation.

The formula used is described in chapter 3.2.6.1. The wavelength λ of the X-ray is set to 1.5406 Å. To choose an efficient 2θ value, the XRD pattern of the crystalline and liquid phases is compared in figure 6.2. In this case we have considered only silicon atoms in the calculation of the intensity of the XRD patterns. The WTMetaD simulation accuracy is not sacrificed because oxygen positions are related to silicon positions when promoting crystallization.

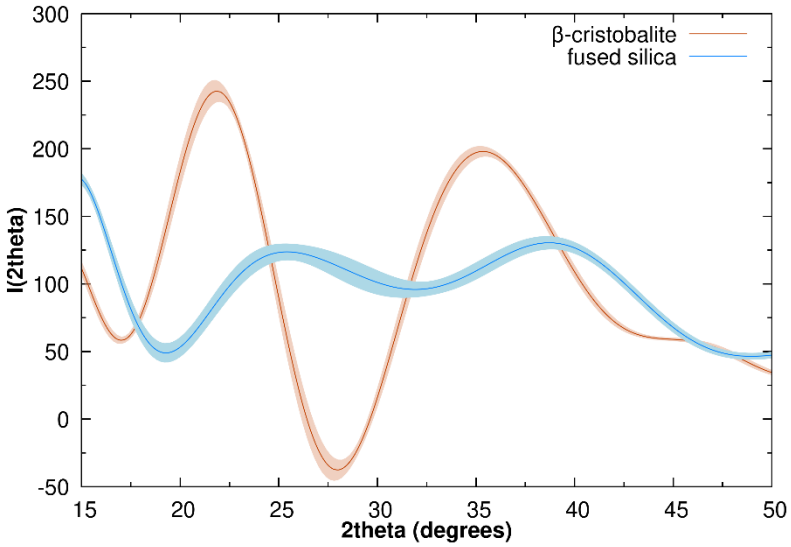

FIG. 6.2. XRD spectra of the crystalline (β-cristobalite) and silica melt by considering only Si atoms. The XRD spectra are averaged along the 2 ns of MD trajectory, and the standard deviation is represented with a shaded region.

The two curves are obtained from 2 ns of unbiased MD simulations of β-cristobalite and silica melt at 2400 K using 192 atoms, which is the size of the investigated system, if a larger model need to be simulated the CV must be evaluated using the corresponding model. The liquid silica has been obtained by melting the crystalline model at high temperature, up to 3500 K, and cooling it down until 2400 K. The peak intensity at $2\theta = 22°$ is found to be suitable for distinguishing the crystalline and amorphous structures.

6.2. Computational details

In this study, all initial configurations were obtained by replicating the β-cristobalite crystalline unit cell (190), which contains 24 atoms in a cubic lattice with size of 7.12 Å, to a larger model. We employed the interatomic potential developed by Pedone et al. (114) for pair-wise short-range interactions, chapter 3.1.2, while long-range Coulomb interactions were described by using Wolf summation method (123). The large-scale atomic/molecular massively parallel simulator (LAMMPS) (191) software patched with the open-source, community-developed PLUMED plugin for molecular dynamics (192,193) version 2.6 was used for all MD and WTMetaD simulations. In all simulations, the Nosé-Hoover thermostat (194) and barostat were employed for performing NVT or NPT simulations at 1 bar. The relaxation times for controlling temperature and pressure were 0.1 ps and 10 ps, respectively. All WTMetaD simulations were performed

using the NPT ensemble. The equation of motion was integrated using the Verlet algorithm (181) with a timestep of 2 fs.

6.2.1. Choice of tested MetaD parameters

The starting point for our investigation is the work of Niu et al. (140) were a system containing 192 atoms has been investigated in a range of temperatures between 2300 K and 2800 K. They have used a WTMetaD simulation where the bias was constructed by depositing Gaussian every 1 ps with width of 5 CV units and height of 40 kJ/mol, with a bias factor of 100. However, the force field employed in this work is not the same, and the results can be different.

To choose the MetaD parameters to be tested, we have considered also the guidelines of the work of Bussi and Branduardi (186).

- First the height ω should be a fraction of $k_B T$ at the desired temperature.

- For the width, σ, a preliminary unbiased MD simulation is performed for each phase involved in the transformation. For the chosen CV, the probability distribution along the sampled CV range is computed and a Gaussian can be fitted on this distribution. This can be done assuming that the free energy landscape minimum is a quadratic minimum. Thus, the width is equal to the standard deviation of the fitted Gaussian.

- To obtain a rough estimation of the deposition rate, τ, a short MD run is performed, and the autocorrelation of the CV is evaluated. With this rule the system can relax between one deposition and the other, avoiding the deposition of Gaussian in the same point of the phase space.

- The most difficult one is the bias factor, γ, related to the ΔT. This value depends on the barrier that separates the metastable basins. Thus, if the barrier is n-times $k_B T$ the bias factor is chosen to be n.

We decided to investigate a system containing 192 atoms (2x2x2 unit cell), as in the paper of Niu et al., first, at 2700 K. As for the height (ω), since $k_B T$ is equal to 22.4 kJ/mol, we decide to test 20 and 60 kJ/mol. Since the standard deviation on the distribution of the CV for unbiased MD simulations of the crystalline and the liquid phases is 7 and 9 CV units respectively, we decided to test 2 and 8 CV units.

We used a fixed deposition rate of 1 ps determined by computing the autocorrelation of the CV in a short MD run. Finally, as for the bias factor we tested values above and below the one used by Niu et al. (140): 20, 50 and 150. The WTMetaD parameters tested are reported in table 6.1.

TABLE 6.1. List of experimental conditions tested to examine the effect of WTMetaD parameters.

n° experiment	**ω (kJ/mol)**	**γ**	**σ (CV units)**

1	20	50	2
2	20	50	8
3	20	150	2
4	60	50	2
5	60	50	8
6	60	150	2
7	60	20	2

All simulations in this test set were performed with a unit cell containing 192 atoms (2x2x2) at T=2700 K. The effect of the temperature was studied at 3200 K and 2700 K. The simulation size effect was studied by performing some simulations with unit cells containing 648 (3x3x3) and 1536 (4x4x4) atoms.

To rigorously investigate the effects of the parameters listed in table 6.1, WTMetaD simulations were performed for 10 μs at 2700 K. In the following, we will show the comparison between the above-mentioned simulations to highlight the most important information. First, we will discuss the procedure used to analyze a single simulation, because it will clarify all results that will follow.

6.3. How to analyze a simulation

The time evolution of the CV used to bias the simulation gives information about the diffusivity of the system between the crystal and amorphous states. In figure 6.3, the simulation n° 4 (ω=60, γ=50, σ=2) is chosen as an example.

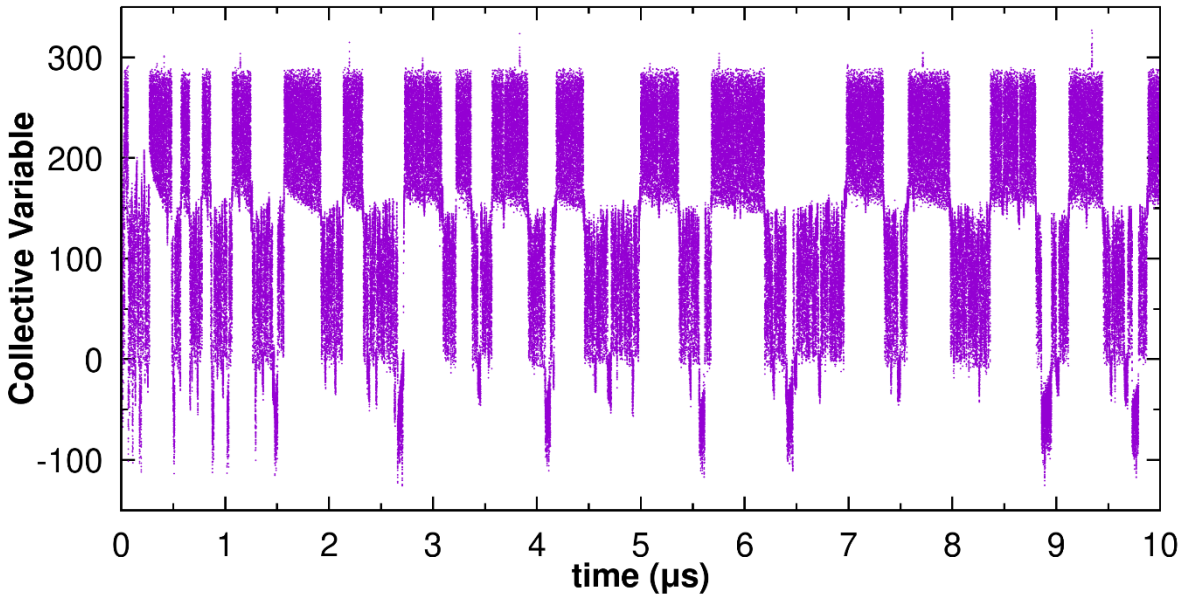

FIG. 6.3. Time evolution of the CV in WTMetaD simulation n° 4 at 2700 K.

The transitions are frequently observed during the simulation. The crystalline phase is located at the high value of the CV, between 150 and 300, while the melt phase is in the region between 0 and 150. The other CV-values explored are associated with high-energy structures, which are not important to understand the mechanism of crystallization.

The trend of the offset energy, $c(t)$, shown in figure 6.4 demonstrates how the applied bias varies. The re-crossing frequency, which is the number of transitions between solid and liquid per unit time during the WTMetaD, can be an indicator of the diffusivity (141). Assuming the adiabatic regime appears from 4 μs, the re-crossing frequency of simulation n° 4 is on average 2.5 re-crossings per microsecond. Note that, as expected from the theory of MetaD, the $c(t)$ rapidly increases in the initial stage followed by a slower increase in the quasi-stationary bias region that indicates that the asymptotic regime in which WTMetaD is valid has been reached. Albeit the achievement of an asymptotic regime has been used as an indication of converged simulations in previous works, we will show in the following that this is not always the case.

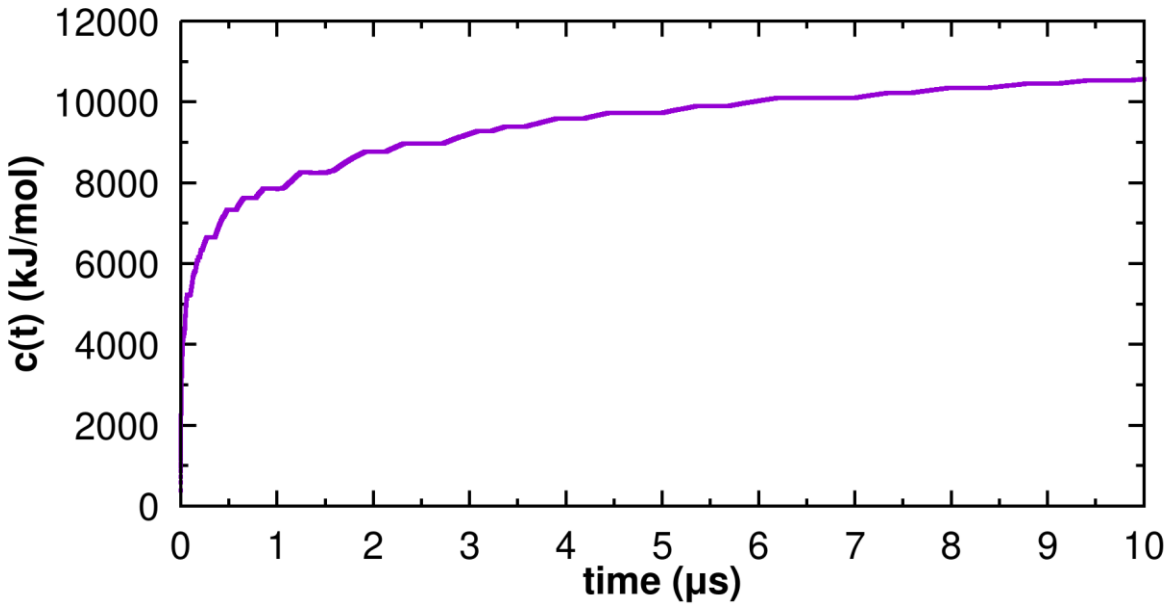

FIG. 6.4. The offset energy $c(t)$ as a function of simulation time for simulation n° 4.

The FES can be evaluated once the adiabatic regime is reached using two approaches. The first approach accumulates the bias and estimates the FES using the equation 3.23. However, if the additional bias is not completely stationary (a criterion satisfied only over infinite time) the calculated FES keeps changing. This behavior is observed in figure 6.5 (a). In fact, the variation of the FES curve tends to decrease as the simulation proceeds, but it does not converge. Interestingly, the estimated FES fluctuates around the correct FES beyond the diffusive regime. Therefore, a cumulative average potential and an average of FES can be evaluated. This procedure is usually applied in the non-tempered MetaD simulations (146), because for the WTMetaD the average FES converges by construction as the applied potential decreases with time (195). It is still a useful procedure, not for the estimation of the error in the free energy calculation, but to understand the convergence. The average FES is reported in figure 6.5 (b). We started to accumulate the potential after the two free-energy wells were filled. Accordingly, the FES curve converges relatively

quickly at around 5-6 μs. The last approach is the reweighting procedure described by equations 3.16 and 3.24. The error of the FES was estimated using the block analysis, paragraph 3.2.4.

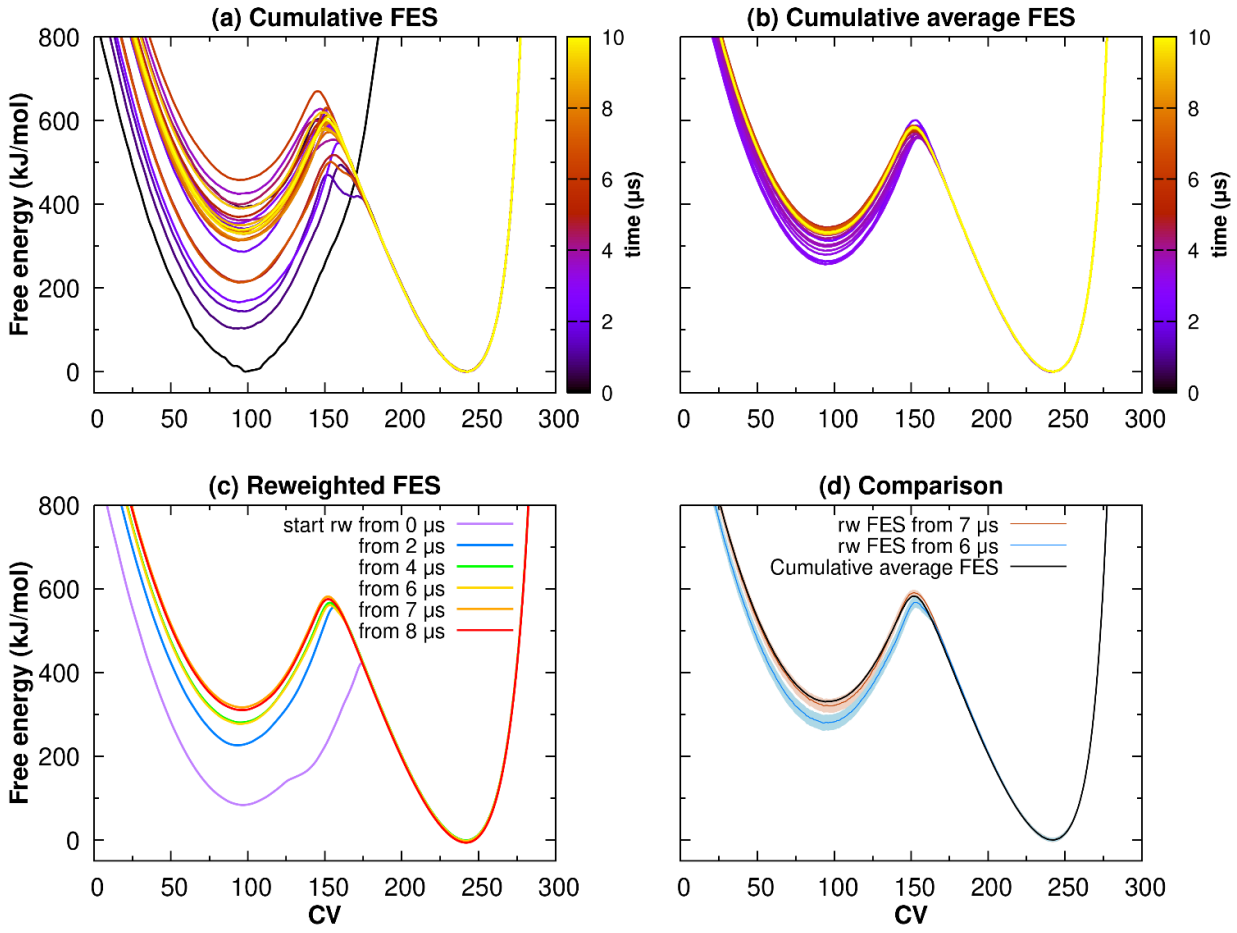

FIG. 6.5. Different methods to calculate FES of simulation n° 4. (a) Cumulative bias is evaluated and using eq. 3.XX free energy is calculated at each time. (b) After a suitable initial time, the average of the cumulative bias at different times is calculated. (c) FESs were evaluated using the reweighting procedure applied starting from different simulation times. (d) Comparisons of final FESs obtained with averaging and reweighting methods; the second ones report the error calculated with the block analysis.

The following step is to understand which part of the simulation must be accounted for accumulating the probability distribution. According to figure 6.4 and figure 6.5 (a), the quasi-static regime has not been reached before 4-5 μs, therefore, we should not take the earlier configurations into account. We selected different starting points to see how the calculated FES changes and progresses over time. Figure 6.5 (c) shows an overview of some reweighted FESs. In this figure, color ranges are associated with five different starting points, as indicated in the legend. Even though the reweighted FESs obtained starting from 0 and 2 μs are not meaningful from a physical viewpoint, they are also compared to understand what happens in the non-adiabatic regime to estimate the FES.

The choice of the starting time is crucial to calculate the correct FES, because, in fact, the reweighted FES keeps changing until 7 μs. After 7 μs, the longer simulation does not vary the FES shape. Figure 6.5 (d) compares the FESs obtained by the cumulative averaging and reweighting procedures. The latter FES is

shown with standard deviations. The FES reweighted form 7 μs agrees well with cumulative averaged one. The sufficiently small error calculated from the block analysis proves the convergence. As shown in figure 6.6, the error was evaluated with different block sizes. The plateau independent from the block dimension after approximately one hundred thousand blocks gives the average error of the FES.

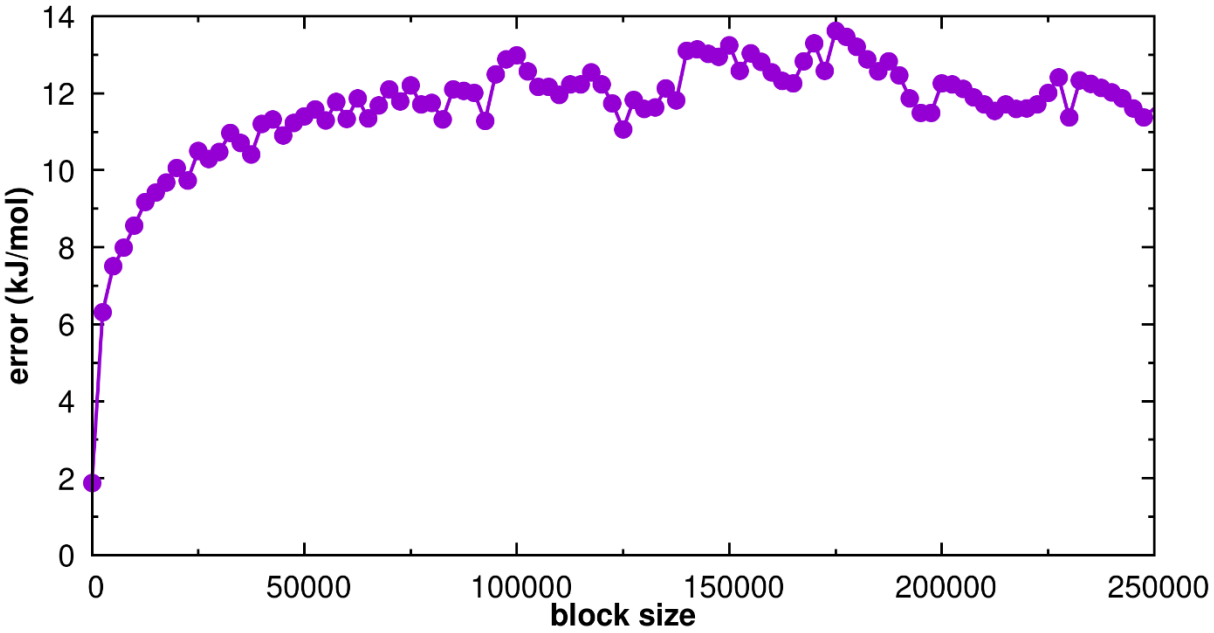

FIG. 6.6. The error of FES obtained from block analysis on probability distribution histogram accumulated starting from 7 μs to 10 μs.

Tiwary and Parrinello (150) defined the time-independent estimator as equation 6.1 to confirm the free energy convergence in a given small region of the CV space:

$$\beta F(\boldsymbol{s}) = \frac{-\gamma V(\boldsymbol{s},t)}{k_B \Delta T} + \log \int d\boldsymbol{s}\, e^{\gamma V(\boldsymbol{s},t)/k_B \Delta T} \tag{6.1}$$

From equation 6.1, the difference between the free energies in two small regions s_1 and s_2 can be obtained:

$$\Delta F_{s_1,s_2} = \frac{-\gamma}{\gamma - 1}\, \Delta V_{s_1,s_2} \tag{6.2}$$

$\Delta F_{s_1,s_2}$ is equivalent to the direct difference in free energy obtained by the accumulated bias within the two states. Because $\Delta F_{s_1,s_2}$ can be calculated during the WTMetaD simulations, it is also an indicator of the FES convergence, at least, at the two small regions s_1 and s_2. We call this parameter $direct\ \Delta F$.

The ΔF between the basins can be also calculated from the probability distributions obtained during the reweighting procedure. The relative reweighted free energy difference between state A and B can be correctly determined from $F(\boldsymbol{s})$ by integrating the probabilities of the two states (according to equation 3.16)

$$\Delta F_{A,B} = \frac{-1}{\beta} \log \frac{P_A}{P_B} = \frac{-1}{\beta} \log \frac{\int_A ds\, e^{-\beta F(s)}}{\int_B ds\, e^{-\beta F(s)}} \tag{6.3}$$

By assuming that states A and B are two wells, the difference in height between the two free energy minima is a possible approximation of ΔF (142), if the shapes of the two basins are similar. We call this parameter $reweighted\ \Delta F$ to use as another estimator of FES convergence despite the lower accuracy. Both the $direct$ and $reweighted\ \Delta F$ should converge to the same value if they are calculated in the same region if the total free energy surfaces agree with each other. If the $reweighted\ \Delta F$ does not agree with the $direct\ \Delta F$, the probability distribution might be corrected avoiding the non-adiabatic region. It is important to ensure that the accumulation is started from the quasi-stationary regime to collect meaningful probability distributions. The $direct$ and $reweighted\ \Delta F$ are less accurate but faster and more practical indexes than the complete FES. In figure 6.7, these estimators are compared.

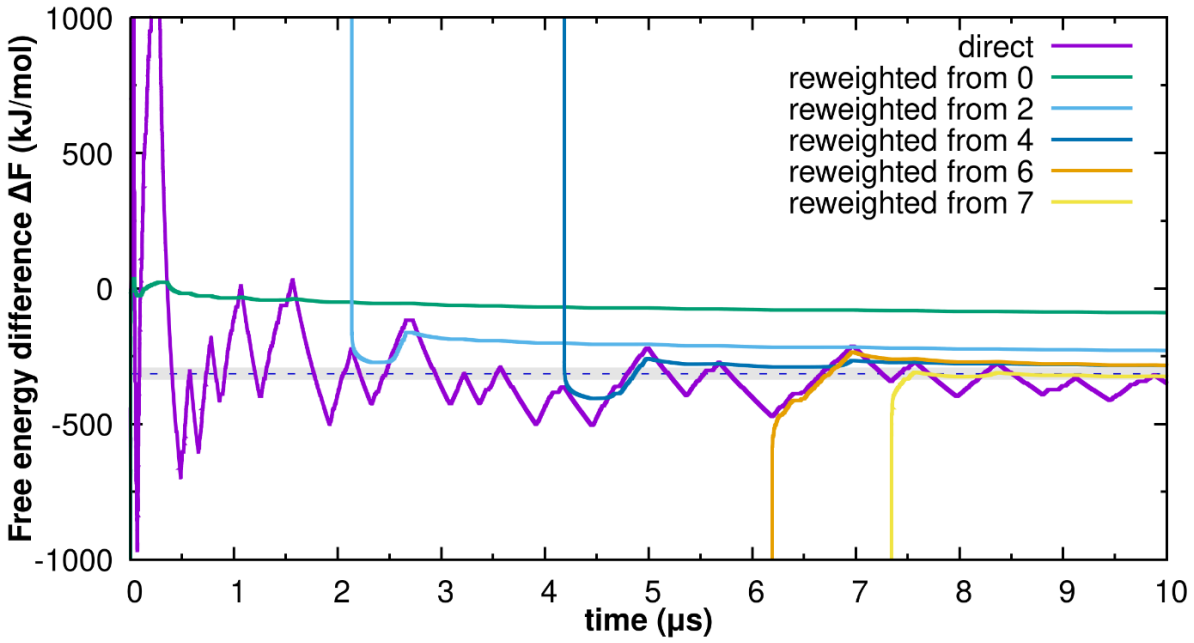

FIG. 6.7. ΔF between the minima of the two states obtained directly from the acting bias and from the reweighting procedure started at different starting times. The dotted line indicates the final average value with a blue stripe representing 1 k_BT width.

The $reweighted\ \Delta F$ converges faster than the $direct\ \Delta F$; however, it converges to the correct value only when it is calculated from the adiabatic regime. The block analysis can be used to judge whether the sampling is sufficient or not.

6.4. Effect of MetaD parameters

In this section, the comparisons between the selected simulations are shown to highlight the importance of the parameter choice. We discuss the best parameter set for obtaining a faster and more accurate convergence.

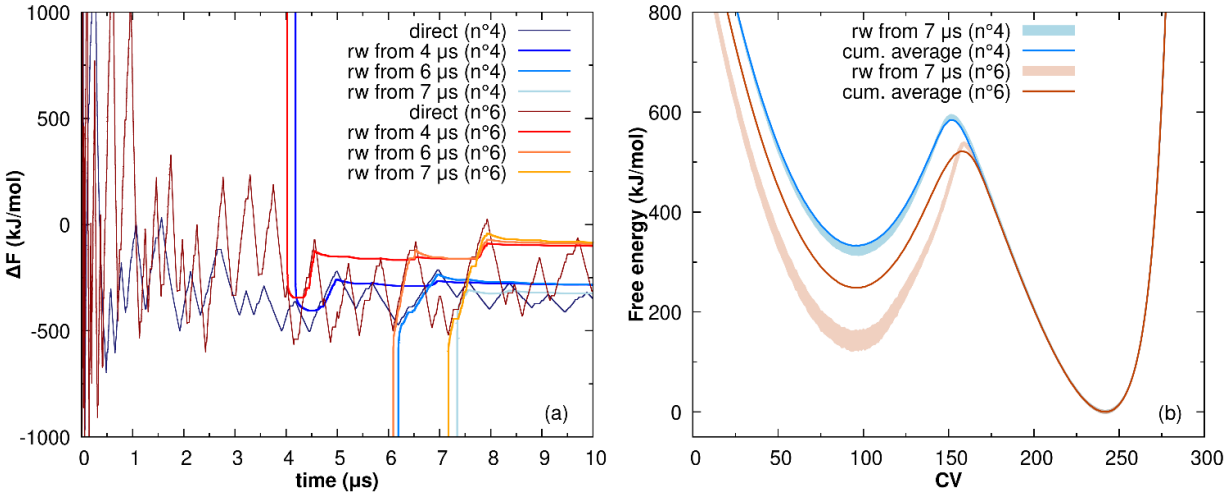

FIG. 6.8. (a) *Direct* and *reweighted ΔF* calculated for simulation n° 4 (ω = 60, γ = 50, σ = 2) and n° 6 (ω = 60, γ = 150, σ = 2), which differ in γ value. (b) Comparison between FESs obtained from the two simulations using reweighting and cumulative average procedures.

Figure 6.8 reports the results of simulations n° 4 (ω = 60, γ = 50, σ = 2) and n° 6 (ω = 60, γ = 150, σ = 2), which differ only in the bias factor value. The *direct* and *reweighted ΔF* are compared to see the effect of the bias factor, γ, in figure 6.8 (a). The *direct ΔF* of n° 6 exhibits a greater fluctuation, meaning considerable variations of the cumulative FESs over time and a higher re-crossing frequency. Contrarily, as shown in figure 6.3, simulation n° 4 (ω = 60, γ = 50, σ = 2) exhibits smaller fluctuations and re-crossing frequency. Figure 6.8 (b) shows that in simulation n° 6 (ω = 60, γ = 150, σ = 2) the reweighted FESs calculated from different starting times do not converge with the average value of the cumulative FES, implying that the adiabatic region is not reached. The time evolution of the CV for simulation n° 6 (shown in figure 6.9) reveals that the bias factor, γ = 150, is too high and pushes the system to explore high-energy CV regions, which are not important to understand melt-crystal transition. With a high bias factor, a high quantity of bias is deposited in a shorter time than the opposite case. If this quantity is higher than necessary, it must be compensated with the addition of smaller gaussian. However, the lowering of the height is slower with a high γ and so longer time is needed to reach convergence. The exploration of phases out of the range of interest can be controlled, constraining the dynamics in a certain region of the CV (196). However, in this case we have not observed an improvement in the convergence speed, since the time spent in the high-energy region is not significant.

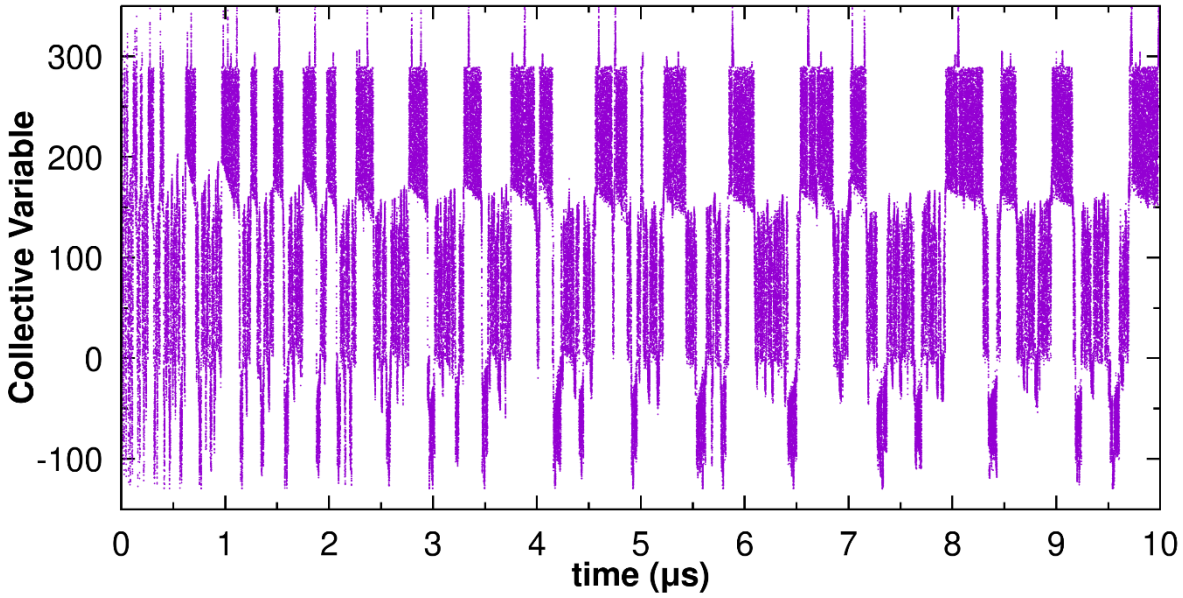

FIG. 6.9. Time evolution of the CV in WTMetaD simulation n° 6 (ω = 60, γ = 150, σ = 2) at 2700 K.

This behavior is observed also in simulation n°3 (ω = 20, γ = 150, σ = 2), which also has a high value of γ, shown in figure 6.10. On the other hand, simulation n° 7 (ω = 60, γ = 20, σ = 2), which has a low γ-value, presents small fluctuations but too low diffusivity (figure 6.11 (a)) to obtain the converged FES in reasonable simulation time. Indeed, the block analysis reported in figure 6.11 (b) confirms that the simulation n° 7 does not reach convergence within 10 μs.

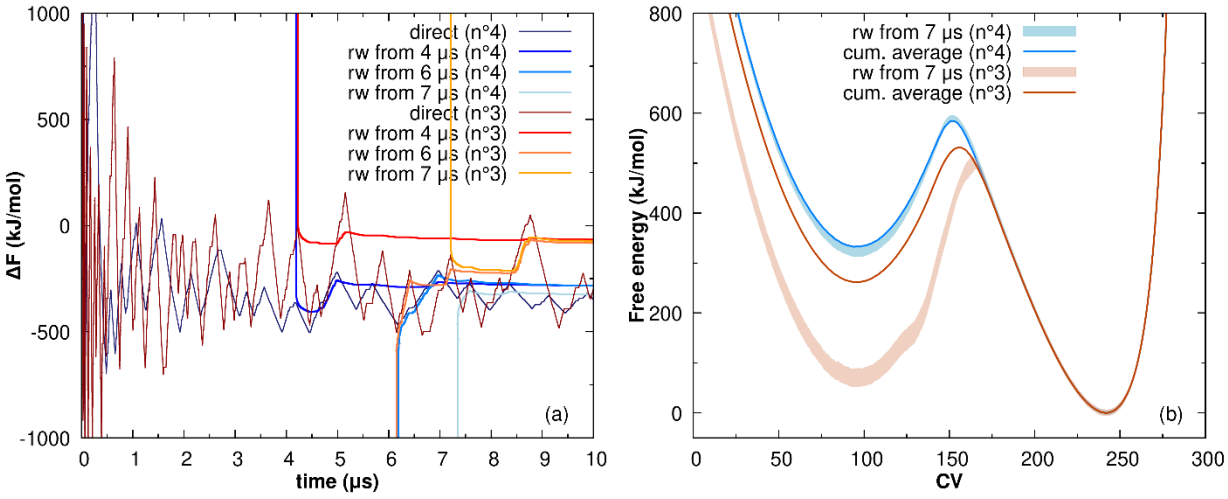

FIG. 6.10. (a) *Direct* and *reweighted ΔF* calculated for simulation n° 4 (ω = 60, γ = 50, σ = 2) and n° 3 (ω = 20, γ = 150, σ = 2). (b) Comparison between FESs obtained from the two simulations using reweighting and cumulative average procedures.

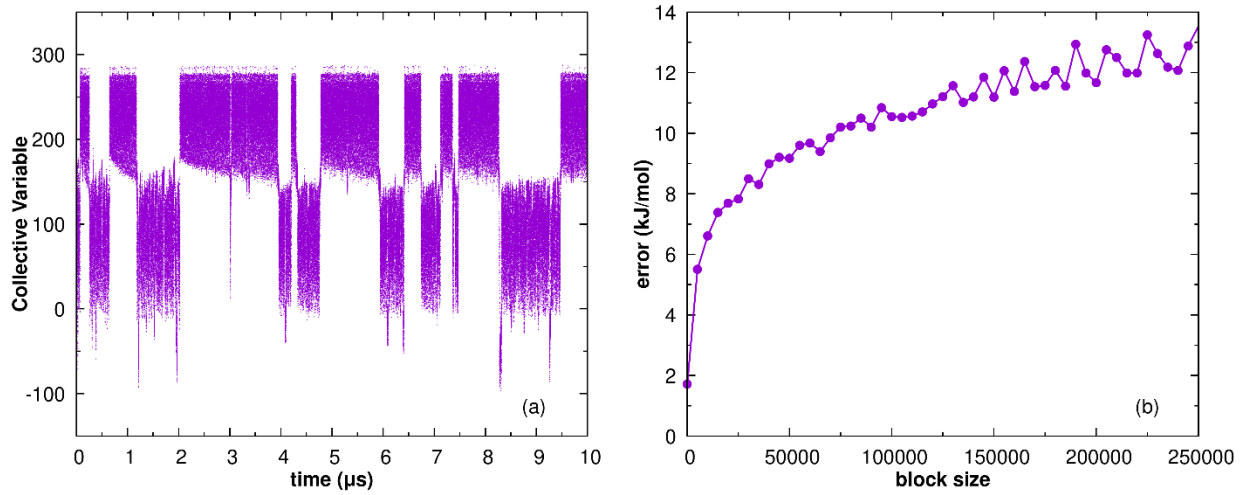

FIG. 6.11. (left) Time evolution of the CV in WTMetaD simulation n° 7 (ω = 60, γ = 20, σ = 2) at 2700 K, (right) estimation of the error using the block analysis on the probability distribution.

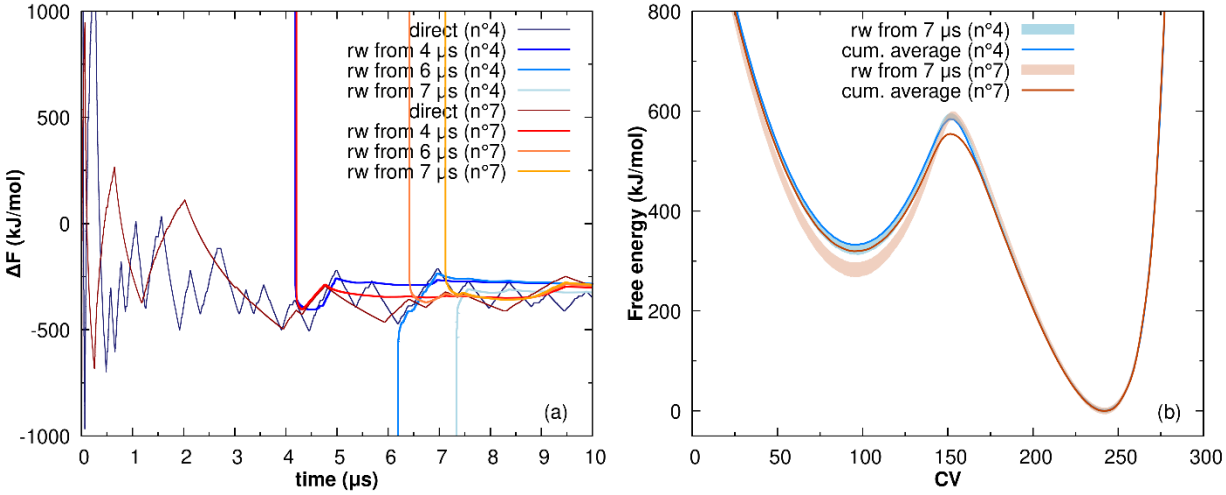

FIG. 6.12. (a) *Direct* and *reweighted* ΔF calculated for simulation n° 4 (ω = 60, γ = 50, σ = 2) and n° 1 (ω = 60, γ = 20, σ = 2). (b) Comparison between FESs obtained from the two simulations using reweighting and cumulative average procedures.

Figure 6.13 compares simulations differing in the height, ω, which was 20 kJ/mol for simulation n° 1 (ω = 20, γ = 50, σ = 2) and 60 kJ/mol for n° 4 (ω = 60, γ = 50, σ = 2). Both the FESs and ΔF almost perfectly matched. The re-crossing frequency is also not affected by the value of ω.

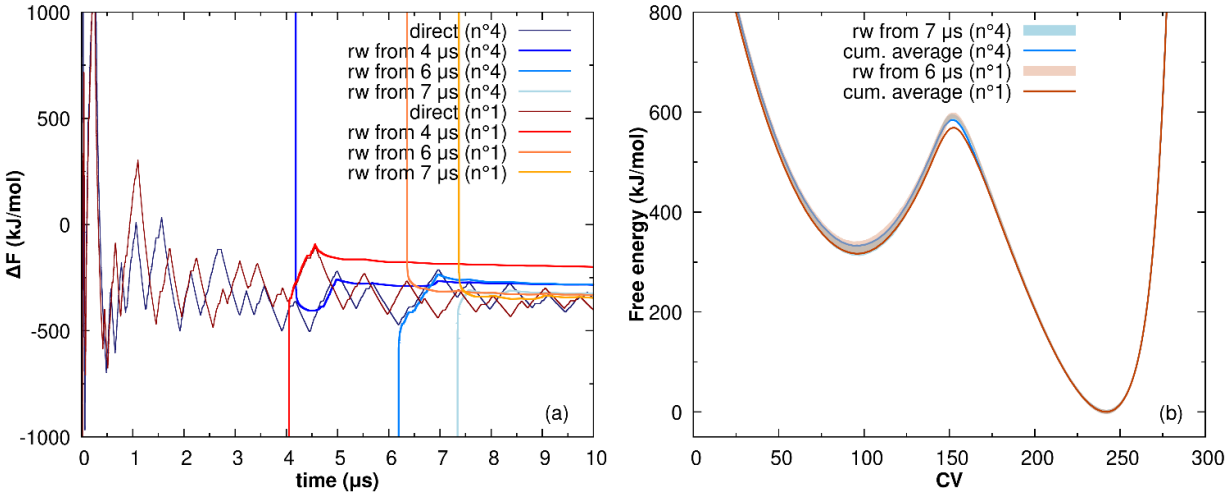

FIG. 6.13. (a) *Direct* and *reweighted ΔF* calculated for simulation n° 4 (ω = 60, γ = 50, σ = 2) and n° 1 (ω = 20, γ = 50, σ = 2), which differ in ω value. (b) Comparison between FESs obtained from the two simulations using reweighting and cumulative average procedures.

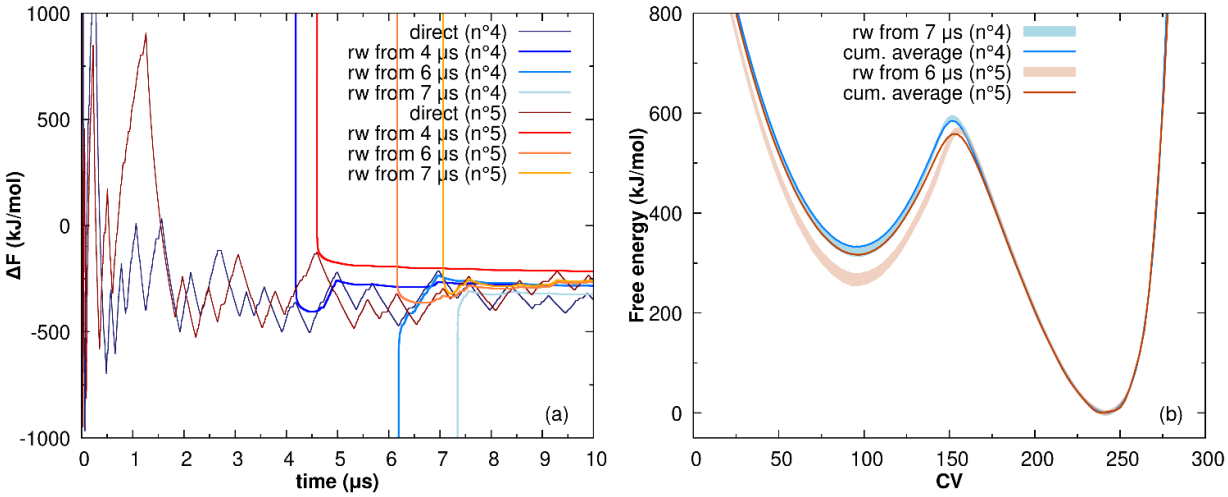

FIG. 6.14. (a) *Direct* and *reweighted ΔF* calculated for simulation n° 4 (ω = 60, γ = 50, σ = 2) and n° 5 (ω = 60, γ = 50, σ = 8), which differ in σ value. (b) Comparison between FESs obtained from the two simulations using reweighting and cumulative average procedures.

Figure 6.14 compares simulations n° 4 and n° 5 differing in the width of the Gaussian: σ = 2 and σ = 8, respectively. The width must be chosen carefully, because it spreads the bias in the region near the explored CV. It accelerates filling the wells in a more efficient way, resulting in a faster decrease in the height of the Gaussians. Contrarily, the phase space associated to each state has to be sufficiently larger than the width of Gaussians, otherwise the bias affects outside of the interested regions. The standard deviations of the CV were approximately 7 CV units and 9 CV units in the crystalline and the melt phases, respectively (see paragraph 6.2.1). Indeed, simulation n° 4 whose σ value is a fraction of the standard deviations converged, while simulation n° 5 did not probably due to the larger bias. Similar behaviors were observed for the other simulations when the Gaussian width is too large.

Only a few simulations, n° 1 (ω = 20, γ = 50, σ = 2) and n° 4 (ω = 60, γ = 50, σ = 2), converged at 2700 K within 10 µs. The agreement between the cumulative average and the reweighted FESs is obtained only

in those two simulations, but also simulation n° 2 (ω = 20, γ = 50, σ = 8), n° 5 (ω = 60, γ = 50, σ = 8) and n° 7 (ω = 60, γ = 20, σ = 2) obtained similar results (see figure 6.12 and 6.15). These results indicate the predominant effect of the bias factor. Increasing the bias factor leads to higher transition rates and affects the exploration of the phase space. An appropriate choice of the bias factor may allow overcoming very high barriers to see unlikely processes, reaching high-energy configurations. On the other hand, exploring such high-energy regions increases the simulation time to reach convergence in the stable regions of interest. In our specific case, γ = 50 is the best choice. σ = 2 is a good choice since it allows to reach convergence faster, while height, ω, is less influential even though simulation n° 1 (ω = 20, γ = 50, σ = 2) reached convergence slightly earlier than n° 4 (ω = 60, γ = 50, σ = 2), as shown in figure 6.13 (a).

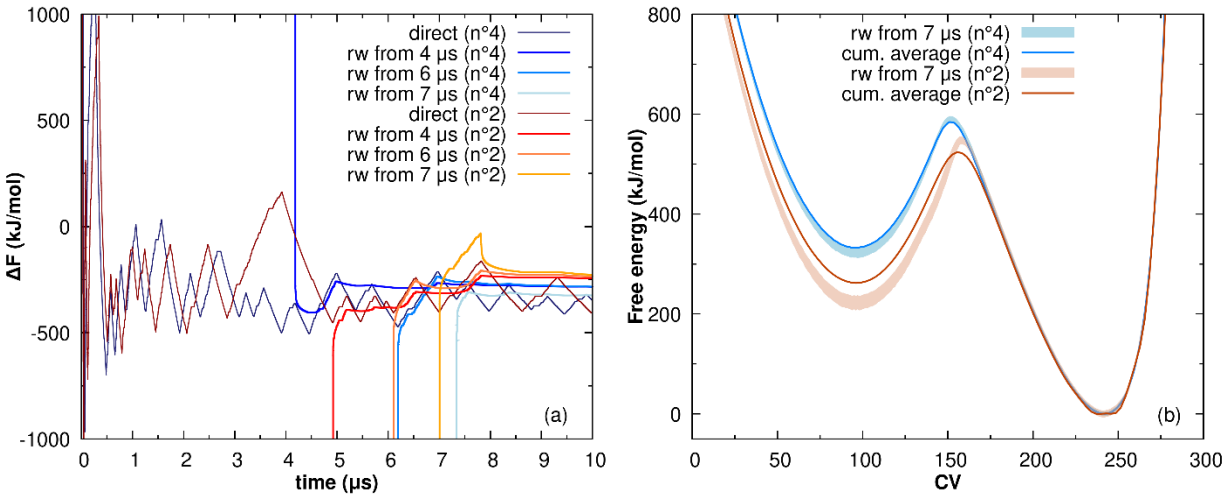

FIG. 6.15. (a) *Direct* and *reweighted ΔF* calculated for simulation n° 4 (ω = 60, γ = 50, σ = 2) and n° 2 (ω = 20, γ = 50, σ = 8). (b) Comparison between FESs obtained from the two simulations using reweighting and cumulative average procedures.

6.5. Effect of temperature

To investigate the effect of the temperature, all experiments in table 6.1 were examined at 3200 K as well, but for the sake of brevity we focus only on the results of experiment n° 4 (ω = 60, γ = 50, σ = 2). Figure 6.16 shows the time evolution of the biasing CV (peak at 2θ = 22°) at the two temperatures. The frequency shuttling between the two states is much higher at 3200 K due to the higher diffusivity and atomic mobility. This enables a more efficient sampling of the configurational space and thus to obtain the crystallization pathway. Consequently, the simulations at higher temperatures converge easier. Figure 6.17 shows the fluctuations of the *direct* and *reweighted ΔF* for the two temperatures.

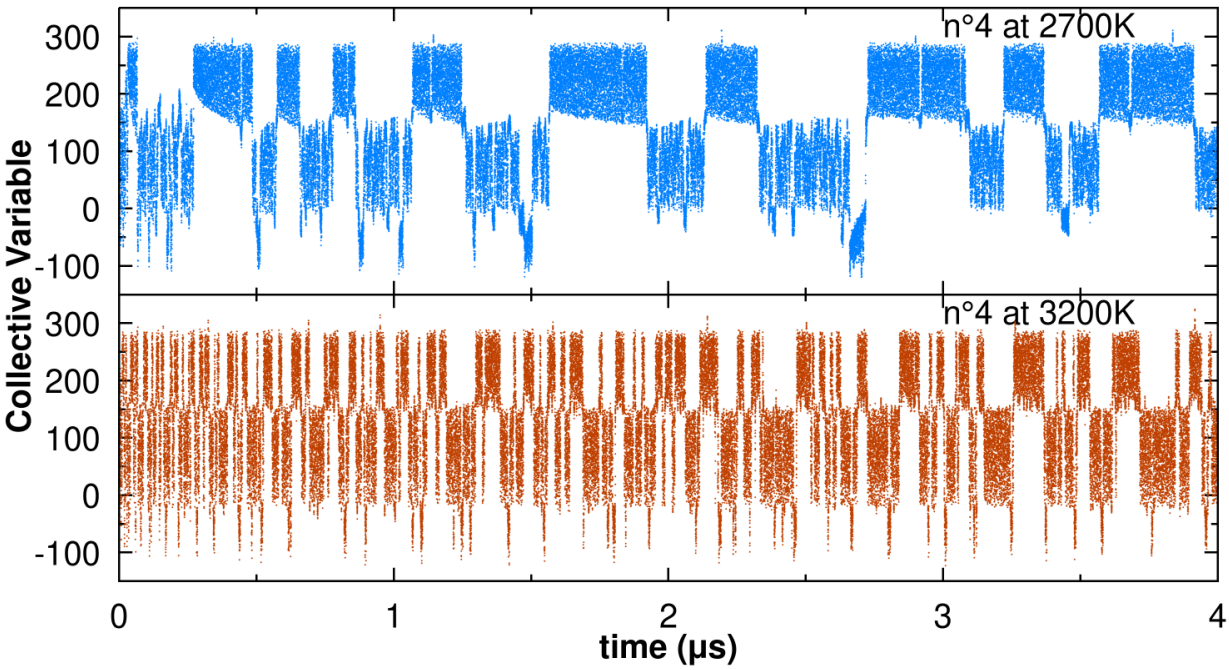

FIG. 6.16. Time evolution of the CV during 4 μs of WTMetaD simulation of experiment n° 4 (ω = 60, γ = 50, σ = 2) at 2700 K and 3200 K.

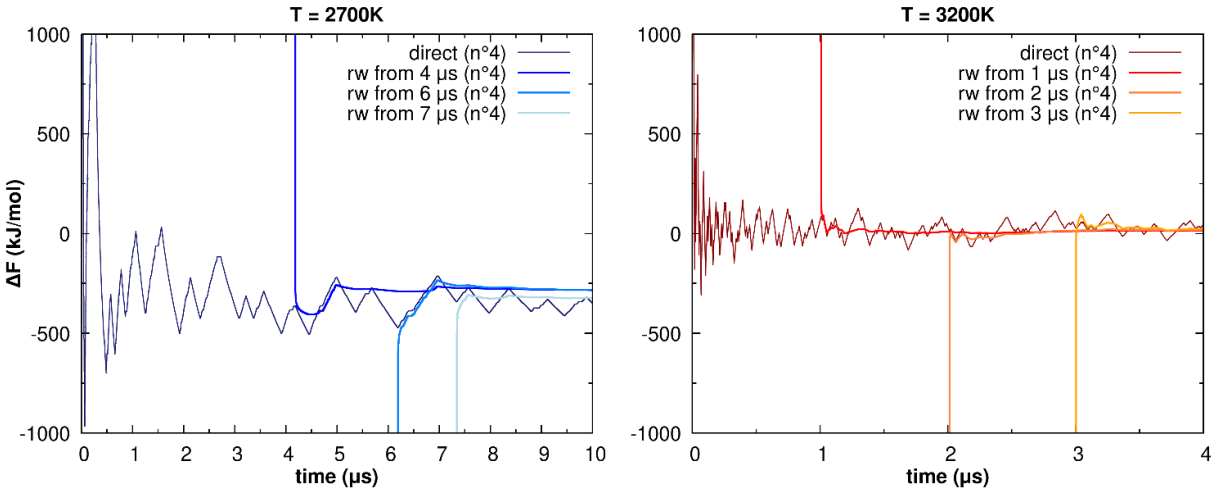

FIG. 6.17. Comparison between *direct* and *reweighted ΔF* for simulation n° 4 (ω = 60, γ = 50, σ = 2) at 2700 K (left) and 3200 K (right).

At 3200 K, the *reweighted* and *direct ΔF* agree well because both converge to the average value within 4 μs, whereas at 2700 K the simulations do not converge within this time. Moreover, lower fluctuations and lower error (6.5 kJ/mol) of the *direct ΔF* are observed at 3200 K with respect to those at 2700 K, at which the error is 12 kJ/mol, as shown in figure 6.6. All simulation conditions in table 6.1 at 3200 K converge towards the same FES faster than at 2700 K regardless of the parameter sets (reported in figure 6.18). Therefore, temperature seems to be the most important factor to reach accurate FES using WTMetaD, especially for highly viscous systems such as silicate melts.

To obtain converged FES at the melting temperature or lower, several tens of microseconds of simulations would be required for silicates. In such cases, one possible alternative method is reweighting a high-temperature distribution probability to a lower temperature one, as described in section 3.2.5.

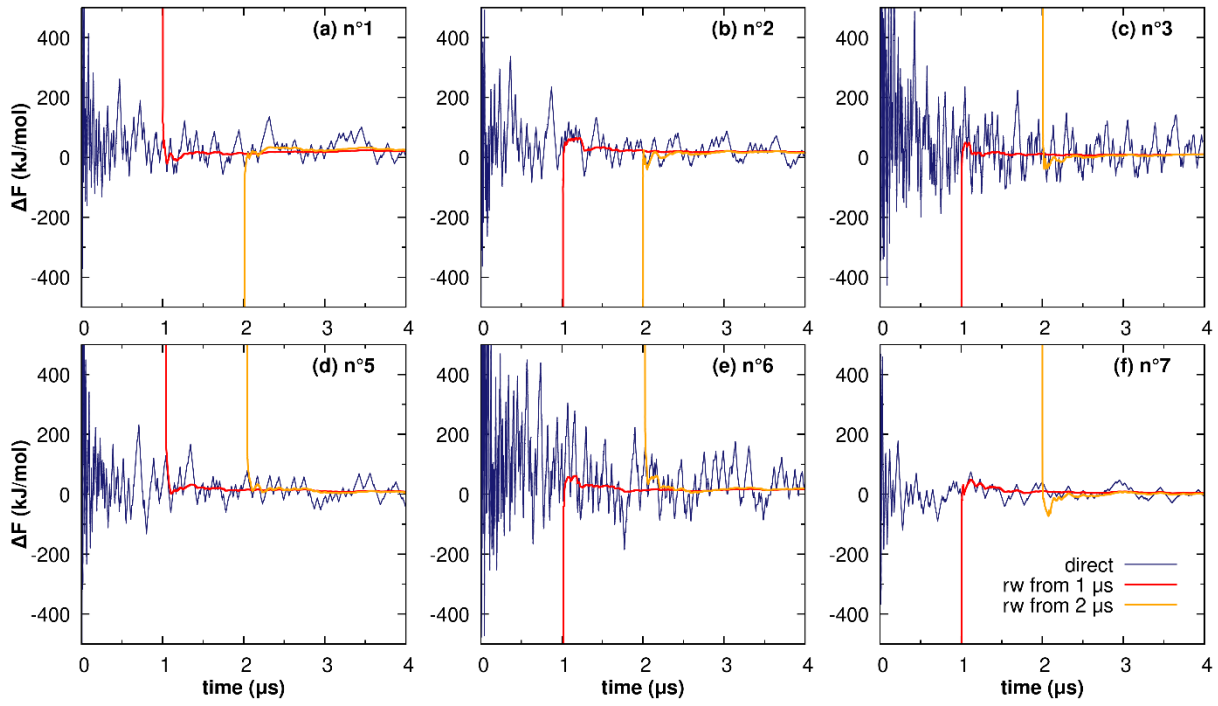

FIG. 6.18. Comparison between direct and reweighted ΔF for simulation n° 1 (ω = 20, γ = 50, σ = 2), 2 (ω = 20, γ = 50, σ = 8), 3 (ω = 20, γ = 150, σ = 2), 5 (ω = 60, γ = 50, σ = 8), 6 (ω = 60, γ = 150, σ = 2), 7 (ω = 60, γ = 20, σ = 2) at 3200 K.

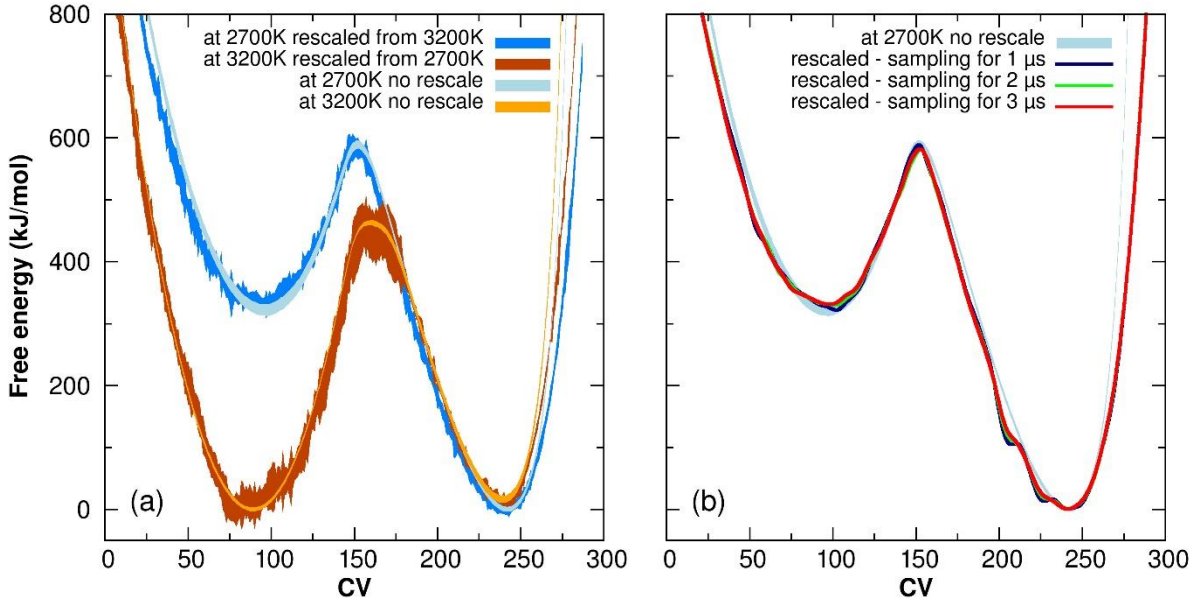

FIG. 6.19. (a) Comparison between FESs calculated directly from the simulations n°4 (ω = 60, γ = 50, σ = 2) at 3200 K (starting from 1 μs) and 2700 K (starting from 7 μs) and using the rescaling procedure from one temperature to the other. (b) The reweighted FES obtained at 2700 K is compared with a rescaled curve from 3200 K using different sampling intervals; the curve becomes smoother as the sampling increases.

The reliability of the temperature reweighting method is verified by evaluating the FES associated with the crystallization of β-cristobalite from silica melt, as shown in figure 6.19. The rescaling procedure was applied at both temperatures using 3 μs of simulations, from 1 to 4 μs at 3200 K and from 7 to 10 μs at 2700 K. These results show that the temperature reweighted FES (from 3200 K to 2700 K) reproduces well (within the simulation error) the FES directly obtained from the WTMetaD simulation at 2700 K, even though with a larger error. The same is true if we convert the FES at 2700 K to 3200 K, confirming the reliability of this approach.

The roughness and the error of the rescaled FES from 2700 K to 3200 K (red curve) in figure 6.19 (a) is higher than that of the rescaled FES from 3200 K to 2700 K (blue curve) because of the poorer sampling performed at lower temperature, 2700 K, and for the large fluctuation of the associated weights. Longer simulations are needed to better sample the phase and make the curve smoother, as observed in figure 6.19 (b). Because it is expected that the roughness of the rescaled FES increases with an increase of the temperature gap, the gap should not exceed 500 – 600 K to avoid undesired artifacts.

6.6. Effect of box dimension

In real materials, homogeneous nucleation occurs stochastically in the bulk of the melt, leading to the formation of several critical nuclei that grow until they impinge on each other to form polycrystalline materials or glass-ceramics. The observation of the whole process in computer experiments would require extremely large simulation models with at least millions of atoms, which are too expensive for MetaD simulations. Because much of the scientific interest is addressed to the formation of critical nuclei, such as CNT, it is worth investigating the initial process of nucleation. In principle, crystallization should be investigated using simulation boxes much larger than the critical nuclei, but this is not always possible since the critical dimensions strongly depend on the materials and in silicates can range from a few angstroms to nanometers (197). Nevertheless, it is thus important to investigate the effect of the system dimensions on the MetaD results. The FES is expected to change with box dimension since both the intensity of the diffraction peaks used as CV and the melting temperature varies as shown in chapter 4.2.1.1 for the lithium disilicate.

6.6.1. Size effect on XRD pattern and melting temperature

The XRD pattern was calculated on boxes with different sizes. Figure 6.20 shows the XRD patterns obtained by averaging the MD-NPT simulations for 2 ns at 2000 K for the simulation boxes containing 192, 648, 1536, 5182, 12288 and 24000 atoms. The main peaks shift toward lower angle and augment their intensity with an increase of the box size. The peak associated to the (111) plane (the one used to bias the simulations) does not vary for systems containing more than 5000 atoms, whereas the other two peaks reach convergence with the larger boxes.

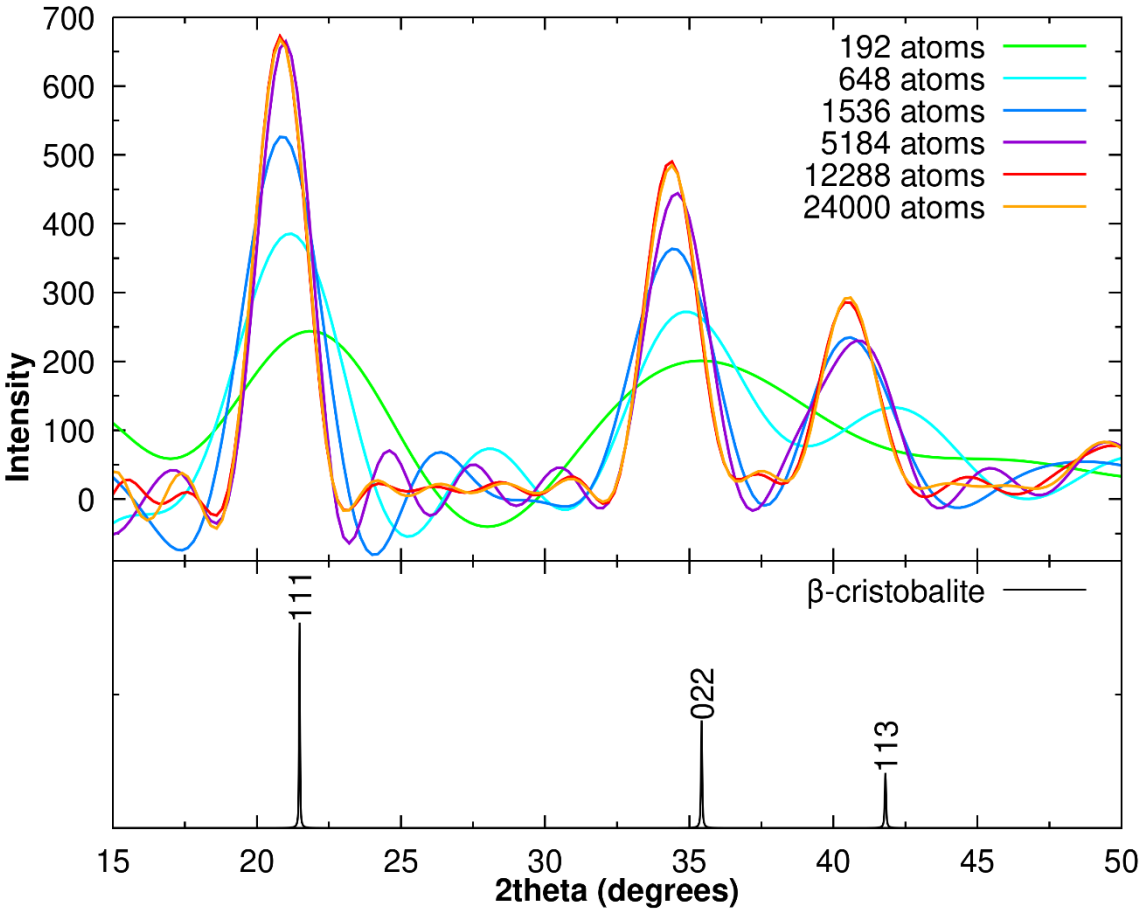

FIG. 6.20. XRD pattern collected during MD run of simulation boxes containing different numbers of atoms compared to perfect β-cristobalite in the plot below.

To investigate how the melting temperature changes system dimension we used the phase coexistence method as proposed by Dozhdikov et al. (160,163) and described in chapter 4.2.1.

The starting configurations were built as rectangular parallelepipeds with z-dimension around 3 times larger than the x and y-dimensions. We replicated the β-cristobalite unit cell 2x2x7, 3x3x8, 4x4x14 and 5x5x20 obtaining simulation boxes with respectively 672, 1728, 5376 and 12000 atoms. Resulting T_m are plotted against box dimensions in figure 6.21.

Figure 6.21 shows that the melting temperature also varies with the simulation box dimension. T_m decreases as the system size increases, until it reaches convergence at around 2670 K. According to this result, it is expected that the FESs might be dependent on the simulation size if the same temperature is assumed. It is thus important to determine the computational melting temperature with the simulation size according to the force field to define the choice of the temperature in the MetaD simulations.

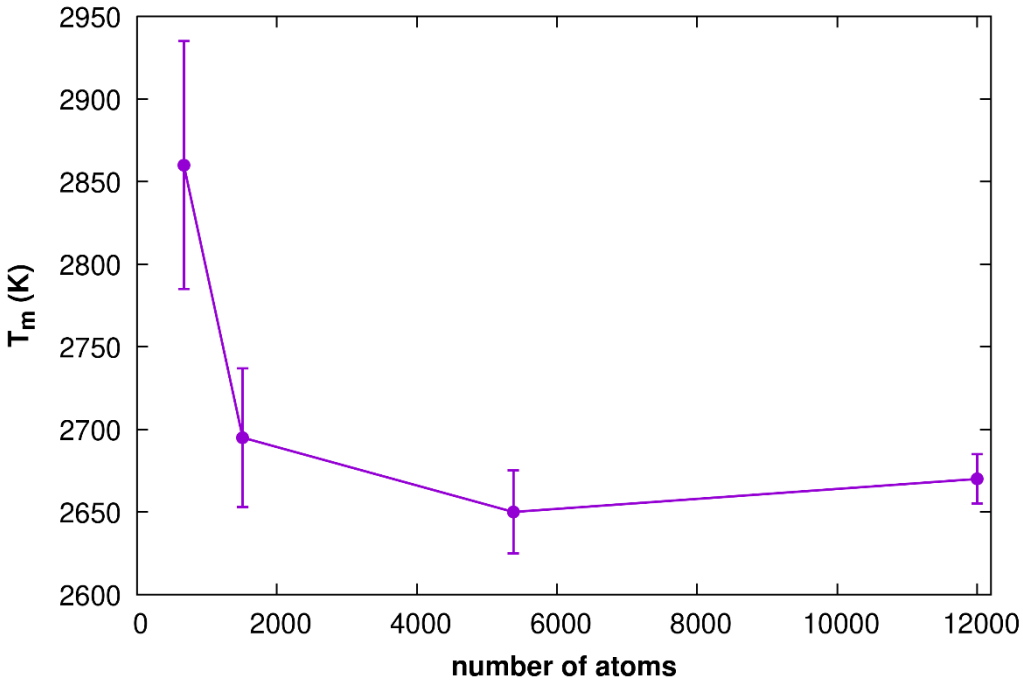

FIG. 6.21. Calculated melting temperature versus system size for silica using the two-phase coexistence method.

6.6.2. Comparison of simulations

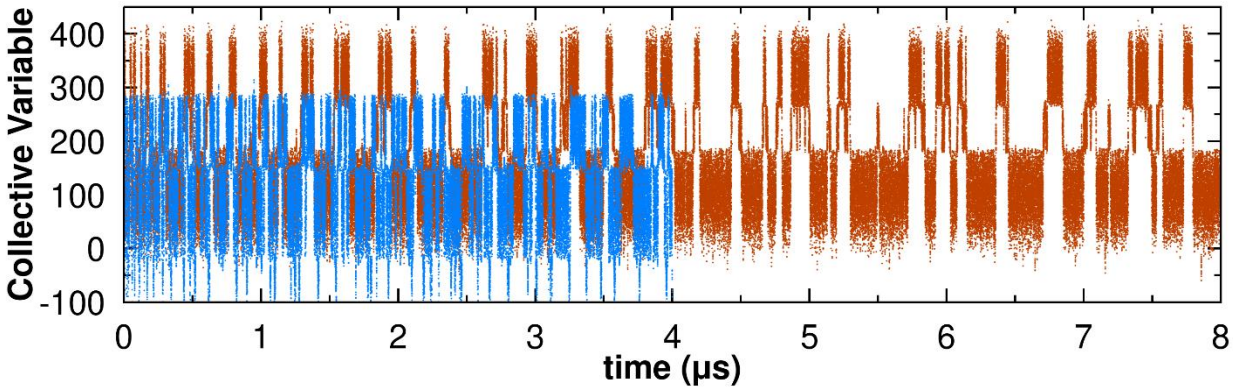

FIG. 6.22. Time evolution of the collective variable during 4 and 8 μs of metadynamics simulation of experiment n° 4 (ω = 60, γ = 50, σ = 2) at 3200 K using a box containing respectively 192 (blue dots) and 648 atoms (orange dots).

Figure 6.22 compares the time evolutions of the biasing CV for MetaD simulations conducted at 3200 K using the parameters set of n° 4 (ω = 60, γ = 50, σ = 2) on the systems with 192 and 648 atoms. The transition frequency decreases, increasing the box size. This is because the increase of the number of atoms augments the accessible configurational space, and, therefore, the complete crystallization of the entire simulation box becomes more difficult. Consequently, longer simulation times are required at the same temperature to obtain the converged FESs with 648 atoms (4 μs) with respect to the system with 192 atoms (1-2 μs).

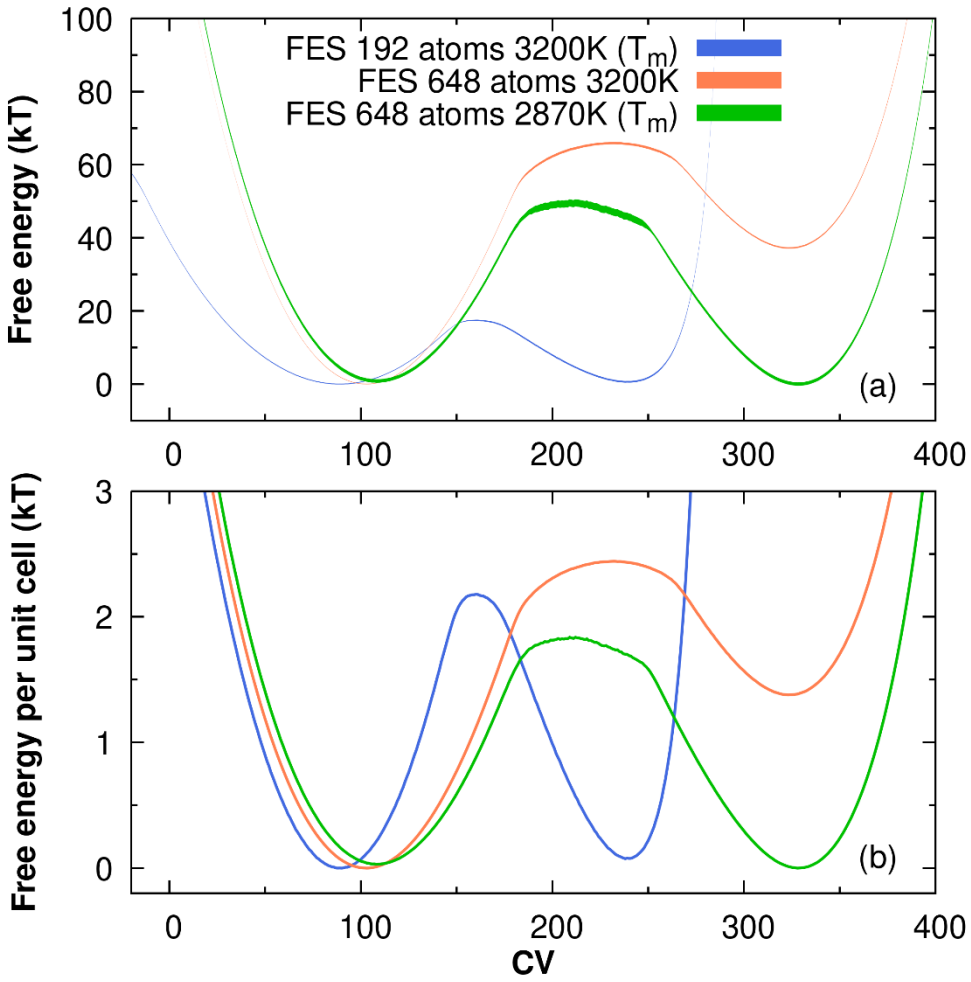

FIG. 6.23. (a) Comparison between FES at 3200 K and at the respective melting temperatures of boxes containing 192 (3200 K) and 648 (2870 K) atoms; (b) FESs normalized by the unit cell number.

Figure 6.23 (a) shows the two FESs computed at 3200 K and at the respective melting temperatures of the 192 (3200 K) and 648 atomic (2870 K) systems. As expected, the energy barrier for crystallization increases with box dimensions from 17 to 66 kT. This implies that different bias factors should be used depending on the simulation size. In the previous sections, we showed that the bias factor of γ = 50 was optimal for the MetaD simulations with 192 atoms at 2700 K, but not at 3200 K. Indeed, the simulations at 3200 K converged faster (1 µs) with the lower bias factor (simulation n° 7, ω = 60, γ = 20, σ = 2). The bias factor of γ = 50 seems to be the best choice for the system with 648 atoms at 3200 K. Contrarily, at lower temperature, T_m = 2870 K, this value is not optimal since the frequency of the transition jumps becomes too low to reach convergence. To accelerate the exploration of the phase space, we had to increase γ to 150.

The normalization of the FESs with respect to the number of the SiO_2 unit cells (figure 6.23 (b)) produces curves with comparable energy barrier, which allows us to make a rough estimation of the barrier height of the bigger system. By assuming the activation energy of ~2 kT per unit cell, we predict a barrier of 130 kT for the system containing 1536 atoms. Indeed, for the larger system, a bias factor of at least 150 or more was used to obtain enough crystallization events, as seen in figure 6.24.

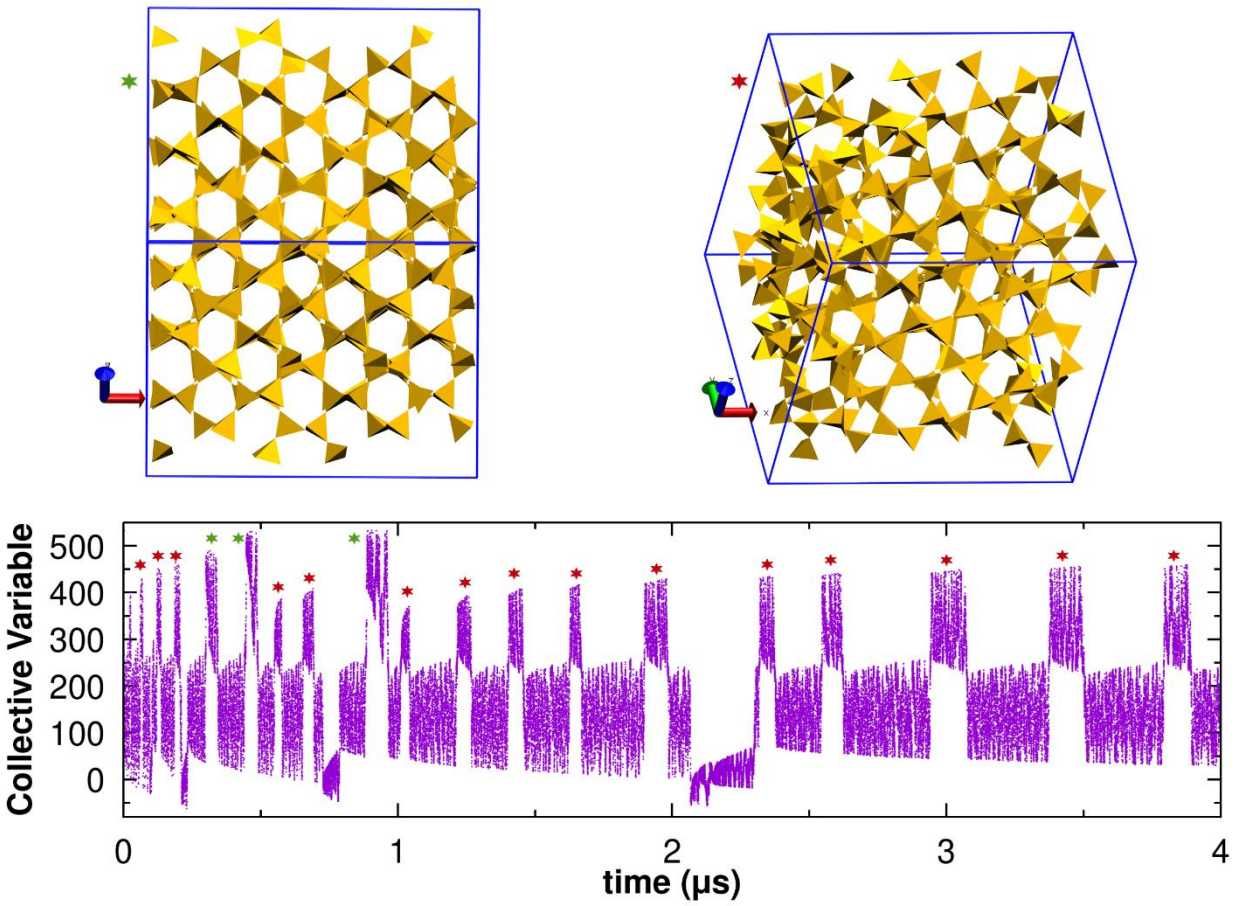

FIG. 6.24. Time evolution of the CV during the WTMetaD simulation with parameters ω = 60, γ = 250, σ = 2 at 3200 K with the system containing 1536 atoms.

Despite a sufficient re-crossing frequency, most of the jumps (red asterisks in figure 6.24) correspond to incomplete crystallization. In fact, the perfect crystal is obtained only when the CV value reaches 400 units (green asterisks in figure 6.24). Therefore, higher bias factor and longer simulation times are necessary to reach converged FES for the larger systems. For instance, the MetaD simulations of 4 μs for a system of 1536 atoms took 27 days on an Intel Xeon 6230 processor (2.10 GHz) with 20 cores. Such a substantial computational cost limits both system size and simulation time.

Although it is difficult to evaluate the converged FES including the complete crystallization path for the larger simulation systems, it is possible to understand the variations of the free energy with the crystal nucleation of n atoms ($F(n)$) owing to the sufficient sampling of various configurations. To determine $F(n)$ the sampled configurations have been reweighted along the cluster dimension n using the same procedure proposed by Niu et al. (140). The local entropy fingerprint was used to identify crystal-like silicon atoms in the structure (see section 3.2.6.3 for its definition) (136,198). The average local entropy ($\bar{s}_s^i$) was calculated only on silicon atoms (i) considering in the computation silicon neighbors (j-atoms) within a cutoff R_{max} = 6.00 Å, with a broadening σ_s = 0.2 Å and averaging within R_a = 3.75 Å. This parameter is able to discriminate the liquid state from the crystalline state and figure 6.25 shows the distributions of the local average entropy obtained during 2 ns of MD run of each system.

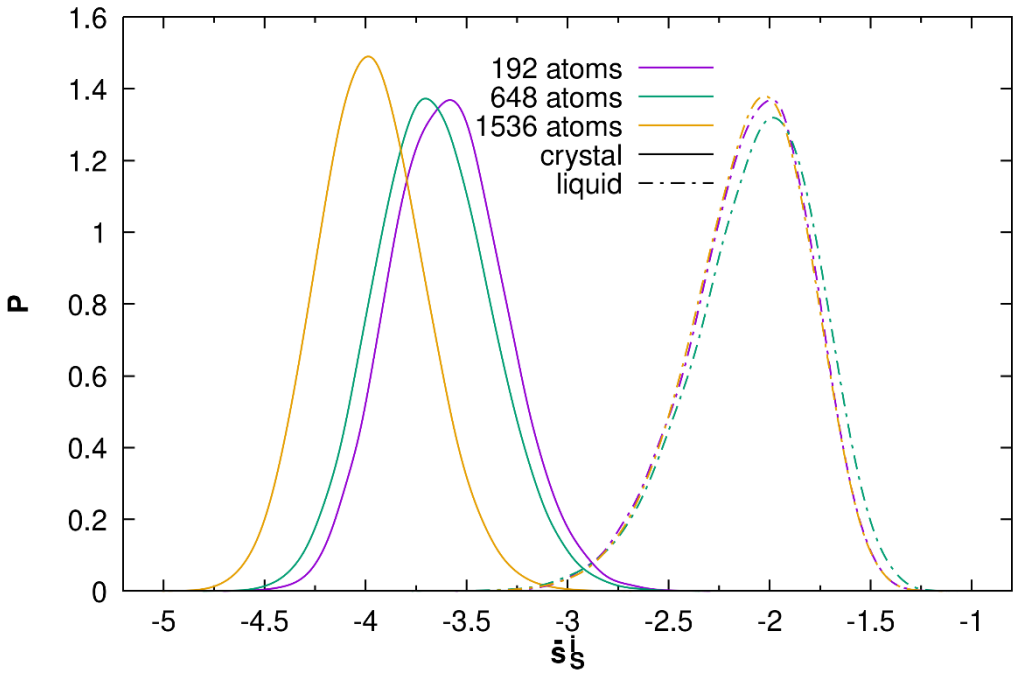

FIG. 6.25. Probability distributions of the average local entropy $\bar{s}_s^i$ of Si atoms considering in the computation (as atoms *j*) only silicon atoms using cutoff radius R_{max} = 6.00 Å, σ_s = 0.2 Å and R_a = 3.75 Å. Systems investigated are crystalline and liquid structure in three different dimension boxes.

We computed the adjacency matrix among those crystal-like atoms, and then the depth first search algorithm (199) was used to identify clusters and count the number of silicon atoms in them. As shown in figure 6.26, FESs were evaluated as a function of n atoms. The free energies (at two temperatures, 3200 K and 2870 K) for the systems with 648 and 1536 atoms were calculated up to a critical value of n (n_c), which corresponds to the largest cluster size to avoid self-interaction of the nucleus (113 and 268 atoms, respectively) (140).

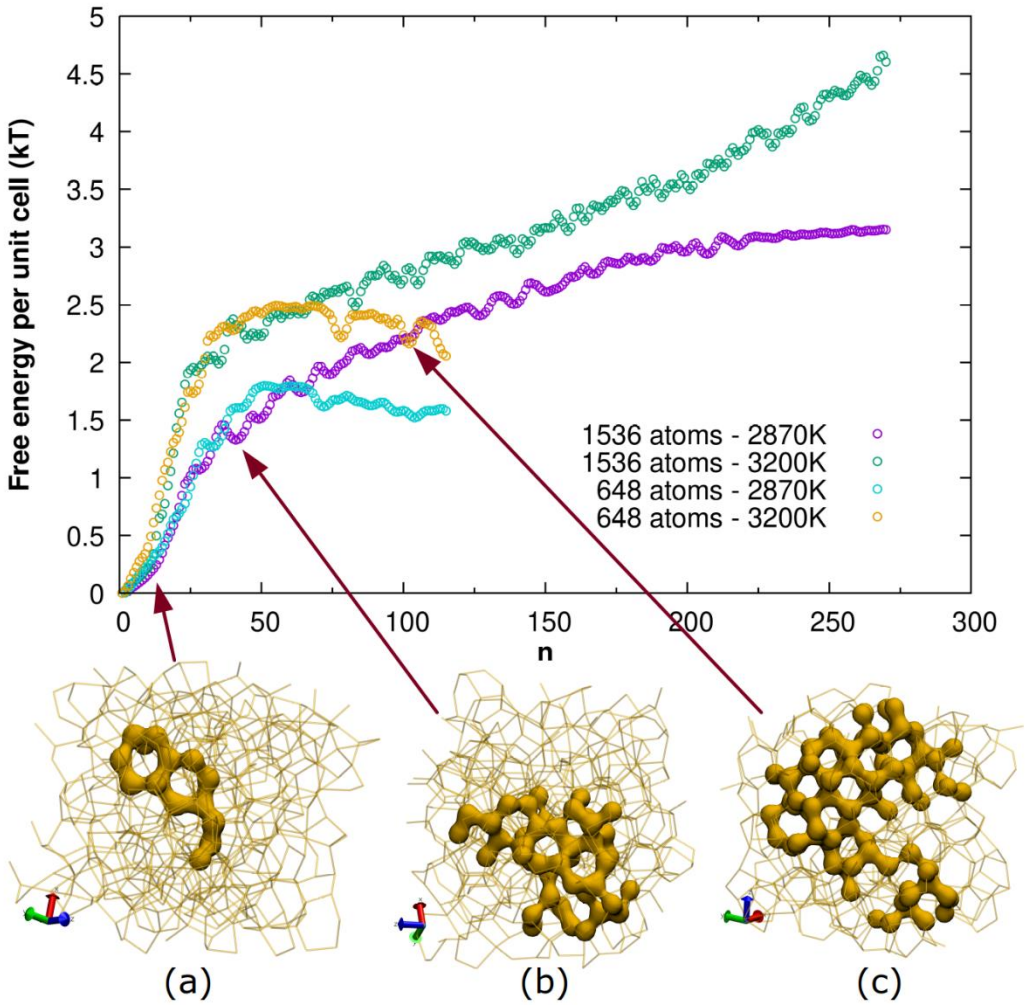

FIG. 6.26. Reweighted free energy per unit cell as a function of cluster size in terms of n° of silicon atoms. The free energies at 3200 and 2870 K computed using the systems with 648 (216 Si atoms) and 1536 (512 Si atoms) atoms are compared. Snapshots (a)-(c) show structures containing a cluster with 15, 42 and 108 Si atoms. In these figures, only Si atoms are shown to highlight the order inside the structures.

The free energy curves at the same temperature are almost the same until 55 and 75 Si atoms at 2870 K and 3200 K, respectively, implying that the initial formation of the crystalline nucleus is independent of the system size. After that, the crystal sizes varied in different ways: the crystalline structures appearing in the larger system steadily kept increasing, while those in the smaller systems plateaued and then decreased. This is clearly a system size effect. $F(n)$ of the small system reaches a maximum and then decreases, as expected from CNT, but the critical nucleus is found to depend on the system size.

In CNT, the free energy is given by the formula 2.2, and it is reported here as a function of the number of particles in the crystalline nucleus n:

$$\Delta G(n) = -\Delta\mu\, n + \gamma_{sl}\, n^{2/3} \tag{6.4}$$

where $\Delta\mu$ is the chemical potential variation associated to melt-crystal phase transition, and γ_{sl} is the interfacial energy. When cluster size is small enough, the free energy for nucleation should follow a 2/3

power low since the interfacial energy dominates. However, this is not true for our observations on the free energy curves at 2870 K up to n ~ 20 Si atoms. At the very beginning of the nucleation where n is less than 20, the free energy variation does not seem to follow the CNT prediction. Subsequently, at n > 20, the slope of the free energy curve increases more quickly up to n = 55 – 60 Si atoms. Figure 6.26 (a) shows that a few 6-membered rings form the initial embryo, whereas the larger clusters shown in figure 6.26 (b) and (c) are made up by 6-membered rings interconnected to form the β-cristobalite crystal. Therefore, it seems that the energy required to form crystalline nuclei whose size is larger than a critical size is not dominated by the formation of the 6-membered rings (which were indeed observed in the melt and in the glass structure) (200,201) but by the interconnection of these rings and their rearrangement along the right directions to form the perfect crystalline structure. Note that the initial slope of $F(n)$ at small n values is steeper at 3200 K compared to 2870 K, implying that even the formation of embryos is more difficult at higher temperature.

6.7. Summary

In this chapter, we systematically investigated the effects of the simulation conditions to efficiently study thermodynamics of silica crystallization into β-cristobalite using MetaD simulations. First, we investigated the influences of the height (ω), width (σ) and bias factor (γ) used to define the biasing Gaussian potential. After that, the effects of the simulation temperature and system size were examined.

Here is a summary of the results:

- Among the Metadynamics parameters (ω, σ and γ) the height value has only a minor effect on the final FES and the time to reach converged results. The width, σ, is effective to obtain converged FES. The appropriate value of σ depends on the fluctuation amplitude of the CV during conventional MD simulations: a half or a third of the fluctuation is a good choice. Too low or too large σ values prevent the convergence. The bias factor γ is the most important parameter; it substantially affects the time to reach convergence. A higher bias factor gives a higher re-crossing frequency, but it leads to depositing a large amount of bias and then exploring high energetic configurations, which do not take part in the transformation. On the other hand, too low values require long simulation to reach the quasi-static regime. This parameter should be chosen in the same magnitude as the crystallization barrier. Unfortunately, this is not known as a priori, and, thus, its estimation is the most difficult step.

- Temperature is another important parameter to study crystallization within a reasonable computational time. At $T > T_m$ the high mobility of the ions allows a fast exploration of the FES, which provides frequent observations of phase transitions. This allows convergence to be reached in significantly shorter time. Consequently, by increasing the temperature the optimal bias factor decreases. We also demonstrated that for high viscous systems such as silica the reliable FES at or below T_m can be estimated through temperature rescaling procedures.

- Size effects were observed for XRD patterns and melting temperature. Consequently, the FES depends on the simulation system size. However, the main characteristics of the FES representing the mechanism of crystallization are maintained.

- A large enough model would be necessary to observe the crystal growth until a real critical size, but the computational cost is too expensive. Even if the FES is not converged, the MetaD simulations provide useful information to understand the mechanism of crystal formation. To do so, a larger bias factor is efficient for the larger simulation models. The lower bound of the bias factor can be estimated from the barrier height for crystallization using smaller systems.

- By analyzing the free energy for nucleation of crystalline clusters as a function of their size, we found that the 6-membered rings form the initial embryos of nucleation. The energy penalty for the cluster formation steeply increases with an increase of the cluster size. The growth of the initial embryos is followed by structural rearrangements to build up the ideal crystalline structure.

Chapter 7. Metadynamics on lithium disilicate

In chapter 5, we approached the crystallization of lithium disilicate using molecular dynamics. We observed that in a glass with the stoichiometry of $Li_2O{\cdot}2SiO_2$ there is a preference for the nucleation of lithium disilicate crystalline phase ($Li_2Si_2O_5$) in the bulk, while on the surface, we found embryos of lithium metasilicate crystal (Li_2SiO_3). Moreover, we could extract an estimation of the nucleation free energy of the two phases mentioned, with the critical radii.

However, the information provided by the MD approach is not complete, since there are many aspects that are left aside. The mechanism of nucleation is not detectable due to the high viscosity and low mobility of atoms. Also, the approximation of the shape of the crystalline nucleus may limit the investigation of the nucleation free energy. We can overcome these limitations and get answers to unsolved questions by using enhanced sampling techniques.

In the last chapter, we have investigated the effect of the parameters used in Well-Tempered Metadynamics simulations (WTMetaD) on the Free-Energy Surface (FES) of the crystallization of β-cristobalite from fused silica. In this chapter, we demonstrate the applicability of this technique to a more complex layered binary silicate system, which is lithium disilicate.

7.1. Collective variables and order parameters used

7.1.1. Choice of XRD peaks

To choose appropriate biasing CVs, we have run unbiased MD simulations of the crystalline lithium silicates and the LS_2 glass at 300 K and 1500 K. According to the simulations, the XRD spectra were computed to find distinguishable peaks of the models, as shown in figure 7.1. The XRD spectra with all atoms (Si, O and Li) and those with only Si atoms were compared in this figure. The employment of the subset of atoms is more efficient since it reduces the computational cost required to compute the CVs, allowing us to simulate larger systems, which is mandatory in crystallization studies. An appropriate biasing CV must distinguish the phases formed along the reaction path that one wants to investigate.

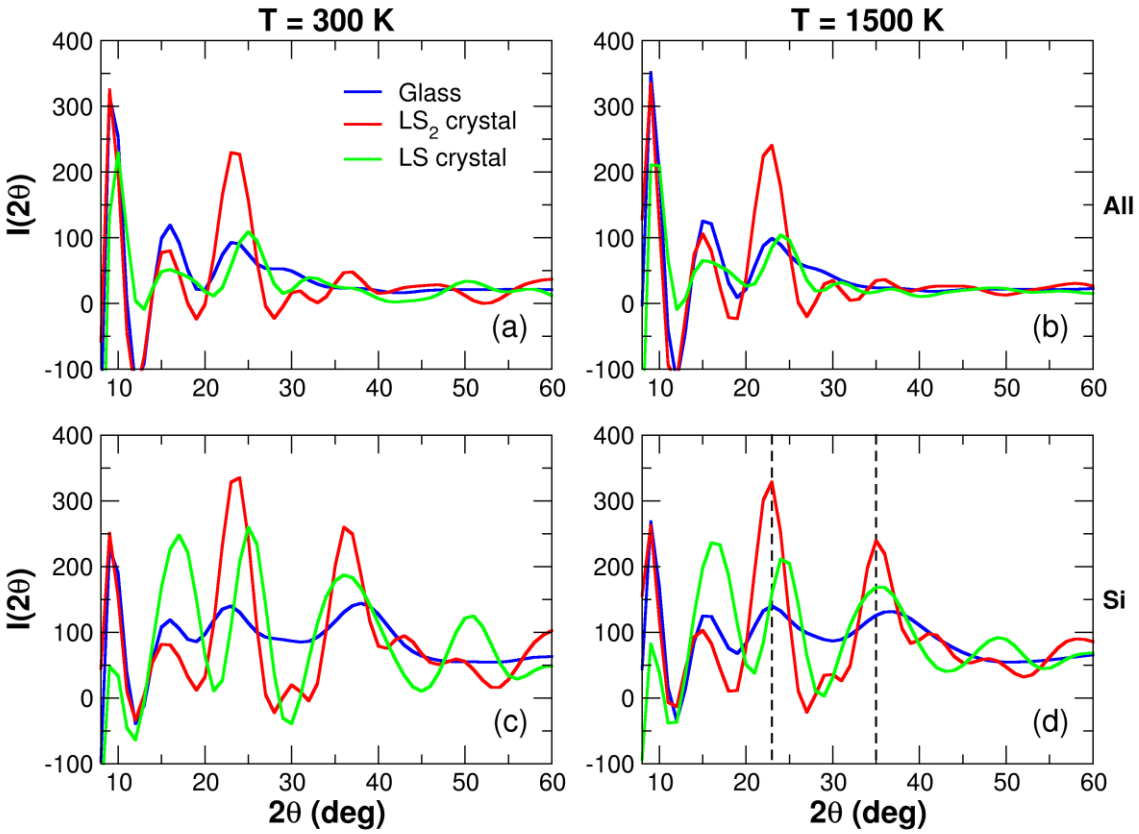

FIG. 7.1. XRD spectra of the investigated systems (LS_2 glass, LS_2, and LS crystals) computed considering all atomic species or only Si atoms in the simulation box computed along 0.5 ns of unbiased MD simulations at 300 K and 1500 K. The XRD spectra are averaged along the MD trajectory.

Only the peak at 2θ = 23° shows a significant difference between the melt and crystalline phases if all atoms are considered in the calculation of the XRD pattern, while several peaks have different intensity considering only Si. Clearly, the peak intensity reduces with temperature, but a huge difference is conserved. The peak at 2θ = 23° (associated to the plane (040), see figure 7.2) seems the most appropriate to distinguish phases at both temperatures, and the other peak at 2θ = 35° (associated to the plane (002), see figure 7.2) can also complement the distinction between the different phases. At 1500 K, the XRD peak $I(2\theta = 23°)$ computed using only Si atoms distinguishes better the LS_2 (330) crystal from the LS_2 glass (140) and LS (160) crystal (the intensity values of the XRD peaks are reported in the parenthesis).

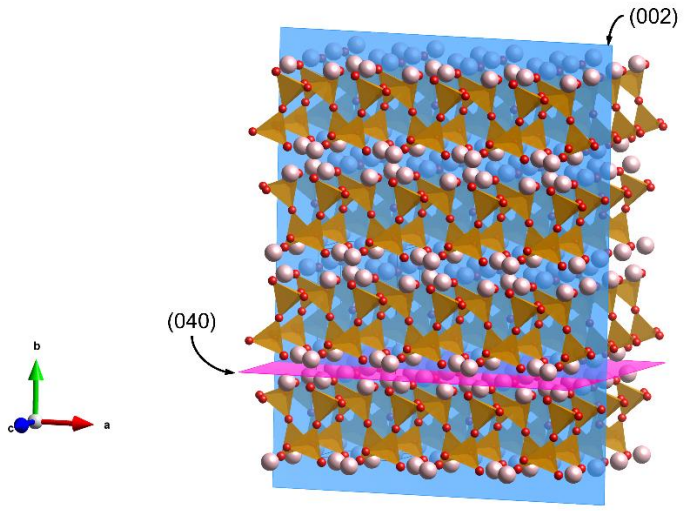

FIG. 7.2. The (040) and (002) planes of the LS_2 crystal are shown.

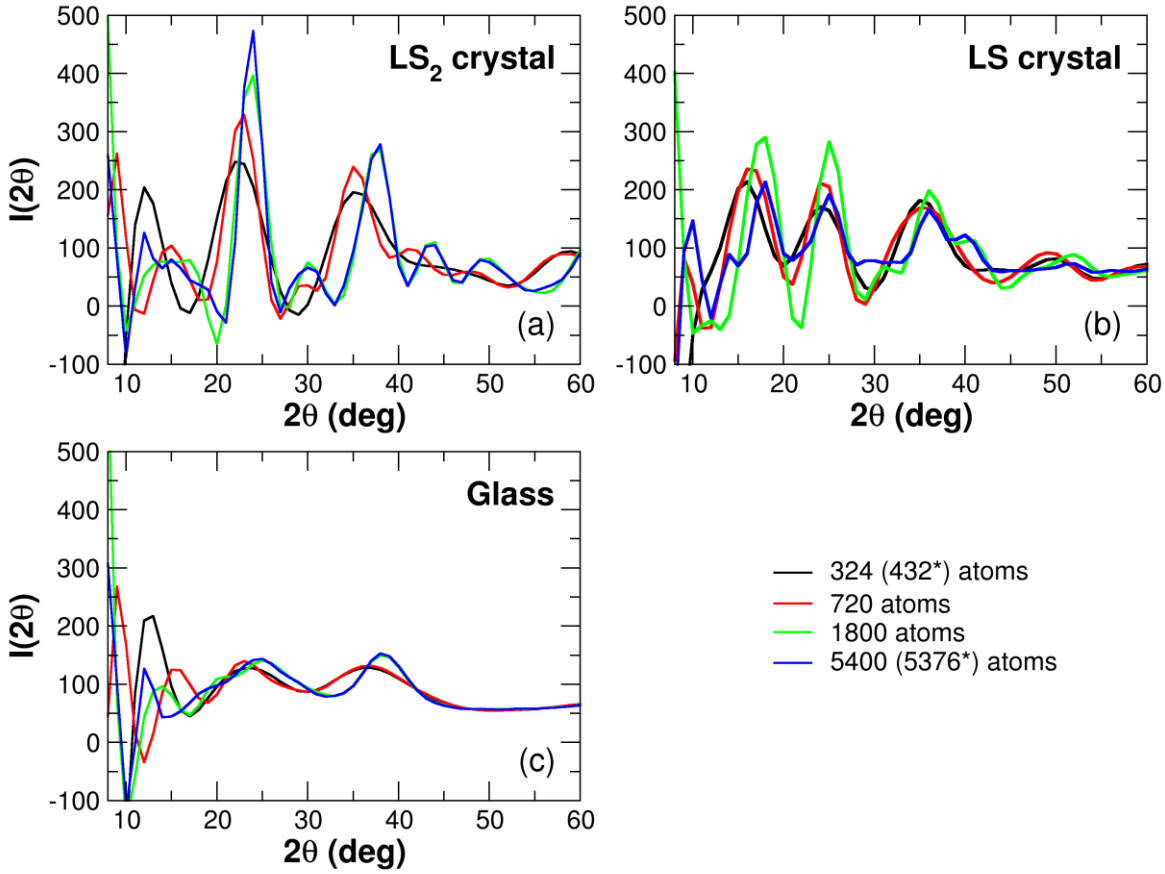

FIG. 7.3. XRD pattern computed using only Si ions of the LS_2 glass, LS_2, and LS crystals of different sizes (from 324 to 5400 atoms) at 1500 K. The symbol "*" indicates a different number of atoms for the LS crystal.

Figure 7.3 shows the XRD spectra computed considering only Si atoms of the investigated systems comparing different sizes at 1500 K to verify the size effect. The XRD spectra present more intense and sharp peaks for larger systems. The only exception is for the LS crystal whose spectrum of the bigger model at 1500 K shows that the system is melting ($T > T_m$, paragraph 4.2). There is a shift of the main peaks at

higher degrees for the LS_2 crystal. Anyway, the systems containing 720 atoms reproduce accurately the peaks at 2θ values larger than 15° (the peaks at lower values are strongly affected by the system dimension as expected) preserving all main information. When a larger system is investigated, the choice of the peak must be adjusted according to the corresponding XRD pattern.

To decide the width of the Gaussians, we evaluated the standard deviation of the CV distribution obtained from an unbiased MD run. For $I(23°)$ the LS_2 crystal and melt phases we obtain respectively 4 and 6 CV units, for $I(35°)$ the standard deviation is 4 and 5 CV units respectively for LS_2 crystal and melt.

7.1.2. Order parameters

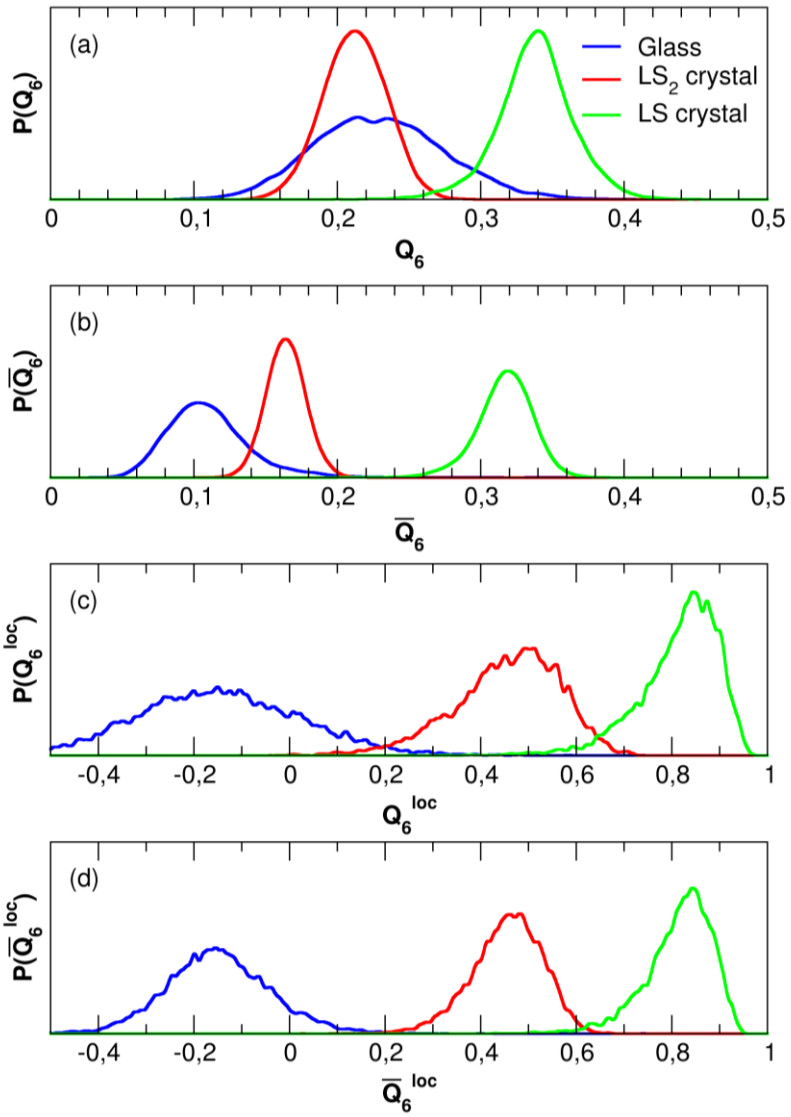

FIG. 7.4. Probability distributions of the Q_6, local Q_6^{loc}, average $\bar{Q}_6$ and local average $\bar{Q}_6^{loc}$ parameters of silicon ions in the LS_2 glass, LS_2, and LS crystals at 800 K. These parameters have been computed considering only silicon ions in the coordination sphere of the central Si ion using R_1 = 6 Å and R_2 = 3.75 Å.

The Steinhardt parameters, presented in chapter 3.2.6.2, were tested to distinguish between the crystalline and glass phases. The most satisfying parameters were obtained using l = 6, calculated on Si ions. The

probability distributions of these parameters in the LS_2 glass, LS_2, LS crystals at 800 K are reported in figure 7.4.

The figure shows that using as cutoffs R_1 = 6 Å and R_2 = 3.75 Å the individual Q_6 parameter is not able to distinguish the glass to the LS_2 crystals whereas the other parameters can distinguish the glass to the LS_2 and LS crystals. Silicon ions exhibit well-separated $\bar{Q}_6^{loc}$ distributions approximately ranging between (-0.4 to 0.2), (0.2 to 0.63), and (0.63 to 1) for the glass, LS_2, and LS crystals, respectively, without significant overlapping. That means that the local structure around each silicon ion can be assigned to one of them.

7.2. Computational details

All simulations were performed using the Large-scale Atomic/Molecular Massively Parallel Simulator (LAMMPS) package (191) patched with the open-source, community-developed PLUMED library (192,193), version 2.5 and 2.6. The Nosé-Hoover (194) thermostat and barostat have been used to perform the MD simulations in an NPT ensemble. The relaxation time for the temperature was set to 0.1 ps, while the relaxation time for pressure was 10 ps with a target pressure of 1 bar. The pairwise PMMCS interatomic potentials developed by Pedone et al. (114) have been employed, using the Wolf summation method to treat long range coulomb interactions (123). The short-range interactions were evaluated with a cut-off distance of 5.5 Å. The equation of motion was integrated using the Verlet algorithm (181) with a timestep of 2 fs. For detailed descriptions see chapter 3.1.

In the following paragraphs are presented several WTMetaD applications at different temperatures, box dimensions and mainly different numbers of CVs. In chapter 7.3, the use of one CV is presented using a box containing 720 atoms in a range of temperature between 1500 K and 2000 K. The CV is the intensity of the peak at 2θ = 23° and the bias is constructed by accumulating Gaussians every 1 ps with width of 2 CV units and height of 40 kJ/mol with a bias factor of 200. In paragraph 7.4 two CVs are employed: they are respectively the intensities of the peaks at 2θ = 23° and 35°. Two box dimensions are investigated with 720 and 1440 atoms respectively at 1800 K. The Gaussians used to accumulate the bias potential are deposited every 1 ps and have a width of 2 and 4 CV units, respectively along the first and second CVs, the height is 100 kJ/mol and the bias factor depends on the box dimension employed: 200 for the 720-atoms containing box and 300 for 1440-atoms containing box.

7.3. Results using 1 CV

From the physical point of view, the melt to crystal transition process should be investigated at the melting temperature or below it since crystallization is thermodynamically favored for undercooled liquids.

The thermodynamic melting temperature of lithium disilicate determined using the coexisting phase method (160,163) described in detail in chapter 4.2 is estimated to be 1200 ± 50 K, which is in fair agreement with

the experimental value of 1307 K (8). However, as shown in figure 7.5, the mobility of silicon species in the timeframes of tens of nanoseconds of MD simulations is extremely low at this temperature, hampering the efficient sampling of the free energy surface (FES) of the system.

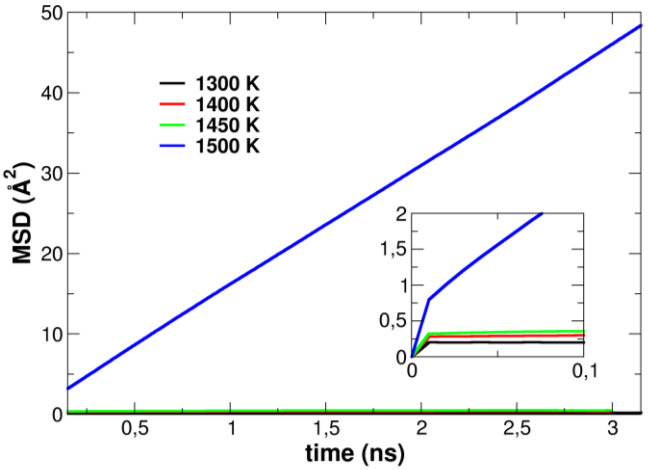

FIG. 7.5. MSD of Si ions in an unbiased MD simulation of LS_2 crystal containing 5400 atoms at 1300, 1400, 1450 and 1500 K.

To overcome this computational issue, we have performed the WTMetaD simulations at 1800 K for 28 μs and then performed a temperature rescaling to 1200 K, as described in detail in the theoretical section 3.2.5 and tested in the case of silica in chapter 6.5.

Thereby, in this work, the simulation model with about 720 atoms was used to evaluate the FES. Note that the melt-crystal transition from the LS_2 melt to the LS_2 crystal can also be observed for the larger models; however, the transition frequency was limited and not enough to obtain converged FES.

7.3.1. Free energy surface calculation

The evolution of the CV of four simulations at different temperatures, 1500, 1600, 1800 and 2000 K, is compared in figure 7.6. The CV varies between two regions, between 0 and 250 and between 250 and 400, approximately, that correspond to the melt and crystalline phases, respectively. Several jumps between the liquid and crystal phases were observed during the simulations at any temperature. The frequency of the transitions increases at higher temperature, but the persistence of crystalline structure shortens because at higher temperature the crystalline structure is less stable than the melt one. Contrarily, at lower temperature, the crystal phase persists for a longer period since the crystal structure becomes more stable. However, as anticipated above, the jump frequency reduces with temperature decreasing because of the reduced silicon diffusivity. Therefore, longer simulations are required to accurately explore the FES at lower temperature. We focus on the simulation at 1800 K, which is shown for the entire 28 μs of simulation in figure 7.7.

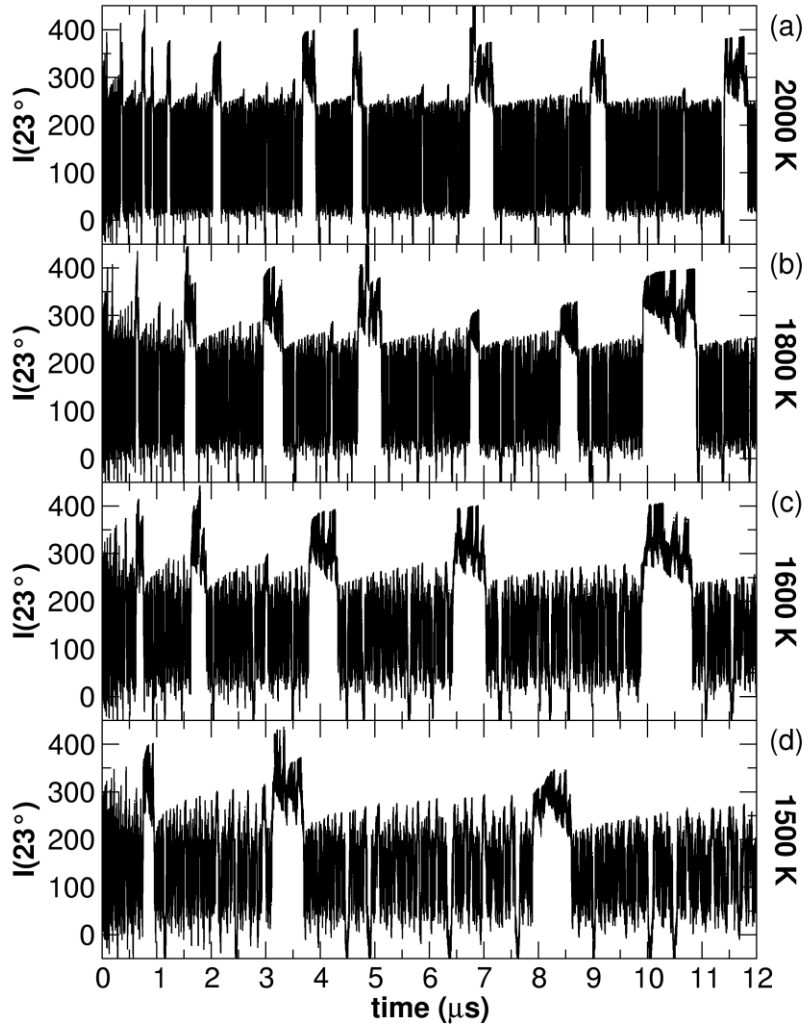

FIG. 7.6. Evolution of CV, the intensity peak at 2θ = 23°, during 12 μs of WTMetaD simulations at four different temperatures.

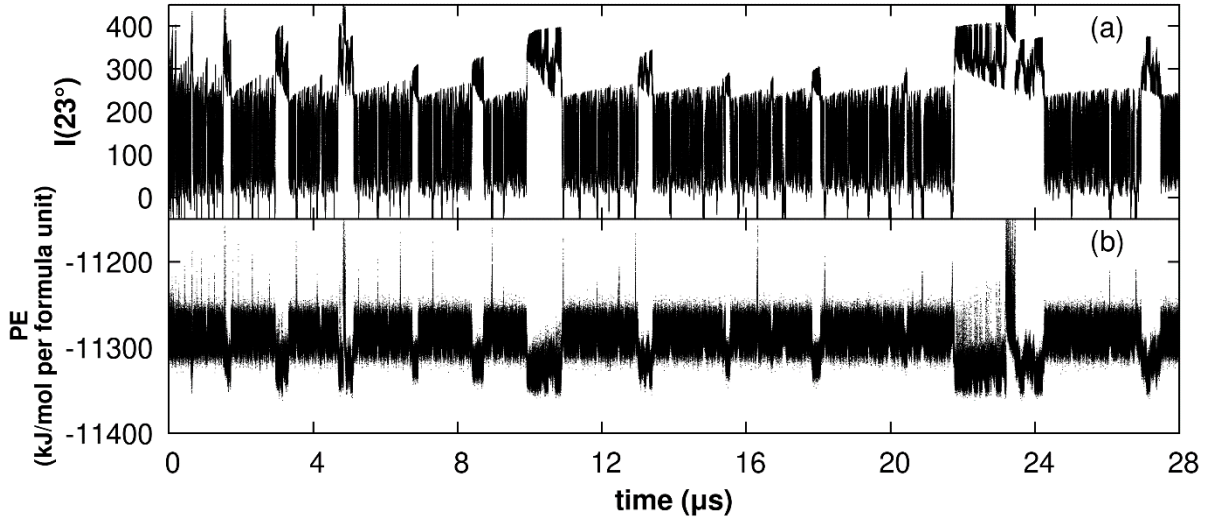

FIG. 7.7. Panel (a) reports the evolution of the intensity peak at 2θ = 23° and panel (b) reports the potential energy both along the 28 μs of WTMetaD simulations at 1800 K biased by 1 CV.

As shown in figure 7.7 (b), the potential energy decreases when $I(23°)$ corresponds to the value of the LS_2 crystal, implying that the jumps of the CVs effectively represent the melt to crystal transitions. This is also confirmed by visual inspection of the simulations and the analysis of the local order parameters that will be presented below.

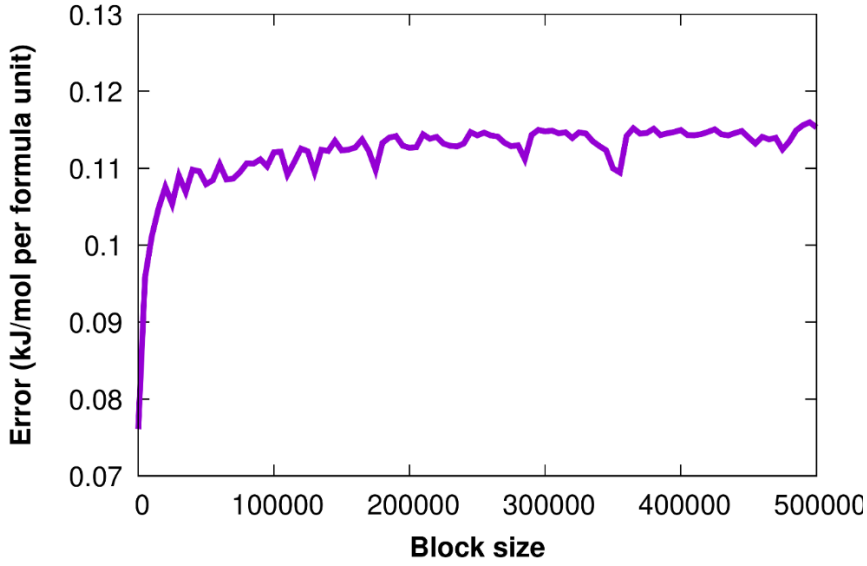

FIG. 7.8. Estimation of the error associated to the FES at 1800 K of the lithium disilicate system through the block analysis.

The block analysis, described in chapter 3.2.4, performed on the WTMetaD at 1800 K reported in figure 7.8 confirms that the simulation has reached convergence (error of 0.11 kJ/mol per formula unit). The FES is calculated using the reweighting procedure proposed by Tiwary et al. (150) and it is reported in figure 7.9.

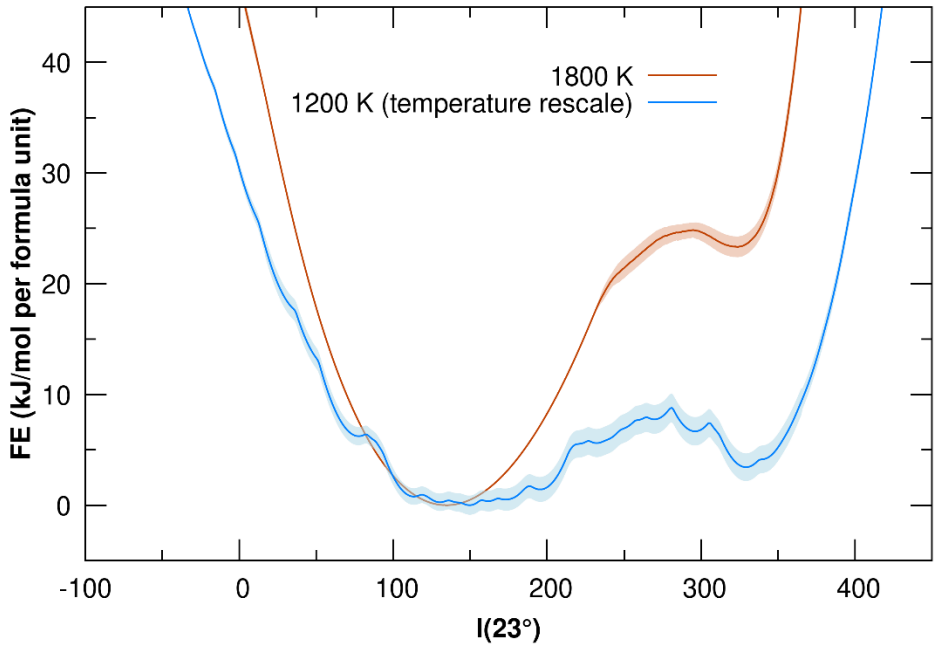

FIG. 7.9. Reweighted FES along biased $I(23°)$ at 1800 K, FES at 1200 K computed with a rescaling of the temperature from the simulation at 1800 K. The shadow region indicates the error associated with the curve.

The FES possesses a large minimum centered at $I(23°)$ = 130, associated to the melt state, and a shallower minimum centered at $I(23°)$ = 325 corresponding to the LS_2 crystal. As expected, the error is higher in the region of the crystal, because of a poorer sampling. In the same figure, the FES at 1200 K is presented and it is obtained from a temperature rescaling procedure from the simulation at 1800 K. The chosen temperature is the melting temperature obtained from the phase coexistence method (section 4.2); thus, it was expected to have both minima at the same value of free energy. The free energy difference between the minima significantly reduces from 1800 K to 1200 K, with the simultaneous increase of the error, obtaining a FES close to the melting temperature. Moreover, in the rescaled FES there are more minima that it is worth investigating if they are artifacts or metastable intermediates of the crystallization process. In figure 7.10 we present the evolution of both CVs ($I(23°)$ and $I(35°)$) individuated in section 7.1.1.

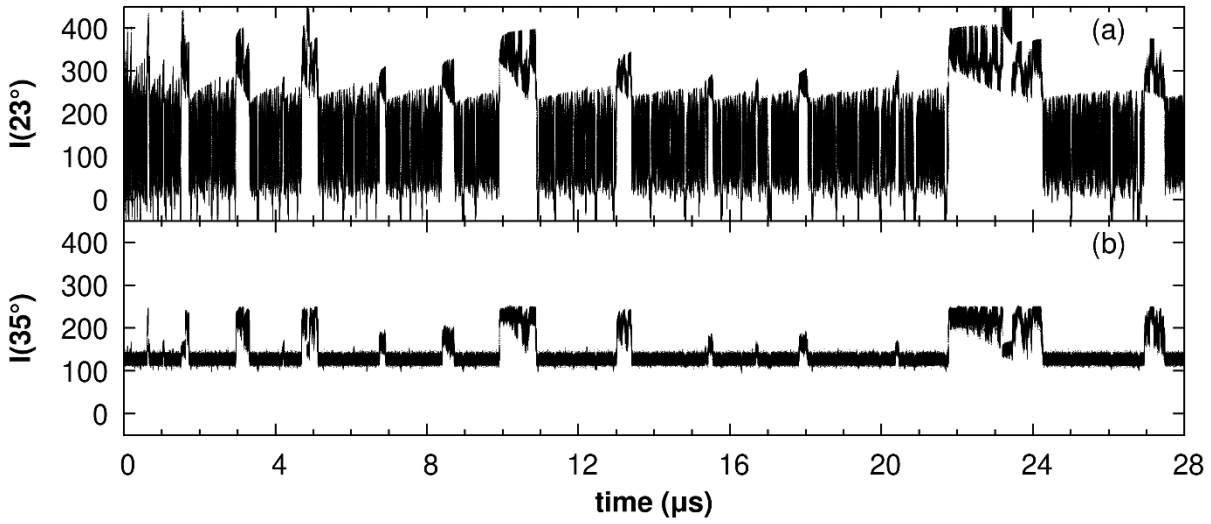

FIG. 7.10. Panel (a) reports the evolution of the intensity peak at 2θ = 23° and panel (b) reports the evolution of the intensity peak at 2θ = 35° during the 28 μs of WTMetaD simulations at 1800 K biased by 1 CV.

The variation of $I(35°)$ is less pronounced than $I(23°)$, but it captures the crystallization events by sampling higher values of this variable. The changes in the values of these two CVs are not completely correlated, since, as we can observe at 23 μs for example, when $I(23°)$ increases, $I(35°)$ decreases. To better analyze contemporary the sampling of the two variables, we apply the reweighting procedure to calculate the probability distribution along both CVs, calculating a 2D FES.

The 2D FES as functions of the biasing CV ($I(23°)$) and the unbiased second CV ($I(35°)$) at 1800 K is shown in figure 7.11 (a). The potential energy reported in figure 7.11 (b) is computed by averaging the punctual values of potential energy along the trajectory at 1800 K as a function of the two CVs and we will call it potential energy surface (PES) for simplicity. The potential energy is used to estimate the FES at 1200 K (see figure 7.11 (c)) by temperature rescaling.

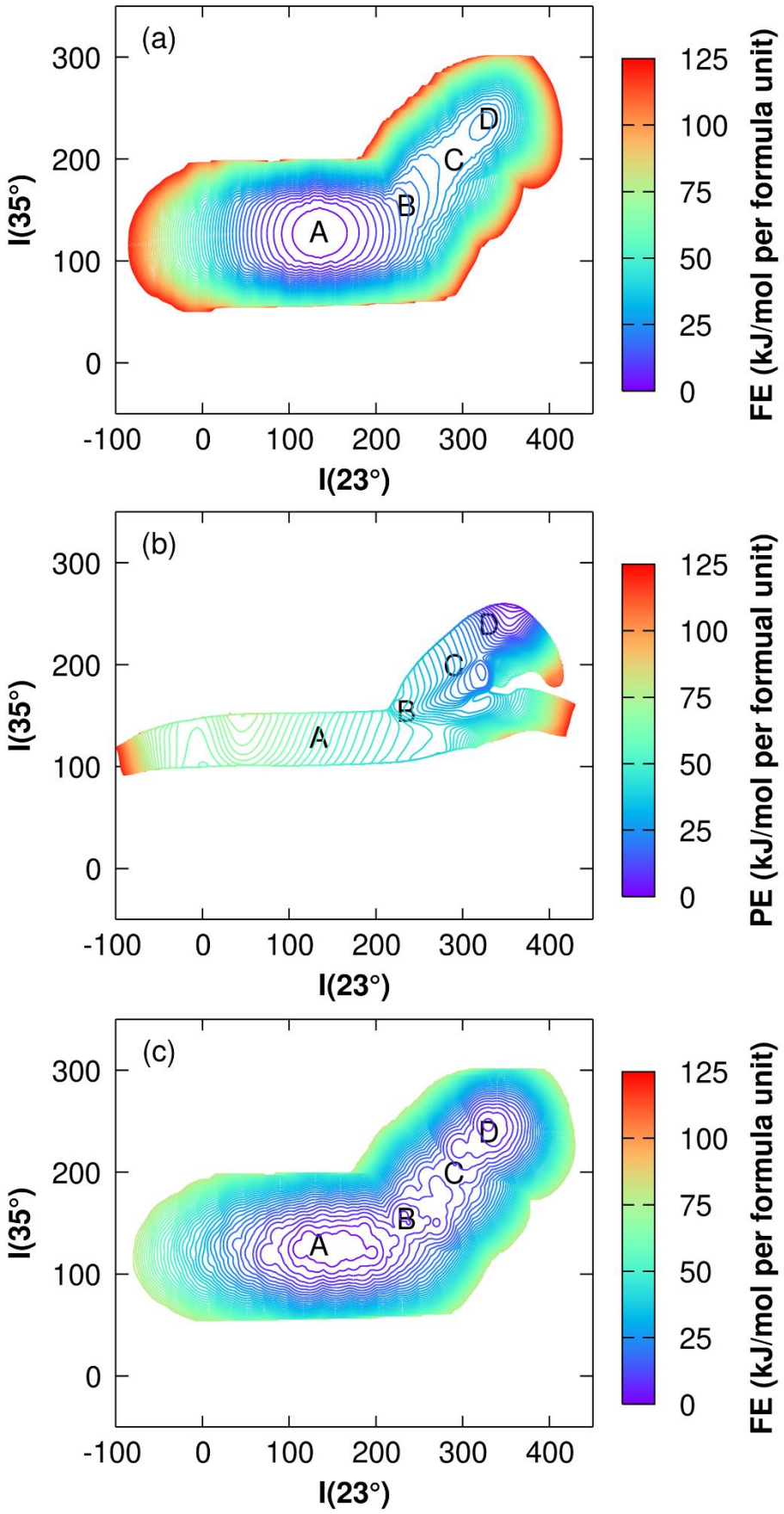

FIG. 7.11. (a) Reweighted 2D FES along biased $I(23°)$ and unbiased $I(35°)$ at 1800 K, (b) potential energy surface obtained from the simulation at 1800 K and (c) 2D FES at 1200 K computed with a rescaling of the temperature from the simulation at 1800 K.

As observed before, the FES at 1800 K possesses a large absolute minimum at $I(23°) \approx 130$ and $I(35°) \approx 120$, associated to the melt state and the other shallower minimum at $I(23°) \approx 325$ and $I(35°) \approx 250$ corresponding to the LS_2 crystal. A flexion of the FES at (240, 150) is also observed. The error of the curves is not shown here for simplicity.

The PES indicates that intermediate states form along the path from the melt to the crystal, which will become more important at lower temperatures, thanks to a low potential energy that increases the value of the weights of these configurations (see equation 3.24). Indeed, the melt state corresponds to a high potential energy region in the PES, the perfect LS_2 crystal phase corresponds to the absolute minimum whereas a second minimum at (300, 190) appears.

The FES at 1200 K shows that the minimum at the melt state does not change with temperature, whereas the FES near the crystalline state is substantially affected. The flexion of the curve at around (240, 150) unit becomes a shallow minimum whereas the crystalline minimum becomes deeper with decreasing the temperature, and the path from the melt state to the crystal becomes more structured, confirming that intermediate structure forms before the perfect crystalline structure appears.

The microstructures at the points A, B, C and D highlighted in figure 7.11 are shown in figure 7.12 and reveal that the intermediate structures from A (melt) and D (crystal) are layered disordered structures (intermediate B and C). Indeed, a few silicon atoms are displaced from the ideal positions in the LS_2 crystal. For instance, some Si ions connect the double layers or disrupt the apparent short 4T chain of the layers, as shown by the green tetrahedral units in figure 7.12 (B) and (C). Iqbal et al. (45,57) observed the formation of two LS_2 phases (α' and β') before the stable crystal. They have attributed α'-LS_2 to a structure (P_{21} space group) with a unit cell half of the LS_2 crystal, while the β' phase was more similar to the stable LS_2 but disordered. There are indeed some similarities with our results, but the XRD spectra of the phases observed experimentally show peaks absent in the intermediate phases that we found.

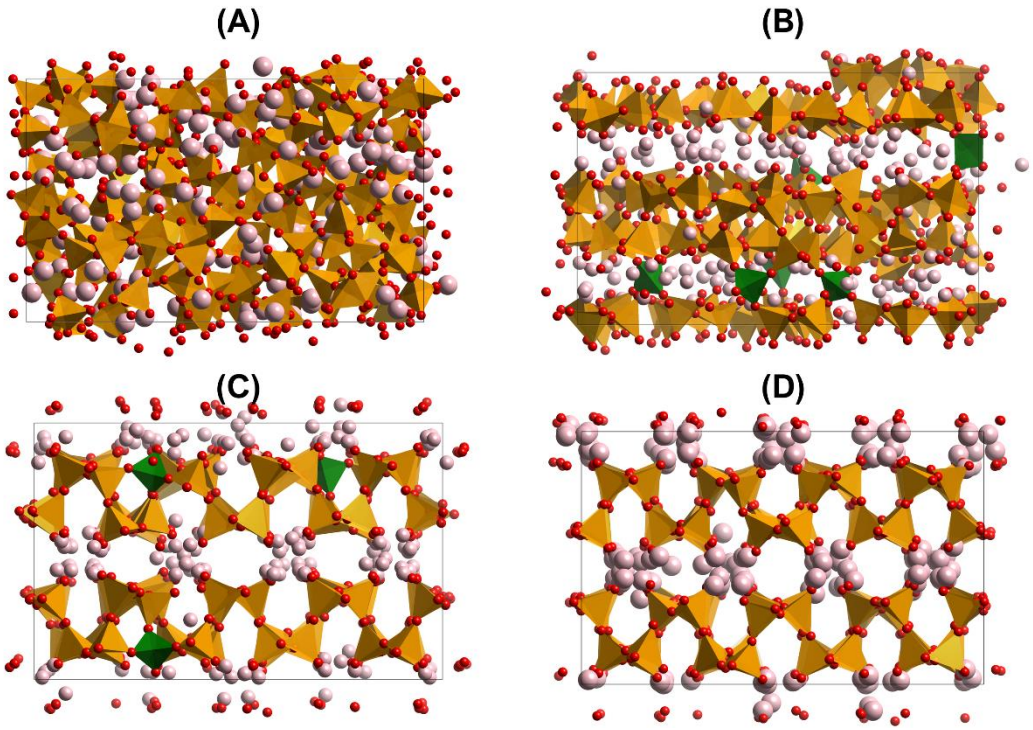

FIG. 7.12. Snapshots representative of the structure of the system at ($I(23°)$, $I(35°)$) (130, 132) (A), (240, 160) (B), (300, 200) (C) and (330, 240) (D) units extracted from WTMetaD simulations at 1800 K. Pink atoms represent lithium, red ones are oxygen while yellow and green tetrahedral are silicon.

7.3.2. Analysis of the crystallization mechanism at atomistic level

To investigate the mechanism of crystallization we have focused our attention on the WTMetaD simulations performed at 1600 K. At this temperature melt-to-crystals transitions are less frequent compared to the case at 1800 K due to the slower diffusion of the atoms, but this allowed us to better follow the sequential steps leading to the crystal formation. All the transitions reported in figure 7.13 were analysed and considered, but a representative transition is highlighted in figure 7.14.

The analysed features are the CVs discussed, intensities of the two peaks at 2θ = 23° and 35°, plot (a) in both figures; (b) is the fraction of Q^n specie of silicon ions (paragraph 1.2); (c) shows the average local Steinhardt parameter $\bar{Q}_6^{loc}$ averaged among the Si atoms in the structure (the use of Q in Q^n species has not to be confused with the Q_6 Steinhardt parameter); (d) is the population of silicon ions with local structure similar to melt, LS_2, and LS crystal (defined using the average $\bar{Q}_6^{loc}$ Steinhardt parameter) with the intervals defined in section 7.1.2. The (e) plot, only present in figure 7.13, represents the evolution of dimension of the two largest crystalline clusters in the simulation box.

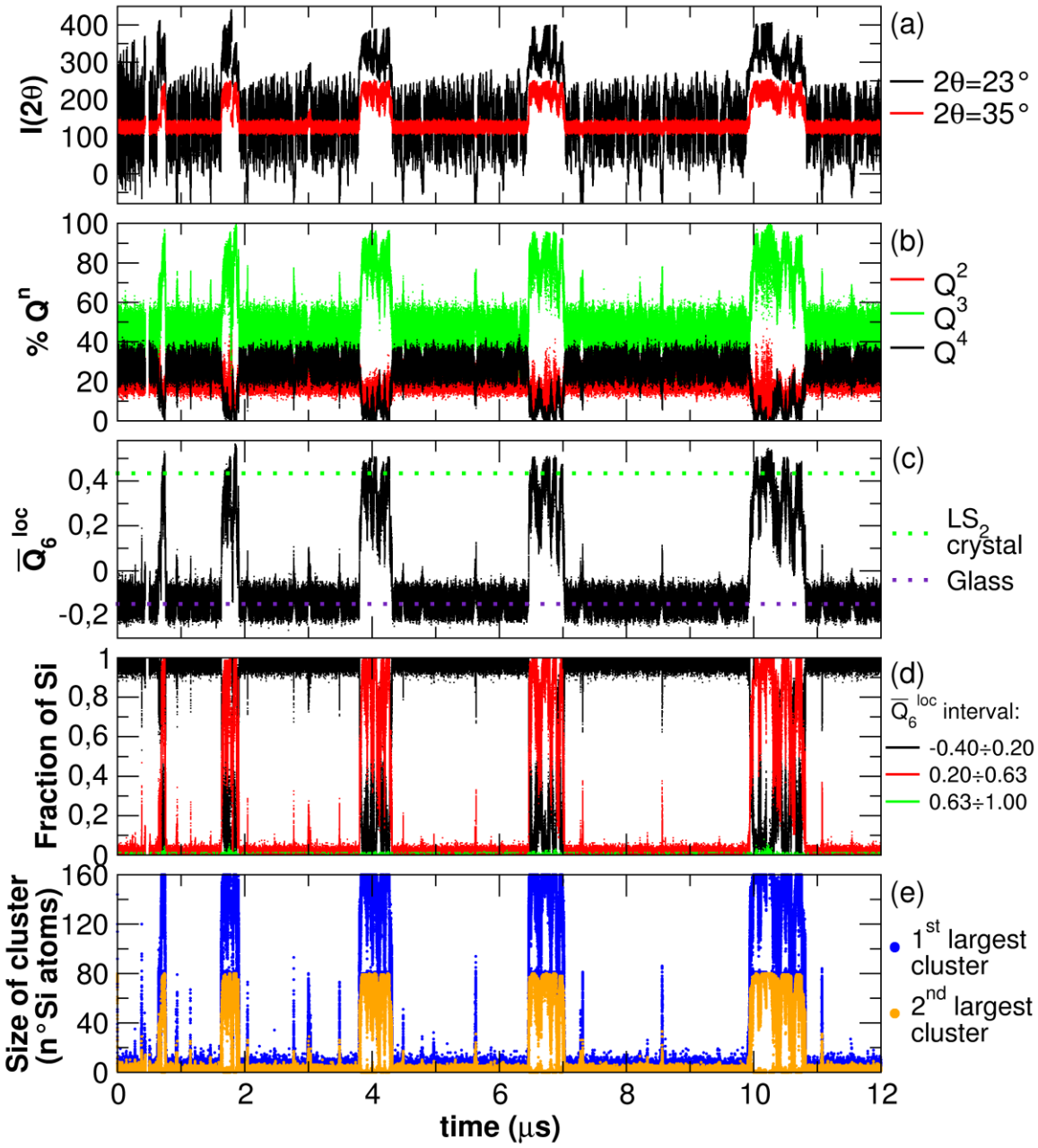

FIG. 7.13. Evolution of different parameters along all the simulation at 1600 K: (a) $I(23°)$ and $I(35°)$, (b) distribution of Q^n specie of Si, (c) $\bar{Q}_6^{loc}$ averaged over all Si atoms, (d) distribution of the Si ions with LS_2 melt, LS_2 and LS crystal-like environments determined using $\bar{Q}_6^{loc}$ and (e) size of the two largest LS_2 crystal-like clusters of Si ions. In the last panel the peaks not corresponding to the LS_2 crystal formation are associated with phase separated high energy structures generated outside the minimum energy crystallization path and thus not discussed here.

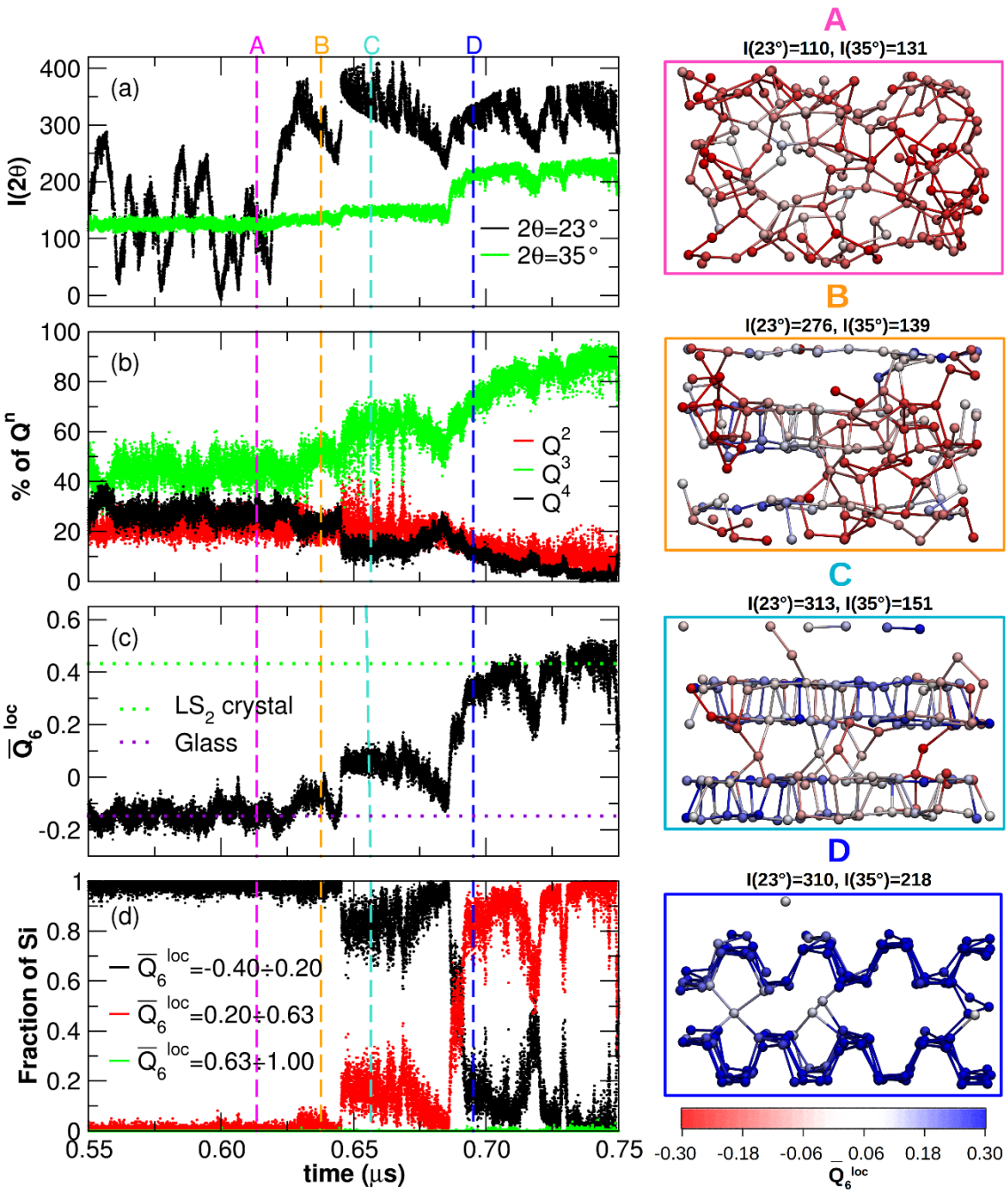

FIG. 7.14. Evolution of (a) $I(23°)$ and $I(35°)$, (b) distribution of Q^n specie of Si atoms, (c) $\bar{Q}_6^{loc}$ averaged over all Si atoms and (d) distribution of the Si ions with LS_2 glass, LS_2 and LS crystals-like environments determined using the local average $\bar{Q}_6^{loc}$ Steinhardt parameter during WTMetaD simulations at 1600 K. The analysis has been performed between 0.55 and 0.75 μs of the trajectory for clarity. On the right are reported the structures extracted from the simulation corresponding to the points indicated with the dashed line in the left graphs. Only Si atoms are shown and colored according to their value of $\bar{Q}_6^{loc}$.

Figure 7.14 highlights the first melt to crystal transition of the simulation at 1600 K (from figure 7.13), between 0.55 and 0.75 μs. According to the $\bar{Q}_6^{loc}$ parameter (figure 7.12 (d)), almost all the silicon is in the melted condition up to 0.62 μs. At around 0.62 μs, $I(23°)$ (plot (a)) suddenly increases to about 250 – 300 units. Simultaneously, the percentage of Q^3 species (plot (b)) as well as the $\bar{Q}_6^{loc}$ value averaged over all silicon ions (plot (c)) starts to increase. In addition, the ratio of silicon ions with an environment similar to

the LS_2 crystals increases to 10 %, implying that a critical crystal nucleus appears in the melt and starts to grow. Interestingly, $I(35°)$ is still fluctuating around the value close to that assumed in the melt up to 0.65 µs, indicating that the crystal nucleus is still disordered, and it needs to cross another energy barrier to become ordered. In other words, metadynamics simulations explore a variety of intermediate states during the melt-to-crystal transition. Several representative snapshots of the structures of (A) the melt state, (B) an initial nucleus, (C) a layered but disordered structure, and (D) an almost perfect LS_2 crystal are displayed in the right panels of figure 7.14. In these snapshots, only silicon ions are displayed in color representing the $\bar{Q}_6^{loc}$ value.

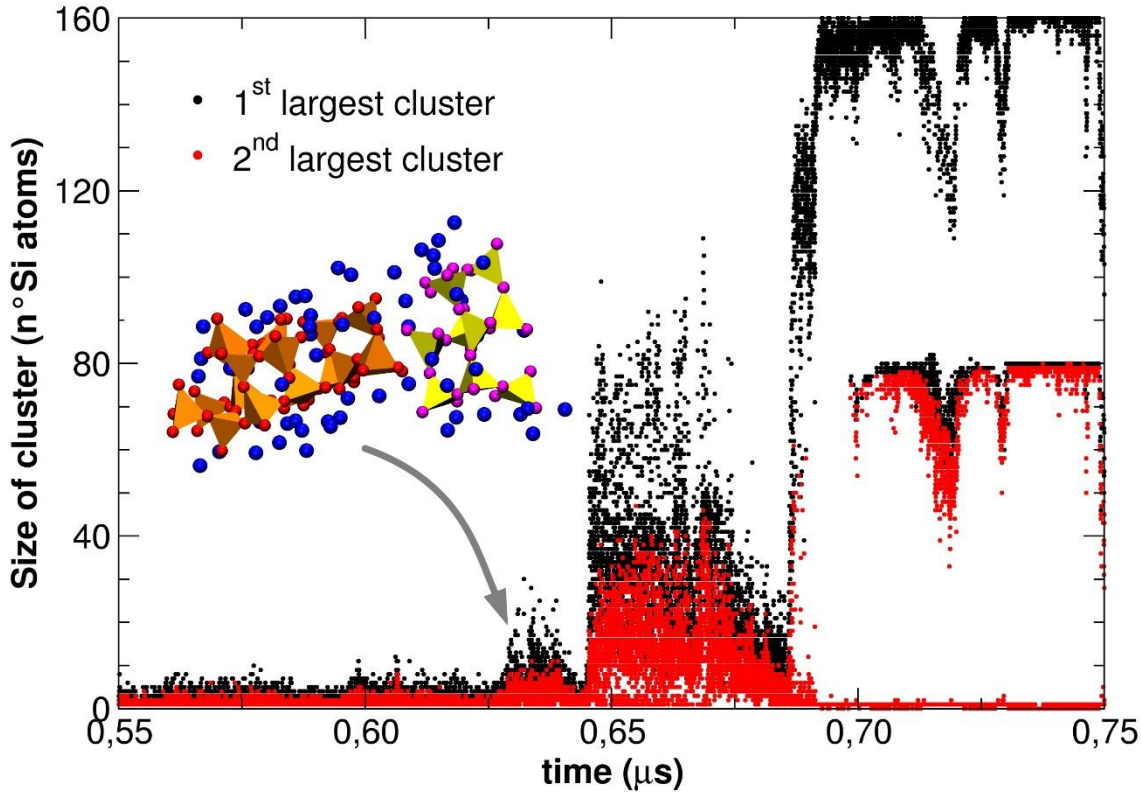

FIG. 7.15. Evolution of the size of the two biggest LS_2 crystal-like clusters of Si ions along a crystallization event during WTMetaD simulations at 1600 K. The insets show the structure of the first (orange tetrahedral, 18 Si atoms) and second (yellow tetrahedral, 10 Si atoms) larger clusters found, Li ions are shown as blue spheres.

To measure the crystal-like cluster size along the WTMetaD simulations, we computed the adjacency matrix between Si ions with LS_2 crystal-like $\bar{Q}_6^{loc}$ values and used a Depth First Search algorithm (199) to find the number of Si ions (N_{Si}) in the clusters, the same procedure has been applied on silica in paragraph 6.6.2. The sizes of the two largest clusters were evaluated, as shown in figure 7.15. The number of Si ions in the two largest clusters fluctuates around 8 – 12 at maximum in the melt state, indicating formation and dissolution of crystal-like tiny embryos, which is also in agreement with the crystalline embryos studied in paragraph 5.1.4. When the crystallization starts, around 0.62 µs, two critical nuclei with about 15 to 30 and 8 to 15 silicon appear, as shown in figure 7.15. Especially, the largest cluster seems to organize the

tetrahedral SiO_4 units in a partially layered structure topologically like that of the LS_2 crystals. The size gradually increases until about 0.65 μs, where $I(35°)$ apparently increases, as shown in figure 7.14 (a).

The second largest nucleus appears simultaneously and is located near the largest one. Then, the two adjacent nuclei coalesced each other to form a larger crystal-like structure possessing an almost complete 2T layer composed of about 40 silicon ions. At the same time, lithium ions around the nucleus (blue spheres in figure 7.15) formed layered structures and promoted the formation of the second silica layer. Consequently, the initial nucleus grows further in a stepwise fashion. After that, both two largest nuclei are enlarged with approximately 80 silicon ions, indicating that the two silicate layers are completely formed. Following the formation of two layers, the largest cluster size goes back and forth between 80 and 160, implying that some disordered silicon ions connect the two layers, as already shown in figure 7.12 (B).

According to the cluster analysis along all the simulations, the critical nucleus size contains between 20 to 40 silicon ions. This agrees well with our MD investigation exploiting the Free Energy Seeding Method described in paragraph 5.3.3 (202), which estimated the critical nucleus with 26 silicon ions. It is worth to highlight that MetaD simulations does not allow to determine the real transient time of the disordered layered structure which promotes the formation of the perfect crystal but reveals that the initial nucleus has a layered disordered structure instead of the spherical perfect crystalline one assumed in CNT.

7.4. Results using 2 CVs

Using 1 CV to drive the WTMetaD, we had access to a single nucleation path. However, we observed that to give a better description of the mechanism, we had to consider also $I(35°)$. The value of this CV changes independently from $I(23°)$, thus it can be used as CV in a metadynamics application. We investigate the crystallization pathways from the stoichiometric LS_2 glass by performing WTMetaD simulations using two CVs, both XRD peaks at 23° and 35°, in order to explore a wider configurational space. We have seen in 7.1.1 that $I(23°)$ is associates to the (040) plane and relates to the formation of layers in the structure, while $I(35°)$ associates to the (002) plane and can be an indicator to identify the ordering inside the layers as demonstrated in the previous chapter.

Two different simulations using unit cells containing 720 and 1440 atoms, respectively, were performed at 1800 K with the computational setting described in section 7.2. We want to highlight that using two collective variables, the phase space to be sampled becomes much broader than in the simulation with 1 CV. Instead of reaching convergence, we decided to use exploratory metadynamics to explore the phase space and try to find new nucleation pathways, as proposed in literature (139,142).

7.4.1. Sampling of the phase space

The simulations were run for 40 μs to ensure a proper sampling of the phase space. In the small model, from the visualization of the time evolution of the CVs in figure 7.16, we can immediately see that crystallization events were observed but there are some differences with respects to the simulation with 1 CV.

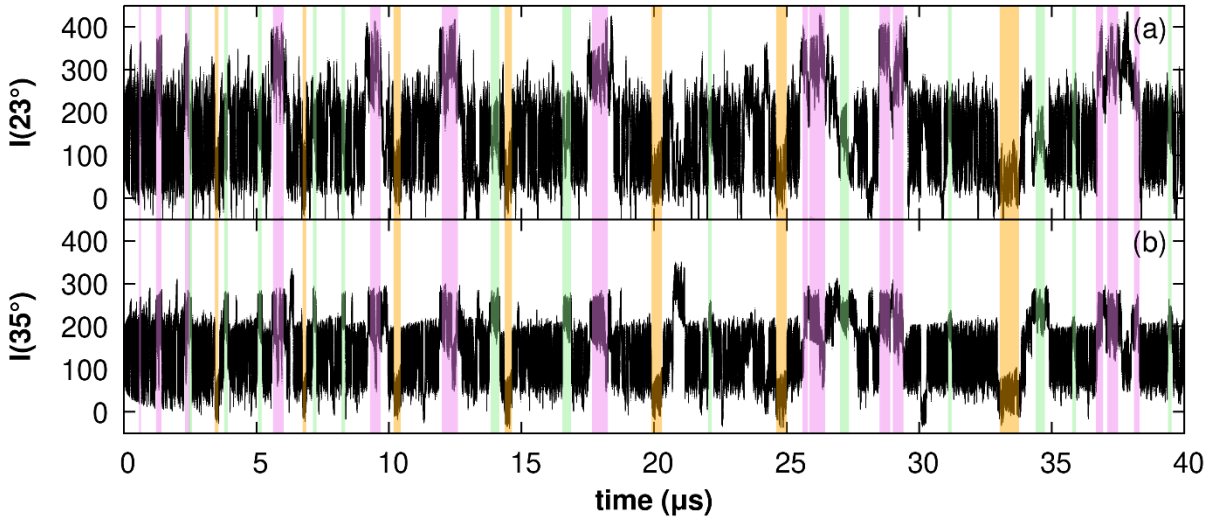

FIG. 7.16. Evolution of the CVs, $I(23°)$ (up) and $I(35°)$ (bottom), along LS_2 simulation at 1800 K using two collective variables of the model containing 720 atoms. With the colored region we identify the phases different from the melt that we observe: violet regions indicate the ordered/disordered stable crystal LS_2 phase, orange and light green regions indicate two new explored regions.

The first CV, $I(23°)$, was used also in the previous application, therefore looking at its evolution solely does not provide any further information compared to figure 7.10. Instead, $I(35°)$ phase space is explored, and it allows to identify the formation of new phases, implying that the second CV is essential to observe the extra phases. Three colors are used to highlight three distinct phase formations different from the melt in figure 7.16. Before analysing the structures associated with the highlighted phases in detail, the temporary FES is calculated and reported in figure 7.17.

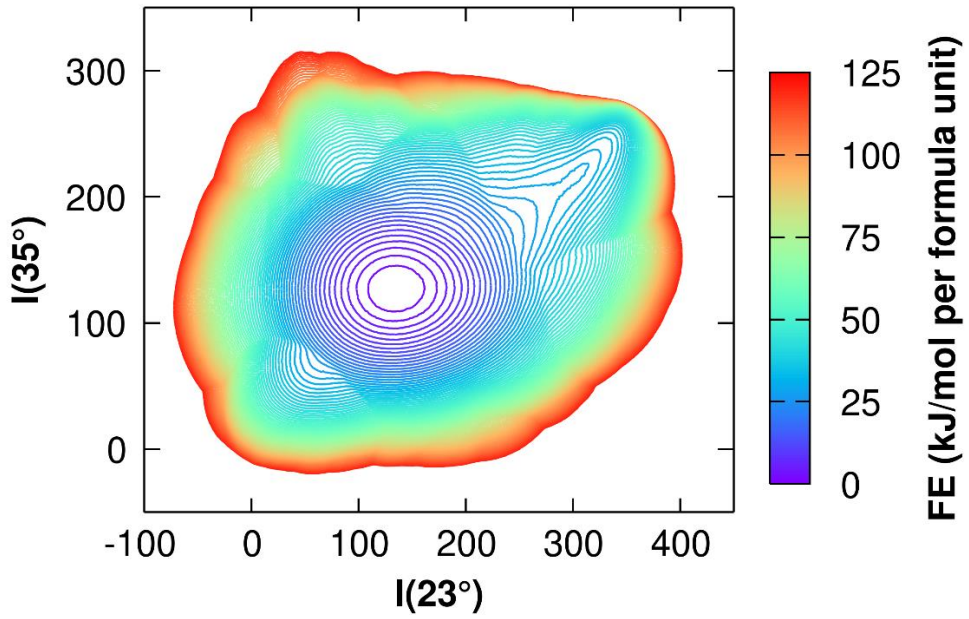

FIG. 7.17. Free energy surface of the explored phase space from the simulation of LS_2 with 720 atoms at 1800 K.

The free energy profile, FE, provided is not converged, but it is much broader and spreads a wider phase space than the case with 1 CV seen in figure 7.11. We can already see a deep minimum associated with the melt and a shoulder corresponding to the LS_2 crystalline structure. The position of the shoulder is at (305, 220), which is slightly shifted from the local minimum in the FES obtained with 1 CV. This is due to a lower sampling of the interested region and confirmed by the fact that the FES in figure 7.17 is not converged. Except for this, the FES reproduces the line-shapes obtained with 1 CV in terms of favorable nucleation pathway, and other minima are not found in the new explored region.

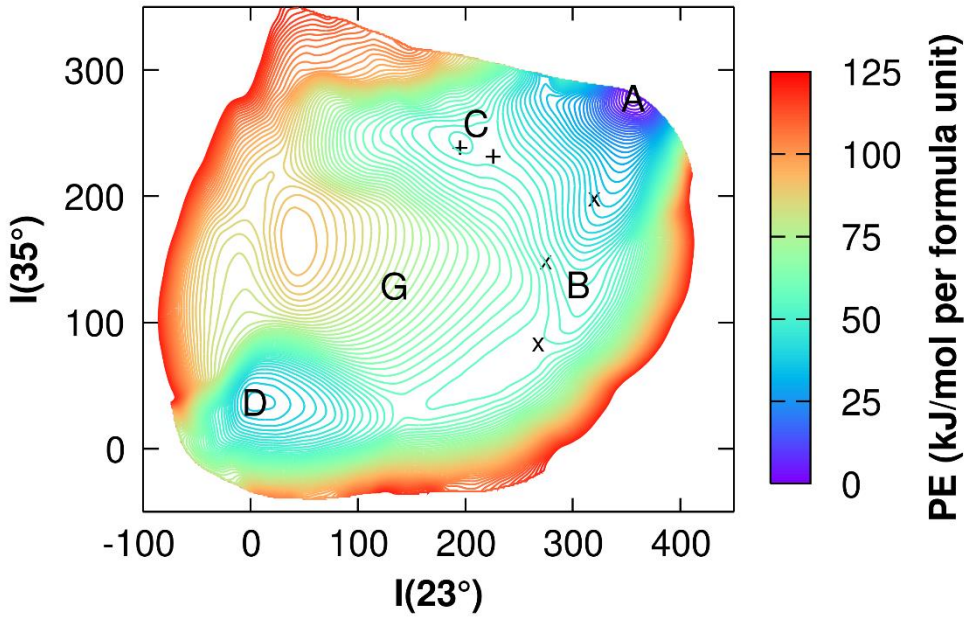

FIG. 7.18. Average potential energy of each point of the explored phase space from the simulation of LS_2 with 720 atoms at 1800 K. From "x" and "+" are extracted configurations respectively from zone B and C and reported in figure 7.18.

In the average potential energy surface (PES) extracted from the simulations with two CVs, shown in figure 7.18, we find multiple minima not observed with the single CV (see figure 7.11 (b)). The deepest minimum marked by A at CVs values (350, 270) corresponds to the perfect stable crystalline phase. In the region B (220-300, 50-200), the layered disordered structure is formed. A and B regions were highlighted in violet in figure 7.16. A range of structures is located in the B region, which are composed of layers with a different level of ordering. In fact, $I(23°)$ value is higher than 200, while the $I(35°)$ range between almost 0 and 200. As observed in the investigation with 1 CV, the first step of nucleation is an increase of the $I(23°)$, arriving in B region, later, with the increasing of the ordering inside layers, the system moves forward to region A. In a small box as the one investigated, a few defects can drastically affect the value of the CV, but in a realistic system, a few defects in the crystalline structure do not have a pronounced effect on the XRD intensity. This minimum of A is not located at the minimum of the FES, even though it is the most stable structure that we can obtain in terms of potential energy, while at the position of the minimum we can observe some small defects that increase the entropy of the structure, lowering the free energy.

From the B region of the PES, three structures (marked with "x") showing layers with a different level of ordering were extracted. One of them, at (268, 85), is found in an energy plateau, whose potential energy is higher than that of the most stable crystal in about 59 kJ/mol per formula unit (f.u.), with no barriers along the path. In figure 7.19 structures extracted are represented in the corresponding area and labeled with the values of the CVs in brackets.

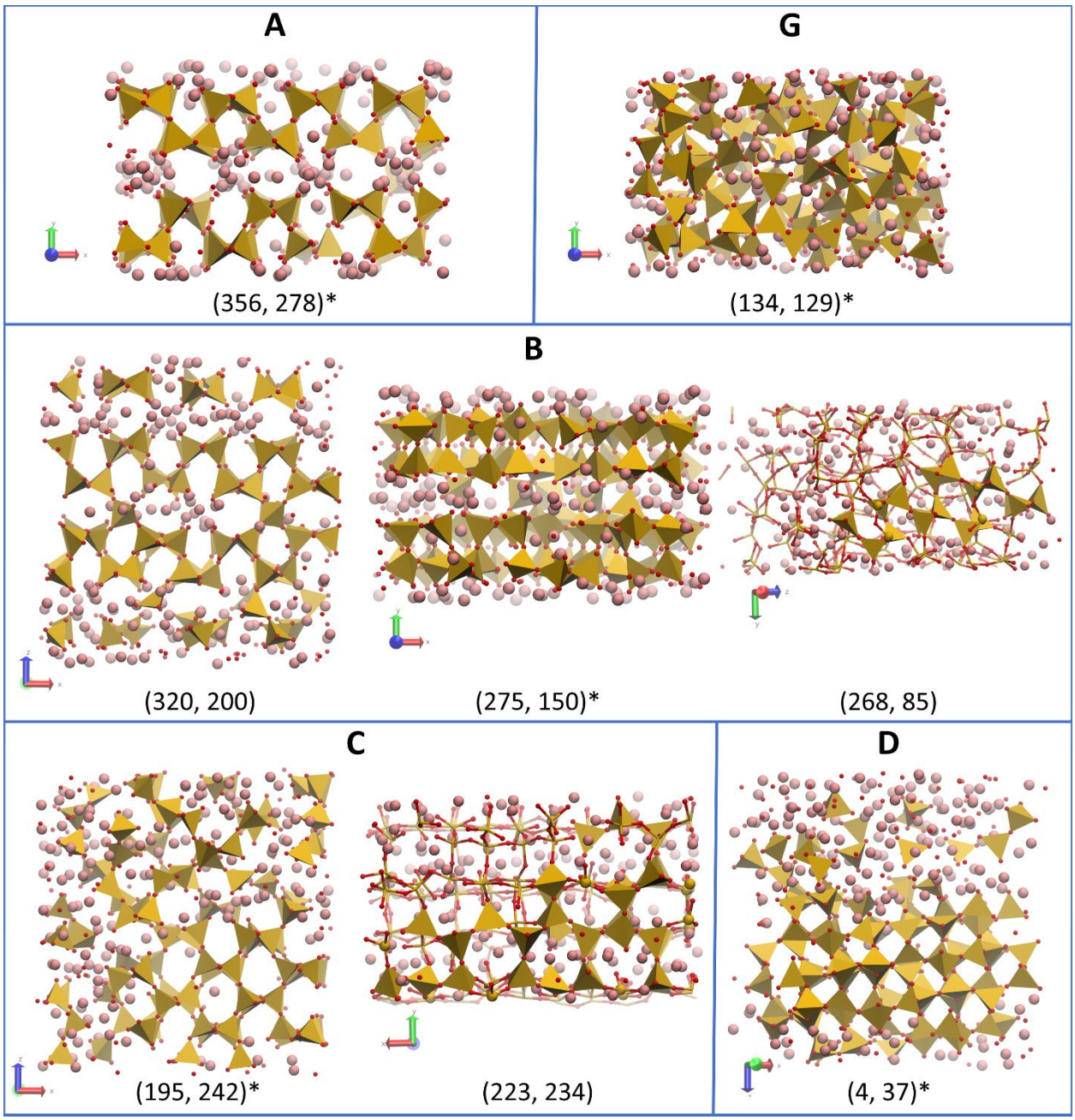

FIG. 7.19. Structures extracted from the simulation at 1800 K of LS_2 containing 720 atoms. The letter in each block corresponds to the region of the PES from which the structures are extracted. A melt configuration is presented in the G block. The multiple structures from regions B and C are related to the points indicated respectively by "x" and "+" in the PES, figure 7.18. In parenthesis the value of the two CVs is indicated. Lithium ions are represented with pink spheres, red spheres are oxygen, while silicon are presented as tetrahedral or as points to highlight some peculiarities. The symbol "*" indicates structures used for the calculation of ionic mobility.

TABLE 7.1. Distribution of % of Q^n species of silicon ions in the five investigated structures at 1000 K.

	Q^0	Q^1	Q^2	Q^3	Q^4
A – LS_2 crystal	0.0	0.0	0.9	99.1	0.0

B – disordered layered	0.2	2.8	17.2	57.5	22.4
C – phase separation	2.1	8.0	19.3	29.5	41.2
D – phase separation	6.4	9.4	9.2	21.7	53.2
Glass	0.0	7.6	19.0	39.9	33.5

Moreover, we further identified new regions labeled by C and D, which correspond to a phase separated into silica and lithium rich zones, as shown in figure 7.19. In the C region of the PES, highlighted in light blue in figure 7.16, the silica-rich phase was made of mainly six membered rings linked by SiO_4 tetrahedra, which consist of the β-cristobalite-like structure, whereas the lithium-rich part contains Q^1 and Q^2 silicon species, see table 7.1 for percentages. The presence of this kind of Q^n species demonstrates the presence of silica chains as in the case of metasilicate phase (see figure 7.19 C (195, 242) and 7.20). The difference in the potential energy between the minima in regions A and C is approximately 20 kJ/mol per f.u. The potential energy barrier to transit from C to A is approximately 2.5 kJ/mol per f.u. An intermediate structure is shown in figure 7.19 C at (223, 234), in which silica layers are interconnected by forming 6-membered rings, as in the silica-rich region found at the local minimum of the PES.

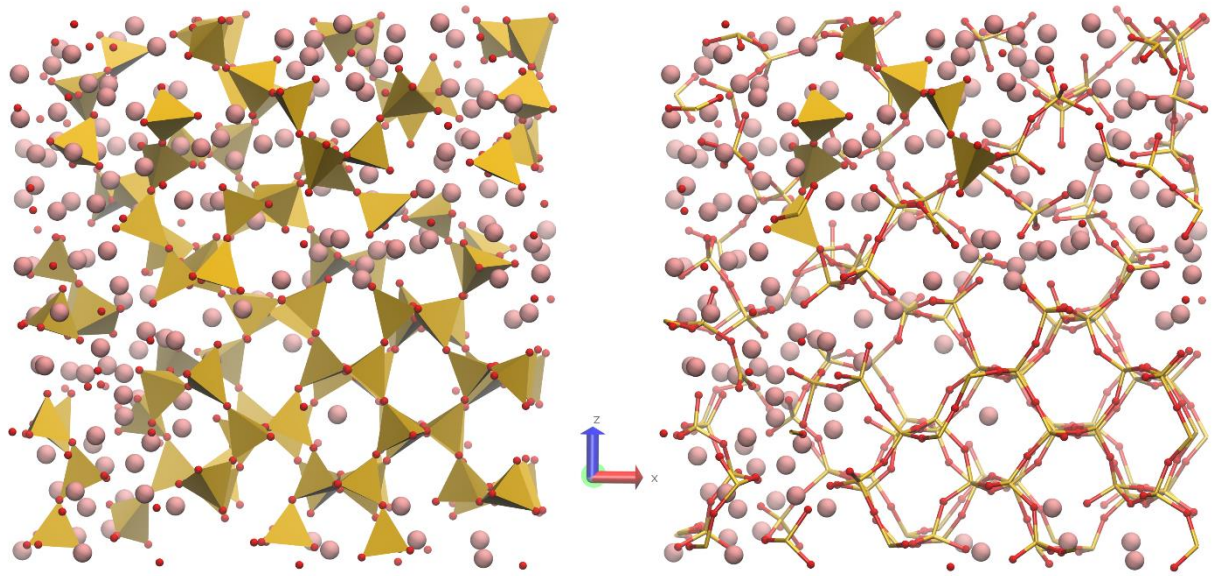

FIG. 7.20. Two visualizations of structure at (195, 242) extracted from C region. On the left, all silicon atoms are represented by tetrahedra; on the right, only silicon atoms that form silica chains are represented by tetrahedra.

On the other hand, the silica-rich phase in the D region, highlighted in orange in figure 7.16, is composed of 4 to 6 membered rings, while the lithium rich region mainly contains amorphous lithium oxide and a few Q^0 and Q^1 silicon species (table 7.1). The inhomogeneous structure is dissimilar to LS_2 crystal, and the potential energy at the minimum in D region is higher than that of the crystalline LS_2 of 40 kJ/mol per f.u.

A high barrier of approximately 20 kJ/mol per f.u. separates the two minima, which is much higher than that from C to A.

The PES obtained from the simulation of the larger model containing 1440 atoms is reported in figure 7.21 using the same 2 CVs used in the small model simulation. We observed the same features as in the case of the smaller simulation box with minor differences. First, the intensity of the XRD peaks was model-size dependent, therefore the stable LS_2 was associated with higher values of the CVs than those with the smaller model, figure 7.3. During the metadynamics simulation, the microstructure crystallized incompletely in the simulation box because the crystal-like silica layers are arbitrarily oriented in the box, as shown in the right side of figure 7.21, although the crystalline structure is obviously recognized from these configurations. Indeed, a major difference in PESs obtained with the two simulation boxes was the absence of the deep minimum of the stable crystal when the larger model was used. Additionally, the region D was wider in the phase space (0-200,0-50) when the larger model was used, in comparison with the small model. In contrast, for both models, the region C was confined in a limited space at the same coordinate, and the barriers between the regions C – A and D – A were reproduced.

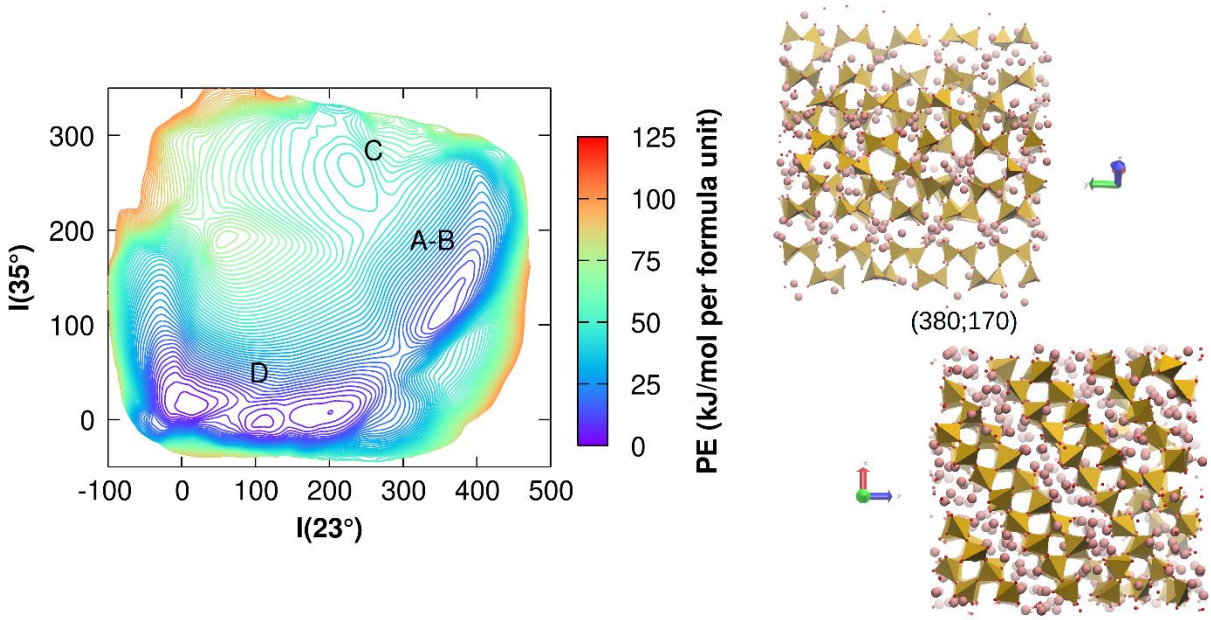

FIG. 7.21. Potential energy of each point of the explored phase space from the simulation of LS_2 with 1440 atoms at 1800 K. On the right, two views of the structure extracted from the surface at (380, 170).

7.5. Ionic mobility in different phases

According to the observation of the new minima in the PES, some questions arise about the nucleation path, especially when the temperature is in the glass transition range (typical temperatures used to trigger crystallization in glasses). The potential energy barriers give only a thermodynamic point of view, enthalpic, of the description of the structural transitions, missing the kinetic aspects. The dynamics of the atoms is also a key factor for the crystallization. Indeed, higher mobility is essential for the glass-crystal transition. In a recent paper of Bradtmuller et al. (68), the structural rearrangements during the crystallization of LS_2 were investigated. They demonstrated that the lithium environment is more sensitive to the heat treatment with respect to the silica network. In fact, lithium exhibited a higher tendency to arrange to become more "crystal-like" even with a short heat treatment, while the silicate species unlikely completed their relaxation before crystal nucleation intervenes. It means that in the first place, lithium movements govern the nucleation. Moreover, a higher kinetic energy of Li ions can facilitate its interaction with silica and the breaking of the Si-O-Si bonds of the network.

Therefore, we performed MD simulations to evaluate the diffusion coefficient of Li ions in representative structures at a temperature range from 350 K to 1200 K. One configuration from each region identified in the PES was investigated. These configurations were extracted from the MetaD simulation, models marked with an "*" in figure 7.18 and relaxed at room temperature. NPT MD simulations were run for each sample for 50 ns at each selected temperature.

In figure 7.22 the diffusion coefficients (logarithmic scale, $\log D$) are plotted against the inverse of the temperature $(1/T)$ (multiplied by 1000 for an easier visualization), and the data points were fitted with an Arrhenius equation to extrapolate the activation energy (E_a) of the diffusive process.

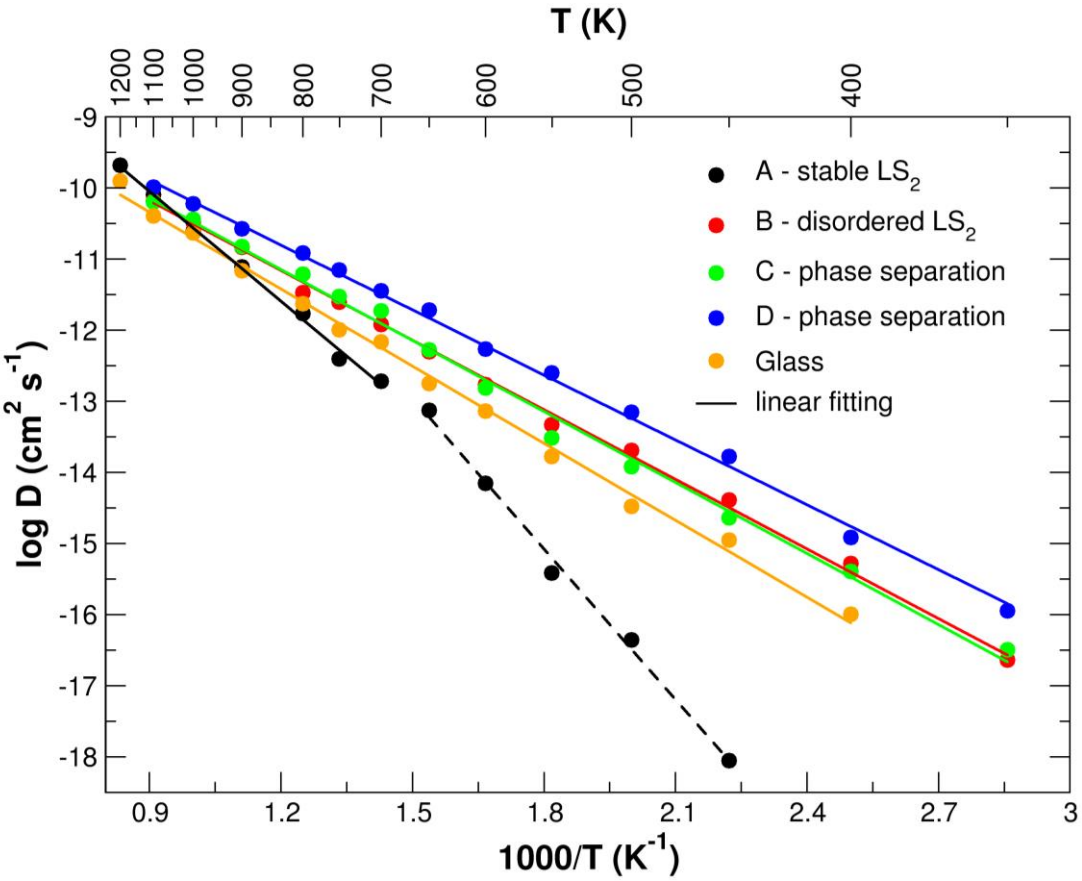

FIG. 7.22. Temperature dependence of diffusion coefficient for Li ions in structures selected from the four regions of the potential energy surface, indicated with "*" in figure 7.18 and the glass. The points are fitted with Arrhenius temperature dependence: $\log D = \log D_0 - \frac{E_a}{RT}$.

The structure at region D exhibited the largest diffusion coefficients and the lowest activation energy E_a = 25.3 kJ/mol thanks to a high concentration of Li in the Li-rich region, as confirmed by the broad first peak of the Li-Li partial distribution function (PDF) in figure 7.23. The Li-rich region in the phase separated structure in C at (195, 242) has instead a lower concentration of Li ions than in D, resulting in a lower diffusivity with activation energy of 27.7 kJ/mol. The crystalline structure with disordered layers, B, has a comparable diffusion coefficient to the one in C-region and E_a = 27.2 kJ/mol. The number of Li ions within the first peak of the PDF, which represent the coordination number, is 5.6, 6.8 and 8.8 respectively for B, C and D structures, confirming a higher clusterization and local concentration for the phase separated structures. Despite a different Li-Li PDF (figure 7.23) between B and C, and a lower Li-Li CN of B, the symmetry of the structures confers the same average mobility to Li ions in the two cases; this point will also be discussed later.

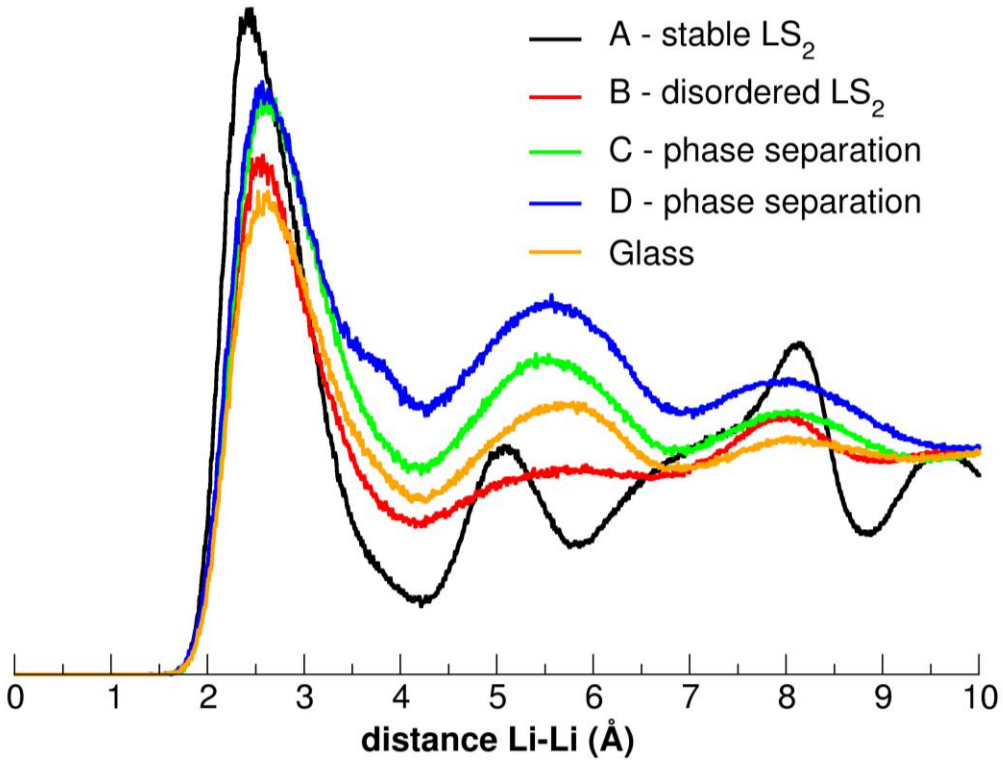

FIG. 7.23, Comparison between Li-Li PDF of extracted structures from all regions of the PES individuated and glassy structure at 600 K.

Since a higher mobility can lead to a faster rearrangement of a structure, both the potential energy barrier height and the ionic diffusivity should be considered to determine the kinetically more favored nucleation path. On the other hand, the intermediate models, B, C and D, have a higher mobility than the LS_2 glass model. In the glass model, the Li ions homogeneously dispersed in the network, which can be confirmed from the Li-Li PDF where the first peak has a lower subtended area, meaning a lower number of Li ions within 4 Å from a central Li. Consequently, the Li ions in LS_2 glass have less accessible Li sites and are less mobile, exhibiting a higher activation energy of 30.0 kJ/mol, as shown in figure 7.22. If the LS_2 glass once transforms into the intermediate phases B or C, the structural transition increases the diffusivity of the atoms, which might drive the following conversion to stable LS_2 crystal.

The stable crystalline phase, A, has the lowest diffusivity owing to the perfectly ordered structure, especially below 900 K. The curve of diffusion coefficient as a function of temperature for the structure A exhibits a folding point, indicating two different ionic diffusion mechanisms. This can be explained by exploiting the anisotropy of the crystalline structure. In the bottom part of figure 7.24 the total diffusion is separated in its components along the x, y and z axis: up to 650 K the diffusive process occurs along the z-axis, while from 700 K the Li ion diffusion along the x-axis becomes relevant. The y-axis diffusion becomes relevant from 900 K, as seen in the orange curve in the bottom part of figure 7.24 or in the mean square displacement (MSD) at 1000 K in the upper part.

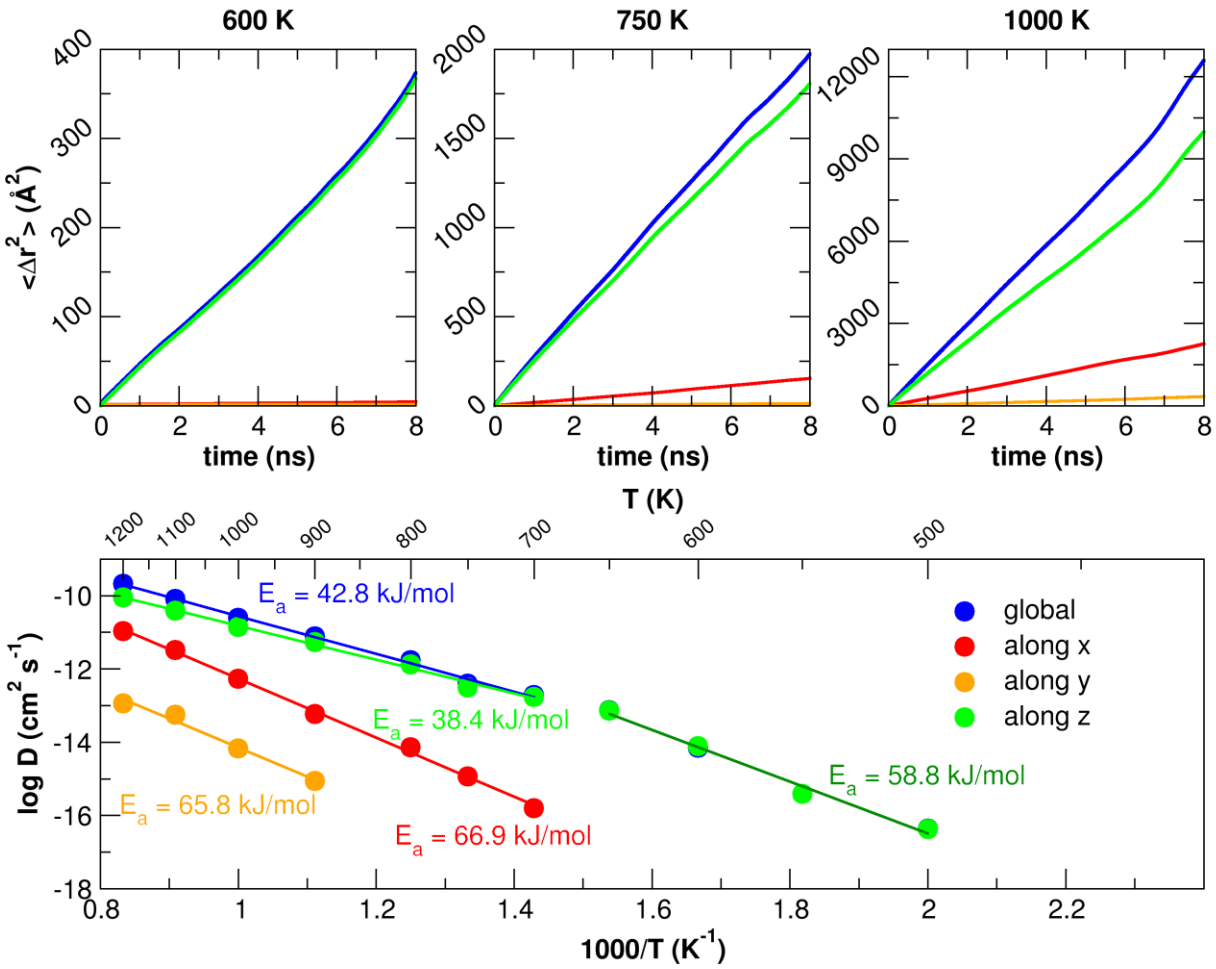

FIG. 7.24. (top) Mean square displacement of Li ions at three different temperatures in the stable crystalline LS_2 and contributions along the three axes. (down) Temperature dependence of Li diffusion coefficient global and along x, y and z axes with calculated activation energy extracted from Arrhenius equation.

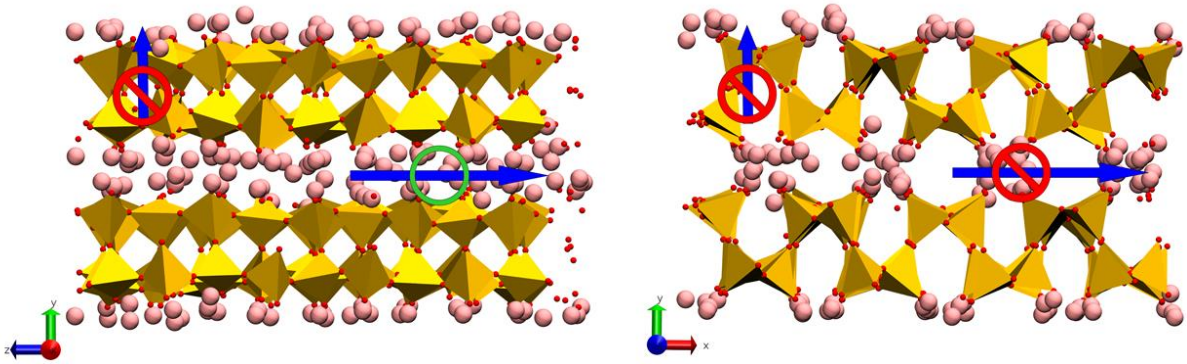

FIG. 7.25. Two views of the stable crystalline structure at 600 K with arrows indicating accessible and not accessible diffusive pathways.

The activation energies are different according to the direction and temperature. Below 650 K since x and y do not take part of the diffusive process the total E_a matches E_a along the z-axis, with a value of 58.8 kJ/mol. At T > 700 K E_a are 66.9 kJ/mol and 38.4 kJ/mol along x-axis and z-axis, respectively. The large difference in activation energy is attributed to the different distances between Li sites along the two axes. In the Li-Li PDF, the first peak at 2.5 Å is associated with the Li-Li distance along the z-axis, while the

second peak at 5.0 Å is the distance between the neighboring sites along the x-axis, see figure 7.25. With increasing temperature, structural disordering of the lithium sites shortens the distance between in-plane lithium ions, and, thus, the Li ions construct a diffusion path in the entire xz plane. Therefore, the diffusion coefficient of the most stable crystalline structure got closer to those of the other inhomogeneous structures above 900 K. Li ions cannot jump between different layers of the crystalline structure (y direction) until 900 K, because of the steric hindrance of silicon tetrahedra, and this direction of diffusion remains limited.

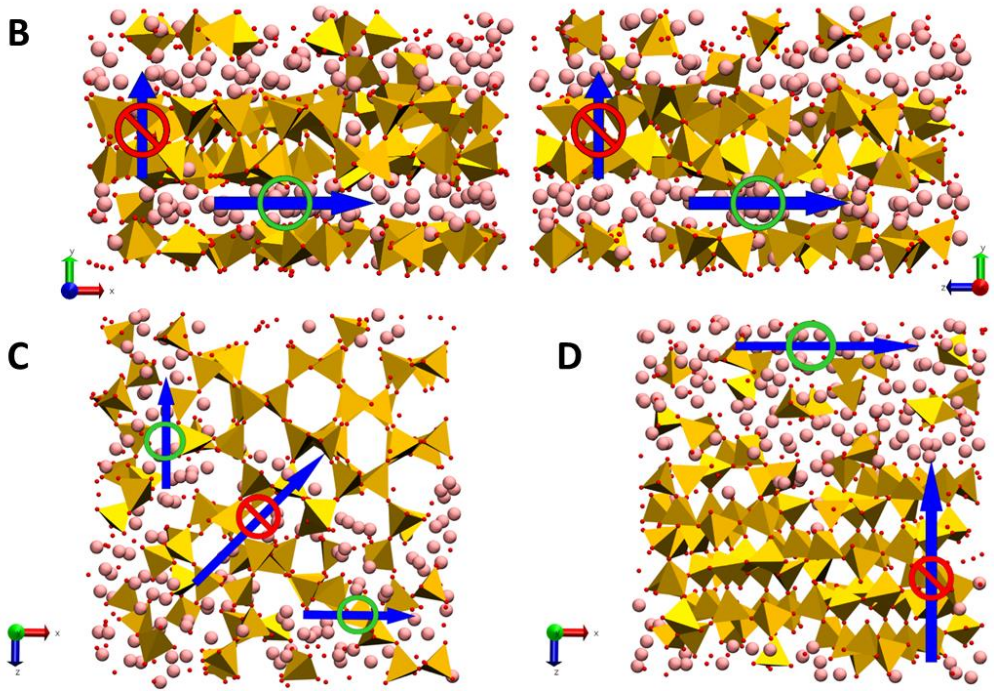

FIG. 7.26. Two views of structure with disordered layers extracted from B region, and structures extracted from C and D region at 600 K with arrows indicating accessible or not accessible diffusive pathways.

Except for the homogeneous glass model, all structures studied present diffusion anisotropy (203,204). Figure 7.26 shows the favorable and unfavorable directions of Li ion diffusion of systems in B, C and D regions. As in crystalline LS_2, the ionic diffusion parallel to y direction is not preferred in the disordered layered structures (B), whereas the ions can diffuse over the xz plane with less limitation than the crystal thanks to the highly disordered configurations at any temperature. In both phase-separated structures (C and D), lithium ions diffuse only in the Li-rich region and do not enter the Si-rich zones within the timeframe of the simulations.

Investigating the mobility of Si and O is also interesting, because the mobility of Li ions can play the first step toward the nucleation, but then Si tetrahedra must rearrange in a crystalline pattern. Therefore, the diffusivity of Si and O is investigated, and the MSD is plotted in figure 7.27.

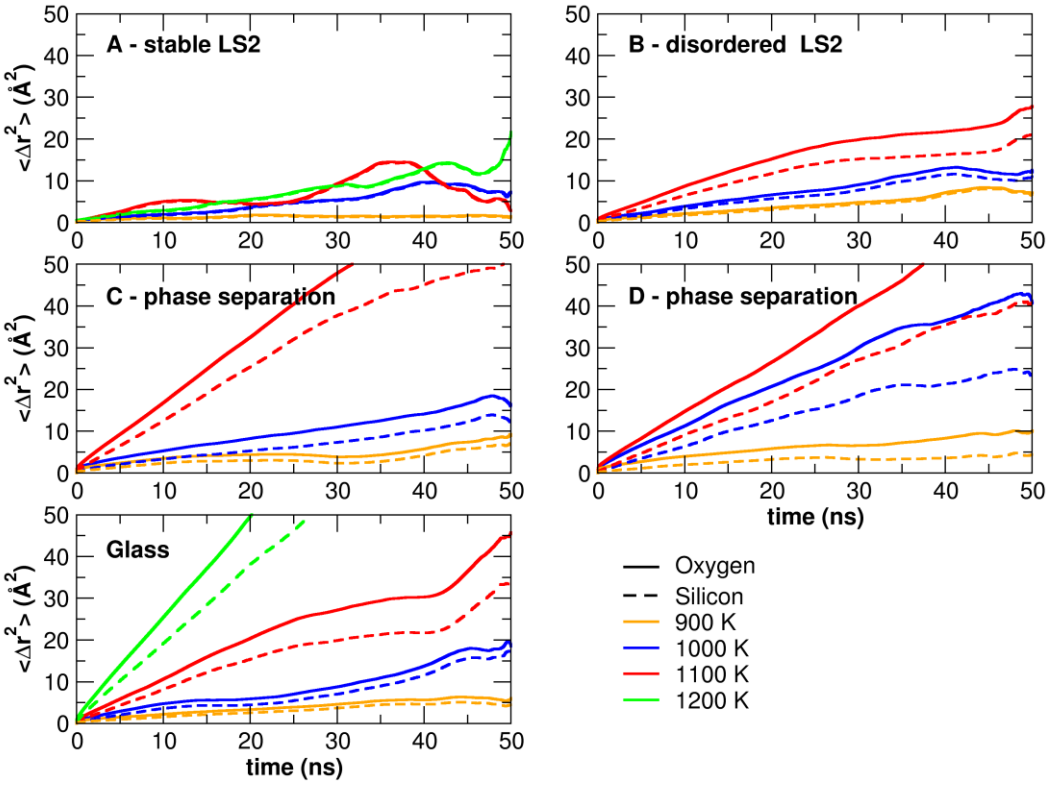

FIG. 7.27. Mean square displacement of silicon and oxygen in the five investigated systems between 900 K and 1200 K.

The mean square displacement of Si and O in the five systems is evaluated between 900 and 1200 K. Below 900 K we observed only the vibration in the Si and O positions, thus the data is not reported. At higher temperature even though the diffusion increases, a diffusive regime is never reached in the timeframe of the simulation, except for the glass at 1200 K, which is above the glass transition temperature, therefore we could not calculate the diffusion coefficient. Moreover, the MSDs of the intermediate structures were comparable at the same temperature, although slightly higher values were obtained in the phase-separated D region. In the LS_2 crystal the mobility of Si and O do not increase with the temperature, confirming the greater stability of this phase.

In figure 7.28 we distinguish the contributions of silicon Q^n species to the overall MSD. According to the environment of each silicon atom, the mobility can change, presenting structures or regions of a structure more suitable to nucleate.

At 1000 K, Q^0 and Q^1 species possess a higher mobility in the phase separated structures, C and D, because they were located inside the Li-rich region, and they thus easily exchange their sites. In the glass, the less linked species had the similar mobility with the higher polymerized Si species, because they were constrained by the entire silica network and different Q^n species are homogeneously spread in the structure. The Q^3 and Q^4 silicon in the Si-rich region of the phase-separated structures, instead, have the comparable mobility with the stable and disordered LS_2 and the glass models, implying that only the lower polymerized

Si species surrounded by Li ions gain the diffusivity. The significant difference in the mobility among Si and O with Li suggests necessity of the longer rearrangement times for silica network; however, the appearance of such mobile Si in the Li-rich region is expected to play an important role to proceed the transformation of the first crystalline nuclei by bypassing the crystallization through the intermediate structures.

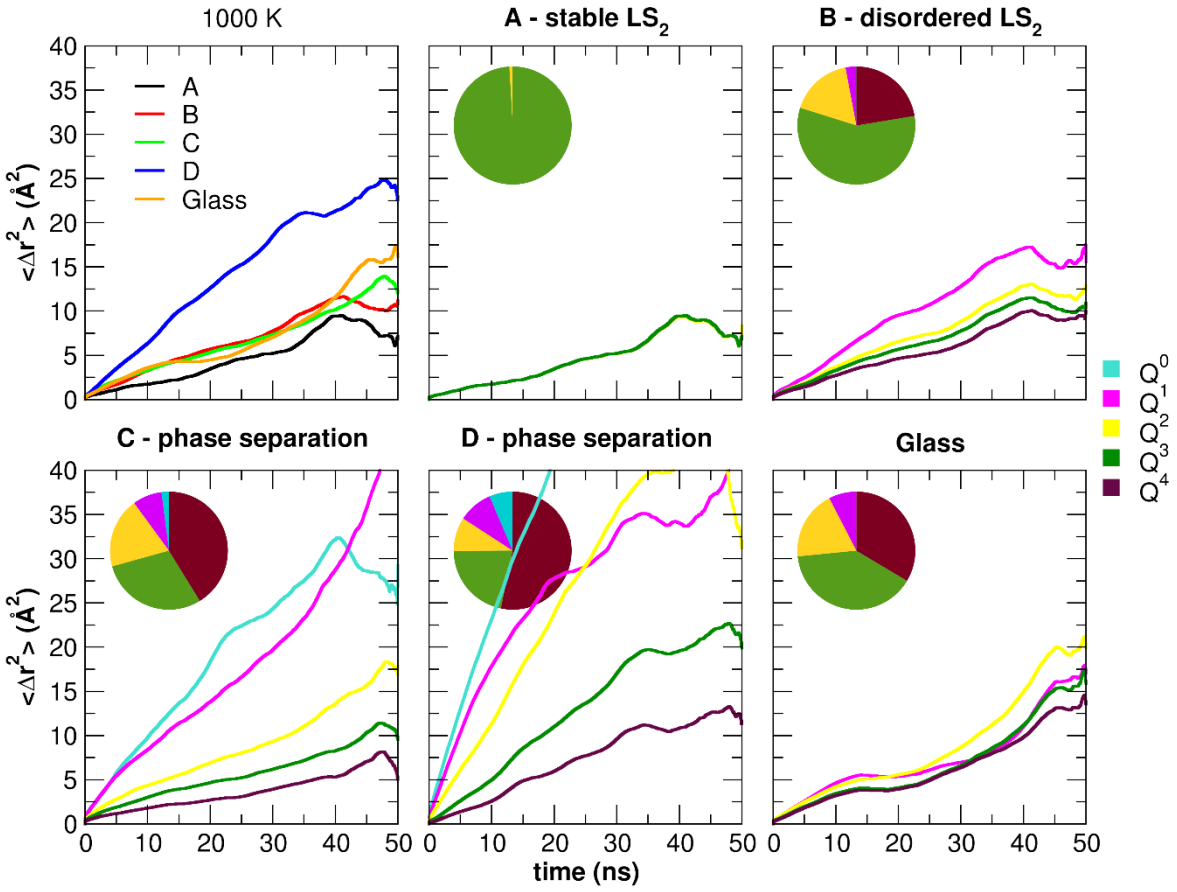

FIG. 7.28. First panel is the comparison between silicon mean square displacement at 1000 K among the studied system. The following five panels show the mean square displacement of each Si Q^n specie in every system. The pie charts represent the distribution of Q^n species in each system as presented in table 7.1.

7.6. Summary

In summary, the employment of two biasing CVs in the MetaD simulations give access to different crystallization pathways and information.

Our simulations show that crystallization in the LS_2 system does not rigorously follow CNT assumptions and occurs following several cooperative steps, which lowers the energy barrier for nucleation. The predominant nucleation pathway in both applications crosses the formation of a disordered layered intermediate phase, which transforms into the stable crystalline phase.

The simulation driven by one CV does not provide any relation between the formation of lithium metasilicate, LS, and LS_2 crystalline phases as proposed in several experimental papers (57,60,184). At a

first sight, any LS germ was observed prior to the LS_2 crystallization implying that a LS nucleus is not a necessarily precursor of the LS_2 precipitation (at least for stoichiometric LS_2 melts). And this is also consistent with our previous MD investigation, in chapter 5, which found that the chain-like microstructures with stoichiometry of LS crystal is formed only at the glass surface (202).

However, when this system is approached using two CVs new possibilities become accessible, even though not energetically accessible at the condition investigated. It is presumable that the other nucleation path becomes potentially accessible if the conditions are changed. Combining the potential energy and the diffusivity information, the intermediate structures in the C region might also transform to stable LS_2 crystal, while the higher potential energy barrier from D-region would limit the possibility to convert to the crystal. Therefore, there exist only two preferable nucleation pathways from LS_2 glass to LS_2 crystal.

The temperature, the composition, the presence of heterogeneities may play the principal roles in the choice of the nucleation path. In a perfect stoichiometric glass, the nucleation path with phase separation is unlikely followed, but, for instance, when defects are present or the glass composition is non-stoichiometric, the formation of a cristobalite nucleus could play a pivotal role as reported by experimental studies (52,184,205,206). Another crucial factor might be the presence of silicate chains. In the lithium-rich region of the configurations in C-region, the silica chains initiated the nucleation of LS crystal. Indeed, in several studies on non-stoichiometric compositions, the formation of LS crystal has been proposed as a precursor of lithium disilicate.

In conclusion, we could observe multiple nucleation pathways for crystallization of LS_2 crystal owing to the enhanced exploration using Metadynamics simulations employed two CVs. The transition paths identified explained the different experimental observations on the nucleation mechanism reported in the studies for stoichiometric and non-stoichiometric lithium disilicate compositions, respectively. The main path involves the direct formation of the LS_2 crystal through the intermediate layered structures. In contrast, the second pathway is initiated by a nucleation of cristobalite-like nuclei to form LS-like crystal, then the LS crystal is converted to LS_2 crystal. The latter mechanism might be subserved by more mobile Li ions in the intermediate structures.

Chapter 8. Conclusions

During my PhD project I have applied several computational methods and protocols to investigate the nucleation and crystallization of lithium disilicate, a well-known system in the glass-ceramics industry. Researchers have been attempting to comprehend the mechanism of crystallization of this system for years. Although this is one of the silicate glasses presenting homogeneous nucleation, there is a lively and open debate on the involvement of metastable phases in the nucleation process. Lithium metasilicate is one of the crystalline phases thought to be involved in the nucleation of lithium disilicate. However, nucleation is a phenomenon that is by its very nature difficult to study experimentally, and it is challenging to use experimental methods to monitor the development of nanometric nuclei. This is the reason why computational techniques are usually employed to shed light on the microstructure and atomistic dynamics of this process.

The importance of nucleation and crystallization of the lithium disilicate and the proposed mechanisms have been reported and discussed in chapter 1. In chapter 2, we have presented the theories of nucleation most used. In chapter 3 we have described the computational techniques used during the project, that is, Molecular Dynamics simulations and Metadynamics. Since an important prerequisite to the study of nucleation and crystallization is the knowledge of the melting temperature, the computation of melting temperature using molecular dynamics simulations has been reported in chapter 4.

In chapter 5, we tested two different strategies to study nucleation using conventional Molecular Dynamics simulations. The first approach assumes that during the quenching of melts, subcritical embryos of the crystal phase are more prone to crystallize. Therefore, we have developed an algorithm to seek such crystalline-like embryos in glass matrixes and applied it on both the bulk and the surface of LS_2 and LS_2P1 (LS2 glass with 1% of P_2O_5 as nucleating agent) glasses. We observed that LS_2 crystalline embryos up to 4.5 Å of dimension can be easily detected in the bulk of both glasses. The presence of a nucleating agent slightly increases the polymerization, increasing the number of Q^4 Si species and decreasing LS-like embryos. On the contrary, on the surface there is a higher concentration of Li ions, which reduces the connections between SiO_4 tetrahedra, increasing the amount of Q^2 Si species, consequently more embryos with LS structure are found. We concluded that while the LS can nucleate on the surface, the LS_2 is more likely to crystallize in the bulk, assisted by the presence of P_2O_5.

In the same chapter, we have applied the Free-Energy Seeding method (FESM) to determine the nucleation free energy of LS_2 and LS crystal in the LS_2 glass matrix. We recovered the critical radii of the two crystals and the activation energy, which agreed fairly well with experimental data. One of the most significant drawbacks of Classical Nucleation Theory is overcome by the FESM, which considers the interfacial energy to be nucleus-size dependent. Unfortunately, this method provides large errors and thus does not provide mechanistic insights on nucleation.

Nucleation is a rare event that occurs beyond the accessible time range of MD. Therefore, to follow the mechanism of nucleation we used Metadynamics simulations, and we have demonstrated in chapters 6 and 7 that it allows us to overcome the time limitation.

In chapter 6, investigated the crystallization of β-cristobalite from the silica melt and systematically studied the effects of all the metadynamics parameters on the convergence of the simulations.

The collective variables more effective to drive crystallization were found to be the intensity of particular X-ray diffraction peaks. Then in chapter 7, we have applied this powerful technique to lithium disilicate using one or two peaks of the X-ray diffraction spectrum.

We observed that the employment of only one CV allows us to explore a smaller region of the phase space and that to obtain only one crystallization pathway. When two CVs are employed, the observation of three different nucleation paths from the liquid to the crystal is made possible by the exploration of a significantly wider phase space. The first one (observed also with one CV) involves the direct formation of a structured, disordered layer that later rearranges internally to transform into an LS_2 crystal. The second path begins with a phase separation that includes a silica-rich zone, with a β-cristobalite structure and a lithium-rich zone that contains silica chains, that resemble the lithium metasilicate crystal. The third path also proposes a phase separation; however, it presents a high potential energy barrier between the intermediate and the LS_2 crystal. The new paths were not energetically favorable under the working conditions and in the stoichiometric LS_2 glass, but we demonstrated that the intermediate phase with the β-cristobalite core has a low potential energy barrier to crystal and a high diffusivity that can promote the transition to LS_2 under certain conditions. A different composition, temperature, or presence of a nucleating agent can change the favorable path, stabilizing one path over another.

Despite the power of WT-MetaD to study crystallization in low viscous systems, it still exhibits several limitations for highly viscous glass-forming systems: (i) the model size is still limited to thousands of atoms; (ii) the employment of temperatures higher than the melting point might prevent the observation of alternative crystallization pathways at lower temperature; (iii) if more than one CV is employed, the time to reach convergence exponentially increases; (iv) the choice of the CV remains a challenging issue, it is hard to find a property able to describe the slow degrees of freedom of the transformation in an efficient way. To get beyond the limitations, longer simulations and a more effective algorithm are required.

In several recent works (146,207) a large number of extensions and variants have been developed and described to improve the efficiency of phase space sampling. Metadynamics and Well-tempered Metadynamics are adaptive biasing potential methods, in which the biasing potential is built on-the fly, as presented in the third chapter. A first approach to improve the performances is to employ the adaptive Gaussians (208), where the width of deposited Gaussians changes according to the phase space, accelerating the exploration, but not changing the MetaD protocol. VES and OPES are two examples of the evolution of Metadynamics. VES (209), variationally enhanced sampling, is based on a variational principle where a functional of a bias potential has to be minimized to recover the free-energy surface. OPES (210,211), on-the-fly probability enhanced sampling, incorporates some idea of the VES and it is designed to be simple and robust with also suboptimal collective variables. Is based on adding a bias to the energy of the system, so the sampled distribution is no longer the Boltzmann one but an easier-to sample target one. These methods have been tested on classical systems, but they proved to be quite promising in improving performance.

The temperature limitation can be addressed using a parallel tempering (212,213). It is a replica exchange technique (214) where several copies of the system at different temperatures are run simultaneously. Then, based on some criterion, the configurations are exchanged between different temperatures. It allows to make configurations at high temperatures available also to the simulation at low temperatures and vice versa. Combined with WTMetaD, parallel tempering is an extremely useful technique to reconstruct the free-energy surface at lower temperatures.

The examples listed are only a fraction of all possible variants of Metadynamics or enhanced sampling techniques, but there are large possibilities of reducing the computational effort.

In contrast, changing the method may not be sufficient if the collective variable is not good enough. Probably, the biggest limitation and challenge derives from the choice of the CV. Over the years, a multitude of CVs have been developed, but depending on the system of interest the list of possibilities may decrease sensibly. In multi-atomistic systems, such as in binary oxides as $Li_2Si_2O_5$, the description of the slow degrees of freedom depends on a large number of order parameters that depends on a combination of collective variables. Recently, dimensionality reduction and deep learning have been proposed to design and optimize the collective variable for the study of the crystallization of different systems, such as CO_2, metallic Na, Mo, NaCl, small organic molecules (153,154,215–217). Machine learning and neural networks are exploited to combine in a non-linear way structural descriptors, to maximize the discriminative power of the collective variable, opening new possibilities in the study of phase transition of complex systems.

Beyond overcoming the aforementioned limitations, future works should be devoted to the investigation of crystallization of LS_2 in the presence of nucleating agents as well as to extend it to other more complex systems.

Although, we are still far from having a complete view of the nucleation process in glass-forming liquids, with this project we have taken a step forward in understanding how the crystallization process can be investigated.

ACKNOWLEDGMENTS

During the three years of PhD, I had the opportunity to meet several professors, researchers, post-doc and doctorate students, to share knowledge and different ways of working. Although during my first two years I could not travel because of COVID-19, I had the opportunity to make the best of the time spent in the research group in Modena, under the supervision of Professor Alfonso Pedone. The suggestions, the help, and the fruitful discussions, are just a few of the reasons why the first person I have to thank is my supervisor Alfonso Pedone. I also want to thank Professor Maria Cristina Menziani, for her wisdom, suggestions, and professionality. All the members of Pedone's group made these three years memorable. First, Marco Bertani, with whom I shared all the good and bad times during these three years, conferences, discussions, fights with scripts, fights with cards. Luca Brugnoli, Annalisa Pallini and Francesco Muniz Miranda are also gratefully acknowledged for their help and simply their presence. We have all collaborated and shared fruitful discussions that I hope will continue in the next years. Some master students also helped me during these three years, and I want to dedicate a special thank you to Serena Pizzirani.

My PhD project was possible thanks to the collaboration with AGC Inc. and in particular with Dr. Shingo Urata, whom I want to thank for giving me the opportunity to challenge myself with all the projects he proposed. We started our collaboration working on the Mixed Alkali Effect on aluminosilicate glasses, then we moved to the study of nucleation of Lithium Disilicate, which is the subject of this thesis. We have worked with some members of AGC, both experimentalists and computationalists, including Dr. Hiroyuki Hijiya, Prof. Kei Maeda. Dr. Yoichi Takato, and I want to thank them all for collaborating and all discussions and suggestions that brought to the conclusion of this thesis.

During the last year, I spent a semester in the Laboratoire de Structure et Dynamique par Résonance Magnétique (LSDRM) CEA Paris-Saclay, under the supervision of Dr. Thibault Charpentier. In this laboratory I could combine computational methods with NMR spectroscopy to study the effect of water alteration on calcium and sodium aluminosilicate glasses. I want to thank Dr. Charpentier and all his team with whom I had great discussion and huge help.

REFERENCES

1. Sosso GC, Chen J, Cox SJ, Fitzner M, Pedevilla P, Zen A, et al. Crystal Nucleation in Liquids: Open Questions and Future Challenges in Molecular Dynamics Simulations. Chem Rev. 2016 Jun 22;116(12):7078–116.

2. Mauro JC, Philip CS, Vaughn DJ, Pambianchi MS. Glass Science in the United States: Current Status and Future Directions. Int J Appl Glass Sci. 2014;5(1):2–15.

3. Hall KWm, Zhang Z, Burnham CJ, Guo GJ, Carpendale S, English NJ, et al. Does Local Structure Bias How a Crystal Nucleus Evolves? J Phys Chem Lett. 2018 Dec 20;9(24):6991–8.

4. C. Sosso G, F. Whale T, A. Holden M, Pedevilla P, J. Murray B, Michaelides A. Unravelling the origins of ice nucleation on organic crystals. Chem Sci. 2018;9(42):8077–88.

5. Jantzen CM, Brown KG, Pickett JB. Durable Glass for Thousands of Years. Int J Appl Glass Sci. 2010;1(1):38–62.

6. Brehault A, Patil D, Kamat H, Youngman RE, Thirion LM, Mauro JC, et al. Compositional Dependence of Solubility/Retention of Molybdenum Oxides in Aluminoborosilicate-Based Model Nuclear Waste Glasses. J Phys Chem B. 2018 Feb 8;122(5):1714–29.

7. Höland W. Glass-Ceramics. In: Bio-Glasses [Internet]. John Wiley & Sons, Ltd; 2012 [cited 2023 Jan 22]. p. 97–105. Available from: https://onlinelibrary.wiley.com/doi/abs/10.1002/9781118346457.ch7

8. Zanotto ED, Tsuchida JE, Schneider JF, Eckert H. Thirty-year quest for structure–nucleation relationships in oxide glasses. Int Mater Rev. 2015 Oct 3;60(7):376–91.

9. Massobrio C, Du J, Bernasconi M, Salmon PS, editors. Molecular Dynamics Simulations of Disordered Materials: From Network Glasses to Phase-Change Memory Alloys [Internet]. Cham: Springer International Publishing; 2015 [cited 2023 Jan 20]. (Springer Series in Materials Science; vol. 215). Available from: https://link.springer.com/10.1007/978-3-319-15675-0

10. Pedone A. Properties Calculations of Silica-Based Glasses by Atomistic Simulations Techniques: A Review. J Phys Chem C. 2009 Dec 10;113(49):20773–84.

11. Soules TF. Computer simulation of glass structures. J Non-Cryst Solids. 1990 Aug 2;123(1):48–70.

12. Zanotto ED, Mauro JC. The glassy state of matter: Its definition and ultimate fate. J Non-Cryst Solids. 2017 Sep 1;471:490–5.

13. Lin C, Rüssel C, Dai S. Chalcogenide glass-ceramics: Functional design and crystallization mechanism. Prog Mater Sci. 2018 Apr 1;93:1–44.

14. Portier J. Halogenide, chalcogenide and chalcohalogenide glasses: materials, models, applications. J Non-Cryst Solids. 1989 Oct 1;112(1):15–22.

15. Lundquist PM, Wortmann R, Geletneky C, Twieg RJ, Jurich M, Lee VY, et al. Organic Glasses: A New Class of Photorefractive Materials. Science. 1996 Nov 15;274(5290):1182–5.

16. Nishiyama N, Amiya K, Inoue A. Novel applications of bulk metallic glass for industrial products. J Non-Cryst Solids. 2007 Oct 15;353(32):3615–21.

17. Mysen B, Richet P. Silicate Glasses and Melts. Elsevier; 2018. 722 p.

18. Shelby JE. Introduction to Glass Science and Technology, 3rd Edition. Royal Society of Chemistry; 2020. 341 p.

19. Huang C, Behrman EC. Structure and properties of calcium aluminosilicate glasses. J Non-Cryst Solids. 1991 May 1;128(3):310–21.

20. XIAO Z, CHENG J, WU H. Effect of Al2O3/SiO2 Ratio on the Viscosity and Workability of High-alumina Soda-lime-silicate Glasses. J Chin Ceram Soc. 2012 Jul 1;40(7):1000–5.

21. Cohen BM, Uhlmann DR, Shaw RR. Optical and electrical properties of lead silicate glasses. J Non-Cryst Solids. 1973 Jul 1;12(2):177–88.

22. Almutawa F, Vandal R, Wang SQ, Lim HW. Current status of photoprotection by window glass, automobile glass, window films, and sunglasses. Photodermatol Photoimmunol Photomed. 2013;29(2):65–72.

23. Lyon KC. Prediction of the Viscosities of "Soda-Lime" Silica Glasses. J Res Natl Bur Stand Sect Phys Chem. 1974;78A(4):497–504.

24. Hater W, Müller-Warmuth W, Meier M, Frischat GH. High-resolution solid-state NMR studies of mixed-alkali silicate glasses. J Non-Cryst Solids. 1989 Dec 4;113(2):210–2.

25. Emerson JF, Stallworth PE, Bray PJ. High-field 29Si NMR studies of alkali silicate glasses. J Non-Cryst Solids. 1989 Dec 4;113(2):253–9.

26. Holand W, Beall GH. Glass-Ceramic Technology. John Wiley & Sons; 2019. 448 p.

27. Fu L, Engqvist H, Xia W. Glass–Ceramics in Dentistry: A Review. Materials. 2020 Jan;13(5):1049.

28. Cormier L, Dargaud O, Menguy N, Henderson GS, Guignard M, Trcera N, et al. Investigation of the Role of Nucleating Agents in MgO−SiO2−Al2O3−SiO2−TiO2 Glasses and Glass-Ceramics: A XANES Study at the Ti K- and L2,3-Edges. Cryst Growth Des. 2011 Jan 5;11(1):311–9.

29. Rampf M, Dittmer M, Ritzberger C, Höland W. Controlled Parallel Crystallization of Lithium Disilicate and Diopside Using a Combination of Internal and Surface Nucleation. Front Mater [Internet]. 2016 [cited 2022 Nov 25];3. Available from: https://www.frontiersin.org/articles/10.3389/fmats.2016.00047

30. Khalkhali Z, Eftekhari yekta B, Marghussian VK. Mechanical and Chemical Properties of Zr and P-Doped Lithium Disilicate Glass Ceramics in Dental Restorations. Int J Appl Ceram Technol. 2012;9(3):497–506.

31. Fokin VM, Souza GP, Zanotto ED, Lumeau J, Glebova L, Glebov LB. Sodium Fluoride Solubility and Crystallization in Photo-Thermo-Refractive Glass. J Am Ceram Soc. 2010;93(3):716–21.

32. Beall GH. Design and Properties of Glass-Ceramics. Annu Rev Mater Sci. 1992;22(1):91–119.

33. Höland W, Rheinberger V, Apel E, van 't Hoen C, Höland M, Dommann A, et al. Clinical applications of glass-ceramics in dentistry. J Mater Sci Mater Med. 2006 Nov 1;17(11):1037–42.

34. Hench LL. Glass and Glass-Ceramic Technologies to Transform the World. Int J Appl Glass Sci. 2011;2(3):162–76.

35. Burke JE. Progress in Ceramic Science: Volume 2. Elsevier; 2013. 286 p.

36. Höland W, Rheinberger V, Apel E, van't Hoen C. Principles and phenomena of bioengineering with glass-ceramics for dental restoration. J Eur Ceram Soc. 2007 Jan 1;27(2):1521–6.

37. Chung KH, Liao JH, Duh JG, Chan DCN. The effects of repeated heat-pressing on properties of pressable glass-ceramics. J Oral Rehabil. 2009;36(2):132–41.

38. Li D, Guo JW, Wang XS, Zhang SF, He L. Effects of crystal size on the mechanical properties of a lithium disilicate glass-ceramic. Mater Sci Eng A. 2016 Jul 4;669:332–9.

39. Fernandes HR, Tulyaganov DU, Ferreira JMF. The role of P2O5, TiO2 and ZrO2 as nucleating agents on microstructure and crystallization behaviour of lithium disilicate-based glass. J Mater Sci. 2013 Jan 1;48(2):765–73.

40. Zheng X, Wen G, Song L, Huang XX. Effects of P2O5 and heat treatment on crystallization and microstructure in lithium disilicate glass ceramics. Acta Mater. 2008 Feb 1;56(3):549–58.

41. Miranda JS, Barcellos AS de P, Campos TMB, Cesar PF, Amaral M, Kimpara ET. Effect of repeated firings and staining on the mechanical behavior and composition of lithium disilicate. Dent Mater. 2020 May 1;36(5):e149–57.

42. Deubener J, Brückner R, Sternitzke M. Induction time analysis of nucleation and crystal growth in di- and metasilicate glasses. J Non-Cryst Solids. 1993 Oct 1;163(1):1–12.

43. Soares PC, Zanotto ED, Fokin VM, Jain H. TEM and XRD study of early crystallization of lithium disilicate glasses. J Non-Cryst Solids. 2003 Dec 1;331(1):217–27.

44. Holland D, Iqbal Y, James P, Lee B. Early stages of crystallisation of lithium disilicate glasses containing P2O5 – An NMR study. J Non-Cryst Solids. 1998 Jul 11;232–234:140–6.

45. Iqbal Y, Lee WE, Holland D, James PF. Metastable phase formation in the early stage crystallisation of lithium disilicate glass. J Non-Cryst Solids. 1998 Feb 1;224(1):1–16.

46. Zanotto ED. Metastable phases in lithium disilicate glasses. J Non-Cryst Solids. 1997 Oct 1;219:42–8.

47. Soares RS, Monteiro RCC, Lima MMRA, Silva RJC. Crystallization of lithium disilicate-based multicomponent glasses – effect of silica/lithia ratio. Ceram Int. 2015 Jan 1;41(1, Part A):317–24.

48. Höland W, Apel E, van ‘t Hoen Ch, Rheinberger V. Studies of crystal phase formations in high-strength lithium disilicate glass–ceramics. J Non-Cryst Solids. 2006 Oct 15;352(38):4041–50.

49. Krüger S, Deubener J, Ritzberger C, Höland W. Nucleation Kinetics of Lithium Metasilicate in ZrO2-Bearing Lithium Disilicate Glasses for Dental Application. Int J Appl Glass Sci. 2013;4(1):9–19.

50. Buchner S, Kulbieda FR, Fokin VM, Soares P, Machado ÁD, Schmelzer JWP, et al. Thermal stability of lithium metasilicate produced under high pressure from lithium disilicate glass. Int J Appl Glass Sci. 2019;10(4):522–31.

51. Goharian P, Nemati A, Shabanian M, Afshar A. Properties, crystallization mechanism and microstructure of lithium disilicate glass–ceramic. J Non-Cryst Solids. 2010 Feb 15;356(4):208–14.

52. Bischoff C, Eckert H, Apel E, M. Rheinberger V, Höland W. Phase evolution in lithium disilicate glass–ceramics based on non-stoichiometric compositions of a multi-component system: structural studies by 29 Si single and double resonance solid state NMR. Phys Chem Chem Phys. 2011;13(10):4540–51.

53. Borom MP, Turkalo AM, Doremus RH. Strength and Microstructure in Lithium Disilicate Glass-Ceramics. J Am Ceram Soc. 1975;58(9–10):385–91.

54. Sycheva GA. Crystal Growth and Nucleation in Glasses in the Lithium Silicate System. J Cryst Process Technol. 2016 Oct 25;6(4):29–55.

55. Zhang P, Li X, Yang J, Xu S. The crystallization and microstructure evolution of lithium disilicate-based glass-ceramic. J Non-Cryst Solids. 2014 Jun 1;392–393:26–30.

56. Huang S, Huang Z, Gao W, Cao P. Trace phase formation, crystallization kinetics and crystallographic evolution of a lithium disilicate glass probed by synchrotron XRD technique. Sci Rep. 2015 Mar 17;5(1):9159.

57. Iqbal Y, Lee WE, Holland D, James PF. Crystal nucleation in P2O5-doped lithium disilicate glasses. J Mater Sci. 1999 Sep 1;34(18):4399–411.

58. James PF, Iqbal Y, Jais US, Jordery S, Lee WE. Crystallisation of silicate and phosphate glasses. J Non-Cryst Solids. 1997 Oct 1;219:17–29.

59. Burgner LL, Weinberg MC, Lucas P, Soares PC, Zanotto ED. XRD investigation of metastable phase formation in Li2O–2SiO2 glass. J Non-Cryst Solids. 1999 Oct 1;255(2):264–8.

60. Burgner LL, Lucas P, Weinberg MC, Soares PC, Zanotto ED. On the persistence of metastable crystal phases in lithium disilicate glass. J Non-Cryst Solids. 2000 Sep 1;274(1):188–94.

61. Zanotto ED, Leite MLG. The nucleation mechanism of lithium dissilicate glass revisited. J Non-Cryst Solids. 1996 Jul 1;202(1):145–52.

62. Mastelaro VR, Zanotto ED. Anisotropic residual stresses in partially crystallized Li2O–2SiO2 glass-ceramics. J Non-Cryst Solids. 1999 Jun 2;247(1):79–86.

63. de Jong BHWS, Supèr HTJ, Spek AL, Veldman N, Nachtegaal G, Fischer JC. Mixed Alkali Systems: Structure and 29Si MASNMR of Li2Si2O5 and K2Si2O5. Acta Crystallogr B. 1998 Oct 1;54(5):568–77.

64. Seemann H. Die Kristallstruktur des Lithiummetasilikates, (Li2SiO3)x. Acta Crystallogr. 1956 Mar 10;9(3):251–2.

65. McKenzie ME, Mauro JC. Hybrid Monte Carlo technique for modeling of crystal nucleation and application to lithium disilicate glass-ceramics. Comput Mater Sci. 2018 Jun 15;149:202–7.

66. McKenzie ME, Goyal S, Loeffler T, Cai L, Dutta I, Baker DE, et al. Implicit glass model for simulation of crystal nucleation for glass-ceramics. Npj Comput Mater. 2018 Nov 6;4(1):1–7.

67. Sun W, Dierolf V, Jain H. Effects of Surface Orientation and Termination Plane on Glass-to-Crystal Transformation of Lithium Disilicate by Molecular Dynamics Simulations. Phys Status Solidi B. 2021;258(9):2000427.

68. Bradtmüller H, Gaddam A, Eckert H, Zanotto ED. Structural rearrangements during sub-Tg relaxation and nucleation in lithium disilicate glass revealed by a solid-state NMR and MD strategy. Acta Mater. 2022 Nov 1;240:118318.

69. Cormier L. Nucleation in Glasses – New Experimental Findings and Recent Theories. Procedia Mater Sci. 2014 Jan 1;7:60–71.

70. Schmelzer JWP, Fokin VM, Abyzov AS, Zanotto ED, Gutzow I. How Do Crystals Form and Grow in Glass-Forming Liquids: Ostwald's Rule of Stages and Beyond. Int J Appl Glass Sci. 2010;1(1):16–26.

71. Kelton KF. Crystal Nucleation in Liquids and Glasses. In: Ehrenreich H, Turnbull D, editors. Solid State Physics [Internet]. Academic Press; 1991 [cited 2022 Nov 30]. p. 75–177. Available from: https://www.sciencedirect.com/science/article/pii/S0081194708601447

72. Fokin VM, Abyzov AS, Zanotto ED, Cassar DR, Rodrigues AM, Schmelzer JWP. Crystal nucleation in glass-forming liquids: Variation of the size of the "structural units" with temperature. J Non-Cryst Solids. 2016 Sep 1;447:35–44.

73. Deubener J. Structural aspects of volume nucleation in silicate glasses. J Non-Cryst Solids. 2005 Jun 15;351(18):1500–11.

74. Vekilov PG. Nucleation. Cryst Growth Des. 2010 Dec 1;10(12):5007–19.

75. Burgner LL. Crystallization kinetics of lithium disilicate and sodium silicate glasses. The University of Arizona ProQuest Dissertations Publishing; 2000.

76. Prado SCC, Rino JP, Zanotto ED. Successful test of the classical nucleation theory by molecular dynamic simulations of BaS. Comput Mater Sci. 2019 Apr 15;161:99–106.

77. Cappelezzo M, Capellari CA, Pezzin SH, Coelho L a. F. Stokes-Einstein relation for pure simple fluids. J Chem Phys. 2007 Jun 14;126(22):224516.

78. Zanotto ED, James PF. Experimental tests of the classical nucleation theory for glasses. J Non-Cryst Solids. 1985 Nov 1;74(2):373–94.

79. JAMES P. KINETICS OF CRYSTAL NUCLEATION IN LITHIUM SILICATE GLASSES. Kinet Cryst NUCLEATION LITHIUM Silic Glas. 1974;

80. Weinberg MC, Zanotto ED. Re-examination of the temperature dependence of the classical nucleation rate: Homogeneous crystal nucleation in glass. J Non-Cryst Solids. 1989 Feb 1;108(1):99–108.

81. Gonzalez-Oliver CJR, James PF. Crystal nucleation and growth in a Na2O.2CaO.3SiO2 glass. J Non-Cryst Solids. 1980 May 1;38–39:699–704.

82. Abyzov AS, Fokin VM, Rodrigues AM, Zanotto ED, Schmelzer JWP. The effect of elastic stresses on the thermodynamic barrier for crystal nucleation. J Non-Cryst Solids. 2016 Jan 15;432:325–33.

83. Tolman RC. The Effect of Droplet Size on Surface Tension. J Chem Phys. 1949 Mar;17(3):333–7.

84. Greenwood GW, Greer AL, Herlach DM, Kelton KF, Zanotto ED, Fokin VM. Recent studies of internal and surface nucleation in silicate glasses. Philos Trans R Soc Lond Ser Math Phys Eng Sci. 2003 Jan 29;361(1804):591–613.

85. Cassar DR, Serra AH, Peitl O, Zanotto ED. Critical assessment of the alleged failure of the Classical Nucleation Theory at low temperatures. J Non-Cryst Solids. 2020 Nov 1;547:120297.

86. Ramírez Acosta MH, Raphael Rodrigues L, Cassar DR, Montazerian M, Peitl Filho O, Dutra Zanotto E. Further evidence against the alleged failure of the classical nucleation theory below the glass transition range. J Am Ceram Soc. 2021;104(9):4537–49.

87. Fokin VM, Zanotto ED, Yuritsyn NS, Schmelzer JWP. Homogeneous crystal nucleation in silicate glasses: A 40 years perspective. J Non-Cryst Solids. 2006 Aug 1;352(26):2681–714.

88. Deubener J. Compositional onset of homogeneous nucleation in (Li, Na) disilicate glasses. J Non-Cryst Solids. 2000 Sep 1;274(1):195–201.

89. Fokin VM, Zanotto ED, Schmelzer JWP. Homogeneous nucleation versus glass transition temperature of silicate glasses. J Non-Cryst Solids. 2003 Jun 15;321(1):52–65.

90. Zanotto ED. Isothermal and adiabatic nucleation in glass. J Non-Cryst Solids. 1987 Mar 1;89(3):361–70.

91. Sen S, Mukerji T. A generalized classical nucleation theory for rough interfaces: application in the analysis of homogeneous nucleation in silicate liquids. J Non-Cryst Solids. 1999 May 1;246(3):229–39.

92. Schmelzer JWP, Gokhman AR, Fokin VM. Dynamics of first-order phase transitions in multicomponent systems: a new theoretical approach. J Colloid Interface Sci. 2004 Apr 1;272(1):109–33.

93. Schmelzer JWP, Boltachev GSh, Baidakov VG. Classical and generalized Gibbs' approaches and the work of critical cluster formation in nucleation theory. J Chem Phys. 2006 May 21;124(19):194503.

94. Guo C, Wang J, Li J, Wang Z, Tang S. Kinetic Pathways and Mechanisms of Two-Step Nucleation in Crystallization. J Phys Chem Lett. 2016 Dec 15;7(24):5008–14.

95. Gebauer D, Kellermeier M, D. Gale J, Bergström L, Cölfen H. Pre-nucleation clusters as solute precursors in crystallisation. Chem Soc Rev. 2014;43(7):2348–71.

96. Ostwald W. Studien über die Bildung und Umwandlung fester Körper: 1. Abhandlung: Übersättigung und Überkaltung. Z Für Phys Chem. 1897 Feb 1;22U(1):289–330.

97. Chung SY, Kim YM, Kim JG, Kim YJ. Multiphase transformation and Ostwald's rule of stages during crystallization of a metal phosphate. Nat Phys. 2009 Jan;5(1):68–73.

98. Lutsko JF, Nicolis G. Theoretical Evidence for a Dense Fluid Precursor to Crystallization. Phys Rev Lett. 2006 Feb 2;96(4):046102.

99. Vekilov PG. Dense Liquid Precursor for the Nucleation of Ordered Solid Phases from Solution. Cryst Growth Des. 2004 Jul 1;4(4):671–85.

100. Allen MP. Introduction to Molecular Dynamics Simulation. Computational soft matter: from synthetic polymers to proteins; 2004. 1–28 p. (NIC; vol. 23).

101. Allen MP, Tildesley DJ. Computer Simulation of Liquids. Oxford University Press; 2017. 641 p.

102. Rowlinson * JS. The Maxwell–Boltzmann distribution. Mol Phys. 2005 Nov 10;103(21–23):2821–8.

103. Alder BJ, Wainwright TE. Studies in Molecular Dynamics. I. General Method. J Chem Phys. 1959 Aug;31(2):459–66.

104. Grubmüller H, Heller H, Windemuth A, Schulten K. Generalized Verlet Algorithm for Efficient Molecular Dynamics Simulations with Long-range Interactions. Mol Simul. 1991 Mar 1;6(1–3):121–42.

105. Van Gunsteren WF, Berendsen HJC. A Leap-frog Algorithm for Stochastic Dynamics. Mol Simul. 1988 Mar 1;1(3):173–85.

106. Hansen JP, McDonald IR, editors. Theory of Simple Liquids. In: Theory of Simple Liquids (Fourth Edition) [Internet]. Oxford: Academic Press; 2013 [cited 2023 Jan 20]. p. i. Available from: https://www.sciencedirect.com/science/article/pii/B9780123870322000131

107. Combes JM, Duclos P, Seiler R. The Born-Oppenheimer Approximation. In: Velo G, Wightman AS, editors. Rigorous Atomic and Molecular Physics [Internet]. Boston, MA: Springer US; 1981 [cited 2023 Jan 20]. p. 185–213. (NATO Advanced Study Institutes Series). Available from: https://doi.org/10.1007/978-1-4613-3350-0_5

108. Woodcock LV, Angell CA, Cheeseman P. Molecular dynamics studies of the vitreous state: Simple ionic systems and silica. J Chem Phys. 1976 Aug 15;65(4):1565–77.

109. Soules TF. Molecular dynamic calculations of glass structure and diffusion in glass. J Non-Cryst Solids. 1982 May 1;49(1):29–52.

110. Soules TF. A molecular dynamic calculation of the structure of sodium silicate glasses. J Chem Phys. 1979 Dec;71(11):4570–8.

111. Mitra SK, Hockney RW. Molecular dynamics simulation of the structure of soda silica. Philos Mag B. 1983 Aug 1;48(2):151–67.

112. Garofalini SH. A molecular dynamics simulation of the vitreous silica surface. J Chem Phys. 1983 Feb 15;78(4):2069–72.

113. Pedone A, Bertani M, Brugnoli L, Pallini A. Interatomic potentials for oxide glasses: Past, present, and future. J Non-Cryst Solids X. 2022 Sep 1;15:100115.

114. Pedone A, Malavasi G, Menziani MC, Cormack AN, Segre U. A New Self-Consistent Empirical Interatomic Potential Model for Oxides, Silicates, and Silica-Based Glasses. J Phys Chem B. 2006 Jun 1;110(24):11780–95.

115. Vashishta P, Kalia RK, Rino JP, Ebbsjö I. Interaction potential for ${\mathrm{SiO}}_{2}$: A molecular-dynamics study of structural correlations. Phys Rev B. 1990 Jun 15;41(17):12197–209.

116. Feuston BP, Garofalini SH. Empirical three-body potential for vitreous silica. J Chem Phys. 1988 Nov;89(9):5818–24.

117. Bertani M, Menziani MC, Pedone A. Improved empirical force field for multicomponent oxide glasses and crystals. Phys Rev Mater. 2021 Apr 7;5(4):045602.

118. Frisch M, Trucks G, Schlegel H, Scuseria G, Robb M, Cheeseman J, et al. Gaussian 09 (Revision A02). Gaussian Inc Wallingford CT. 2009 Jan 1;

119. Toukmaji AY, Board JA. Ewald summation techniques in perspective: a survey. Comput Phys Commun. 1996 Jun 1;95(2):73–92.

120. Deserno M, Holm C. How to mesh up Ewald sums. II. An accurate error estimate for the particle–particle–particle-mesh algorithm. J Chem Phys. 1998 Nov 8;109(18):7694–701.

121. Essmann U, Perera L, Berkowitz ML, Darden T, Lee H, Pedersen LG. A smooth particle mesh Ewald method. J Chem Phys. 1995 Nov 15;103(19):8577–93.

122. Carré A, Berthier L, Horbach J, Ispas S, Kob W. Amorphous silica modeled with truncated and screened Coulomb interactions: A molecular dynamics simulation study. J Chem Phys. 2007 Sep 21;127(11):114512.

123. Fennell CJ, Gezelter JD. Is the Ewald summation still necessary? Pairwise alternatives to the accepted standard for long-range electrostatics. J Chem Phys. 2006 Jun 21;124(23):234104.

124. Nose S. Constant-temperature molecular dynamics. J Phys Condens Matter. 1990 Dec;2(S):SA115.

125. Martyna GJ, Tobias DJ, Klein ML. Constant pressure molecular dynamics algorithms. J Chem Phys. 1994 Sep;101(5):4177–89.

126. Moore CC. Ergodic theorem, ergodic theory, and statistical mechanics. Proc Natl Acad Sci. 2015 Feb 17;112(7):1907–11.

127. Baidakov VG, Protsenko KR. Spontaneous Crystallization of a Supercooled Lennard-Jones Liquid: Molecular Dynamics Simulation. J Phys Chem B. 2019 Sep 26;123(38):8103–12.

128. Tipeev AO, Zanotto ED. Nucleation kinetics in supercooled Ni50Ti50: Computer simulation data corroborate the validity of the Classical Nucleation Theory. Chem Phys Lett. 2019 Nov 16;735:136749.

129. Tipeev AO, Zanotto ED, Rino JP. Crystal Nucleation Kinetics in Supercooled Germanium: MD Simulations versus Experimental Data. J Phys Chem B. 2020 Sep 10;124(36):7979–88.

130. Valsson O, Tiwary P, Parrinello M. Enhancing Important Fluctuations: Rare Events and Metadynamics from a Conceptual Viewpoint. Annu Rev Phys Chem. 2016;67(1):159–84.

131. Barducci A, Bonomi M, Parrinello M. Metadynamics. WIREs Comput Mol Sci. 2011;1(5):826–43.

132. Laio A, Parrinello M. Escaping free-energy minima. Proc Natl Acad Sci. 2002 Oct;99(20):12562–6.

133. Giberti F, Salvalaglio M, Mazzotti M, Parrinello M. Insight into the nucleation of urea crystals from the melt. Chem Eng Sci. 2015 Jan 6;121:51–9.

134. Gaines E, Maisuria K, Tommaso DD. The role of solvent in the self-assembly of m-aminobenzoic acid: a density functional theory and molecular dynamics study. CrystEngComm. 2016 Apr 18;18(16):2937–48.

135. Quigley D, Rodger PM. Free energy and structure of calcium carbonate nanoparticles during early stages of crystallization. J Chem Phys. 2008 Jun 14;128(22):221101.

136. Piaggi PM, Valsson O, Parrinello M. Enhancing Entropy and Enthalpy Fluctuations to Drive Crystallization in Atomistic Simulations. Phys Rev Lett. 2017 Jul 6;119(1):015701.

137. Ahlawat P, Dar MI, Piaggi P, Grätzel M, Parrinello M, Rothlisberger U. Atomistic Mechanism of the Nucleation of Methylammonium Lead Iodide Perovskite from Solution. Chem Mater. 2020 Jan 14;32(1):529–36.

138. Ronneberger I, Zhang W, Eshet H, Mazzarello R. Crystallization Properties of the Ge2Sb2Te5 Phase-Change Compound from Advanced Simulations. Adv Funct Mater. 2015;25(40):6407–13.

139. Ahlawat P, Hinderhofer A, Alharbi EA, Lu H, Ummadisingu A, Niu H, et al. A combined molecular dynamics and experimental study of two-step process enabling low-temperature formation of phase-pure α-FAPbI3. Sci Adv. 2021 Oct 19;7(17):eabe3326.

140. Niu H, Piaggi PM, Invernizzi M, Parrinello M. Molecular dynamics simulations of liquid silica crystallization. Proc Natl Acad Sci. 2018 May 22;115(21):5348–52.

141. Zhang YY, Niu H, Piccini G, Mendels D, Parrinello M. Improving collective variables: The case of crystallization. J Chem Phys. 2019 Mar 7;150(9):094509.

142. Invernizzi M, Parrinello M. Making the Best of a Bad Situation: A Multiscale Approach to Free Energy Calculation. J Chem Theory Comput. 2019 Apr 9;15(4):2187–94.

143. Torrie GM, Valleau JP. Nonphysical sampling distributions in Monte Carlo free-energy estimation: Umbrella sampling. J Comput Phys. 1977 Feb 1;23(2):187–99.

144. Kästner J. Umbrella sampling. WIREs Comput Mol Sci. 2011;1(6):932–42.

145. Laio A, Gervasio FL. Metadynamics: a method to simulate rare events and reconstruct the free energy in biophysics, chemistry and material science. Rep Prog Phys. 2008 Nov;71(12):126601.

146. Bussi G, Laio A. Using metadynamics to explore complex free-energy landscapes. Nat Rev Phys. 2020 Apr;2(4):200–12.

147. Barducci A, Bussi G, Parrinello M. Well-Tempered Metadynamics: A Smoothly Converging and Tunable Free-Energy Method. Phys Rev Lett. 2008 Jan 18;100(2):020603.

148. Laio A, Rodriguez-Fortea A, Gervasio FL, Ceccarelli M, Parrinello M. Assessing the Accuracy of Metadynamics. J Phys Chem B. 2005 Apr 1;109(14):6714–21.

149. Singh S, Chiu C cheng, de Pablo JJ. Flux Tempered Metadynamics. J Stat Phys. 2011 Nov 1;145(4):932–45.

150. Tiwary P, Parrinello M. A Time-Independent Free Energy Estimator for Metadynamics. J Phys Chem B. 2015 Jan 22;119(3):736–42.

151. Schäfer TM, Settanni G. Data Reweighting in Metadynamics Simulations. J Chem Theory Comput. 2020 Apr 14;16(4):2042–52.

152. Bussi G, Tribello GA. Analyzing and Biasing Simulations with PLUMED. Methods Mol Biol. 2019;

153. Karmakar T, Invernizzi M, Rizzi V, Parrinello M. Collective variables for the study of crystallisation. Mol Phys. 2021 Mar 1;0(0):e1893848.

154. Neha, Tiwari V, Mondal S, Kumari N, Karmakar T. Collective Variables for Crystallization Simulations─from Early Developments to Recent Advances. ACS Omega [Internet]. 2022 Dec 27 [cited 2023 Jan 2]; Available from: https://doi.org/10.1021/acsomega.2c06310

155. Warren BE. X-ray Diffraction. Courier Corporation; 1990. 402 p.

156. Lodesani F, Tavanti F, Menziani MC, Maeda K, Takato Y, Urata S, et al. Exploring the crystallization path of lithium disilicate through metadynamics simulations. Phys Rev Mater. 2021 Jul 30;5(7):075602.

157. Lodesani F, Menziani MC, Urata S, Pedone A. Biasing crystallization in fused silica: An assessment of optimal metadynamics parameters. J Chem Phys. 2022 May 21;156(19):194501.

158. Quigley D, Rodger PM. A metadynamics-based approach to sampling crystallisation events. Mol Simul. 2009 Jun 1;35(7):613–23.

159. Separdar L, Rino JP, Zanotto ED. Molecular dynamics simulations of spontaneous and seeded nucleation and theoretical calculations for zinc selenide. Comput Mater Sci. 2021 Feb 1;187:110124.

160. Zou Y, Xiang S, Dai C. Investigation on the efficiency and accuracy of methods for calculating melting temperature by molecular dynamics simulation. Comput Mater Sci. 2020 Jan 1;171:109156.

161. Lodesani F, Menziani MC, Hijiya H, Takato Y, Urata S, Pedone A. Structural origins of the Mixed Alkali Effect in Alkali Aluminosilicate Glasses: Molecular Dynamics Study and its Assessment. Sci Rep. 2020 Feb 19;10(1):2906.

162. Yip S, Li J, Tang M, Wang J. Mechanistic aspects and atomic-level consequences of elastic instabilities in homogeneous crystals. Mater Sci Eng A. 2001 Oct 31;317(1):236–40.

163. Dozhdikov VS, Basharin AYu, Levashov PR. Two-phase simulation of the crystalline silicon melting line at pressures from –1 to 3 GPa. J Chem Phys. 2012 Aug 7;137(5):054502.

164. Humphrey W, Dalke A, Schulten K. VMD: Visual molecular dynamics. J Mol Graph. 1996 Feb 1;14(1):33–8.

165. Chen ET, Barnett RN, Landman U. Crystal-melt and melt-vapor interfaces of nickel. Phys Rev B. 1989 Jul 15;40(2):924–32.

166. Ribeiro-Silva CI, Rino JP, Gonçalves LGV, Picinin A. An effective interaction potential for gallium phosphide. J Phys Condens Matter. 2011 Jan;23(5):055801.

167. Zhang W, Peng Y, Liu Z. Molecular dynamics simulations of the melting curve of NiAl alloy under pressure. AIP Adv. 2014 May;4(5):057110.

168. Lusvardi G, Malavasi G, Menabue L, Menziani MC, Pedone A, Segre U. A Computational Tool for the Prediction of Crystalline Phases Obtained from Controlled Crystallization of Glasses. J Phys Chem B. 2005 Nov 1;109(46):21586–92.

169. Sapozhnikov FA, Ionov GV, Dremov VV. An adaptive template method for analyzing crystal structures and defects in molecular dynamics simulations of high-rate deformations. Russ J Phys Chem B. 2008 Apr 1;2(2):238–45.

170. Smith W, Forester TR. DL_POLY_2.0: A general-purpose parallel molecular dynamics simulation package. J Mol Graph. 1996 Jun 1;14(3):136–41.

171. Longstaffe JG, Werner-Zwanziger U, Schneider JF, Nascimento MLF, Zanotto ED, Zwanziger JW. Intermediate-Range Order of Alkali Disilicate Glasses and Its Relation to the Devitrification Mechanism. J Phys Chem C. 2008 Apr 1;112(15):6151–9.

172. Mastelaro VR, Zanotto ED, Lequeux N, Cortès R. Relationship between short-range order and ease of nucleation in Na2Ca2Si3O9, CaSiO3 and PbSiO3 glasses. J Non-Cryst Solids. 2000 Feb 1;262(1):191–9.

173. Van Vleck JH. The Dipolar Broadening of Magnetic Resonance Lines in Crystals. Phys Rev. 1948 Nov 1;74(9):1168–83.

174. Zanotto ED, Müller E. A simple method to predict the nucleation mechanism in glass. J Non-Cryst Solids. 1991 Jul 1;130(2):220–1.

175. Espinosa JR, Vega C, Valeriani C, Sanz E. Seeding approach to crystal nucleation. J Chem Phys. 2016 Jan 21;144(3):034501.

176. Sanz E, Vega C, Espinosa JR, Caballero-Bernal R, Abascal JLF, Valeriani C. Homogeneous Ice Nucleation at Moderate Supercooling from Molecular Simulation. J Am Chem Soc. 2013 Oct 9;135(40):15008–17.

177. Espinosa JR, Sanz E, Valeriani C, Vega C. Homogeneous ice nucleation evaluated for several water models. J Chem Phys. 2014 Nov 14;141(18):18C529.

178. Goswami A, Dalal IS, Singh JK. Seeding method for ice nucleation under shear. J Chem Phys. 2020 Sep 7;153(9):094502.

179. Zimmermann NER, Vorselaars B, Quigley D, Peters B. Nucleation of NaCl from Aqueous Solution: Critical Sizes, Ion-Attachment Kinetics, and Rates. J Am Chem Soc. 2015 Oct 21;137(41):13352–61.

180. Sun Y, Song H, Zhang F, Yang L, Ye Z, Mendelev MI, et al. Overcoming the Time Limitation in Molecular Dynamics Simulation of Crystal Nucleation: A Persistent-Embryo Approach. Phys Rev Lett. 2018 Feb 23;120(8):085703.

181. Allen MP, Tildesley DJ. Computer Simulation of Liquids. Clarendon Press; 1989. 412 p.

182. Sycheva GA. Homogeneous and Heterogeneous Crystal Nucleation in Glass of the Li2O–SiO2 System. Glass Phys Chem. 2018 May 1;44(3):183–91.

183. Urata S. An efficient computational procedure to obtain a more stable glass structure. J Chem Phys. 2019 Dec 14;151(22):224502.

184. Soares RS, Monteiro RCC, Lima MMRA, Silva RJC. Crystallization of lithium disilicate-based multicomponent glasses – effect of silica/lithia ratio. Ceram Int. 2015 Jan 1;41(1, Part A):317–24.

185. Fokin VM, Zanotto ED. Crystal nucleation in silicate glasses: the temperature and size dependence of crystal/liquid surface energy. J Non-Cryst Solids. 2000 Mar 2;265(1):105–12.

186. Bussi G, Branduardi D. Free-Energy Calculations with Metadynamics: Theory and Practice [Internet]. Reviews in Computational Chemistry Volume 28. 2015 [cited 2021 Oct 12]. Available from: https://www.infona.pl//resource/bwmeta1.element.wiley-6143-n9781118889886-ch1

187. Heaney PJ, Prewitt CT, Gibbs GV. Silica: Physical Behavior, Geochemistry, and Materials Applications. Walter de Gruyter GmbH & Co KG; 2018. 624 p.

188. Wagstaff FE. Crystallization and Melting Kinetics of Cristobalite. J Am Ceram Soc. 1969;52(12):650–4.

189. Bourova E, Richet P. Quartz and Cristobalite: high-temperature cell parameters and volumes of fusion. Geophys Res Lett. 1998;25(13):2333–6.

190. Peacor DB. High-temperature single-crystal study of the cristobalite inversion. Z Für Krist - Cryst Mater. 1973 Dec 1;138(1–6):274–98.

191. Thompson AP, Aktulga HM, Berger R, Bolintineanu DS, Brown WM, Crozier PS, et al. LAMMPS - a flexible simulation tool for particle-based materials modeling at the atomic, meso, and continuum scales. Comput Phys Commun. 2022 Feb 1;271:108171.

192. Tribello GA, Bonomi M, Branduardi D, Camilloni C, Bussi G. PLUMED 2: New feathers for an old bird. Comput Phys Commun. 2014 Feb 1;185(2):604–13.

193. The PLUMED consortium. Promoting transparency and reproducibility in enhanced molecular simulations. Nat Methods. 2019 Aug;16(8):670–3.

194. Evans DJ, Holian BL. The Nose–Hoover thermostat. J Chem Phys. 1985 Oct 15;83(8):4069–74.

195. Bussi G, Laio A, Tiwary P. Metadynamics: A Unified Framework for Accelerating Rare Events and Sampling Thermodynamics and Kinetics. In: Andreoni W, Yip S, editors. Handbook of Materials Modeling: Methods: Theory and Modeling [Internet]. Cham: Springer International Publishing;

2020 [cited 2021 Nov 23]. p. 565–95. Available from: https://doi.org/10.1007/978-3-319-44677-6_49

196. Crespo Y, Marinelli F, Pietrucci F, Laio A. Metadynamics convergence law in a multidimensional system. Phys Rev E. 2010 May 7;81(5):055701.

197. Sycheva GA. 50-Year Anniversary of the Method of Determining the Parameters of Crystal Nucleation in Inorganic Glasses. Inorg Mater. 2020 Dec 1;56(13):1338–51.

198. Piaggi PM, Parrinello M. Entropy based fingerprint for local crystalline order. J Chem Phys. 2017 Sep 21;147(11):114112.

199. Tribello GA, Giberti F, Sosso GC, Salvalaglio M, Parrinello M. Analyzing and Driving Cluster Formation in Atomistic Simulations. J Chem Theory Comput. 2017 Mar 14;13(3):1317–27.

200. Deng B, Shi Y, Yuan F. Investigation on the structural origin of low thermal expansion coefficient of fused silica. Materialia. 2020 Aug 1;12:100752.

201. Vollmayr K, Kob W, Binder K. Cooling-rate effects in amorphous silica: A computer-simulation study. Phys Rev B. 1996 Dec 1;54(22):15808–27.

202. Lodesani F, Menziani MC, Maeda K, Takato Y, Urata S, Pedone A. Disclosing crystal nucleation mechanism in lithium disilicate glass through molecular dynamics simulations and free-energy calculations. Sci Rep. 2020 Oct 20;10(1):17867.

203. Habasaki J, Ngai KL. Molecular dynamics study of heterogeneous dynamics in lithium disilicate crystal. J Electroceramics. 2015 Feb 1;34(1):43–56.

204. Gonçalves LGV, Rino JP. Diffusion mechanisms in lithium disilicate melt by molecular dynamics simulation. J Non-Cryst Solids. 2014 Oct 15;402:91–5.

205. Gaddam A, Fernandes HR, Tulyaganov DU, Ribeiro MJ, Ferreira JMF. The roles of P2O5 and SiO2/Li2O ratio on the network structure and crystallization kinetics of non-stoichiometric lithium disilicate based glasses. J Non-Cryst Solids. 2018 Feb 1;481:512–21.

206. Huang S, Huang Z, Gao W, Cao P. In Situ High-Temperature Crystallographic Evolution of a Nonstoichiometric Li2O·2SiO2 Glass. Inorg Chem. 2013 Dec 16;52(24):14188–95.

207. Hénin J, Lelièvre T, Shirts MR, Valsson O, Delemotte L. Enhanced sampling methods for molecular dynamics simulations. Living J Comput Mol Sci [Internet]. 2022 [cited 2023 Mar 8];4(1). Available from: http://arxiv.org/abs/2202.04164

208. Branduardi D, Bussi G, Parrinello M. Metadynamics with Adaptive Gaussians. J Chem Theory Comput. 2012 Jul 10;8(7):2247–54.

209. Valsson O, Parrinello M. Variational Approach to Enhanced Sampling and Free Energy Calculations. Phys Rev Lett. 2014 Aug 27;113(9):090601.

210. Invernizzi M, Parrinello M. Rethinking Metadynamics: From Bias Potentials to Probability Distributions. J Phys Chem Lett. 2020 Apr 2;11(7):2731–6.

211. Invernizzi M. OPES: On-the-fly Probability Enhanced Sampling Method. Il Nuovo Cimento C. 2021 Sep 3;44(405):1–4.

212. Bussi G, Gervasio FL, Laio A, Parrinello M. Free-Energy Landscape for β Hairpin Folding from Combined Parallel Tempering and Metadynamics. J Am Chem Soc. 2006 Oct 1;128(41):13435–41.

213. Hukushima K, Nemoto K. Exchange Monte Carlo Method and Application to Spin Glass Simulations. J Phys Soc Jpn. 1996 Jun 15;65(6):1604–8.

214. Sugita Y, Okamoto Y. Replica-exchange molecular dynamics method for protein folding. Chem Phys Lett. 1999 Nov 26;314(1):141–51.

215. Lam J, Pietrucci F. Critical comparison of general-purpose collective variables for crystal nucleation. Phys Rev E. 2023 Jan 24;107(1):L012601.

216. Bonati L, Rizzi V, Parrinello M. Data-Driven Collective Variables for Enhanced Sampling. J Phys Chem Lett. 2020 Apr 16;11(8):2998–3004.

217. Chen M. Collective variable-based enhanced sampling and machine learning. Eur Phys J B. 2021 Oct 20;94(10):211.

LIST OF PUBLICATIONS

1. Muniz-Miranda, F.; Lodesani, F.; Tavanti, F.; Presti, D.; Malferrari, D.; Pedone, A. *Supercritical CO2 Confined in Palygorskite and Sepiolite Minerals: A Classical Molecular Dynamics Investigation*. The Journal of Physical Chemistry C **2016**, 120 (47), 26945–26954. https://doi.org/10.1021/acs.jpcc.6b09983.

2. Lodesani, F.; Menziani, M. C.; Hijiya, H.; Takato, Y.; Urata, S.; Pedone, A. *Structural Origins of the Mixed Alkali Effect in Alkali Aluminosilicate Glasses: Molecular Dynamics Study and Its Assessment*. Scientific Reports **2020**, 10 (1), 2906. https://doi.org/10.1038/s41598-020-59875-7.

3. Lodesani, F.; Menziani, M. C.; Maeda, K.; Takato, Y.; Urata, S.; Pedone, A. *Disclosing Crystal Nucleation Mechanism in Lithium Disilicate Glass through Molecular Dynamics Simulations and Free-Energy Calculations*. Scientific Reports **2020**, 10 (1), 17867. https://doi.org/10.1038/s41598-020-74764-9.

4. Delaye, J.-M.; Gac, A. L.; Macaluso, S.; Angeli, F.; Lodesani, F.; Charpentier, T.; Peuget, S. *Investigation of Alumino-Silicate Glasses by Coupling Experiments and Simulations: Part I - Structures*. Journal of Non-Crystalline Solids **2021**, 567, 120936. https://doi.org/10.1016/j.jnoncrysol.2021.120936.

5. Delaye, J.-M.; Le Gac, A.; Macaluso, S.; Angeli, F.; Lodesani, F.; Charpentier, T.; Peuget, S. *Investigation of Alumino-Silicate Glasses by Coupling Experiments and Simulations: Part II - Radiation Effects*. Journal of Non-Crystalline Solids **2021**, 569, 120969. https://doi.org/10.1016/j.jnoncrysol.2021.120969.

6. Lodesani, F.; Tavanti, F.; Menziani, M. C.; Maeda, K.; Takato, Y.; Urata, S.; Pedone, A. *Exploring the Crystallization Path of Lithium Disilicate through Metadynamics Simulations*. Physical Review Materials **2021**, 5 (7), 075602. https://doi.org/10.1103/PhysRevMaterials.5.075602.

7. Lodesani, F.; Menziani, M. C.; Urata, S.; Pedone, A. *Biasing Crystallization in Fused Silica: An Assessment of Optimal Metadynamics Parameters*. The Journal of Chemical Physics **2022**, 156 (19), 194501. https://doi.org/10.1063/5.0089183

8. Lodesani, F.; Menziani, M. C.; Urata, S.; Pedone, A. *Evidence of Multiple Crystallization Pathways in Lithium Disilicate: a Metadynamics Investigation*. The Journal of Physical Chemistry Letters **2023**,14, 1411–1417. https://doi.org/10.1021/acs.jpclett.2c03563